Heterogeneous (HG) Blankets for Improved Aircraft Interior Noise Reduction

Kamal Idrisi

Dissertation submitted to the faculty of the
Virginia Polytechnic Institute and State University
in partial fulfillment of the requirements for the degree of

Doctor of Philosophy
in
Mechanical Engineering

Marty Johnson, Chairman
James Carneal
Rob Clark
Daniel Inman
Alessandro Toso
Ralf Gramlich

November 6, 2008

Blacksburg, VA

Key words: vibration-damping materials and structures, sound isolating elements, impedance and mobility methods (IMM)

Heterogeneous (HG) Blankets for Improved Aircraft Interior Noise Reduction

Kamal Idrisi
Marty Johnson, Chairman
Vibrations and Acoustics Laboratories

(ABSTRACT)

This study involves the modeling and optimization of heterogeneous (HG) blankets for improved reduction of the sound transmission through double-panel systems at low frequencies. HG blankets consist of poro-elastic media with small, embedded masses, operating similar to a distributed mass-spring-damper system. Although most traditional poro-elastic materials have failed to effectively reduce low-frequency, radiated sound from structures, HG blankets show significant potential.

A design tool predicting the response of a single-bay double panel system (DPS) with, acoustic cavity, HG blanket and radiated field, later a multi-bay DPS with frames, stringers, mounts, and four HG blankets, was developed and experimentally validated using impedance and mobility methods (IMM). A novel impedance matrix formulation for the HG blanket is derived and coupled to the DPS using an assembled matrix approach derived from the IMM.

Genetic algorithms coupled with the previously described design tool of the DPS with the HG blanket treatment can optimize HG blanket design. This study presents a comparison of the performance obtained using the genetic algorithm optimization routine and a novel interactive optimization routine based on sequential addition of masses in the blanket.

This research offers a detailed analysis of the behavior of the mass inclusions, highlighting controlled stiffness variation of the mass-spring-damper systems inside the HG blanket. A novel, empirical approach to predict the natural frequency of different

mass shapes embedded in porous media was derived and experimentally verified for many different types of porous media. In addition, simplifying a model for poro-elastic materials for low frequencies that Biot and Allard originally proposed and implementing basic elastomechanical solutions produce a novel analytical approach to describe the interaction of the mass inclusions with a poro-elastic layer.

A full-scale fuselage experiment performed on a Gulfstream section involves using the design tool for the positions of the mass inclusions, and the results of the previously described empirical approach facilitate tuning of the natural frequencies of the mass inclusions to the desired natural frequencies. The presented results indicate that proper tuning of the HG blankets can result in broadband noise reduction below 500Hz with less than 10% added mass.

To my parents Jamila and Abderrahman and my grandfather Driss

Acknowledgements

First, I would like to express my sincere gratitude to my advisor, Dr. Marty Johnson, for being an amazing mentor and great friend. Words cannot describe how thankful I am for having had the opportunity to work with him for the last three years.

I would like to acknowledge my committee member and good friend Dr. Ralf Gramlich who has been my mentor throughout my undergraduate studies at Technical University of Darmstadt (TUD). He is the main reason why I wanted to become a Ph.D in first place.

I would also like to express my gratitude to Dr. James Carneal who was my co-advisor for the first half of my doctorial studies. Thank you for helping me to grow as a person and as a researcher.

This project was supported by SMD Corp. under a NASA SBIR grant A2.04-9836. I am thankful to my committee member and sponsor, Dr. Robert Clark, for encouraging and supporting me throughout my research. Also, thanks to my co-sponsor Curtis Michel for the great input throughout the SMD presentations. I would like to thank my committee members Dr. Daniel Inman as well as Dr. Alessandro Toso for helping and guiding me every time they had a chance.

I would like to thank the director of the Vibrations and Acoustics Laboratories, Dr. Chris Fuller coming, who came up with the 'Heterogeneous Blankets' idea in first place. My thesis wouldn't even exist without him.

Special thanks to Dr. Manfred Hampe and Barbara Seifert at TUD for giving me the opportunity to study abroad at Virginia Tech as well as for supporting me throughout the last three years. Also, thanks to Dr. Holger Hanselka for supporting my future carrerer.

I would like to thank Dr. Paolo Gardonio for the chance to work with him at the Institute of Sound and Vibration in Southampton over the past summer. I based a lot of my research on his theories which is why I was honored to work with him in first place. He is one of the most positive thinking and encouraging professors I have met so far in my life.

I would especially like to thank Dr. Mike Kidner for all the great input at the beginning of my doctorial studies. It has been a pleasure to work with him as he is an expert in the field of poro-elastic media.

Next, I would like to thank the VAL family. It has been a great pleasure working with them over the past years. I couldn't think of a better work environment. I would especially like to thank Gail Coe, my "American mother", for all the great support. Thanks to Dan Mennitt for his great input and help as well as for being an amazing office mate. Special thanks to my colleagues Ben Smith, Tim Wiltgen, Min Lee for that unbelievable trip to Panama City during Spring Break '07. I would also like to thank the various past and current members: Cory Papenfuss, Marcel Remilleux, Tom Saux, Mark Sumner, Philip Gillett, Elizabeth Hoppe, Yannic Morel, Sean Egger, and Kyle Schwartz. I wish them all great success in their future academic and professional lives.

I would also like to thank my former students: Rachel Scott, Parham Sahidi, Holger Werschnik, Florian Boess, and of course the German dream team Andreas Wagner and David Bartylla.

Being so far away from home over the last three years would have not been easy without the support of my friends here in the U.S. My sincere gratitude to my great friend Judicita Condezo and her parents Oscar and Carmen. I really enjoyed the time I spend with them at all the family cook-outs, gatherings, etc. This made me feel like I had a second family here in the U.S. Thank you for that.

I would also like to thank my fellow salseros at SalsaTech for making my stay at Tech the best time of my life. It was a pleasure to serve as the president of such a great organization for over two years. Thanks to my performance team dance partner Erika Kellar for bearing with me for such a long time. Thanks to Brian Murphy for introducing me to salsa and working with me on my leadership skills. I am also very grateful for my friendship to Emily Anderson for making me a better person every day of my life. Thanks especially to my favorite dancer in D.C. Lorena Guerra-Murcia, my favorite salsa girls in Blacksburg Julia Malapit, Rachel Baldini, Brianna Horricks, and all my other salsa friends: Diego Cortes, Tamara Chilton, Kelly Gibbs, Jocelyn Casto, Ilaria Brun del Re, Kate Tressler, Alex Schwartz, Kelsie Ostergarrd, Rachel and

Jessica Wunderlich, Nikolas Sweet, Alejandro Medina, Christin Alleyne, Shelby Davies-Sekle, Jonathan Bonilla, Chaky Sriranganathan, Junior Villegas, Tony Ponce, Elizabeth Bonnell, Danoosh Kapadia, Diego Benitez, Trevor kennedy, Emily Anderson, Kristin Bowers, Kerry Waite, Paul Pallante, and of course one of my favourite people: Rajesh Thirugnanam. Also, thanks to my non-salsa friends Jamal Albarghouti, Younes Benchekroun, Wael Hijazi, Saif Rayyan, Melissa Denby, Rangi Jericevich, William Kaal, Richard Kerr, Brian Stanek, Stephen Daniel, Haitham Rabadi, Gaith Rabadi, Sven Dorosz, Chanda Leckie and her parents Barbara and Arlen, Courtney Lynne, and Jon Rice.

I can not forget about my friends back in Germany: Christian Nolda, Lars Fetzer, Christos Alexandrakis, Joerg Schwab, Harald Zuber, Mathias Nalepa and Stephan Goessmann. Thanks to my best friend Daniel Theurich for being a loyal and stand up guy. I couldn't have done it without him.

At this point I would also like to thank the Virginia Tech writing center for all the help with my English.

The final words of acknowledgement are reserved for my family. Thanks to my grandfather *Driss* for believing in me for all my life. He died the day I first came to America as the proudest grandfather on earth. It was his dream for me to be the first Ph.D. in my family and I must say I was very driven by his pride throughout my life. Thanks to the most important person in my life: my mother *Jamila*, who is the most loving and understanding person I know. Thank you for your unconditional love. Thanks to my father *Abderrahman* for always having my back no matter what happens. Knowing that took a lot of pressure off me during my doctorial studies. Special thanks to *Hanan* and *Iman* for being the two greatest sisters ever. I owe everything I achieve in life to my family's love, constant support and incredible patience.

Table of Contents

List of Tables

List of Figures

Unless otherwise noted, all images are property of the author.

1. INTRODUCTION

There has been substantial research over the last five decades on control of aircraft cabin noise as private and commercial civil aviation is one of the major categories of flying. Civil aviation is more then ever an important transportation method for many people worldwide. The suppression of aircraft interior noise is of major importance as the environment inside aircrafts affects pilots, crew and passengers. Noise and vibration inside aircraft cabins cause increasing risks in health and in particular performance of flight crew and cabin crew as well as a discomfort for the passengers [1,2]. This thesis presents part of the work that has been done to develop a new passive noise control device that is used to reduce aircraft interior noise across a broad band frequency spectrum.

1.1. Aircraft interior noise

Significant process has been made in the last five decades in the understanding, prediction and control of interior aircraft noise [3]. Aircraft interior noise can be caused by four major sources: Propeller noise, jet noise, turbulent boundary layer noise and structure borne noise.

There are many applications in which propeller noise is a serious problem or a cause for concern. The commercial usage of propeller driven aircraft is limited by high levels of cabin noise. Propeller noise and can be described by discrete tones at the fundamental blade passage frequency (BPF) of the engines and its harmonics [4]. These discrete tones are most dominant at low frequencies (below 500 Hz) where traditional passive treatments have only little effect.

The airborne transmission of jet noise is mainly associated with aircraft that have wing-mounted engines, and it affects cabin regions aft of the engine exhaust, particularly when the engines are mounted close to the fuselage. The cabin noise increases with decreasing the distance of the two engines and the fuselage [3]. An example of the influence of jet noise is demonstrated in the rear of the passenger cabin of a Convair 779 airplane which had wing-mounted jet engines is given in [5].

The introduction of turbojet-powered commercial aircraft with flight speeds much higher then those of propeller driven airplanes have brought the focus on aircraft

interior noise control to turbulent boundary layer noise or aerodynamic noise in general. In 1940 it was recognized that aerodynamic noise is most significant at aircraft speeds above 200mph [6]. Flight tests have been conducted with driving an airplane with power off and by measuring twin-engine airplanes in flight level [7,8] and it was concluded that that aerodynamic noise is a significant contributor to the mid and high frequency cabin sound pressure levels.

Both, jet noise and turbulent boundary layer noise are broadband and jet noise is usually present in regions on the rear of the fuselage where boundary layer noise is shifted to lower frequencies because of the thicker boundary layer. Thus the separation of this two noise sources to the fluctuating pressures measured on the exterior of an airplane is a challenge. Cross-spectrum and correlation techniques have been applied to separate the two contributions to the exterior pressure field on the aft region of the fuselage of a Boing 737 [9,10].

Engine-induced structure-borne noise caused by out-of-balance forces within the engines [3] cause vibrations into the fuselage shell which radiate sound into the aircraft interior. The focus in the last three decades was brought to this noise source contribution due to the large numbers of jet-powered aircraft with engines mounted directly on the rear fuselage wall [11]. The structurally excited noise components of the aircraft take place at the rotating frequencies of the fan and compressor and usually occur around $75 - 200$ Hz [3].

1.2. Control of aircraft interior noise

There are several methods to reduce the interior noise levels, including source reduction, active [12] and passive control of the aircraft transmission paths, and active control of the sound field [13,14]. Aircraft interior noise has been an important part of noise control research since the 1930s [15]. A schematic of an aircraft interior examined in this work is shown in Figure 1-1 consisting of five components: the source panel or fuselage, HG blanket, air cavity, the receiving panel or trim, and acoustic free field.

Active methods [16,17] have been extensively studied and have been applied in practice in propeller driven aircraft, but use is limited as passive control systems are less expensive, less complicated and do not require any control energy.

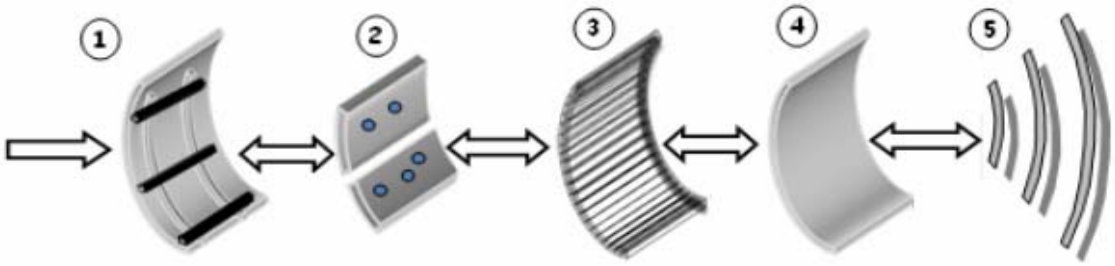

Figure 1-1: Objects incorporated in mathematical model of DPS: Fuselage(1), HG blanket(2), air cavity(3), trim(4) and interior acoustic field(5)

Passive treatments used in civil aircraft can be broadly grouped into damping materials and acoustic absorbers. Acoustic barriers are too heavy for aircraft application. Damping material with different configurations can be mounted on the fuselage skin [18] as well as to frames, stringers [19] (Figure 1-1(1)) and the trim panels [20] (Figure 1-1(2)). Parts of the damping material often consist of viscoelastic material which dissipates energy in addition to adding stiffness and mass. However, it is also known to have a limited operating temperature range. Although the damping of viscoelastomers is high, the stiffness of the material changes rapidly with temperature caused by both external conditions and internal heating due to energy dissipation. Acoustic absorbers such as fiberglass or polyamide reduce the sound in enclosures by converting the mechanical motion of the air particles into low-level heat. The control of low frequency noise in aircraft is a challenge due to the weight and thickness restrictions imposed on any acoustic treatment. Typically the thickness of a passive noise control treatment limits the bandwidth over which the treatment will be effective [21,22]. For example, Baumgartl [23] presented the sound absorbance as a function of wave frequency for several thicknesses of melamine foam as a function of frequency and showed that the absorbance was highly dependent upon the thickness of the treatment and that thick layers are required for the absorption of low frequencies. For instance, the degree of sound absorption for 50mm thick foam at 500Hz is 0.5 and drops down rapidly to a absorption value of 0.05 at 100Hz. A measurement conducted in the Vibrations and Acoustics Laboratories (VAL) by Dr. Johnson and Dr. Carneal

shown in Figure 1-2 illustrates once more the weak low frequency performance of acoustic foam to control the radiated sound of a base plate. Figure 1-2(a) shows the schematic of the experimental rig used in VAL's TL facility: Acoustic melamine foam was mounted on top of an aircraft panel. The sound power radiation of the panel with and without acoustic foam has been compared. It has been found that passive treatments positioned inside the fuselage shell of an aircraft, where the fuselage dimensions limit the thickness of the blankets to a few inches, causes the acoustic blankets to be ineffective at frequencies below about 500Hz.

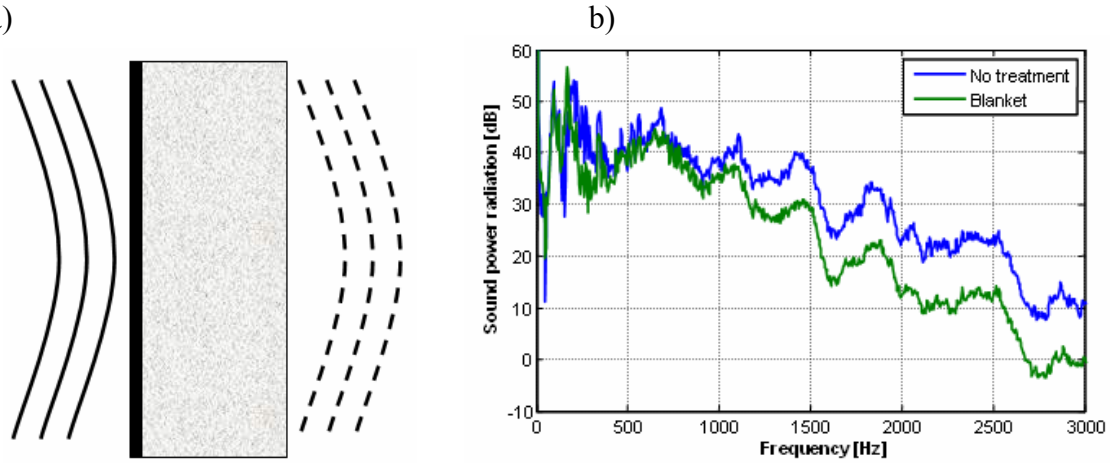

Figure 1-2: Schematic of plate with acoustic foam mounted on top (a) and measured radiated sound power from the panel with and without passive treatment.

One method to control low frequency transmissions uses damped resonant devices such as Helmholtz resonators, dynamic vibration absorbers, and tuned vibration dampers. These have been shown to provide significant reduction at low frequencies while limiting the added mass to 10% of the untreated structure [24]. However, these are additional devices that must be used as well as traditional passive treatments. Another passive control method was the isolation of the interior shell which was mounted at locations on the floor where the vibration levels were low [25]. This application has been restricted to relatively small cabins.

From the above analysis, it is evident that an integrated passive solution that can control noise transmission across the entire bandwidth is needed. One resonant device developed and tested for broadband control in the last decade is the distributive vibration absorber which consists of a plate bonded to sound absorbing foam. The

resonance of the distributive vibration absorber can be tuned by varying the loading mass, or the stiffness of the spring. The distributive vibration absorbers were tested on a cylindrical shell. Experimental results have shown that these devices were very effective at reducing the vibration response at targeted resonant peaks at lower frequencies [26]. Once this technology was proven, the natural progression was to insert the masses inside the porous media instead of mounting the distributive vibration absorber on top of the porous layer. This way, the stiffness of the poro-elastic material was used as spring elements of the distributive vibration absorber. This leads to the development of a new passive control treatment for sound transmission through base structures, which is called a heterogeneous (HG) blanket.

1.3. HG blanket concept

HG blankets combine the two main passive control mechanisms (damping and dynamic absorption) into a single control treatment that has the potential to control a wide frequency range. The HG blanket consists of poro-elastic media such as acoustic foam with small embedded masses, which act similarly to a distributed mass-spring-damper-system as seen in Figure 1-3 (a).

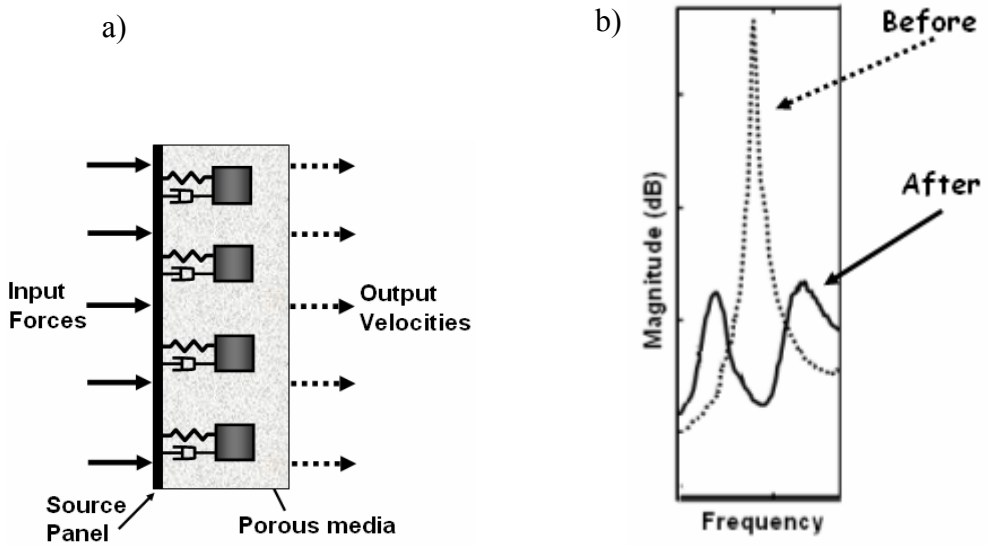

Figure 1-3: Schematic of plate with: (a) HG blanket mounted on top and (b) schematic of damped mode split effect of the HG blanket on targeted base structure mode.

In present literature, the HG blanket concept evolved through a series of steps, starting with a single-point absorber (as shown in Figure 1-4(I)), extended to multiple absorbers acting over a distributed space, (Figure 1-4(II) and ref. [27]), extended further to multiple masses coupled together (Figure 1-4(III) and refs. [28,29]), and finally broadened to the full HG concept. In the full HG concept, multiple mass inclusions are placed inside of a continuous (porous) media to simulate a distributed mass-spring-damper system (Figure 1-4(IV)) that operates at low frequency where the blanket is no longer an effective passive absorber. By employing an acoustic treatment (i.e. the porous media) to provide the stiffness for the mass inclusions, the HG blanket concept combines both of the main types of passive control mechanisms, damping (high frequencies) and dynamic absorption (low frequencies), into a single treatment designed to control a wide frequency range. The acoustic treatment, or porous media, is a complex structure with coupled fluid and solid properties [30]. However, in the low frequency regime where the mass inclusions resonate, the polymer matrix or foam provides the majority of the stiffness that act against the mass inclusions.

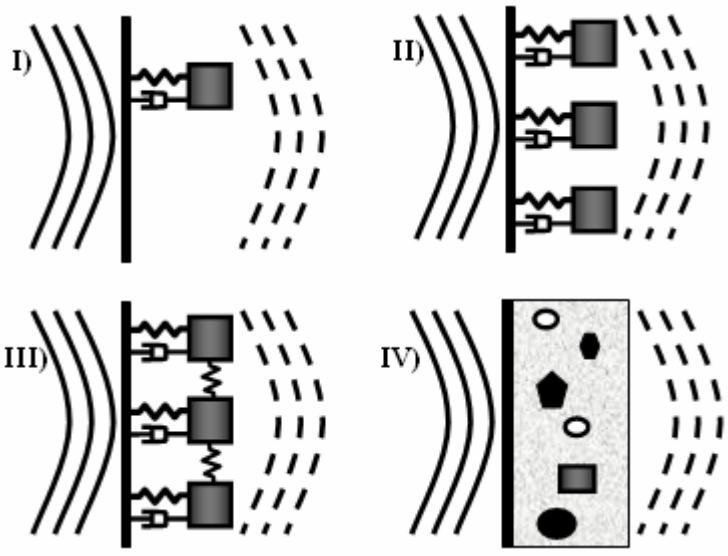

Figure 1-4: Schematic of the development of the HG blanket

Recent experimental investigations carried out by Kidner et al.[31,32] as well as numerical and experimental studies conducted by Sgard, Atalla, and Amedin [33,34]

showed that HG blankets have shown significant potential to reduce low frequency radiated sound from structures, where traditional poro-elastic materials have little effect [21,22]. This can be accomplished without losing the good performance at high frequencies due to the porous media. Kidner et al.also came to the conclusion that HG blankets can be more efficient when the embedded masses are positioned to target certain modes instead of randomly distributing the masses. In order to target a plate mode, it is necessary to "tune" the embedded mass to the desired frequency as well as position it at certain anti-node lines of the mode. "Tuning" the mass insertions can be achieved by varying the depth of the mass position inside the poro-elastic media, or by varying the weight and mass shape of the embedded mass [35]. Proper "tuning" of the masses will result into a mode split of the targeted resonance of the base structure. Following traditional tuned vibration absorber theory [36], the targeted resonance peak is then split into two resultant peaks, one above and one below the original peak. If the damping ratio is correctly designed [37], both resultant resonant frequencies have lower and more damped amplitudes then the original resonance as shown in Figure 1-3(b). Note that one can reduce the two "resultant" peaks even more if the damping is optimized.

1.4. Thesis overview and contributions

As a first step to model the interior of an aircraft with sandwiched HG blanket, a mathematical model of a single-bay double panel system (DPS) with, acoustic cavity, HG blanket and radiated field was developed using impedance and mobility methods (IMM) proposed by Firestone [38,39] and O'Hara [40], further developed by Gardonio[41]. Panneton and Atalla proposed a model of an acoustic blanket with a FE-scheme [42]. A novel impedance matrix formulation for the HG blanket is derived and coupled to the DPS using an assembled matrix approach derived from the IMM [43]. Experimental measurements validated the predicted responses of the source and the receiver panel due to a point force acting on the DPS [44,45]. As a more rigorous model of the fuselage interior, the single-bay DPS was then extended to a multi-bay DPS with frames, stringers, mounts, and four HG blankets [46]. The predicted response of the animated MPS was compared to measurements and proved viable.

This work presents a theoretical and experimental comparison of different design techniques for allocating the location of embedded masses using the single-bay DPS [47]. These design techniques include the random placement of the mass inclusions, placement using a modal design, and an extensive search for the best location for specific sound transmissions with specific design constraints. Measurements accurately agree between the results of the modal design and the results of the extensive search [48]. Genetic algorithms coupled with the previously described design tool of the DPS with the HG blanket treatment can optimize HG blanket design. This study presents a comparison of the performance obtained using the genetic algorithm optimization routine and a novel interactive optimization routine based on sequential addition of masses in the blanket [49]. After each mass is added, the study requires finding the optimal location and design for the next mass. When all of the masses are added, the algorithm then reassesses the design of the first mass and continues until the design has converged. This technique leads to good attenuation with reduced computational burden. Variations in mass location and system parameters are investigated. Coupling between masses modeled as dynamic vibration absorbers (DVA) and the modes of a clamped rectangular plate probe the sensitivity of the HG blanket design [50].

This study extensively examines the behavior of the mass inclusion inside the poro-elastic media both numerically and experimentally. The concept of an HG blanket used to control the sound transmission through double-panel system for aircraft applications has already been developed in the literature. However, deficiencies in methodical property control exist and therefore the prime objective of this research is to provide a simple method to predict and control material properties of the heterogeneous blankets through alteration of mass and stiffness parameters with the size, varied shape, and placement of the mass inclusions. Control of these parameters is necessary if optimized heterogeneous (HG) blankets targeted to specific applications are to be successfully developed. This research offers a detailed analysis of the behavior of the mass inclusions, highlighting controlled stiffness variation of the mass-spring-damper systems inside the HG blanket. Characteristic parameters of the HG blanket like the "footprint," "effective area," and the "mass interaction distance" are defined and confirmed through mathematical calculations and experimental results [35]. A novel,

empirical approach to predict the natural frequency of different mass shapes embedded in porous media was derived and experimentally verified for many different types of porous media, including melamine foam, polyurethane, and polyamide [51]. A maximum error of 8% existed for all the predictions made in this document. In addition, simplifying a model for poro-elastic materials for low frequencies that Biot [52] and Allard [53] originally proposed and implementing basic elastomechanical solutions produce a novel analytical approach to describe the interaction of the mass inclusions with a poro-elastic layer [54]. The analytical approach formulated with varied shape of the mass inclusions and the thickness and elastic properties of the poro-elastic layer predicts the effective stiffness. The experimental validation is included, and a simplified equation to calculate the effective stiffness of a HG blanket is proposed. To determine the interaction between two mass inhomogeneities, the stress field inside the porous material will be evaluated with focus on the stresses at the base plane (fuselage). These studies are used to gain physical insight into the effect of the parameters on the performance of the HG blanket, leading to effective optimization and improved production methodologies

A full-scale fuselage experiment performed on a Gulfstream section involves using the MPS design tool for the positions of the mass inclusions, and the results of the "effective area" approach facilitate tuning of the natural frequencies of the mass inclusions to the desired natural frequencies. The fuselage without any passive treatment is compared to the cases with added porous media and HG blanket. The presented results indicate that proper tuning of the HG blankets can result in broadband noise reduction below 500Hz with less than 10% added mass.

2. SINGLE-BAY DOUBLE PANEL SYSTEM

A single bay double panel system is modeled and validated in this chapter as a first step to predict the response of an aircraft interior. An experimental investigation of HG blanket mounted on both the fuselage and the trim panel is presented.

2.1. Mathematical model

This section presents the mathematical model used to predict the sound radiation and vibration response of a double panel system with sandwiched HG blanket. The system investigated consists of 5 components: the fuselage panel or fuselage, HG blanket, air cavity, the trim panel or trim, and the acoustic free field, which are all shown in Figure 2-1.

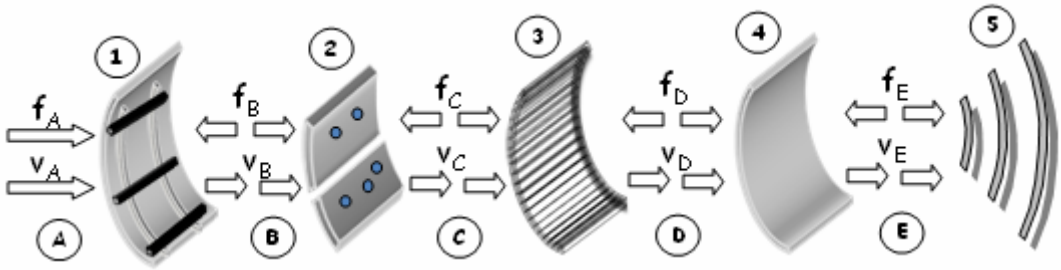

Figure 2-1: Objects incorporated in mathematical model of the double panel system: Fuselage(1), HG blanket(2), air cavity(3), trim(4) and interior acoustic field(5). Interfaces between objects are noted with capital letters A-E.

The fuselage and trim were both modeled as flat plates [55], where the plate modes from Warburton [56] were used. The foam is modeled using poro-elastic finite elements based on fundamental fluid, structural, and coupled fluid-structural equations given by Panneton and Atalla [33,34,57]. A mesh of 8-node brick elements has been used. The HG blanket itself was developed adding point masses to the poro-elastic mass matrix. The air cavity is modeled using the modes for a rectangular rigid wall volume, and the modes are given by Kinsler and Frey [58]. The radiation into the acoustic free field is modeled as per Elliott and Johnson [60] using an elemental radiator approach. Note that the diagonal terms lead to a singularity, but the problem can be avoided as per Bai and Tsao [61] by changing the domain from rectangular to

circular in the Rayleigh formula, or as per Berkhoff [62] using the Boundary Element Method.

To combine the individual models into a system, the forces and velocities at the interfaces need to be equated. This can be achieved most effectively using the impedance and mobility method, which couples the components together at discretized locations on the interfaces. The impedance and mobility method was originally proposed by Firestone [38,39] and O'Hara [40], further developed by Gardonio and Brennan [63,64].

For this work, all subsystems were discretized using a 5x5 grid as shown in Figure 2-2. For a given component, at each frequency, a mobility matrix can be formed that describes the relationship between all output velocities and all forces in a 25 x 25 matrix. The matrices describing the behavior of each component are calculated by the aforementioned analytical and finite element models. The detailed derivation of these matrices is beyond the scope of this paper, and can be found in the references. These matrices can then be assembled into a larger system matrix, which is described in detail later.

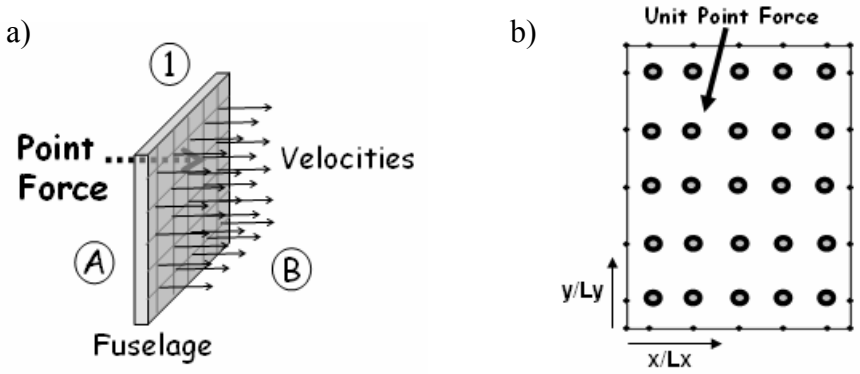

Figure 2-2: Schematic of: (a) point force acting off center on a fuselage with 25 output velocities at grid nodes and (b) the 5x5 node points used to compare theory and experiment for the double panel system along with the position of the unit point force excitation.

For this derivation, the low frequency assumption is used, i.e. the subsystems of the double panel system are assumed to be moving with transverse motion only, therefore moments and axial forces are neglected. In addition, it should be noted that the panels of a civil aircraft fuselage are curved and coupled through mounts while the

numerical model in this work assumes flat panels and coupling of the fuselage and trim panel through the air cavity. This is a common assumption widely used in literature [66]. The next sections will present the mobility and impedance expressions for the subsystems as well as the coupling equations used to build the DPS design toll. A comparison of theory and experiment will prove the mathematical model valid.

2.1.1 Plate mobility matrix

The dynamics of a rectangular plate are considered in terms of a point mobility matrix. Consider a set of points on the surface of the plate where normal forces are applied (represented by vector **f**) and another set of points where normal surface velocities are measured (represented by vector **v**) as indicated in Figure 2-3. Therefore, the velocity and force can be related by the mobility matrix:

$$\mathbf{v} = \mathbf{M}\mathbf{f} \tag{2-1}$$

For a general case the vector **v** contains the three components of the point velocity vector ($\dot{u}$, $\dot{v}$ and $\dot{w}$) and the three angular velocities ($\dot{\theta}_x$, $\dot{\theta}_y$ and $\dot{\theta}_z$) but in this case we take into account only the out-of-plane dynamics. So, the m_{ii} term of **M** indicates the **point mobility** at *i*, while m_{ij} indicates the **transfer mobility** between *i* (where **v** is evaluated) and *j* (where **f** is applied).

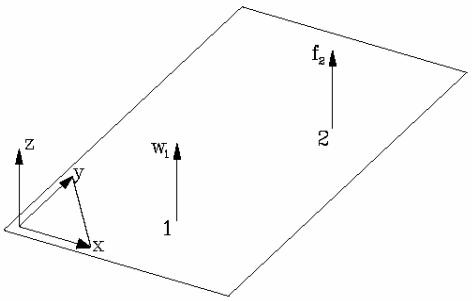

Figure 2-3: Notation for velocities and forces on a Plate

The mobility matrix can be derived assuming "classical plate theory" for thin plates. The equation of motion for transverse displacement of a thin plate is

$$D\left(\frac{\partial^4 w}{\partial x^4}+2\frac{\partial^4 w}{\partial x^2\partial y^2}+\frac{\partial^4 w}{\partial y^4}\right)+\rho h\frac{\partial^2 w}{\partial t^2}=-p(x,y,t) \tag{2-2}$$

where h is the plate thickness, ρ is the material density, p is the external load applied and D is the flexural stiffness, defined as:

$$D=\frac{Eh^3}{12\left(1-\upsilon^2\right)}, \tag{2-3}$$

where E and ν are respectively the material Young modulus and Poisson coefficient. Considering the free vibrations of the plate in vacuum, it is possible to evaluate the natural frequencies ω_{mn} (integers m and n are the modal numbers) of vibration and the normal modes given by Warburton [56]. The corresponding mode shapes ψ_{mn} with respect to various boundary conditions are given by Gardonio and Brennan [65]. The generic term m_{ij} of the mobility matrix can be calculated as

$$m_{ij}\left(\omega\right)=\frac{\dot{w}_i}{f_j}=j\omega\sum_{m=1}^{\infty}\sum_{n=1}^{\infty}\frac{\psi_{mn}\left(x_i,y_i\right)\psi_{mn}\left(x_j,y_j\right)}{\Lambda\left[\omega_{mn}^2\left(1+j\eta\right)-\omega^2\right]} \tag{2-4}$$

where η is the loss factor ($\eta = 2\xi$ where ξ is the modal damping) and Λ is the modal mass which depends on the normalization of the modes and the modes depends on the boundary conditions. For example for the simply supported case, the modal mass is:

$$\Lambda=\frac{\rho h L_x L_y}{4} \tag{2-5}$$

where L_x is the plate length and L_y is the plate width. In a real application we are interested in a limited frequency band so the model indexes are finite such as N and M. Using the matrix notation ($\mathbf{\Psi}$ for the eigenvectors) and defining a diagonal matrix that contains the denominator and the common term ($j\omega$);

$$\mathbf{A}=\begin{bmatrix}\ddots & & \\ & \frac{j\omega}{\Lambda\left[\omega_{mn}^2\left(1+j\eta\right)-\omega^2\right]} & \\ & & \ddots\end{bmatrix} \tag{2-6}$$

with N by M modes where $n=1 \rightarrow N$ and $m=1 \rightarrow M$. The mobility matrix can be written as:

$$\mathbf{M}=\mathbf{\Psi}_{\mathbf{v}}^{\mathrm{T}}\mathbf{A}\mathbf{\Psi}_{\mathbf{f}} \tag{2-7}$$

where $\boldsymbol{\Psi_v}$ is a $N \times M \times N_v$ matrix with the eigenvectors evaluated in the measuring points and $\boldsymbol{\Psi_f}$ is a $N \times M \times N_f$ matrix with the eigenvectors evaluated in the forcing points. The final mobility matrix will be $N_v \times N_f$ (number of velocity measurement and force application points) so is not necessarily square.

2.1.2 Cavity impedance matrix

The pressure field inside the enclosure can be described by the acoustical wave equation that in its homogeneous form [58,59] is:

$$\nabla^2 p - \frac{1}{c^2}\frac{\partial^2 p}{\partial t^2} = 0 \tag{2-8}$$

Using the separation of variables, the solution can be written as:

$$p(\alpha) = A_\alpha \sin k_\alpha \alpha + B_\alpha \cos k_\alpha \alpha \qquad \alpha = x, y, z \tag{2-9}$$

and

$$p(t) = A_t \sin \omega t + B_t \cos \omega t \tag{2-10}$$

that leads to the equation:

$$k_x^2 + k_y^2 + k_z^2 - \frac{\omega^2}{c^2} = 0 \tag{2-11}$$

hence, the natural resonant frequency for the enclosure:

$$f = \frac{c}{2\pi}\sqrt{k_x^2 + k_y^2 + k_z^2} \tag{2-12}$$

Assuming that the enclosure is rectangular with rigid walls we have:

$$k_\alpha = \frac{n_\alpha \pi}{L_\alpha} \qquad n_\alpha \in N + \{0\} \tag{2-13}$$

And the corresponding mode shapes are:

$$\Phi_{ijk} = K_{ijk} \cos\frac{i\pi x}{L_x} \cos\frac{j\pi y}{L_y} \cos\frac{k\pi z}{L_z} \tag{2-14}$$

The normal modes are orthogonal, so

$$\int_V \Phi_{ijk}\Phi_{mno} dV = \begin{cases} 0 & \{i,j,k\} \neq \{m,n,o\} \\ V_N & \{i,j,k\} = \{m,n,o\} \end{cases} \tag{2-15}$$

where V_N is the normalization factor. Choosing K_{ijk} equal to

$$K_{ijk} = \sqrt{\frac{2P}{L_x L_y L_z}} \tag{2-16}$$

where P is the number of nonzero indices, then $V_N = 1$. In order to take into account the

forcing terms, the non homogeneous version of (2-8) is considered. And the pressure field is described by means of the previous mode shapes:

$$p(x,y,z,t)=\sum_{n=1}^{\infty}P_n(t)\Phi_n(x,y,z) \tag{2-17}$$

The modal force can be written as:

$$F_n(t)=\int_V\frac{1}{V}\frac{\partial Q}{\partial t}\psi_n dV-\int_S\frac{\partial^2 w}{\partial t^2}\psi_n dS \quad \xrightarrow{No\ \ Sourses\ \ inside\ \ cavity} \quad =-\int_S\frac{\partial^2 w}{\partial t^2}\psi_n dS \tag{2-18}$$

where the first term will be neglected due to the fact that it takes into account the sources with volume velocity Q and in the examined case there are no sorces inside the cavity. The velocity on the top surface of the poro-elastic layer (w) is not known as a function but as a set of discrete values over the FEM grid. Hence, assuming a uniform acceleration around each node the force can be written as:

$$F_n(t)=\sum_{i=1}^{N}\frac{\partial^2 w_i}{\partial t^2}\Phi_n(x_i,y_i)s_i \tag{2-19}$$

where s_i is the area surrounding each node. In the frequency domain, the force can be written in terms of the velocity field on the top surface of the foam and the prior equation becomes:

$$F_n(\omega)=\sum_{i=1}^{N}j\omega\frac{\partial w_i(x_i,y_i)}{\partial t}\Phi_n(x_i,y_i)s_i \tag{2-20}$$

Going into the frequency domain and adding a damping term to eq. (2-8) gives the following expression:

$$-\omega^2P_n+2\delta_nP_nj\omega+\omega_n^2P_n=\left(\frac{\rho c^2}{V_n}\right)\sum_{i=1}^{N}j\omega\frac{\partial w(x_i,y_i)}{\partial t}\Phi_n(x_i,y_i)s_i \tag{2-21}$$

Hence,

$$\left(-\omega^2+2\delta_nj\omega+\omega_n^2\right)P_n=\left(\frac{\rho c^2}{V_n}\right)\sum_{i=1}^{N}j\omega\frac{\partial w(x_i,y_i)}{\partial t}\Phi_n(x_i,y_i)s_i \tag{2-22}$$

Solving for the modal pressure amplitude:

$$P_n=\frac{\left(\frac{\rho c^2}{V_n}\right)\sum_{i=1}^{N}j\omega v_{poro}(x_i,y_i)\Phi_n(x_i,y_i)s_i}{\left(-\omega^2+2\delta_nj\omega+\omega_n^2\right)} \tag{2-23}$$

using the following vector notation:

$$\mathbf{v_{poro}}=[v_1(x_1,y_1)\quad v_2(x_2,y_2)\quad ...v_N(x_N,y_{N1})]^T \tag{2-24}$$

and

$$\mathbf{\Phi_n} = [\Phi_n(x_1, y_1) \quad \Phi_n(x_2, y_2) \quad ...\Phi_n(x_N, y_{N1})]^T \tag{2-25}$$

The sum can be written as

$$\sum_{i=1}^{N} j\omega v_{poro}(x_i, y_i)\Phi_n(x_i, y_i)s_i = j\omega \mathbf{\Phi_n^T} \begin{bmatrix} \backslash & & \\ & \mathbf{S} & \\ & & \backslash \end{bmatrix} \mathbf{v_{poro}} \tag{2-26}$$

and the pressure can be written as:

$$P_n(\bar{x}, \omega) = \mathbf{Z}\mathbf{v_{poro}} \tag{2-27}$$

the impedance matrix can finally be described with the following equation:

$$\mathbf{Z} = \frac{\left(\frac{\rho c^2}{V_n}\right) j\omega \mathbf{\Phi_n^T} \begin{bmatrix} \backslash & & \\ & \mathbf{S} & \\ & & \backslash \end{bmatrix}}{\left(-\omega^2 + 2\delta_n j\omega + \omega_n^2\right)} \tag{2-28}$$

Note that we treated the problem as a "hard" boundary condition:

$$\frac{1}{\rho}\frac{\partial p}{\partial n} = 0 \tag{2-29}$$

2.1.3 Radiation impedance matrix

The acoustic power radiated from a structure can be calculated in terms of normal surface velocity and pressure vectors *evaluated on the surface* of the vibrating element as:

$$\mathbf{W} = \frac{S}{2}\mathrm{Re}\left[\mathbf{v^H p}\right] \tag{2-30}$$

where *H* refers to Hermitian; on the surface of the source the pressure can be related to the normal velocity by means of the radiation impedance matrix $\mathbf{Z}(\omega)$;

$$\mathbf{p} = \mathbf{Z}\mathbf{v} \tag{2-31}$$

The radiation impedance matrix can be derived using Boundary Element Method or Rayleigh integral formula in the case of planar sources in a baffle. This leads to the following expression:

$$Z(\omega)=\rho c\begin{bmatrix} d & -\frac{jkS}{2\pi}\frac{e^{jkr_{12}}}{r_{12}} & \cdots & -\frac{jkS}{2\pi}\frac{e^{jkr_{1N}}}{r_{1N}} \\ -\frac{jkS}{2\pi}\frac{e^{jkr_{21}}}{r_{21}} & d & \cdots & -\frac{jkS}{2\pi}\frac{e^{jkr_{2N}}}{r_{2N}} \\ \vdots & \vdots & \ddots & \vdots \\ -\frac{jkS}{2\pi}\frac{e^{jkr_{N1}}}{r_{N1}} & \cdots & \cdots & d \end{bmatrix} \tag{2-32}$$

Diagonal terms lead to a singularity but the problem can be avoided as in Bai and Tsao [61] changing the domain from rectangular to circular in the Rayleigh formula, or as in Berkhoff [62] using the Boundary Element Method. The two expressions are respectively:

$$d_{Bai}=\frac{1}{2}\left(k\sqrt{\frac{S}{\pi}}\right)-j\frac{8}{3\pi}\left(k\sqrt{\frac{S}{\pi}}\right) \qquad d_{Berkhoff}=1-e^{jk\sqrt{S/\pi}} \tag{2-33}$$

Note that impedance is given in a pressure- velocity and not in a force- velocity relationship. Since the velocity is given with respect to every single surface and is not a volume velocity with the force must be calculated as,

$$\mathbf{f}=S\mathbf{p} \tag{2-34}$$

and the mobility matrix for the radiation field can be calculated as:

$$\mathbf{M}=S*\mathbf{Z}^{-1} \tag{2-35}$$

2.1.4 Impedance and mobility matrix for poro-elastic media

The basic equations for the poro-elastic model where presented by Allard [53] and further developed for the HG blanket by Gautam [67]. The basic equation of the FE-model is defined such as:

$$\mathbf{f}=\mathbf{G}_{\mathbf{Poro}}\mathbf{x}, \tag{2-36}$$

where **f** and **x** are column vectors of the applied nodal forces and the nodal displacements, respectively. $\mathbf{G}_{\mathbf{Poro}}$ is derived from the equation of motion for the poroelastic medium

$$\mathbf{G}_{\mathbf{Poro}}(\omega)=-\omega^2\mathbf{M}_{\mathbf{P}}+j\omega\mathbf{C}_{\mathbf{P}}(\omega)+\mathbf{K}_{\mathbf{P}}(\omega) \tag{2-37}$$

$\mathbf{M}_{\mathbf{P}}$, $\mathbf{C}_{\mathbf{P}}$ and $\mathbf{K}_{\mathbf{P}}$ are the equivalent "mass", "damping" and "stiffness" matrices and ω is the circular frequency. In order to get the relationship between force and velocity at the

boundary condition nodes (base and top nodes) and the nodes in between, (A.1) can be written as

$$\begin{Bmatrix} \mathbf{f}_{\mathbf{NBC}} \\ \mathbf{f}_{\mathbf{BC}} \end{Bmatrix} = \begin{bmatrix} \mathbf{G}_{11} & \mathbf{G}_{12} \\ \mathbf{G}_{21} & \mathbf{G}_{22} \end{bmatrix} \begin{Bmatrix} \mathbf{x}_{\mathbf{NBC}} \\ \mathbf{x}_{\mathbf{BC}} \end{Bmatrix}, \tag{2-38}$$

with $\mathbf{f}_{\mathbf{BC}} = \begin{Bmatrix} \mathbf{f}_{\mathbf{BC_{Bs}}} \\ \mathbf{f}_{\mathbf{BC_{Bf}}} \\ \mathbf{f}_{\mathbf{BC_{Ts}}} \\ \mathbf{f}_{\mathbf{BC_{Tf}}} \end{Bmatrix}, \mathbf{f}_{\mathbf{NBC}} = \begin{Bmatrix} \mathbf{f}_{\mathbf{NBC_S}} \\ \mathbf{f}_{\mathbf{NBC_f}} \end{Bmatrix}, \mathbf{x}_{\mathbf{BC}} = \begin{Bmatrix} \mathbf{x}_{\mathbf{BC_{Bs}}} \\ \mathbf{x}_{\mathbf{BC_{Bf}}} \\ \mathbf{x}_{\mathbf{BC_{Ts}}} \\ \mathbf{x}_{\mathbf{BC_{Tf}}} \end{Bmatrix}, \mathbf{x}_{\mathbf{NBC}} = \begin{Bmatrix} \mathbf{x}_{\mathbf{NBC_S}} \\ \mathbf{x}_{\mathbf{NBC_f}} \end{Bmatrix}$,

where for the force $\mathbf{f}_{\mathbf{BC}}$ the first indexes "BC" and "NBC" stand for the boundary condition and non- boundary condition nodes, respectively and the second indexes "Bs", "Bf", "Ts" and "Tf" stand for the bottom nodes – solid phase/ fluid phase and the top- nodes solid phase/ fluid phase, respectively. The force and displacement relationship of the nodes with fixed boundary conditions are obtained by setting the external force at the non- boundary condition nodes to zero ($\mathbf{f}_{\mathbf{NBC}}$=0):

$$\mathbf{f}_{\mathbf{BC}} = \left(\mathbf{G}_{22} - \mathbf{G}_{21}\mathbf{G}_{11}^{-1}\mathbf{G}_{12}\right)\mathbf{x}_{\mathbf{BC}}. \tag{2-39}$$

However, since $\mathbf{v}_{\mathbf{BC}} = j\omega\mathbf{x}_{\mathbf{BC}}$, the impedance at the boundary is given by:

$$\mathbf{Z} = \frac{1}{j\omega}\left(\mathbf{G}_{22} - \mathbf{G}_{21}\mathbf{G}_{11}^{-1}\mathbf{G}_{12}\right), \tag{2-40}$$

and the mobility matrix is the inverse of the impedance matrix:

$$\mathbf{M} = \mathbf{Z}^{-1}. \tag{2-41}$$

Depending on the boundary conditions, the velocity of the fluid phase and solid phase do not necessarily need to be the same. Therefore it is necessary to split up the impedance or mobility matrix in a solid-solid phase, solid-fluid phase, fluid-solid phase and fluid-fluid phase seeing how half of the rows in the impedance or mobility matrix are due to the fluid phase and the other half due to the solid phase of the poro-elastic material. The impedance and mobility matrix can then be split up into:

$$\mathbf{Z} = \begin{bmatrix} \mathbf{Z}_{ss} & \mathbf{Z}_{sf} \\ \mathbf{Z}_{fs} & \mathbf{Z}_{ff} \end{bmatrix} \text{ and } \mathbf{M} = \begin{bmatrix} \mathbf{M}_{ss} & \mathbf{M}_{sf} \\ \mathbf{M}_{fs} & \mathbf{M}_{ff} \end{bmatrix},$$

with

$$\mathbf{Z}_{ss} = \begin{bmatrix} \mathbf{Z}_{Bss} \\ \mathbf{Z}_{Tss} \end{bmatrix}, \mathbf{Z}_{sf} = \begin{bmatrix} \mathbf{Z}_{Bsf} \\ \mathbf{Z}_{Tsf} \end{bmatrix}, \mathbf{Z}_{fs} = \begin{bmatrix} \mathbf{Z}_{Bfs} \\ \mathbf{Z}_{Tfs} \end{bmatrix}, \mathbf{Z}_{ff} = \begin{bmatrix} \mathbf{Z}_{Bff} \\ \mathbf{Z}_{Tff} \end{bmatrix},$$

and

$$\mathbf{M}_{ss} = \begin{bmatrix} \mathbf{M}_{Bss} \\ \mathbf{M}_{Tss} \end{bmatrix}, \mathbf{M}_{sf} = \begin{bmatrix} \mathbf{M}_{Bsf} \\ \mathbf{M}_{Tsf} \end{bmatrix}, \mathbf{M}_{fs} = \begin{bmatrix} \mathbf{M}_{Bfs} \\ \mathbf{M}_{Tfs} \end{bmatrix}, \mathbf{M}_{ff} = \begin{bmatrix} \mathbf{M}_{Bff} \\ \mathbf{M}_{Tff} \end{bmatrix},$$

where the indexes "B" and "T" represent the bottom and top nodes respectively. The stress and strain relationship for a porous material can be written as

$$\boldsymbol{\sigma}_s = \mathbf{D}_s \boldsymbol{\varepsilon}_s + \mathbf{D}_{sf} \boldsymbol{\varepsilon}_f, \tag{2-42}$$

$$\boldsymbol{\sigma}_f = \mathbf{D}_f \boldsymbol{\varepsilon}_f + \mathbf{D}_{sf} \boldsymbol{\varepsilon}_s = h\mathbf{p}. \tag{2-43}$$

In which ε_s and ε_f are strain vectors for the solid and the fluid phases, respectively and σ_s and σ_f are the stress vectors of the solid and fluid phases. Respectively, where h is the porosity of the poro-elastic material and **p** is the pore fluid pressure**.** $\mathbf{D_s}$**,** $\mathbf{D_f}$**,** and $\mathbf{D_{sf}}$ are the matrices of the elastic coefficients related to the solid phase, the fluid phase and the strain coupling between both phases, respectively. The solid phase stress and strain are the force per unit area and the spatial gradient of the solid phase displacement. The fluid phase stress is the pressure and the fluid phase strain is the volumetric strain, or the divergence of the volume displacement. The total stress on a boundary is the summation of the solid phase and fluid phase stress

$$\boldsymbol{\sigma} = \boldsymbol{\sigma}_s + \boldsymbol{\sigma}_f \tag{2-44}$$

The effective displacement of the boundary depends on if it is a fluid phase or solid boundary. Consider a very thin layer of fluid phase just in front of the porous material. The effective velocity at the boundary is $(1-h)\mathbf{v_s} + h\mathbf{v_f}$. In this case the relationship between the force acting on the porous material and the velocity of the solid phase at the boundary is given with the mobility matrix $\mathbf{M_f}$ such that

$$\mathbf{M}_f \mathbf{f}_f = (1-h)\mathbf{v}_s + h\mathbf{v}_f. \tag{2-45}$$

Consider an infinitesimally thin structural boundary, such that the fluid phase and solid phase velocities are the same. In this case the relationship between the force acting on the fluid phase and the total velocity at the boundary is given by the mobility matrix $\mathbf{M}_s$ such that

$$\mathbf{v}_s = \mathbf{M}_s \left(\mathbf{f}_s + \mathbf{f}_f \right) . \tag{2-46}$$

The relationship between the solid phase and fluid phase velocities and forces in the finite element model are

$$\mathbf{v}_s = \mathbf{M}_{sf} \mathbf{f}_f + \mathbf{M}_{ss} \mathbf{f}_s , \tag{2-47}$$

$$\mathbf{v}_f = \mathbf{M}_{ff} \mathbf{f}_f + \mathbf{M}_{fs} \mathbf{f}_s , \tag{2-48}$$

$$\mathbf{f}_s = \mathbf{Z}_{sf} \mathbf{v}_f + \mathbf{Z}_{ss} \mathbf{v}_s , \tag{2-49}$$

$$\mathbf{f}_f = \mathbf{Z}_{ff} \mathbf{v}_f + \mathbf{Z}_{fs} \mathbf{v}_s . \tag{2-50}$$

The total force $\mathbf{f}$ applied on the porous material is split into a force applied on the solid phase $\mathbf{f}_s$ and on the fluid phase $\mathbf{f}_f$, therefore it is assumed that

$$\mathbf{f}_s = (1-h)\mathbf{f} \text{ and } \mathbf{f}_f = h\mathbf{f} . \tag{2-51}$$

Hence,

$$\mathbf{v}_s = \left(\mathbf{M}_{sf} + \frac{1-h}{h} \mathbf{M}_{ss} \right) \mathbf{f}_f , \tag{2-52}$$

$$\mathbf{v}_f = \left(\mathbf{M}_{ff} + \frac{1-h}{h} \mathbf{M}_{fs} \right) \mathbf{f}_f . \tag{2-53}$$

Using the above equations, the mobility and impedance matrices of a porous material in contact with an air cavity can be expressed as:

$$\mathbf{M}_f = h\mathbf{M}_{ff} + (1-h)(\mathbf{M}_{fs} + \mathbf{M}_{sf}) + \frac{(1-h)^2}{h} \mathbf{M}_{ss} , \tag{2-54}$$

$$\mathbf{Z}_f = \left(h\mathbf{M}_{ff} + (1-h)(\mathbf{M}_{fs} + \mathbf{M}_{sf}) + \frac{(1-h)^2}{h} \mathbf{M}_{ss} \right)^{-1} . \tag{2-55}$$

When calculating the impedance and mobility matrices with solid boundary, the solid phase velocity $\mathbf{v}_s$ and the fluid phase velocity $\mathbf{v}_f$ are equal:

$$\mathbf{v} = \mathbf{v}_s = \mathbf{v}_f \,. \tag{2-56}$$

Hence,

$$\mathbf{f}_s = \left(\mathbf{Z}_{sf} + \mathbf{Z}_{ss}\right)\mathbf{v}_s \,, \tag{2-57}$$

$$\mathbf{f}_f = \left(\mathbf{Z}_{ff} + \mathbf{Z}_{fs}\right)\mathbf{v}_s \,. \tag{2-58}$$

The mobility and impedance matrices of a porous material in contact with an elastic structure can be expressed such as:

$$\mathbf{Z}_s = \mathbf{Z}_{sf} + \mathbf{Z}_{ss} + \mathbf{Z}_{ff} + \mathbf{Z}_{fs} \,, \tag{2-59}$$

$$\mathbf{M}_s = \left(\mathbf{Z}_{sf} + \mathbf{Z}_{ss} + \mathbf{Z}_{ff} + \mathbf{Z}_{fs}\right)^{-1} \,. \tag{2-60}$$

The given impedance and mobility matrices in (2-54), (2-55), (2-59) and (2-60) can be used to describe the HG blanket used in the impedance and mobility method depending on the boundary conditions.

2.1.5 Matching nodes of the HG blankets, plate and the free field

After deriving the individual IMM equations, an interface system must be developed to interface the plate, heterogeneous blankets, and the acoustic free field. The problem and solution are now described. The finite element model of the poro-elastic material has four nodes on each side of an element. However, the radiation impedance matrix is evaluated at the center of each node. To match the two objects one could evaluate the velocity at the center of the surface of the finite element model; however, one could also define a non uniform grid and cut out the outer nodes.

Figure 2-4 shows a simple example of a 5x5 poro-elastic material model (green and red nodes) on a plate (black nodes). In order to match the radiation mobility matrix, the outer nodes (red) of the poro-elastic material model have been positioned half the distance away from the inner nodes (green) relative to each other. Once the impedance matrix is calculated for the 5x5 matrix, the red nodes will be deleted (by introducing a new indexing system) and the mobility matrix will be computed with a 3x3 grid size. Thus if one wants a 5x5 mobility or impedance matrix for the poro-elastic media, the FE model initially has to create a 7x7 grid.

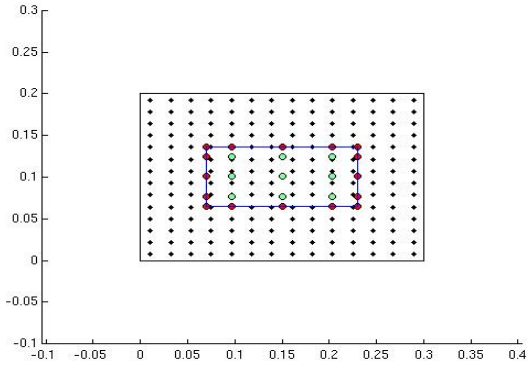

Figure 2-4: 5x5 poro-elastic material model on a plate; Outer nodes (red) of the poro-elastic material model positioned twice the distance away from the inner nodes (green) relative to each other

2.1.6 Input forces

Two main input forces are considered in this thesis, a point force excitation and plane wave pressure.

The point force excitation is applied on one of the grid points of the left side of the plate or the bottom surface of the poro-elastic media. Considering the generic equation that relates the velocity with the force:

$$v(x,y,\omega) = M(x,y,\omega) f(x,y,\omega) \tag{2-61}$$

It is necessary to provide a force in the frequency domain (ω dependency) for each point to be excited (space dependency). It has been chosen to apply a force with a unit constant spectrum in the frequency band of interest. In this way it is possible to find directly the transfer function of the system in terms of velocity over force.

The plane wave pressure that impinges on the left side of the plate or the bottom surface of the poro-elastic material is considered the blocked pressure (twice the amplitude of the incident pressure). Considering θ the angle from the vector normal to the surface and φ the angle from the positive x direction on the plate. The incident plane wave equation [68,69,70] is:

$$p_i(x,y,t) = P_i e^{j(\omega t - k_x x - k_y y)} \tag{2-62}$$

Where the wavenumber in x-direction is given by $k_x = -k\sin(\theta)\cos(\varphi)$ and the wavenumber in y-direction is given by $k_y = -k\sin(\theta)\cos(\varphi)$ where $k = \frac{\omega}{c}$ is the wavenumber (c = speed of sound).

2.1.7 System studied

The DPS studied consists of a source and a receiving panel. The source panel, referred to as the "fuselage," can be excited with by force or forces. For the work presented here a unit force acting at x/L_x=0.3 and y/L_y=0.7 on the fuselage panel is used. The receiving panel is referred to as the "trim" panel.

Figure 2-1 shows the system studied in the mathematical model. The modeled objects are labeled 1 through 5, which are the fuselage, HG blanket, cavity, trim and radiation field, respectively. The interfaces of this subsystem are labeled A-E which are the input force/fuselage, fuselage/HG blanket, HG blanket/cavity, cavity/trim and trim/radiation field interfaces, respectively.

2.1.8 Explicit coupling equations for the system

To couple the objects, a linear system of equations was derived using the continuity of velocity and equilibrium of forces at all interfaces A→E. Mobility and impedance representations for each object 1→5 were derived. The impedance and mobility matrices have three indexes. The first index stands for the object number. The second index points out the interface at which the forces on the objects act. The third index shows at which interface the velocities are computed. For example, at a given frequency, the complex mobility matrix $\mathbf{M_{1AB}}$ would describe the velocities at interface B due to forces acting on interface A acting through the first object (1). Hence, $\mathbf{M_{1AB}}$ is a transfer mobility matrix with the input force described by the complex vector $\mathbf{f_A}$ and output velocities described by a complex vector $\mathbf{v_B}$. Figure 2-2 shows a schematic of the fuselage with the input point force off center and the 25 output velocities that describe one column of the mobility matrix $\mathbf{M_{1AB}}$. The impedance matrices $\mathbf{Z}$ are indexed analog to the mobility matrices. The coupling equations for interface B are:

$$\mathbf{v_B} = \mathbf{M_{1AB}}\mathbf{f_A} - \mathbf{M_{1BB}}\mathbf{f_B} \qquad (2\text{-}63)$$

$$\mathbf{f_B} = \mathbf{Z_{2BB}}\mathbf{v_B} + \mathbf{Z_{2BC}}\mathbf{v_C} \quad (2\text{-}64)$$

$\mathbf{M_{1BB}}$ and $\mathbf{f_B}$ are the mobility of the fuselage [55] (modeled using analytical plate equations) and the force acting at the interface B, respectively. $\mathbf{Z_{2BB}}$ and $\mathbf{Z_{2BC}}$ (see Appendix A) are derived from the finite element model for the HG blanket. The equations for interface C are:

$$\mathbf{f_C} = -\mathbf{Z_{2CB}}\mathbf{v_B} - \mathbf{Z_{2CC}}\mathbf{v_C} \quad (2\text{-}65)$$

$$\mathbf{f_C} = \mathbf{Z_{3CC}}\mathbf{v_C} - \mathbf{Z_{3CD}}\mathbf{v_D} \quad (2\text{-}66)$$

$\mathbf{Z_{2CB}}$ and $\mathbf{Z_{2CC}}$ are also calculated from the finite element model. $\mathbf{Z_{3CC}}$ and $\mathbf{Z_{3CD}}$ [58] (calculated using the modes for a rectangular rigid wall volume) are the input and transfer impedance of the cavity, respectively. The equations for interface D are as follows:

$$\mathbf{f_D} = \mathbf{Z_{3DC}}\mathbf{v_C} - \mathbf{Z_{3DD}}\mathbf{v_D} \quad (2\text{-}67)$$

$$\mathbf{v_D} = \mathbf{M_{4DD}}\mathbf{f_D} - \mathbf{M_{4ED}}\mathbf{f_E} \quad (2\text{-}68)$$

with $\mathbf{Z_{3DC}}$ and $\mathbf{Z_{3DD}}$ [58] being the cavity transfer and output impedance respectively. The coupling equations for the last interface, E, are

$$\mathbf{v_E} = \mathbf{M_{4DE}}\mathbf{f_D} - \mathbf{M_{4EE}}\mathbf{f_E} \quad (2\text{-}69)$$

$$\mathbf{f_E} = \mathbf{Z_{5EE}}\mathbf{v_E} \quad (2\text{-}70)$$

where the mobility matrices of the trim are $\mathbf{M_{4DD}}$, $\mathbf{M_{4DE}}$, $\mathbf{M_{4ED}}$, and $\mathbf{M_{4EE}}$ (calculated similar to the fuselage mobility matrices). The velocity at the trim surface is then multiplied by the radiation impedance matrix $\mathbf{Z_{5EE}}$ (Eq. (8)) as per Elliott et al., Bai et al. and Berkhoff [60-62] (derived using Boundary Element Method or Rayleigh integral formula in the case of planar sources in a baffle) to account for radiation loading $\mathbf{f_E}$. It should be noted that in practice, accelerometers were used to measure the fuselage and trim response. In order to match theory with experiment, these accelerometers were modeled as lumped masses placed on the plates at the nodes at which the accelerometers were positioned. The derivation of the explicit coupling matrices makes it possible to solve for the velocities and forces at the interfaces of interests.

2.1.9 Assembled matrix representation

There are several potential methods to solve the above set of coupled equations, from direct algebraic manipulation to a matrix method. Solving for each variable individually by manipulating (2-63)-(2-70) is a tedious process and prone to mathematical errors, so it was decided to write the linear set of coupled equations as an assembled matrix:

$$\underbrace{\begin{bmatrix} \mathbf{M_{1BB}} & \mathbf{I} & \mathbf{0} & \mathbf{0} & \mathbf{0} & \mathbf{0} & \mathbf{0} & \mathbf{0} \\ \mathbf{I} & \mathbf{-Z_{2BB}} & \mathbf{0} & \mathbf{-Z_{2BC}} & \mathbf{0} & \mathbf{0} & \mathbf{0} & \mathbf{0} \\ \mathbf{0} & \mathbf{Z_{2CB}} & \mathbf{I} & \mathbf{Z_{2CC}} & \mathbf{0} & \mathbf{0} & \mathbf{0} & \mathbf{0} \\ \mathbf{0} & \mathbf{0} & \mathbf{I} & \mathbf{-Z_{3CC}} & \mathbf{Z_{3CD}} & \mathbf{0} & \mathbf{0} & \mathbf{0} \\ \mathbf{0} & \mathbf{0} & \mathbf{0} & \mathbf{-Z_{3DC}} & \mathbf{Z_{3DD}} & \mathbf{I} & \mathbf{0} & \mathbf{0} \\ \mathbf{0} & \mathbf{0} & \mathbf{0} & \mathbf{0} & \mathbf{I} & \mathbf{-M_{4DD}} & \mathbf{M_{4ED}} & \mathbf{0} \\ \mathbf{0} & \mathbf{0} & \mathbf{0} & \mathbf{0} & \mathbf{0} & \mathbf{-M_{4DE}} & \mathbf{M_{4EE}} & \mathbf{I} \\ \mathbf{0} & \mathbf{0} & \mathbf{0} & \mathbf{0} & \mathbf{0} & \mathbf{0} & \mathbf{I} & \mathbf{-Z_{5EE}} \end{bmatrix}}_{\mathbf{A}} \underbrace{\begin{bmatrix} \mathbf{f_B} \\ \mathbf{v_B} \\ \mathbf{f_C} \\ \mathbf{v_C} \\ \mathbf{v_D} \\ \mathbf{f_D} \\ \mathbf{f_E} \\ \mathbf{v_E} \end{bmatrix}}_{\mathbf{x}} = \underbrace{\begin{bmatrix} \mathbf{M_{1AB}f_A} \\ \mathbf{0} \\ \mathbf{0} \\ \mathbf{0} \\ \mathbf{0} \\ \mathbf{0} \\ \mathbf{0} \\ \mathbf{0} \end{bmatrix}}_{\mathbf{b}} \tag{2-71}$$

which can then be solved by inverting the matrix **A** as well as iteratively. Matrix A is a sparse and almost block diagonal matrix and therefore efficiently invertible [71]. Taking a closer look at **A**, one can recognize that it consists of small sub matrices such as

$$\begin{bmatrix} \mathbf{-Z_{3CC}} & \mathbf{Z_{3CD}} \\ \mathbf{-Z_{3DC}} & \mathbf{Z_{3DD}} \end{bmatrix} \tag{2-72}$$

which represent the cavity in the observed case. This shows that it is very easy to add more levels of complexity to an existing system using the matrix formulation, without needing to use algebraic manipulation.

2.2. Comparison between theory and experiment

This section presents the experimental validation of a DPS with and without the HG blanket. Figure 2-5 (a) shows the schematic of the experimental setup with the two clamps (1,6) supporting the clamped boundary conditions of the fuselage (2) and the trim (5). The HG blanket (3) is attached to the "interior" of the fuselage. A heavy aluminum block was used as the frame (4). Pictures of the experimental setup in Figure 2-5 (b) show the accelerometer position and grid (left) and the frame (right). A roving modal hammer excited the fuselage at all of the grid points, and transfer functions from

the hammer to accelerometer were measured. Using reciprocity, these can be converted to a roving accelerometer and a constant position point force excitation, which matches the model. See Appendix A for more details on experimental techniques.

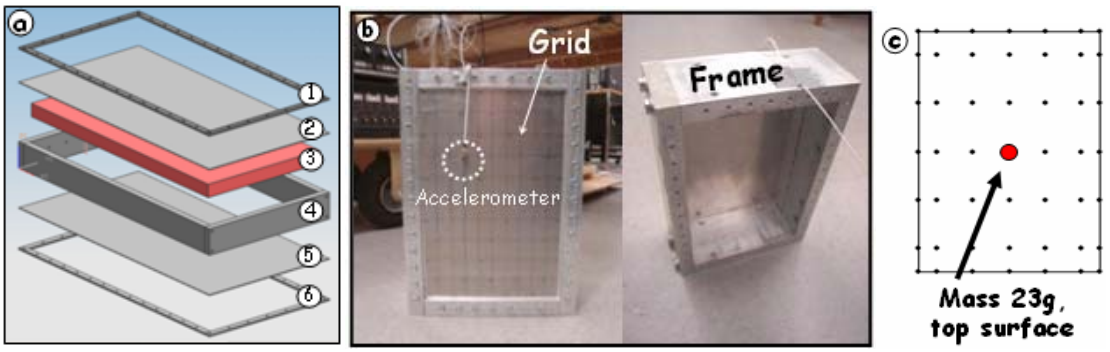

Figure 2-5: Experimental setup: schematic (a) and pictures (b) showing the accelerometer position (left) as well as the frame (right), (c) shows the mass position and weight of the HG blanket.

Throughout this thesis, *the spatially averaged squared velocity* of the fuselage V_f and trim V_t are used to present the predicted response of the double panel system. At each frequency of interest, V_f and V_t are calculated from 25 by 1 complex vectors of fuselage and trim velocities $\mathbf{v_f}$ and $\mathbf{v_t}$:

$$\begin{aligned} \mathbf{V_f} &= \frac{\mathbf{1}}{\mathbf{N}} \mathbf{v_f}^{\mathbf{H}} \mathbf{v_f} \\ \mathbf{V_t} &= \frac{\mathbf{1}}{\mathbf{N}} \mathbf{v_t}^{\mathbf{H}} \mathbf{v_t} \end{aligned} \tag{2-73}$$

These measures are directly proportional to the kinetic energy of the plates as per Gardonio and Elliott [17]. Furthermore the *total sound power* radiated from the double panel system with sandwiched HG blanket can be expressed as follows,

$$P_t = \frac{1}{N} \mathbf{v_t^H Z_{5EE} v_t} \tag{2-74}$$

where $\mathbf{Z_{5EE}}$ is the radiation matrix used in (2-70) as per Elliott et al., Bai et al. and Berkhoff [60-62]. These calculations can then be performed over the frequencies range of interest (0-500Hz).

2.2.1 Experimental validation for a plate with accelerometer

In order to validate a complex system such as the DPS with sandwiched HG blankets, both panels used for the DPS were validated individually. The data of the two single panels was then used in the analytical model of the DPS. This section presents the experimental validation of a single plate (used later on as the fuselage panel) with clamped boundary conditions and a 4g accelerometer placed at an off center position *x/Lx*=0.1and *y/Ly*=0.7 as shown in Figure 2-2(b).

2.2.1.1. Accounting for the mass of the accelerometer

The accelerometer was modeled as a lumped mass and coupled to the plate in order to build a more accurate mobility matrix for the plate. Figure 2-6 shows the free body diagram of a plate with and without taking the mass of the accelerometer *m* into account.

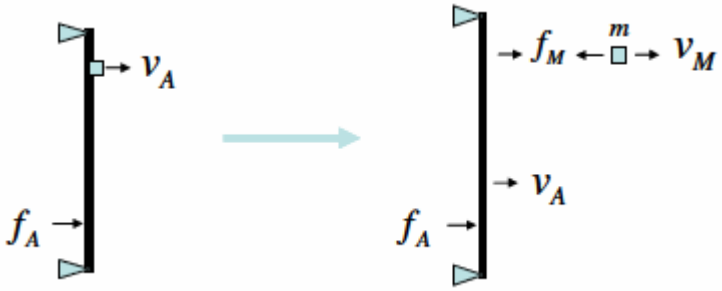

Figure 2-6: (a) shows the free body diagram of a plate with and without taking the mass m of the accelerometer into account

The equations for the plate modeled with a lumped mass on top of it with an input force $\mathbf{f_A}$ and output velocity $\mathbf{v_A}$, where the force due to the mass *m* is $\mathbf{f_M}$ and the velocity of the mass at the mass location is $\mathbf{v_M}$, solved for $\mathbf{v_A}$, is given by:

$$\begin{aligned} \mathbf{v_M} &= \mathbf{M_0 f_M} = \mathbf{M_{MA} f_A} - \mathbf{M_{MM} f_M} \\ \rightarrow \mathbf{f_M} &= \left[\mathbf{M_0} + \mathbf{M_{MM}}\right]^{-1} \mathbf{M_{MA} f_A} \end{aligned} \tag{2-75}$$

$$\mathbf{v_A} = \mathbf{M_{AA} f_A} - \mathbf{M_{AM} f_M} = \left[\mathbf{M_{AA}} - \mathbf{M_{AM}}\left[\mathbf{M_0} + \mathbf{M_{MM}}\right]^{-1} \mathbf{M_{MA}}\right]\mathbf{f_A} \tag{2-76}$$

$\mathbf{M_0}$ is the mobility of the mass m, $\mathbf{M_{AA}}$, $\mathbf{M_{AM}}$, $\mathbf{M_{MA}}$, and $\mathbf{M_{MM}}$ are input and transfer plate mobility matrices with respect to the plate locations (index "A") and mass

locations (index "M"). The output velocity $\mathbf{v_A}$ in (2-76) which describes the velocity at all locations on the plate, is expressed as an augmented mobility matrix $\mathbf{M_{equivalent}}$ times the input force where

$$\mathbf{M}_{equivalent} = \mathbf{M}_{AA} - \mathbf{M}_{AM}\left[\mathbf{M}_{0} + \mathbf{M}_{MM}\right]^{-1}\mathbf{M}_{MA} \qquad (2\text{-}77)$$

2.2.1.2. Experimental results

Table 2-1 presents a list all the important data regarding the experimental test. To match the experimental fuselage panel in the analytical model, the aspect ratio has been changed on both plates within 2-3% of the measured values, and the damping ratio for all modes has been set to 0.006, which is typical for a clamped aluminum plate.

Table 2-1: Model parameters of SPS with clamped BC's used for the exp. validation of the analytical model

Parameter	Value	Units
	Material properties of single plate	
Length	0.307	m
Width	0.206	m
Thickness	0.0008	m
Density	2700	kg/m^3
Modulus of elasticity	$7*10^{10}$	N/m^2
Poisson's ratio	0.3	-

Figure 2-7 presents the experimental validation of a clamped plate with the experimental data presented in Table 2-1. The analytical model matches the experiment satisfactory in the presented frequency range from 50-1000Hz.

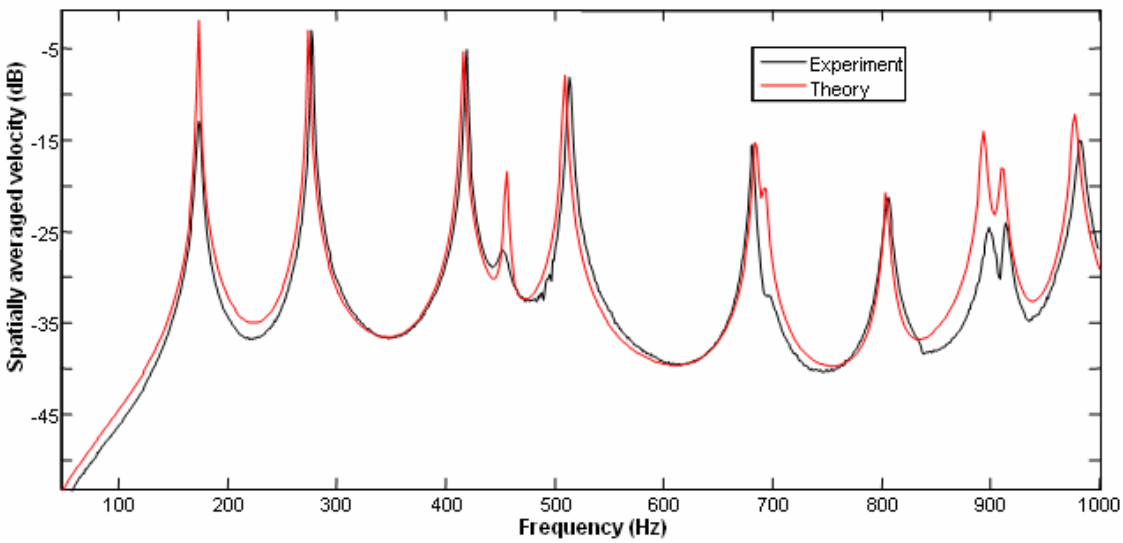

Figure 2-7: Experimental validation of a clamped plate excited in non center position

$M_{equivalent}$ equivalent was used when modeling both the fuselage and the trim and the result was a better match between the experiment and theory, not only at higher, but also at low frequencies (below 400Hz), where the additional lumped mass of the accelerometer would result in an asymmetry of the plate and would let the uneven modes become more dominant when computing the DPS [72]. Both, the receiver and the source plate of the DPS were validated individually. The matching results were similar, hence only the experimental validation of the source plate is presented.

2.2.2 Experimental validation for DPS

This section presents the results of the experimental validation of the coupled DPS without the HG blanket present. Table 2-2 lists all important properties of the DPS with two clamped plates used for the experimental validation of the analytical model. As above, the aspect ratio has been changed on both plates within 2-3% of the measured values, and the damping ratio for all modes has been set to 0.006.

Figure 2-8 (a) shows the experimental validation of the double panel system on the fuselage side, excited at x/L_x=0.1 and y/L_y=0.7 as shown in Figure 2-2. Theory and experiment match very well and the dynamics of the fuselage are all captured with a high level of detail. Most of the discrepancies can be explained by slight differences in damping level between experiment and theory. For simplicity, the analytical model

uses a constant damping term for all of the modes and the damping was not changed from mode to mode. This can be particularly seen at the third mode, around 200Hz, which is much lower in the measured spectrum than in the model. However, the third experimental mode is an even-odd mode (2-1) [73] which does not couple very well to the cavity and thus is not very important for sound transmission.

Table 2-2: Model parameters of the double panel system with two clamped plates.

Parameter	Value	Units
	Material properties of the Fuselage	
Length	0.307	m
Width	0.206	m
Thickness	0.0008	m
Density	2700	kg/m^3
Modulus of elasticity	$7*10^{10}$	N/m^2
Poisson's ratio	0.3	-
	Material properties of the Cavity	
Thickness	0.1	m
Density	1.2	kg/m^3
Speed of sound	343	m/s
Damping	0.01	-
	Material properties of the Trim	
Length	0.307	m
Width	0.206	m
Thickness	0.0012	m
Density	2700	kg/m^3
Modulus of elasticity	$7*10^{10}$	N/m^2
Poisson's ratio	0.3	-

Figure 2-8 (b) presents the experimental validation of the double panel system on the receiving side, measured at 25 points with the fuselage panel excited at acting at x/L_x=0.1 and y/L_y=0.7 as shown in Figure 2-2. The comparison shows a good match across the frequency range of interest (50 to 500 Hz) and should be sufficiently accurate to capture all of the important physics concerned with sound transmission through the double panel system. The discrepancies at low frequencies are a result of minor frame motions which cause a zero in the measured response at around 40Hz. The frame in the model is assumed to be rigid but the experimental frame, although heavy, was not perfectly attached to ground. As expected, exact matching between model and experiment becomes difficult as the system complexity increases.

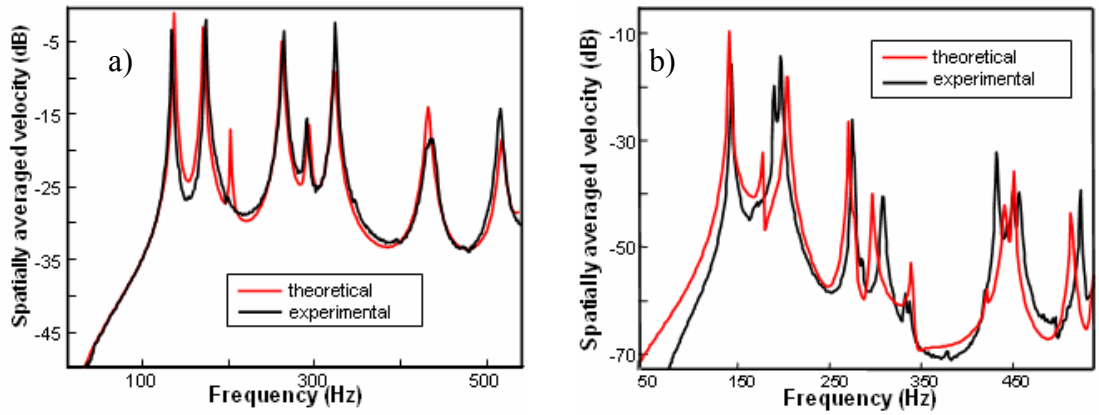

Figure 2-8: Experimental validation of (a) the fuselage and (b) the trim panel of a double panel system measured at 25 points. A unit point force was applied at a non center position on the fuselage panel.

2.2.3 Experimental validation for DPS with sandwiched HG blanket

This section presents the experimental validation for a DPS with HG-blanket embedded. The HG-blanket has one mass inserted inside the poro-elastic media, placed in the center of the plate, near the surface of the poro-elastic media to target the 1-1 mode. This is shown in Figure 2-5(c).

Details of how the embedded masses are tuned to certain natural frequencies are presented in [35]. The total weight of the embedded masses of all HG blankets

presented in this paper is approximately 10% of the fuselage panel weight. Other than the inclusion of the HG blankets, the experimental setup used for the experimental validation of the double panel system is identical with the one used in this section. Due to the addition of the HG blanket the cavity thickness is reduced due to the fact that the distance between fuselage and trim is kept constant. Table 2-3 presents the HG blanket properties as well as the modified cavity parameters for the experimental validation of the double panel system with HG blanket inside. The fuselage and trim parameters are shown on the previous section in Table 2-2.

Figure 2-9 shows the comparison of predicted (a) and measured (b) spatially averaged velocity of the DPS source panel with and without sandwiched HG blanket. The HG blanket is designed to target the 1-1 mode of the fuselage at approximately 130Hz. A unit point force was applied at a non center position, shown in Figure 2-6 at the source panel to excite all plate modes. Theory and experiment show the same trends: It can be seen that the mode split around 130Hz caused a significant drop in the vibration response.

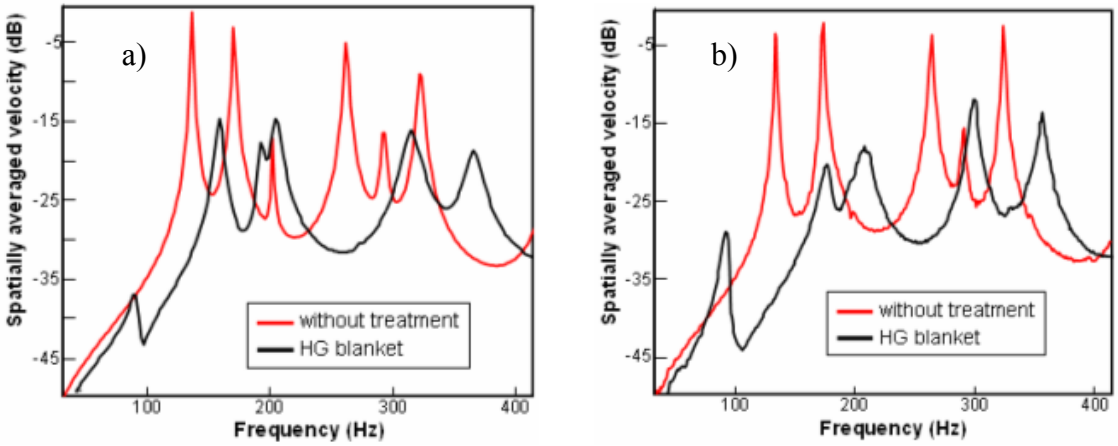

Figure 2-9: Comparison of spatially averaged velocity of a source panel inside a double panel system with and without sandwiched HG blanket. a) predicted response; b) measured response

Table 2-3: Model parameters of HG blanket and cavity.

Parameter	Value	Units
	Material properties of the HG blanket	
Length	0.298	m
Width	0.198	m
Thickness	0.05	m
Density	50	kg/m^3
Modulus of elasticity	$2.2*10^5$	N/m^2
Poisson's ratio	0.3	-
Tortuosity	1.7	-
Flow resistivity	$3.2*10^4$	Ns/m^4
Porosity	0.95	-
Atmospheric pressure	$1.0325*10^5$	N/m^2
Structural damping	0.0001	-
Viscous characteristic length	$5*10^{-5}$	-
Thermal characteristic length	$1.1*10^{-4}$	-
Total weight of embedded masses	23	g
	Material properties of the Cavity	
Thickness	0.05	m
Density	1.2	kg/m^3
Speed of sound	343	m/s
Damping	0.01	-

Figure 2-10 shows the comparison of predicted (a) and measured (b) spatially averaged velocity of the DPS receiving panel with and without sandwiched HG blanket. One can see that the mode split of the first fuselage mode around 130Hz in Figure 2-9 caused by the HG blanket, also resulted in a mode split for the first mode of the trim panel, since the fuselage and trim panels are highly coupled by the air cavity at this mode. Hence, a drop in the vibration response of the fuselage caused a drop in vibration response of the trim. It can be seen in Figure 2-10 that the drop in the vibration response due to the mode split at around 130Hz is quite significant.

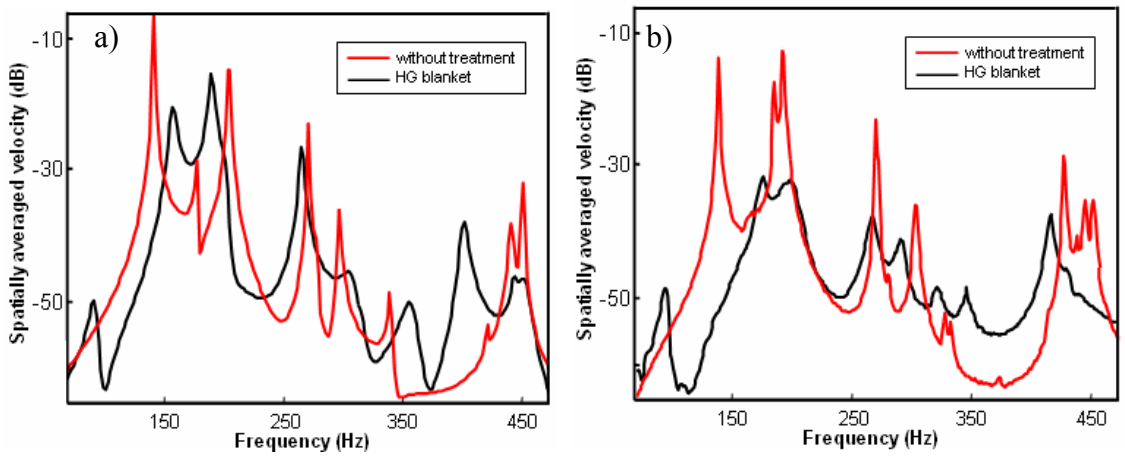

Figure 2-10: Comparison of spatially averaged velocity of a receiving panel inside a double panel system with and without sandwiched HG blanket. a) predicted response; b) measured response

Figure 2-11 shows the experimental validation of the power radiated from the trim panel of the DPS with sandwiched HG blanket. Plotted are the spectral density on the left and one-third octave band on the right. The results of the experimental validation in the frequency of interest show that the dynamics of the fuselage are captured. The results match up well at lower frequencies by duplicating the physics of the 1-1 mode split on the fuselage. The damping levels do not match perfectly at the modes but the overall dB level is well matched. From the DPS without the HG blanket to the DPS with HG blanket, a significant level of complexity has been added to the analytical model. The one-third octave band plot verifies once again that the theoretical model captures the basic physics of the system studied.

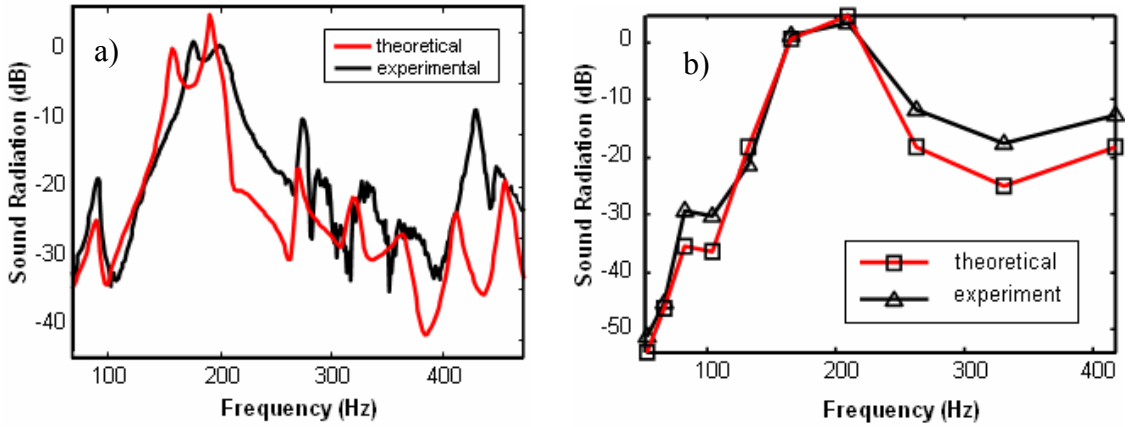

Figure 2-11: Comparison of experimental and predicted radiated sound power of the receiving side of a DPS with sandwiched HG blanket. Plotted are the spectral density (a) and one-third octave band (b). HG blanket is designed to target the 1-1 mode of the source pane. A unit point force was applied at a non center position on the source panel

In summary, the above results show that an effective model has been developed and verified. The results presented using an HG blanket targeting the first mode of the fuselage also show the potential of the HG blanket to reduce the interior noise levels of an aircraft by targeting fuselage modes in the low frequency region, i.e. below 500Hz. In order to make the design tool more user friendly, a user interface was developed which is presented in Appendix B.

2.3. Double HG blankets

Experimental demonstrations of the HG blanket inside the DPS presented in the previous section have shown that it is possible to control the vibration of the source panel fairly easy. It seems that the masses inside the poro-elastic media have to be positioned at the anti-node lines of the source panel and tuned to the right frequencies to target certain modes of the source panel. Controlling the vibration response of the receiver panel, by controlling the vibration response of the source panel, was a much harder task. Every mode in the source panel couples differently into the receiver panel modes. Some fuselage modes transfer less energy into the system then others as shown in the "modal" design case in the previous section. The following experiment addresses this problem by attaching the HG blanket on both, the trim and the fuselage, in order to control the trim response directly. This is referred to as the "double HG blanket".

2.3.1 Single versus double HG blankets

This section compares a DPS with single and double HG blankets inside. Figure 2-12 shows the experimental configuration of the DPS for the double HG blanket measurements with a) a single HG blanket (2'' thick HG blanket on top of fuselage and 2'' thick cavity between HG blanket and trim) and b) a double HG blanket (2'' thick HG blanket on top of fuselage, 1'' thick HG blanket on top of trim and 1'' thick cavity in between both HG blankets). The trim has a HG blanket attached that is half as thick as the HG blanket attached to the fuselage. The fuselage is 0.8mm thick and the trim is 1.2mm thick. This means that the modes of the trim are higher than the fuselage modes. Thus, the masses inside the HG blanket attached to the trim panel have to be positioned at a lower depth than the masses inside the poro-elastic media attached to the fuselage. The HG blankets used in the following experiments are designed to target the first two modes of the plates they are attached to. This is in reference to the modal design strategy which will be discussed in section 4.1.1.2.

a) b)

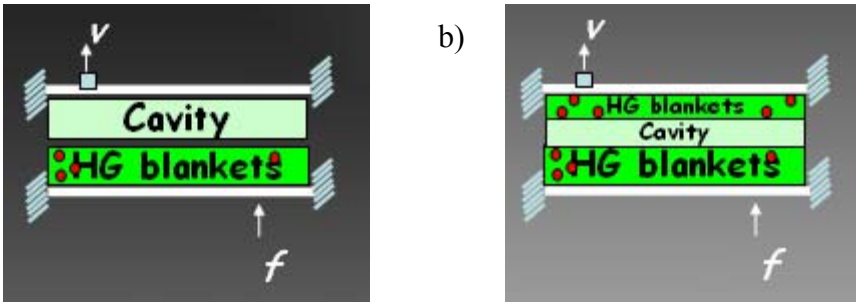

Figure 2-12: Experimental configuration of single bay DPS with a) single HG blanket (2'' thick HG blanket on top of fuselage and 2'' thick cavity between HG blanket and trim) and b) a double HG blanket (2'' thick HG blanket on top of fuselage, 1'' thick HG blanket on top of trim and 1'' thick cavity in between both HG blankets)

Figure 2-13 presents the measured spatially averaged velocity of the fuselage of a DPS for three cases. With HG blankets on top of both, the trim and the fuselage panel (red), with an HG blanket on top of the fuselage (black) and just by itself (blue) in the frequency range of 0-1000Hz. The focus is on the difference between using a single and a double HG blanket, as the effectiveness of the HG blanket compared to the bare case was already shown in the previous section. Before looking at this result, one

would expect that the vibration response of the source panel should not change significantly, seeing how the configuration on that side has not been changed. The fuselage is still controlled by the HG blanket. In fact, the response in both cases at low frequencies is almost identical. However, from 450Hz to 750Hz the response increases and this could be caused by a different coupling between the two panels. In both measurements, the poro-elastic media still damps out the vibration response at frequencies above 500Hz.

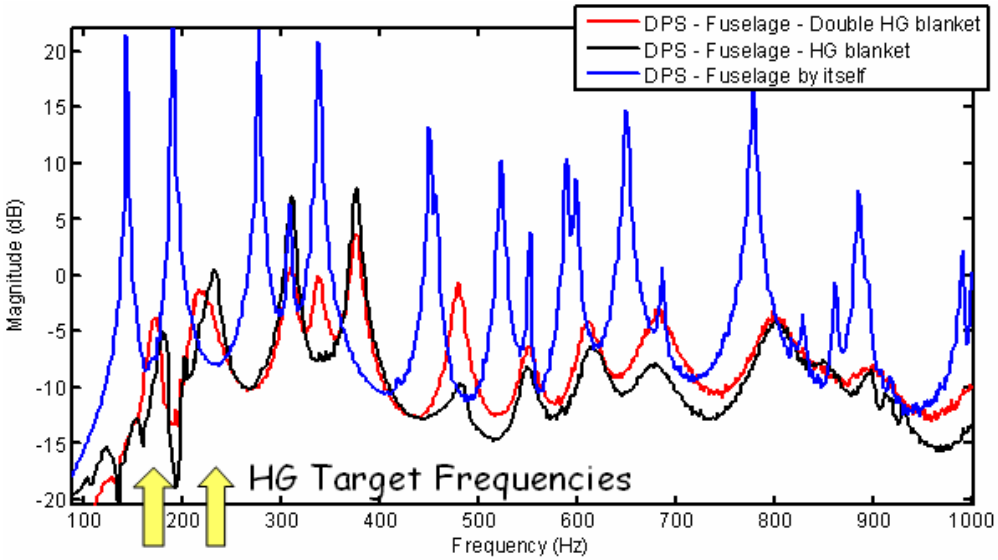

Figure 2-13: Measured spatially averaged velocity of the excitation side (fuselage) of a DPS by it self (blue) and with sandwiched single (black) and double (red) HG blanket

Figure 2-14 presents the spatially averaged velocity of the trim of a DPS in three cases: HG blankets on top of both, the trim and the fuselage panel (red), with an HG blanket on top of the fuselage (black) and just by itself (blue) in the frequency range of 0-1000Hz. Again, the focus in this plot is really the comparison between the single and the double HG blanket configuration. Before looking at the measurements one would expect improvements when controlling the vibration response of the trim panel in the DPS directly with the additionally attached HG blanket. First, the HG blanket is directly attached to the trim and designed to target the first two modes. Prior results have shown that by reducing the first mode of the fuselage, the first mode of the trim is reduced. Therefore, a real improvement would only be expected for controlling the second mode. Second, the poro-elastic media on top of the trim is expected to damp

out the response of the trim at frequencies above 500Hz. The layer of poro-elastic media on top of the trim is very thin, so that the frequency at which the poro-elastic media will damp out the vibration response of the trim panel is expected to get shifted to higher frequencies.

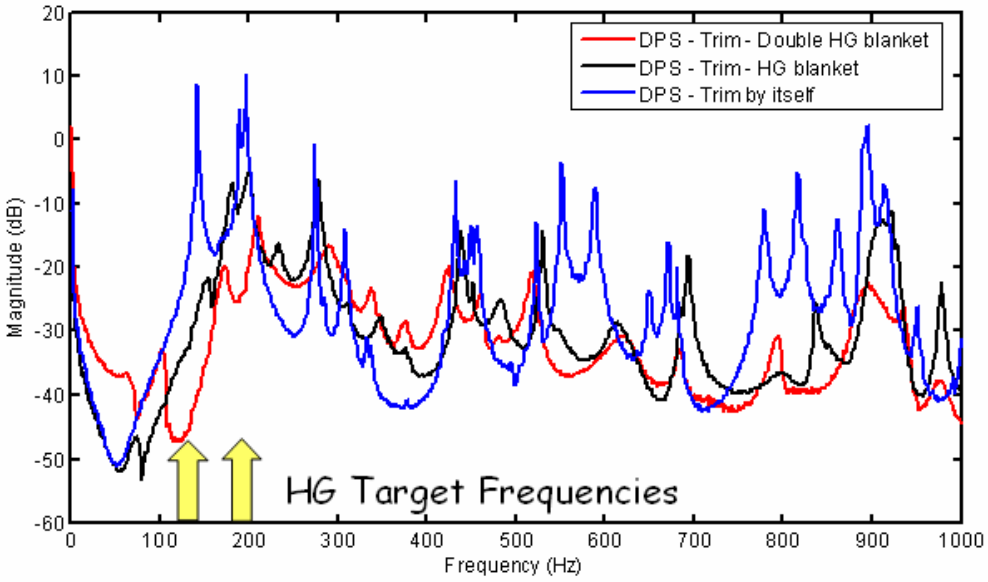

Figure 2-14: Experimental vibration response of the receiver side (trim) of a DPS by it self (blue) and with sandwiched single (black) and double (red) HG blanket

The results in Figure 2-14 show the two expected improvements. However, if one compares the first mode of the trim with and without the second HG blanket on top of the trim, a large difference can be seen. It was expected that the first mode on the trim side would not change, seeing how it was already reduced by a significant amount when using the single HG blanket to control the fuselage. The black line in Figure 2-14 indicates that after splitting the first mode of the fuselage, two modes were created in both the source and receiver panel that were at a lower amplitude. By attaching the HG blanket to the trim, one could target either one of these two modes with tuning the mass inside the poro-elastic media to the right frequency. In other words, the second HG blanket on top of the trim was really used to split one of the two modes that came out if splitting the first mode of the fuselage. The vibration response for the first mode decreased when using the double HG blanket by targeting the first mode of the fuselage twice. Furthermore, it was possible to target the 2-1 mode of the trim directly with the HG blanket attached on the trim. It was not possible to target this certain mode by just

controlling the fuselage. Finally, in both cases the response of the trim at higher frequencies was reduced due to the attached poro-elastic media.

In conclusion, a comparison between a single and a double HG blanket inside a DPS was presented. By attaching a second HG blanket on the trim side, the trim response could be decreased by a significant amount. At low frequencies, it was possible to target modes on the trim which were not easy to reduce by just controlling the fuselage. Additionally, modes that were reduced on the trim side by attaching the HG blanket on the fuselage could be further reduced by targeting them directly on the trim.

2.3.2 Weight reduction for double- HG blankets

A comparison between a single and a double HG blanket inside a DPS was presented in the last section, which led to the following question: *Is it more efficient to design the double HG blankets such that each trim mode is controlled by the HG blanket on the fuselage side or on the trim side?*

In order to answer this question, three double HG blankets were compared (see Figure 2-15): the first double HG blanket (1) is designed to target the 1-1 mode and the 2-1 mode of both, the fuselage and the trim. The second HG blanket (2) targets the 1-1 mode of the fuselage and the 1-1 mode and the 2-1 mode of the trim. The third HG blanket (3) targets the 1-1 mode of the fuselage and the 2-1 mode of the trim.

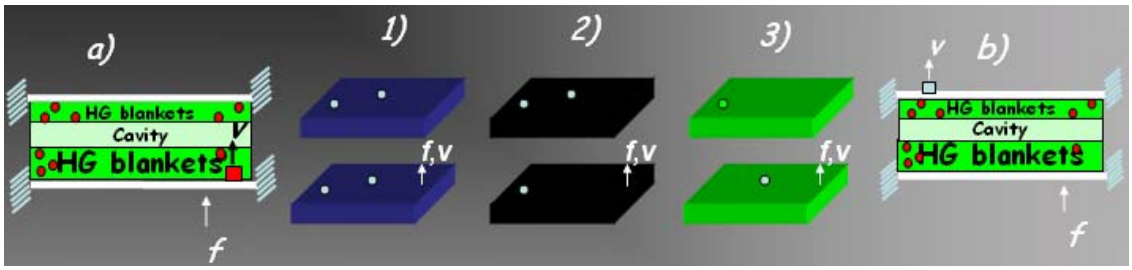

Figure 2-15: Schematic of the HG blankets used in the double HG blanket experiments. Measured is the fuselage (a) and trim (b) response.

Figure 2-16 shows the spatially averaged velocity of the fuselage (schematic shown in Figure 2-15(a)) of a DPS with and without three different (sandwiched) double HG blankets. The two yellow arrows highlight the resonant frequencies of the fuselage targeted with the HG blankets. The green and black line look similar, as both

double HG blankets have the same mass insertion on the poro-elastic media block glued on top of the fuselage. The blue line in comparison is around 3dB lower below 200Hz. This can be explained due to the additional mass insertion of the HG blanket on the fuselage side represented by the blue line shown in Figure 2-15.

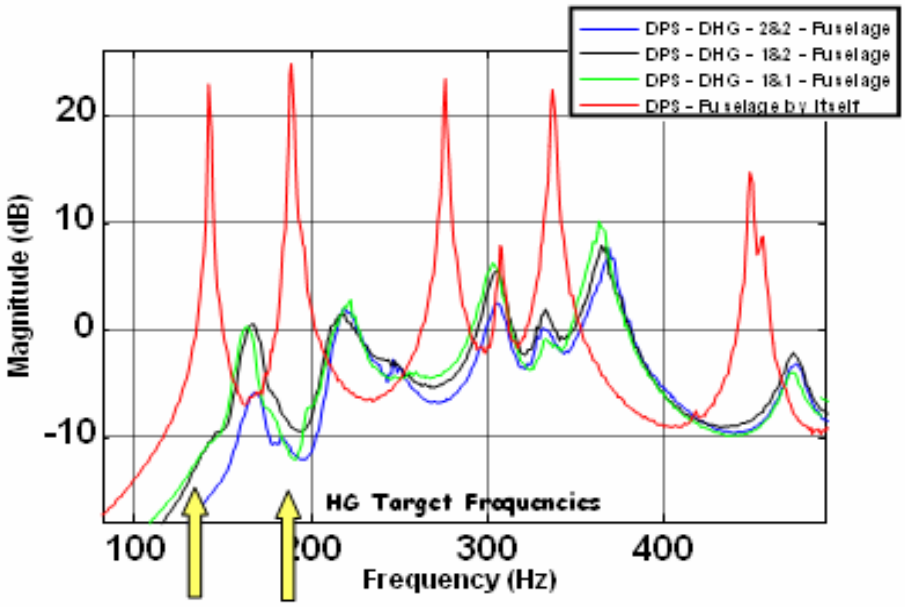

Figure 2-16: Experimental vibration response of a DPS. Plotted is the averaged velocity squared of the source panel with no treatment compared to three double HG blankets

Figure 2-17 shows the spatially averaged velocity of the trim (schematic shown in Figure 2-15(b)) of a DPS with and without three double HG blankets. The blue and the black line are almost identical. This is due to the fact that the two HG blankets on top of the trim are identical. The only difference is the blanket on top of the fuselage. However, the double HG blanket represented by the blue line has an additional mass on the fuselage side targeting the 2-1 mode of the fuselage. Prior results have shown that the control of the 2-1 mode on the fuselage does not effect the trim response. Hence, the 2nd mass insertion of the double HG blanket on the fuselage side has no effect. The response of the green line compared to the black line is higher by a small amount. This is due to the additional mass insertion of the HG blanket on the trim represented by the black line. Note the additional mode split around 110Hz going from the green to the black line which is due to a repeated mode split of the 1-1 mode on the fuselage side.

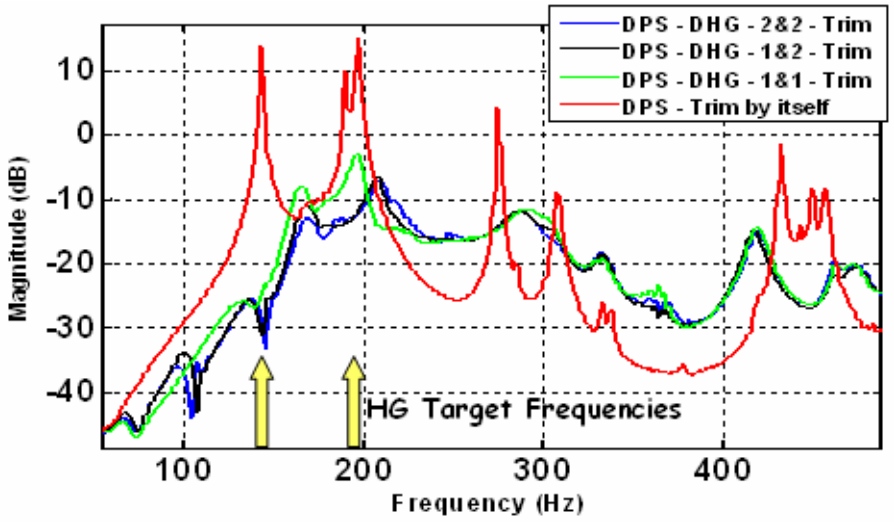

Figure 2-17: Experimental vibration response of a DPS. Plotted is the spatially averaged velocity of the receiving panel with no treatment compared to three double HG blankets

The main goal of this project is to reduce the sound and vibration of the trim panel inside the trim panel. All three double HG blankets are designed to target the first two modes of the DPS. The experimental results show that the double HG blanket can be designed quite efficiently in terms of reducing the vibration response versus the weight of the HG blankets: The HG blankets on the two panels need to be designed such that the trim panel modes which are difficult to control using an HG blanket on the fuselage side are controlled directly on the trim panel. The modes that are easily controlled by a HG blanket on the fuselage panel should be targeted directly on the fuselage side. The results also show that it is very inefficient to target modes on the trim side when they were already reduced on the fuselage side, like for example the 1-1 mode in the prior presented case.

Note that there are practical implementation issues associated with the double HG blankets. Adding HG blankets to aircraft trim panels will result in an increase in manufacturing costs. Furthermore, the trim panel tends to be more heavily damped than the fuselage panel, and thus, will respond less to the damping effects of a porous layer.

3. MULTI-BAY DOUBLE PANEL SYSTEM

The work presented in the last chapter on the design tool included a theoretical model of a double panel system with a single HG blanket inside. As a step between a fuselage with multiple skin pockets and the single-bay double panel system (DPS), more layers of complexity were added to the existing model. This chapter includes a detailed derivation and analysis of a multi-bay double panel system (MPS) with four skin pockets and HG blankets of different dimensions including the frames, stringers and cavity inside the MPS. Finally, this chapter presents a comparison between theory and experiment of a MPS with sandwiched HG blankets.

3.1. Mathematical model

The mathematical model for the MPS consists of six elements (fuselage, frame/stringer, HG blankets, mounts, cavity and trim). Figure 3-1 shows a 3-D computer generated model of the parts that are included. The model is numerated from (1) – (9). The fuselage (2) is being clamped to a solid structure (3) using four clamps (1). The stringer (7) and frame (5) are mounted on top of the fuselage without touching each other (there is a notch inside the frame). Four HG blankets (4) with different dimensions are glued on top of the fuselage in-between the frame and stringer. Two angles (6) are attached to the structure (3) in order to hold eight of the twelve mounts (8) (the other four mounts are held by the frame (5)). A trim (9) built out of aluminum material was mounted on top of the 12 mounts.

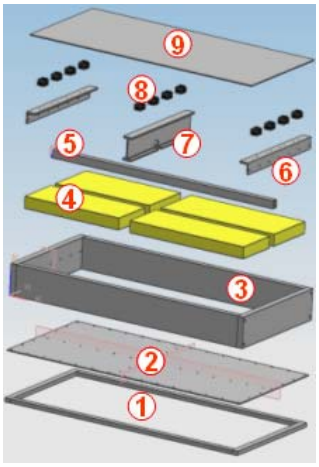

Figure 3-1: 3-D model of multi bay double panel system with sandwiched HG blanket

3.1.1 Frame and stringers

The frame and stringers shown in Figure 3-1 are modeled as beams with different cross-sectional areas (a box-section for the stringers and an I-section for the frame) and free-free BC's. Section 3.1.1.1 includes the derivation of the mobility matrix of a beam in general. However, the key is the second moment of inertia, seeing how frames and stringers have different cross sectional areas. The formulae of the second moment of inertia for a box-section as well as an I-section are presented. Finally, the coupling equations for coupling a beam to a plate are given.

3.1.1.1. Mobility matrix for free-free beam

This section lists the most important equations to obtain the natural frequencies and mode shapes for a beam with free-free BC. An expression for the mobility matrix of a beam with free-free BCs is shown at the end of this section. Natural frequencies for beams in general are [64]:

$$\omega_n = \sqrt{\frac{EI}{\rho S}} k_{nb}^2 \tag{3-1}$$

Where the even rigid body modes for a free- free beam is:

$$\psi_n(x) = 1 \tag{3-2}$$

and the rocking rigid body mode for free-free beam is:

$$\psi_n(x) = \sqrt{3}\left(\frac{1-2x}{l}\right) \tag{3-3}$$

the mode shapes for free-free beams at frequencies larger than zero are:

$$\psi_n(x) = (\cosh k_{nb}x + \cos k_{nb}x) - \sigma_n(\sinh k_{nb}x + \sin k_{nb}x) \tag{3-4}$$

with

$$\sigma_n = \frac{\cosh k_{nb}l - \cos k_{nb}l}{\sinh k_{nb}l - \sin k_{nb}l} \tag{3-5}$$

and

$$k_{nb} = \frac{(2n+1)\pi}{2} \tag{3-6}$$

The mobility matrix of a beam with free-free BCs for a force excitation at x_i and transverse velocity response at x_j is given by:

$$M_{ij} = j\omega \sum_{n=1}^{\infty} \frac{\psi_n(x_i)\psi_n(x_j)}{\rho Sl(\omega_n^2(1+j\eta)-\omega^2)} \tag{3-7}$$

3.1.1.2. Second moment of inertia for frame and stringer

The mobility expression in 3.1.1.1 can be used to obtain the mobility matrix with given mode shapes and natural frequencies. Both the frame and stringer are built with the same material so the difference really are the cross sectional areas and the resultant moments of inertia. Figure 3-2 shows a schematic version of the box-cross section of the beam used as a stringer in the experimental setup.

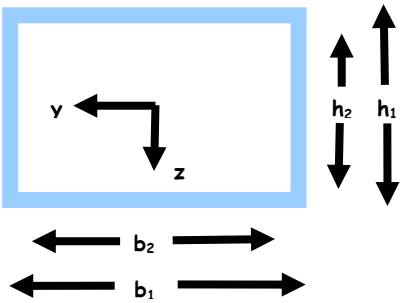

Figure 3-2: Box- cross section of the beam used for the stringer

The second moment of inertia with bending moment around the y- axis is:

$$I_Y = \frac{b_1 h_1^3 - b_2 h_2^3}{12}, \tag{3-8}$$

where the second moment of inertia for the square with the dimensions h_1 and b_1 are subtracted from second moment of inertia for the square with the dimensions h_2 and b_2. The surface area of the box- section is:

$$S = b_1 h_1 - b_2 h_2 \tag{3-9}$$

Figure 3-3 shows a schematic of the I-cross section of the beam used as a frame in the experimental setup.

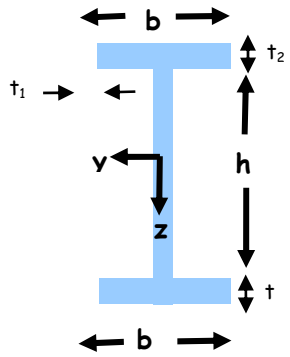

Figure 3-3: I-cross section of the beam used for the frame in experimental setup

The derivation for the second moment of inertia is mathematically more involved as the I-section used for the MPS experimental rig has two different thicknesses t_1 and t_2. The second moment of inertia is:

$$I_y = \frac{t_1 h^3}{12} + 2\left(\frac{b t_2^3}{12} + \left(\frac{h}{2} + \frac{t_2}{2}\right)^2 b t_2\right) \tag{3-10}$$

With the surface area:

$$S = t_1 h + t_2 b \tag{3-11}$$

3.1.1.3. Mobility matrix equations for beam coupled to a plate

In the last chapter the equations for coupling a lumped mass on top of a plate were given. An equivalent mobility matrix was derived that allowed the mass on top of the plate and the plate itself to be treated as one single object with one mobility matrix. Equations for the lumped mass on the plate were used to model the accelerometer used for the experimental validation of the DPS and gave significantly better results especially at low and high frequencies.

The previously discussed equivalent matrix method can also be used to couple larger distributed structures to multiple nodes on the plate. For example, the beams discussed above were added to the plate using this approach and were coupled to lines of nodes on the plates. Figure 3-4 shows the free body diagram of a plate with and without the coupled beam.

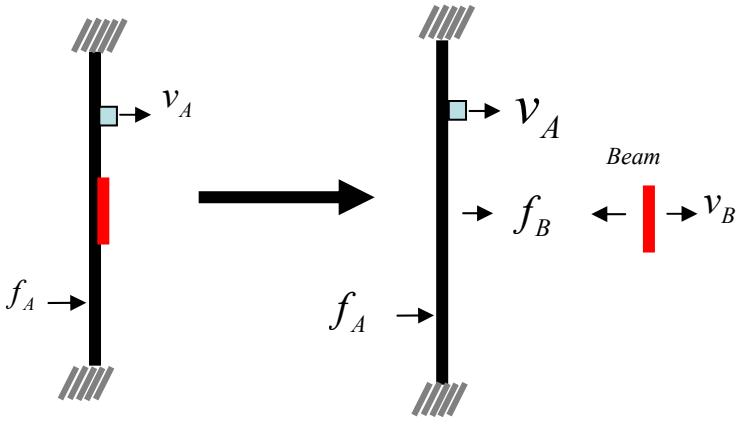

Figure 3-4: Free body diagram of a plate with and without beam acting as an individual object

The equations for the plate modeled with a beam on top of it, i.e with an input force $\mathbf{f_A}$ and output velocity $\mathbf{v_A}$ and a force due to the beam $\mathbf{f_B}$ and velocity of the beam $\mathbf{v_B}$, are presented below. Solving for $\mathbf{v_A}$:

$$\begin{aligned} v_B &= M_0 f_B = M_{BA} f_A - M_{BB} f_B \\ \Rightarrow f_B &= \left[M_0 + M_{BB}\right]^{-1} M_{BA} f_A \end{aligned} \tag{3-12}$$

$$v_A = M_{AA} f_A - M_{AM} f_M = \left[M_{AA} - M_{AM} \left[M_0 + M_{MM}\right]^{-1} M_{MA} \right] f_A \tag{3-13}$$

$\mathbf{M_0}$ is the mobility of the beam m. $\mathbf{M_{AA}}$, $\mathbf{M_{AM}}$, $\mathbf{M_{MA}}$, and $\mathbf{M_{MM}}$ are input and transfer plate mobility matrices with respect to the plate locations (index "A") and beam locations (index "M"). The output velocity $\mathbf{v_A}$ in (3-13), which describes the velocity at all locations on the plate, is expressed as an augmented mobility matrix $\mathbf{M_{equivalent}}$ times the input force where

$$M_{equivalent} = M_{AA} - M_{AB} \left[M_0 + M_{BB}\right]^{-1} M_{BA} \tag{3-14}$$

$\mathbf{M_{equivalent}}$ is used to now describe a fuselage panel with beam on top. In the design tool an equivalent mobility matrix $\mathbf{M_{equivalent}}$ for the stringer on top of the plate was used to describe the mobility of the fuselage-stringer system. The derived matrix $\mathbf{M_{equivalent}}$ can then be used as a "new plate mobility matrix" $\mathbf{M_{AA}}$. Therefore, in the case of having one stringer and one frame, the matrix $\mathbf{M_{equivalent}}$ has to be computed twice iteratively to add the two components to the plate.

3.1.2 Cavity study

The air gap in the DPS was modeled as a single rectangular cavity. Since the objective is to model a MPS with frames and stringers on top of the fuselage, this section considers the question: *does the air gap in between the fuselage and the trim still act as a single rectangular cavity, or as multiple coupled cavities*?

Figure 3-5 shows a schematic of the MPS with two different ways to model the air gap. On the left hand side of Figure 3-5**,** the air gap is modeled as two small thin cavities coupled to a bigger thin cavity, which is more geometrically correct. In this configuration, the frame which is 3'' high acts like a wall in-between two rectangular cavities. On the right hand side of Figure 3-5**,** the air gap is modeled as a big rectangular cavity. On top of these two cavities, a third rectangular cavity, with the width of the two smaller cavities, is positioned right next to the trim.

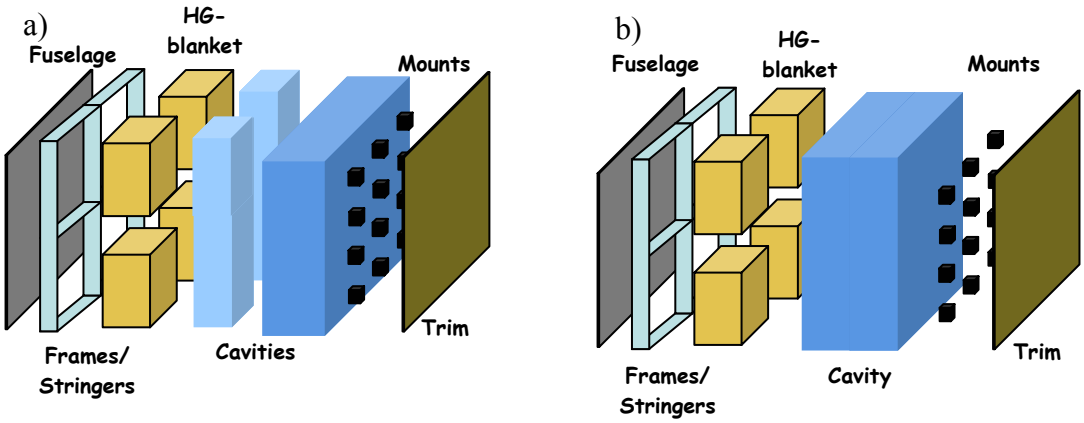

Figure 3-5: (a) MPS with model of two smaller cavities coupled to four HG blankets and additional big cavity block coupled to the trim side; (b) MPS with model of one thick cavity between HG blankets and trim

In order to model both air gaps (shown in Figure 3-5), to investigate if there are major differences, the correctness of the coupling of two rectangular cavities has been verified in 3.1.2.1. In 3.1.2.2 a comparison between the two air gaps is presented.

3.1.2.1. A study on the coupling of two rectangular cavities

In order to model the air gap shown in Figure 3-5 (a), three rectangular cavities have to be coupled together. The question that is answered in this section is: *is the*

continuity of pressure and displacement on the interface nodes of the cavities correctly included when using the IMM?

In order to prove this, a thick rectangular cavity was compared to two thin cavities (when coupled together) having the same dimensions as the thick cavity. Figure 3-6 shows the response of the three cavities (same width and length) with different thicknesses. Note that the three cavities have modes at the same frequencies (in the frequency range of interest), since the lower modes are due to the resonant response of the air along the length and width dimensions of the cavity, and not due to the thickness. The overall response is lower for the thicker cavities, since the larger volume leads to less compression of the air, and therefore to less pressure transmitted across the cavity.

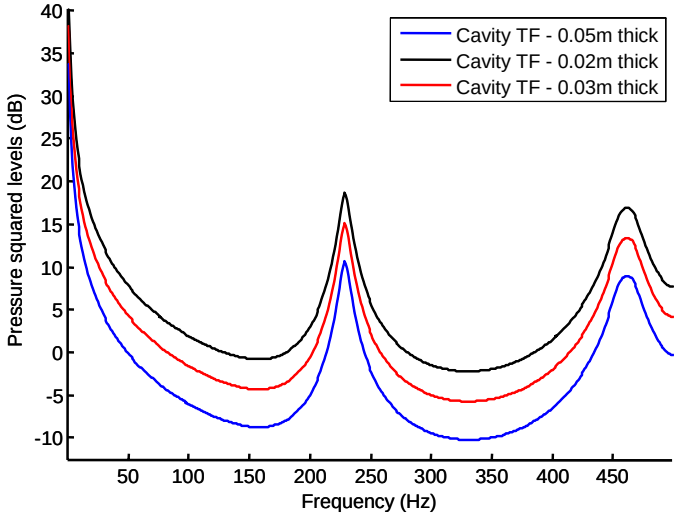

Figure 3-6: Pressure squared levels of three air cavities with same base (length x width) dimensions and different thicknesses

Similar to the principle of an equivalent mobility matrix derived earlier for lumped masses and beams on top of plates, an equivalent impedance matrix will be derived to describe the impedance of two cavities coupled together acting as one big cavity. Figure 3-7 shows the free body diagram of two coupled cavities acting as one big cavity (a) or acting as two cavities with individual impedance matrices (b).

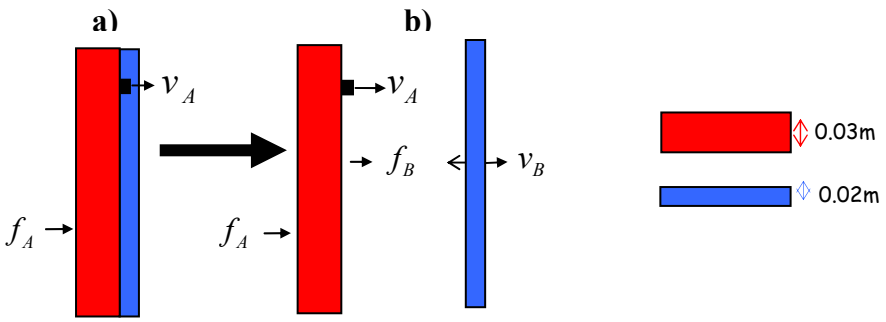

Figure 3-7: Free body diagram of two rectangular cavities coupled together

In order to avoid confusion, the two cavities coupled together will be referred to as the red cavity and the blue cavity as shown in Figure 3-7. The equations for the coupled rectangular cavities with an input force $\mathbf{f_A}$ and output velocity $\mathbf{v_A}$, where the force due to the blue cavity acting on the red cavity is $\mathbf{f_B}$ and the velocity of the blue cavity is $\mathbf{v_B}$. Solving for $\mathbf{f_A}$:

$$\begin{aligned} \mathbf{f_B} &= \mathbf{Z_{bAB}}\mathbf{v_B} = \mathbf{Z_{rBA}}\mathbf{v_A} - \mathbf{Z_{rBB}}\mathbf{v_B} \\ \Rightarrow \mathbf{v_B} &= \left[\mathbf{Z_{bAB}} + \mathbf{Z_{rBB}}\right]^{-1}\mathbf{Z_{rBA}}\mathbf{v_A} \end{aligned} \tag{3-15}$$

$$\mathbf{f_A} = \mathbf{Z_{rAA}}\mathbf{v_A} - \mathbf{Z_{rAB}}\mathbf{v_B} = \left[\mathbf{Z_{rAA}} - \mathbf{Z_{rAB}}\left[\mathbf{Z_{bAB}} + \mathbf{Z_{rBB}}\right]^{-1}\mathbf{Z_{rBA}}\right]\mathbf{v_A} \tag{3-16}$$

The impedance matrices consist of point impedances which are computed for the nodes at the locations (grid points) at which the two cavities interact. $\mathbf{Z_{bAB}}$ is the transfer impedance of the blue cavity. $\mathbf{Z_{rBA}}$ is the impedance of the red cavity from all locations in the red cavity to the location of the blue cavity, $\mathbf{Z_{rAM}}$ is the impedance from the blue cavity location to all locations on the red cavity, $\mathbf{Z_{rAA}}$ is the impedance matrix that describes all impedances from all locations on the red cavity to all locations on the red cavity and $\mathbf{Z_{rMM}}$ is the red cavity impedance from the blue cavity location to the blue cavity location. The output velocity $\mathbf{v_A}$ in (3-17), which describes the velocity at all locations at the red cavity, is expressed as an augmented impedance matrix $\mathbf{Z_{equivalent}}$ times the input force where:

$$\mathbf{Z_{equivalent}} = \mathbf{Z_{AA}} - \mathbf{Z_{AB}}\left[\mathbf{Z_0} + \mathbf{Z_{BB}}\right]^{-1}\mathbf{Z_{BA}} \tag{3-17}$$

$\mathbf{Z}_{\mathbf{equivalent}}$ can be seen as an equivalent impedance of two coupled cavities. Note that in the example used in this chapter, the nodes at the locations at which the red and the blue cavities interact are identical.

Figure 3-8 shows the result of comparing a thick rectangular cavity to two thinner cavities coupled together. The two cavities were coupled, reversed and coupled again. The two cavities coupled together have an identical response compared to the thick cavity, which is independent in the way the two smaller cavities are coupled. This result proves that two objects described with impedance matrices can be coupled correctly using the IMM.

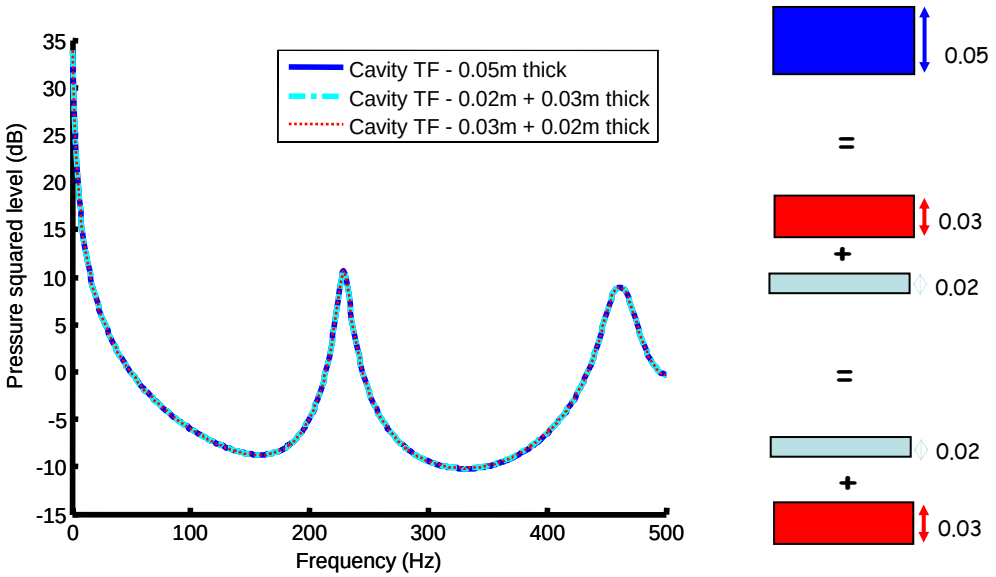

Figure 3-8: Pressure squared levels of 0.05m thick cavity vs. two coupled cavities (0.02m + 0.03m thick)

3.1.2.2. A comparison of two cavities inside the MPS

In this section a comparison between a thick cavity and the three thin cavities shown in Figure 3-5 is presented. Figure 3-9 (a) shows the pressure squared levels of the two small cavities (black and red, schematic in Figure 3-9 (b)) individually and acting as a larger cavity next to each other shown in blue. Finally, the pressure squared levels of a single thin cavity with larger dimensions in width and length is shown in blue, which has an additional mode at 220Hz due to its larger transverse dimension.

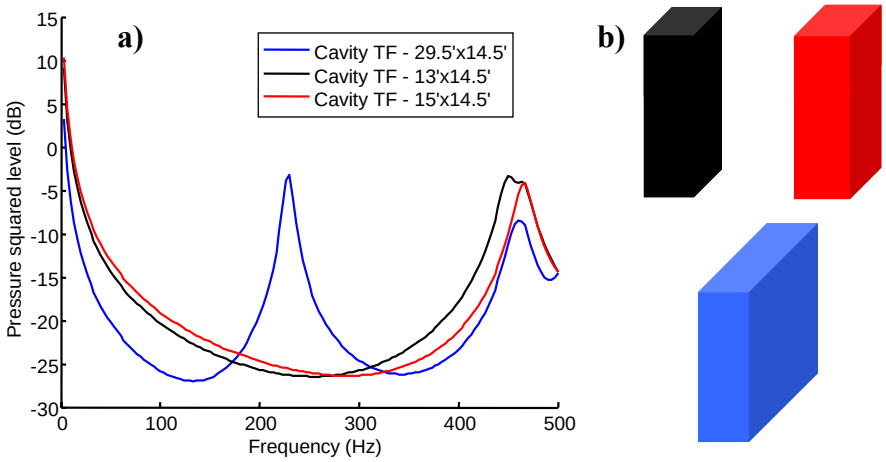

Figure 3-9: Pressure squared levels of rectangular cavities with various dimensions

Figure 3-10 (a) presents a comparison of the pressure squared levels of the three cavities coupled together (schematic in Figure 3-10 (b)) to one larger cavity. Both transfer functions have similar characteristics and modes that lie very close to each other in terms of frequencies and magnitudes. For the experimental validation of the MPS, the larger cavity in blue will be used due to shorter computational time.

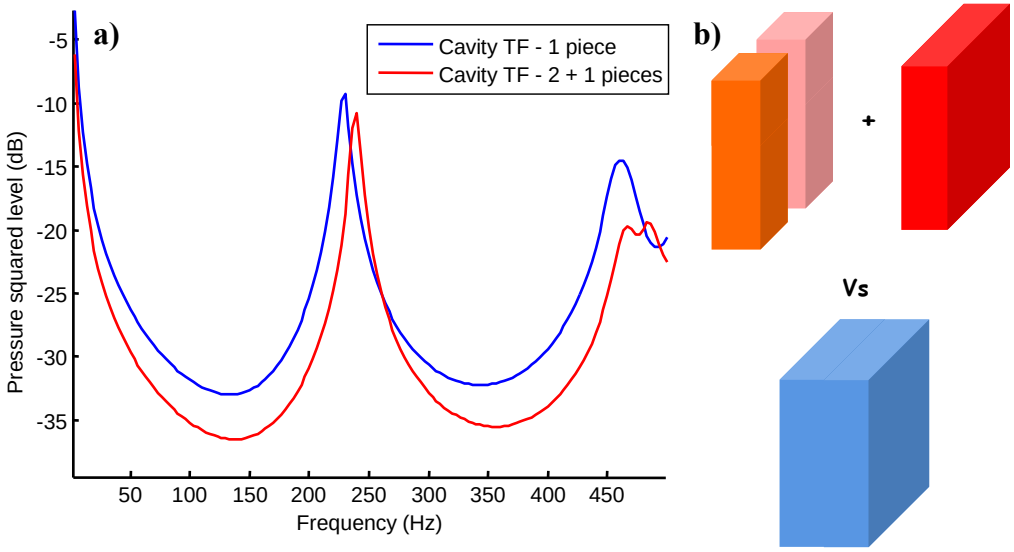

Figure 3-10: Two cavities without space in between coupled to a rectangular cavity with same thickness vs. one rectangular cavity with same dimensions

3.1.3 Modeling mounts inside MPS

As an approximation, the mounts were modeled as a mass-spring/damper-mass system shown in Figure 3-11. The masses m_1 and m_2 are connected with a spring and a damper.

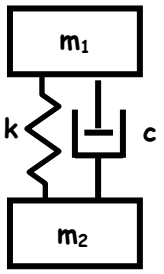

Figure 3-11: Figure of a mount modeled in the design tool as a mass-spring/damper-mass system.

The impedance, $\mathbf{Z}_{m1}$, of the first mass is by definition proportional to the frequency:

$$\mathbf{Z}_{\mathbf{m_1}} = j\omega m_1 \tag{3-18}$$

The impedance of the spring is inversely proportional to the frequency. And the spring constant is *k*. The impedance is:

$$\mathbf{Z}_{\mathbf{k}} = \frac{k}{j\omega} \tag{3-19}$$

The impedance for the damper is:

$$\mathbf{Z}_{\mathbf{c}} = c \tag{3-20}$$

Analogous to the first mass, the impedance of the second mass is:

$$\mathbf{Z}_{\mathbf{m_2}} = j\omega m_2 \tag{3-21}$$

Using Firestone's [74] derivation for impedances in series, the total impedance matrix for the mounts is:

$$\mathbf{Z}_{\mathbf{T}} = \frac{\mathbf{1}}{\frac{\mathbf{1}}{\mathbf{Z}_{\mathbf{m_1}}} + \frac{\mathbf{1}}{\mathbf{Z}_{\mathbf{k}} + \mathbf{Z}_{\mathbf{c}}} + \frac{\mathbf{1}}{\mathbf{Z}_{\mathbf{m_2}}}} \tag{3-22}$$

In order to obtain the material properties of the mounts used in the later experimental validation, the mount was analyzed in a shaker experiment. The mount

was therefore glued to a shaker. A 12 g steel block and a 1 g accelerometer were then placed on top of the mount. Figure 3-12 shows a picture of this experiment (a) and the transfer function of the measurement (b).

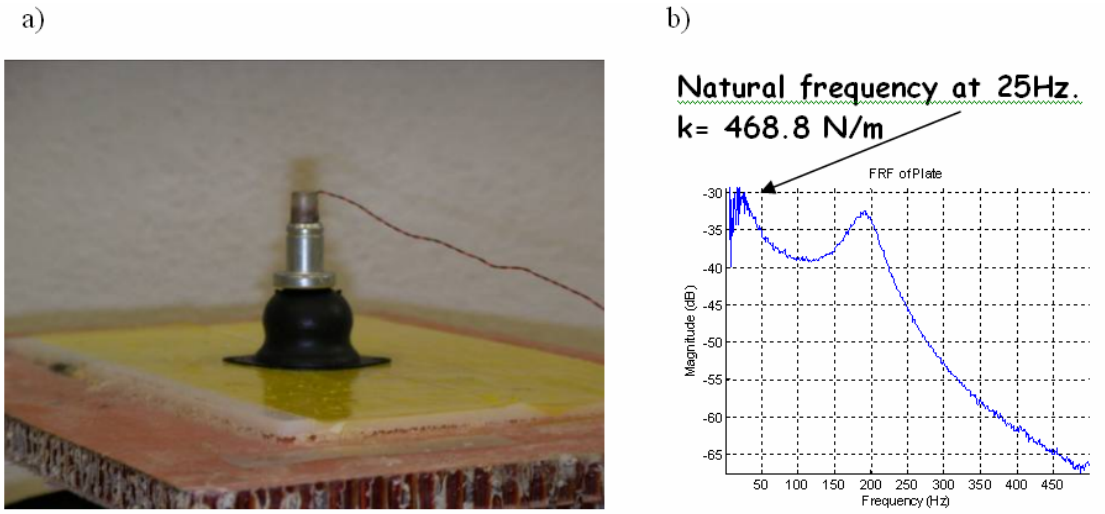

Figure 3-12: a) Picture of experimental setup to find the mount properties. Mount is set on top of a shaker and a mass connected to an accelerometer was positioned on top of a shaker, b) response of the mount used in the shaker experiment

The first natural frequency was measured at 25Hz which results in a stiffness coefficient of k=468.8N/m. The second natural frequency is a rocking mode. Note that in the model the mount is assumed linear which is not the case if the neoprene-bubble-mount is deformed excessively.

3.1.4 Coupling equations for mounts inside MPS

Modeling the MPS with HG blankets and mounts is different to modeling the other configurations since the mounts do not touch the HG blanket and are mounted directly to the fuselage and the trim panel i.e. they bypass the HG blanket and acoustic cavity. This section first presents the modeling of the MPS without the HG blankets as an intermediate step. After the impedance of the mounts was derived and the spring constant was obtained in the prior section, the mounts were incorporated into the MPS. The most convenient way seems to be the addition of nodes into the system, which connect the two plates directly with each other without a cavity in between. Figure 3-13 shows the system to be modeled. The fuselage is already modeled as a plate with frame

and stringer on top and the only components between the trim and the fuselage are the cavity and the mounts.

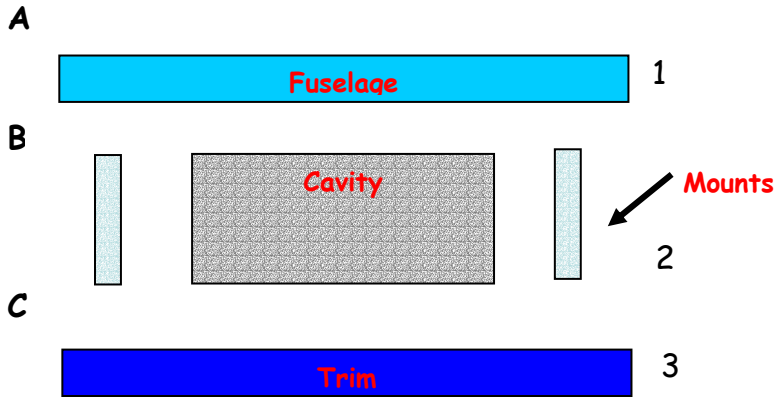

Figure 3-13: MPS connected with mounts and cavity in between

Figure 3-14 shows the top view of the system between the interfaces B and C in Figure 3-13. The blue nodes marked with a 'x' are the 225 cavity nodes. The idea is to add extra nodes, the mount nodes, noted as red stars in Figure 3-14 that describe the physics between the two plates connected by this set of mounts.

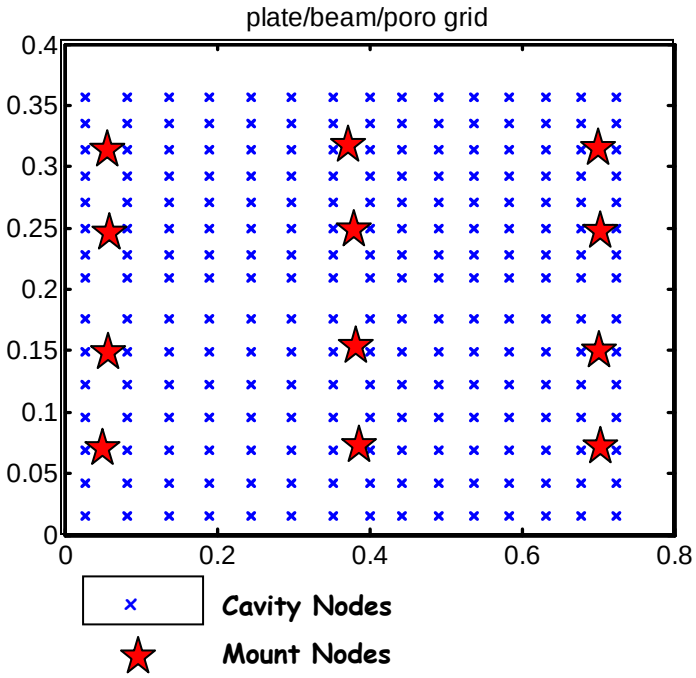

Figure 3-14: Nodes for the MPS looking through the MPS. The cavity nodes are in the grey area and the mount nodes are presented as red stars.

The key to this derivation of the equations for the coupled MPS with mounts inside is to understand that the basic equations presented in section 2.1.8 for the DPS do not change. Instead, the assembled matrix in 2.1.9 gets extended where the number of added columns and rows is equal to the number of mounts added to the system. The explicit set of equations, not including the HG blanket, are:

$$\mathbf{v_B} = \mathbf{M_{1AB}}\mathbf{f_A} - \mathbf{M_{1BB}}\mathbf{f_B} \tag{3-23}$$

$$\mathbf{f_{B_{Cav}}} = \mathbf{Z_{2BB_{Cav}}}\mathbf{v_{B_{Cav}}} - \mathbf{Z_{2BC_{Cav}}}\mathbf{v_{C_{Cav}}} \tag{3-24}$$

$$\mathbf{f_{C_{Cav}}} = \mathbf{Z_{2CB_{Cav}}}\mathbf{v_{B_{Cav}}} - \mathbf{Z_{2CC_{Cav}}}\mathbf{v_{C_{Cav}}} \tag{3-25}$$

$$\mathbf{v_c} = \mathbf{M_{3CC}}\mathbf{f_c} \tag{3-26}$$

$\mathbf{M_{1AB}}$ and $\mathbf{M_{1BB}}$ are the mobility matrices of the fuselage [55]. $\mathbf{Z_{2CCcav}}$, $\mathbf{Z_{2CDcav}}$ $\mathbf{Z_{2DCcav}}$ and $\mathbf{Z_{2DDcav}}$ [58] are the input and transfer impedance matrices of the cavity. The mobility matrix of the trim $\mathbf{M_{3CC}}$ is analogous to the mobility matrix of the fuselage just with different BCs. In addition to the presented set of equations, an additional set of equations was derived to describe the interaction between the plates and the mounts in the MPS:

$$\mathbf{f_{B_M}} = \mathbf{Z_{2BB_M}}\mathbf{v_{B_M}} - \mathbf{Z_{2BC_M}}\mathbf{v_{C_M}} \tag{3-27}$$

$$\mathbf{f_{C_M}} = \mathbf{Z_{2CB_M}}\mathbf{v_{B_M}} - \mathbf{Z_{2CC_M}}\mathbf{v_{C_M}} \tag{3-28}$$

The input and transfer impedance matrices of the mounts are $\mathbf{Z_{2CC_M}}$, $\mathbf{Z_{2CD_M}}$ $\mathbf{Z_{2DC_M}}$ and $\mathbf{Z_{2DD_M}}$. The velocity and force vectors $\mathbf{v_B}$, $\mathbf{v_C}$, $\mathbf{f_B}$ and $\mathbf{f_C}$ include both, the cavity and mount nodes:

$$v_B = \begin{Bmatrix} v_{B_{Cav}} \\ v_{B_M} \end{Bmatrix}, v_C = \begin{Bmatrix} v_{C_{Cav}} \\ v_{C_M} \end{Bmatrix}, f_B = \begin{Bmatrix} f_{B_{Cav}} \\ f_{B_M} \end{Bmatrix}, f_C = \begin{Bmatrix} f_{C_{Cav}} \\ f_{C_M} \end{Bmatrix} \tag{3-29}$$

The assembled matrix comes out to be the following:

(3-30)

$$\underbrace{\begin{bmatrix} \mathbf{M_{1BB}} & \mathbf{I} & \mathbf{0} & \mathbf{0} \\ \mathbf{I} & \begin{bmatrix} -\mathbf{Z_{2BB_{Cav}}} & \mathbf{0} \\ \mathbf{0} & -\mathbf{Z_{2BB_M}} \end{bmatrix} & \begin{bmatrix} \mathbf{Z_{2BC_{Cav}}} & \mathbf{0} \\ \mathbf{0} & \mathbf{Z_{2BC_M}} \end{bmatrix} & \mathbf{0} \\ \mathbf{0} & \begin{bmatrix} -\mathbf{Z_{2CB_{Cav}}} & \mathbf{0} \\ \mathbf{0} & -\mathbf{Z_{2CB_M}} \end{bmatrix} & \begin{bmatrix} \mathbf{Z_{2CC_{Cav}}} & \mathbf{0} \\ \mathbf{0} & \mathbf{Z_{2CC_M}} \end{bmatrix} & \mathbf{I} \\ \mathbf{0} & \mathbf{0} & \mathbf{I} & -\mathbf{M_{3CC}} \end{bmatrix}}_{\mathbf{A}} \underbrace{\begin{bmatrix} \mathbf{f_B} \\ \mathbf{v_B} \\ \mathbf{f_C} \\ \mathbf{v_C} \end{bmatrix}}_{\mathbf{X}}$$

In order to check the correctness of the code for the MPS with the mounts included, the operating deflection shape of the system was observed at chosen frequencies. Figure 3-15 presents a plot of the predicted velocity from 10-105Hz of a coupled MPS with mounts (without HG blanket) computed at fuselage and trim panel (a). It also presents the 3-D model of the computed configuration (b) and the operating deflection shape of the trim (free-free BC, (1)), trim mounts (2), fuselage mounts (3) and fuselage plate (clamped BC, 4) at 62Hz (2^{nd} mode, (c)). It was found to be more useful to present the operating deflection shape of the mount nodes independent from the panel nodes to ensure a realistic movement of the mounts. The fuselage moves in a 2-1 mode, where the plate is divided into four skin pockets due to its frame and stringer. As expected the trim panel which seems to have small amplitude at the mount points and deformed at all the non-mount points implying that the main mechanism of excitation at this resonance is through the acoustic cavity.

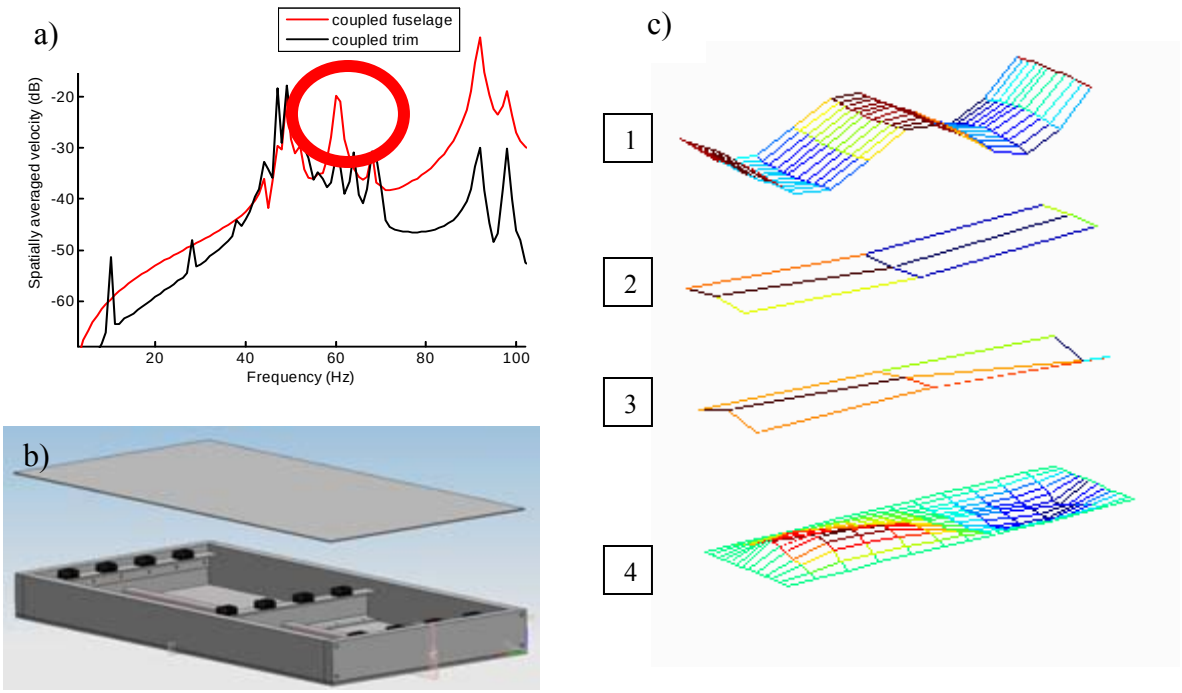

Figure 3-15: a) Plot of predicted spatially averaged velocity from 10-105Hz of a coupled multi bay double panel system with mounts and without HG blanket computed at source (fuselage) and receiver (trim) side, b) 3-D model of the computed configuration and c) Operating deflection shape of the trim panel (free- free BC, 1), trim mounts (2), fuselage mounts (3) and fuselage panel (clamped BC, 4) at 62Hz (2nd mode)

In conclusion, the assembled matrix for the MPS including mounts was derived and the predicted response was analyzed to assure the correctness of the design tool. The next step is the incorporation of the HG blanket into the design tool.

3.1.5 Fully coupled MPS with HG blankets

This section presents the coupling equations for the final MPS design tool with both mounts and HG blanket. The operating deflection shape of the complete MPS system will be presented at a chosen frequency.

Figure 3-16 presents a schematic of the theoretical model for the MPS design tool. The interfaces are denoted A, B, C and D. The frame and stringer are modeled as beams attached to certain nodes of the fuselage. These nodes are denoted with "I". The frame and stringer are directly coupled to the cavity; hence the frame and stringer are in between the interface B and C. The HG blanket is coupled to the fuselage and the

cavity. The HG blankets nodes are denoted as “II”. The cavity which is coupled to the frame and stringer and the HG blanket includes both nodes “I” and “II”. The mounts are coupled to the fuselage and the trim panel. The nodes for the mounts are denoted with “III”.

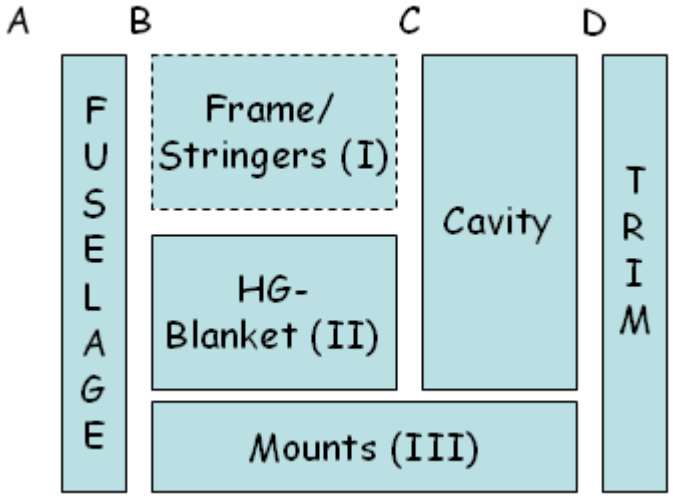

Figure 3-16: Schematic of the theoretical MPS model

The key to the MPS derivation is to understand that the system has to be broken down into the three node groups. Each of these node groups couples different parts of the MPS. Once the problem is setup as shown in Figure 3-16, the derivation of the IMM coupling equations becomes fairly straight forward. The fuselage is coupled to all three node groups as shown in (3-31):

$$\begin{Bmatrix} \mathbf{v}_{B,I} \\ \mathbf{v}_{B,II} \\ \mathbf{v}_{B,III} \end{Bmatrix} = \mathbf{M}_{AB_F} \begin{Bmatrix} \mathbf{f}_{A,I} \\ \mathbf{f}_{A,II} \\ \mathbf{f}_{A,III} \end{Bmatrix} - \mathbf{M}_{BB_F} \begin{Bmatrix} \mathbf{f}_{B,I} \\ \mathbf{f}_{B,II} \\ \mathbf{f}_{B,III} \end{Bmatrix} \tag{3-31}$$

The sub index “F” represents the fuselage. The fuselage is then coupled to the HG blankets (“HG”) and the mounts (“M”). The HG blankets are coupled to the cavity in (3-32) and (3-34), the mounts are directly coupled to the trim panel in (3-33):

$$\mathbf{f}_{B,II} = \mathbf{Z}_{2BB}\mathbf{v}_{B,II} + \mathbf{Z}_{2BC}\mathbf{v}_{C,II} \tag{3-32}$$

$$\mathbf{f}_{B,III} = \mathbf{Z}_{BB_M}\mathbf{v}_{B,III} - \mathbf{Z}_{BD_M}\mathbf{v}_{D,III} \tag{3-33}$$

$$\mathbf{f}_{C,II} = \mathbf{Z}_{2CB}\mathbf{v}_{B,II} + \mathbf{Z}_{2CC}\mathbf{v}_{C,II} \tag{3-34}$$

The cavity ("Cav") couples the frame, stringer and the HG blankets to the trim panel (3-35) and (3-36) which is attached to the mounts as shown in (3-37):

$$\begin{Bmatrix} \mathbf{f}_{B,I} \\ \mathbf{f}_{C,II} \end{Bmatrix} = \mathbf{Z}_{CC_{Cav}} \begin{Bmatrix} \mathbf{v}_{B,I} \\ \mathbf{v}_{C,II} \end{Bmatrix} - \mathbf{Z}_{CD_{Cav}} \begin{Bmatrix} \mathbf{v}_{D,I} \\ \mathbf{v}_{D,II} \end{Bmatrix} \tag{3-35}$$

$$\begin{Bmatrix} \mathbf{f}_{D,I} \\ \mathbf{f}_{D,II} \end{Bmatrix} = \mathbf{Z}_{DC_{Cav}} \begin{Bmatrix} \mathbf{v}_{B,I} \\ \mathbf{v}_{C,II} \end{Bmatrix} - \mathbf{Z}_{DD_{Cav}} \begin{Bmatrix} \mathbf{v}_{D,I} \\ \mathbf{v}_{D,II} \end{Bmatrix} \tag{3-36}$$

$$\mathbf{f}_{D,III} = \mathbf{Z}_{DB_M} \mathbf{v}_{B,III} - \mathbf{Z}_{DD_M} \mathbf{v}_{D,III} \tag{3-37}$$

Finally, the mobility matrix representing the free-free trim panel couples the velocities and forces of all node groups as shown in (3-38):

$$\begin{Bmatrix} \mathbf{v}_{D,I} \\ \mathbf{v}_{D,II} \\ \mathbf{v}_{D,III} \end{Bmatrix} = \mathbf{M}_{DD_T} \begin{Bmatrix} \mathbf{f}_{D,I} \\ \mathbf{f}_{D,II} \\ \mathbf{f}_{D,III} \end{Bmatrix} \tag{3-38}$$

The reason why this is still a fully coupled system is once again because the fuselage and trim matrices are fully populated. This takes care of describing the different interactions between the mounts, HG blankets and cavity dynamics to the fuselage and trim panel. It was decided for brevity not present the assembled matrix derived from the coupling equations. The matrix consists of 14x14 components which exceeds the size of a page.

One way to analytically verify the MPS design tool is to look at the operating deflection shape of the MPS at various frequencies and look if the predicted behavior is realistic and similar to the deflection shapes presented in the last section. Figure 3-17 presents a 3-D model of multi bay double panel system (a) with sandwiched HG blankets (1 mass, 23g – top center at each of the four sub sections) and the operating deflection shape (b) predicted with the design tool at 104Hz, with the fuselage excited with a point force at an off center position and velocities predicted at 130 points throughout the MPS system. Shown is the trim (i), trim mounts (ii), HG blanket with one mass (iii), fuselage mounts (iv) and fuselage panel (v).

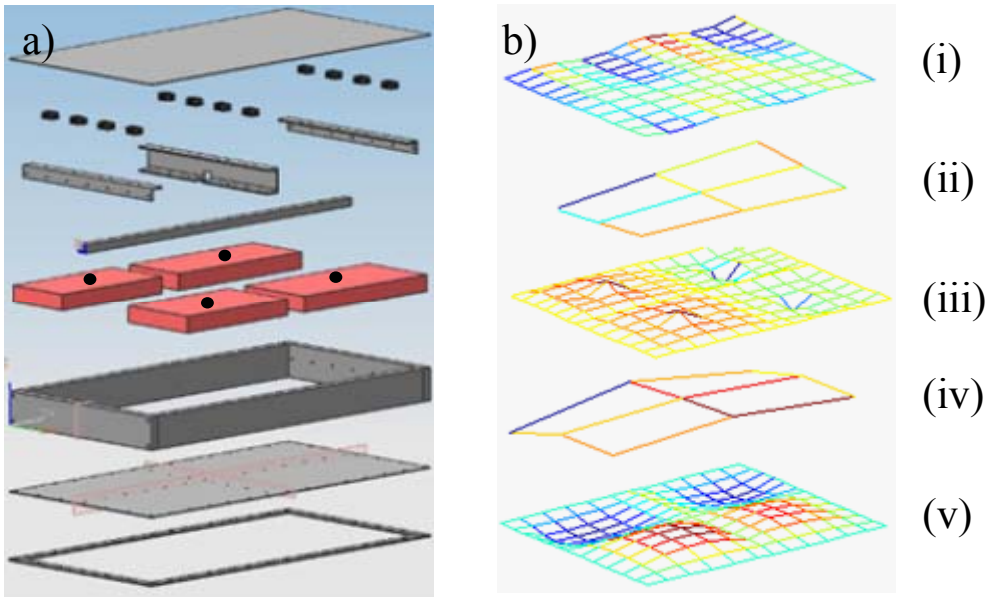

Figure 3-17: a) 3-D model of multi bay double panel system with sandwiched HG blanket (1 mass, 17g – top center at each of the four sub sections) and b) operating deflection shape predicted with design tool at 104Hz with fuselage excited at off center position and velocity predicted at 130 points throughout the MPS system. Shown is the trim (i), trim mounts (ii), HG blanket with one mass (iii), fuselage mounts (iv) and fuselage panel (v)

The frame and stringer on top of the fuselage divide the plate into four skin pockets, with each of the quadrants moving as a single plate by itself. At the chosen frequency two of the four quadrants on each of the two sides divided by the stringer are moving in phase (v). In (iii) the top surface of the HG blankets is animated. The four masses at each of the four quadrants, when excited, are moving up and down while two of each side move in phase and both masses on each side move out of phase. It was found to be more interesting to plot the mount nodes independent from the panel nodes (ii, iv). Once again, similar to the results shown in the previous section, the trim (i) seems to have reduced amplitude at the mount points and deformed at all the non-mount points.

3.2. Comparison between theory and experiments

This section presents a comparison of predicted and measured spatially averaged velocity of both the fuselage and the trim response due to a point force excitation on the fuselage panel.

As shown previously, Figure 3-1 shows a 3-D computer generated model of the MPS experimental rig without the trim panel. The outer dimensions of the solid structure are 42'' x 21.5'' x 4'' with 1'' thick walls. The clamps (1) holding the fuselage (2) to the structure (3) have thin slots inside in order to increase the pressure acting on the fuselage (2). The stringer (7) has a box-cross section with outer dimensions of 1'' x 1'' and the frame (5) has an I-cross section with the dimensions 1.5'' x 3''. The frame (5) and angles (6) are the support for the neoprene mounts (8) with a height of 0.75'' and a maximum diameter of 0.256''. The four areas for the poro-elastic media are: 10'' x 17.5'', 8.5'' x 17.5'', 10'' x 21'' and 8.5'' x 21'' which are reasonably close to the Gulfstream fuselage in the VT facilities presented in chapter 5. A simplified technical drawing of the MPS without the trim panel including the most important dimensions is shown in Figure 3-18.

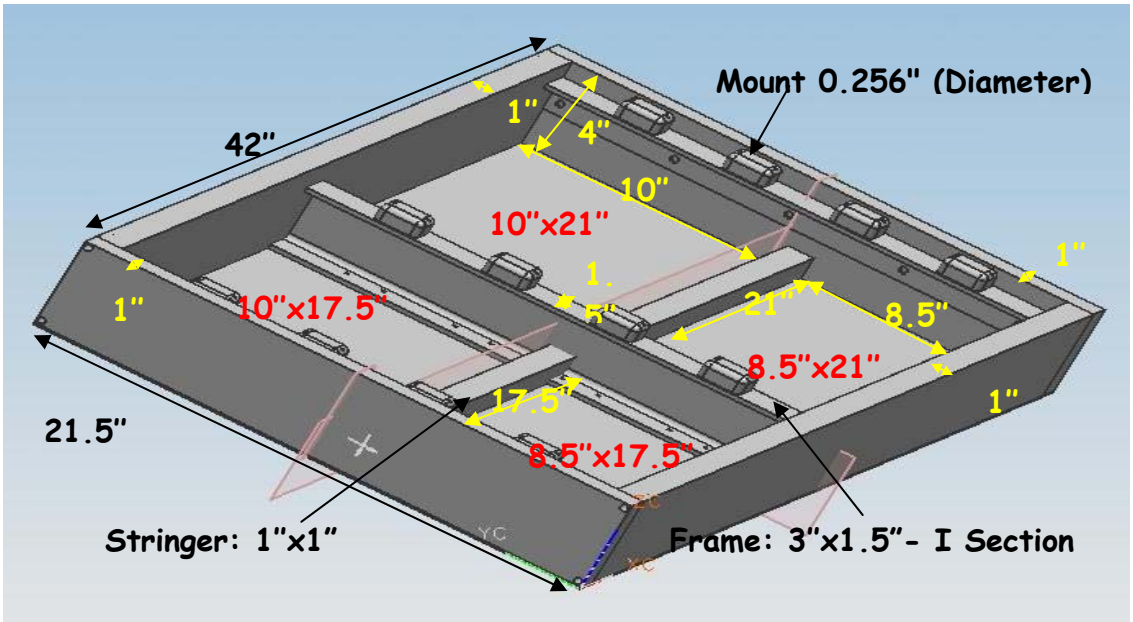

Figure 3-18: 3-D simplified technical drawing of multi bay double panel system

Figure 3-19 presents the picture of the front (a) and the back (b) view of the complete MPS experimental rig. The MPS fuselage which is clamped to a heavy aluminum block is 0.8mm thick. The aluminum trim panel is 1.2mm thick and mounted on top of twelve mounts and sealed with tape on the edges. The accelerometer is placed

off center, close to the upper left edge on the fuselage panel and close to the upper right edge on the trim panel. The MPS was excited at 121 points on the fuselage side.

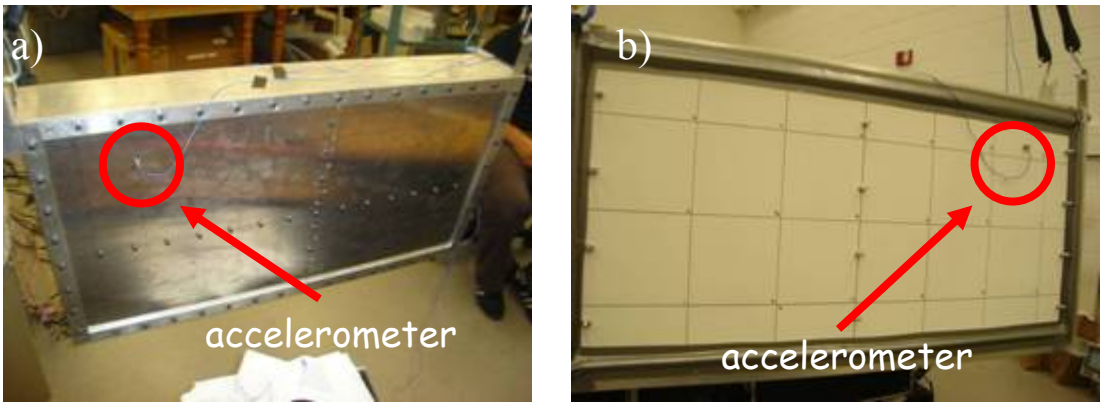

Figure 3-19: MPS experimental setup with front (a) and back (b) view. Accelerometers were placed on source and receiving panel as shown in the pictures

The fuselage has four skin pockets, due to the frame and stringer. The four HG blankets placed on the skin pockets are chosen to not be completely identical in terms of the mass inclusion configuration. The two largest skin pockets have a 17g mass on top of the poro-elastic media. The third and fourth largest skin pockets have an HG blanket with a 14g and 11.3g mass inclusion on top of the poro-elastic block, respectively. All mass inclusions are placed on the center of each poro-elastic block to target the 1-1 mode of each skin pocket. Figure 3-20 shows a 3-D model of the two cases compared in both theory and experiment: MPS and poro-elastic media with and without mass inclusions.

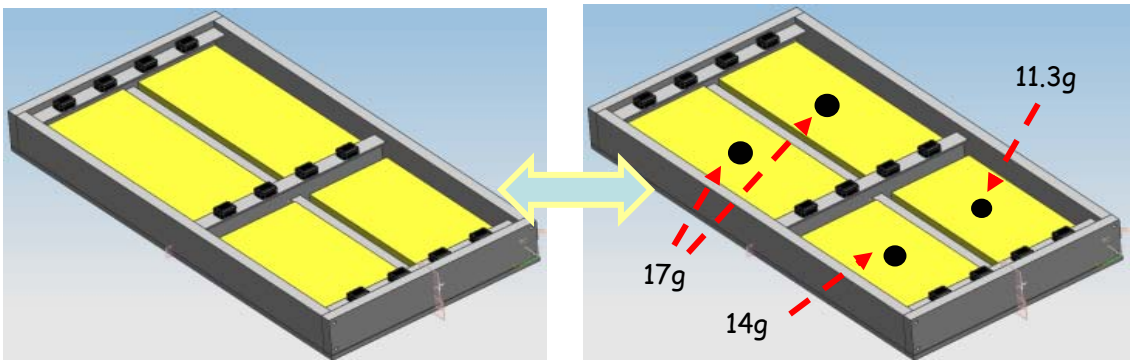

Figure 3-20: 3-D model of two cases compared in experimental validation of MPS

Figure 3-21 presents a schematic of the side view of the MPS with measured fuselage (a) and trim panel (b). Note that in the prediction, a point force was applied at an off center position; however, the velocities were predicted at 121 points. In the measurement, a point force was applied at each of the 121 node points using a modal hammer and the velocities due to each point force are measured and spatially averaged. This is essentially the same due to reciprocity.

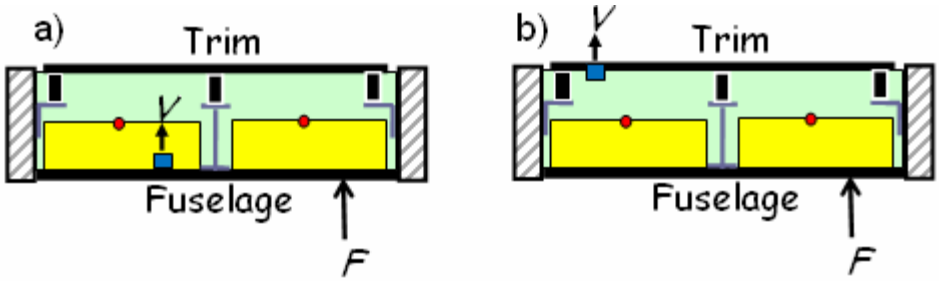

Figure 3-21: Schematic of a) fuselage and b) trim measurement for experimental validation of MPS

The predicted spatially averaged velocity of the fuselage of a MPS with sandwiched poro-elastic material vs. HG blankets targeting the 1-1 mode of each of the four sub panels is shown in Figure 3-23. The HG blankets reduce the fuselage vibration around 100-170Hz and around 250Hz. Note that the HG blankets are not optimized. Once the HG blankets are tuned to the right natural frequency, they have potential to reduce the fuselage response by a significant amount.

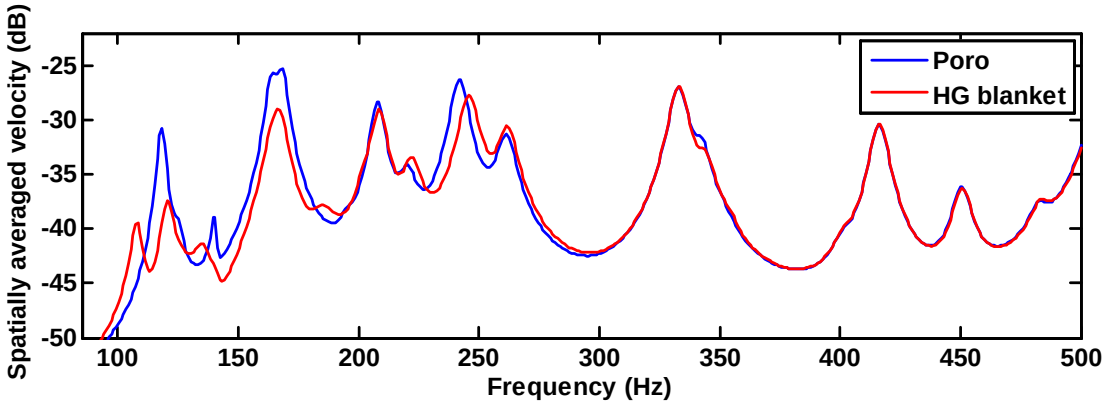

Figure 3-22: Predicted spatially averaged velocity of the fuselage panel of a MPS with sandwiched porous layer (blue) and with sandwiched HG blanket

Figure 3-23 shows the measured spatially averaged velocity of the fuselage panel of a MPS with sandwiched poro-elastic layer (blue) and with sandwiched HG blankets (red) from 70-500Hz. Just like in the prediction in Figure 3-22 the measurement shows a decrease in vibration response around 100-170Hz and around 250Hz. The vibration level of both predictions and measurements are similar, and the dynamics are captured to a reasonable level of detail considering that the MPS design tool describes a fairly complicated system with six structural/acoustic components that are coupled.

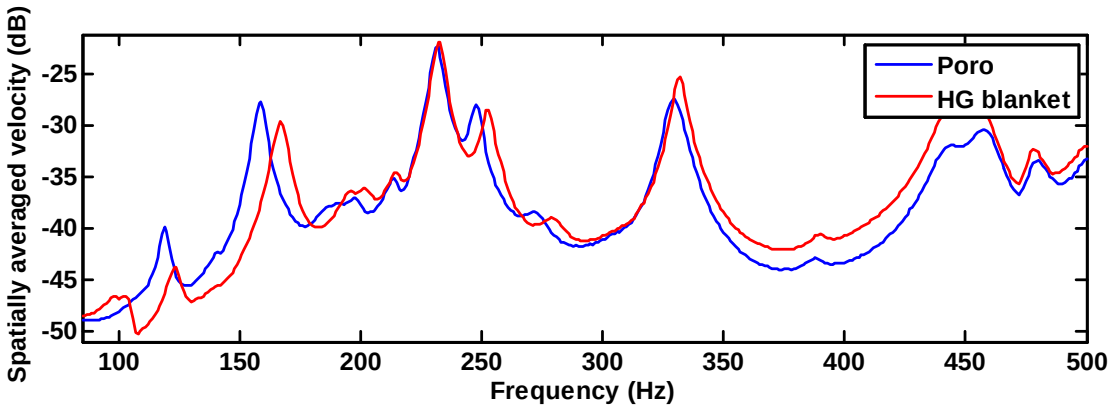

Figure 3-23: Measured spatially averaged velocity of the fuselage panel of a MPS with sandwiched porous layer (blue) and with sandwiched HG blanket

The predicted spatially averaged velocity of the trim panel inside the MPS with sandwiched poro-elastic material vs. HG blankets is presented in Figure 3-24. The HG blankets reduce the vibration response of the trim panel around 100-170Hz and around 235Hz similar to the fuselage panel. After 360Hz, the trim response does not change. This does make sense as the HG blankets are tuned to frequencies below 260Hz.

Figure 3-25 shows the measured spatially averaged velocity of the trim panel of a MPS with sandwiched poro-elastic layer (blue) and with sandwiched HG blankets (red) from 50-400Hz. The vibration level is similar in both prediction and measurement. One can see the effect due to the mass inclusions between 100- 200Hz. However, at higher frequencies, both measured curves are dissimilar, which could be due to repeatability or flanking issues in the experimental setup. The trim panel is mounted on top of 12 mounts and sealed with tape. Each measurement involves taking the trim panel off and then replacing it, in order to add the mass inclusions inside the

porous-media. Furthermore, the model assumes a perfectly sealed cavity which is not guaranteed using tape. However, it was necessary to use tape for the trim panel as the model assumes free-free BC's which is closer to an aircraft model than a clamped plate.

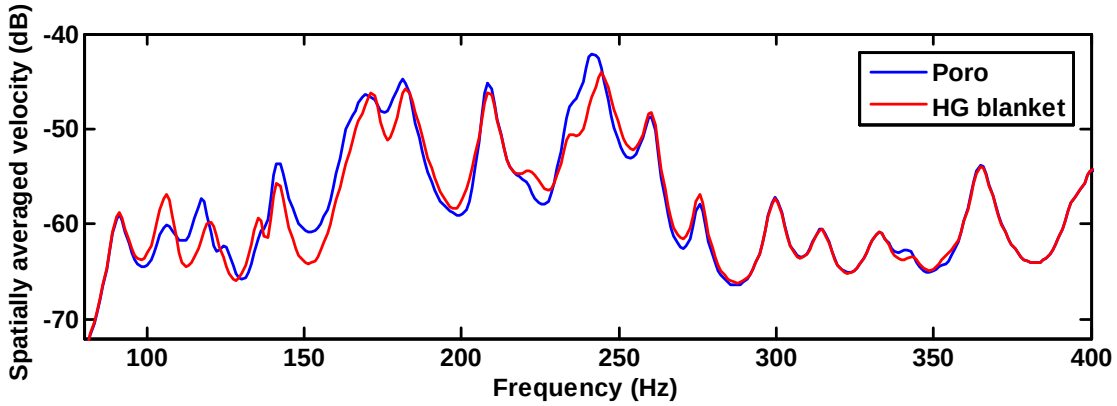

Figure 3-24: Predicted spatially averaged velocity of the trim panel of a MPS with sandwiched porous layer (blue) and with sandwiched HG blanket (red)

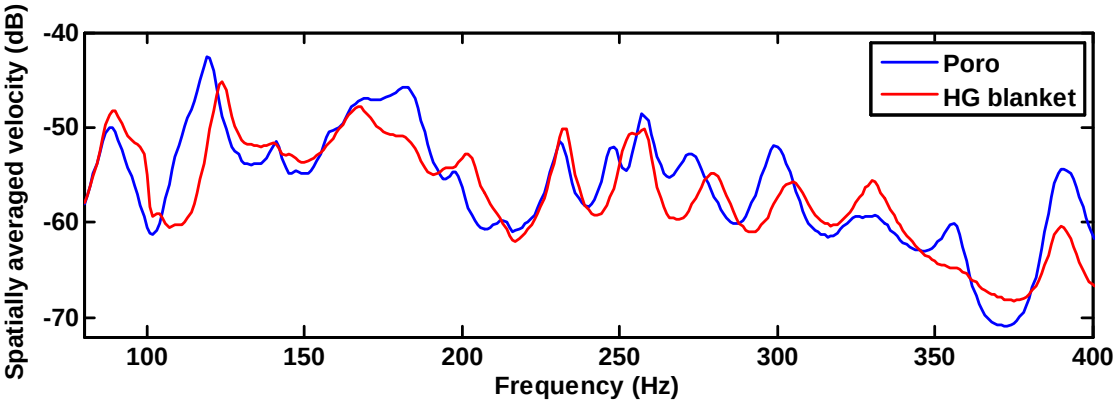

Figure 3-25: Measured spatially averaged velocity of the trim panel of a MPS with sandwiched porous layer (blue) and with sandwiched HG blanket

4. OPTIMIZATION OF HG BLANKET

This chapter specifically presents a discussion of different HG blanket design strategies which will conclude that optimization routines are needed to improve the HG blanket performance. Finally a sensitivity study was conducted to study the manufacturing tolerances of optimal HG blankets.

4.1. HG blanket design strategies

Various design strategies can be pursued to position the masses inside the porous layer. The most straightforward design strategy is to randomly place the mass inclusions [75]. This strategy is very robust to variations in the structure or error in placement as the positions do not depend on the parameters and dimensions of the structure. The downside of this strategy is that it is likely to lead to non-optimal performance of the HG blanket. Another design strategy is the "modal design" of the HG blanket. In this case, the positioning of the mass inclusions is designed to target the modes of the base structure. This design strategy should lead to a better targeted performance than the random placing strategy—depending on the sensitivity of the system. However, the modal design strategy requires information about the structure, and the designing engineer needs to have knowledge of how to "tune" the HG blanket properly. Another design strategy is to use an optimization strategy with a numerical design tool. Genetic algorithms, for example, could be used to search for a good HG blanket design while staying within certain design parameters. However, the optimal result may be sensitive to changes in the structure, construction, and performance may be degraded in practice. Furthermore, the optimization algorithm could require significant computational effort.

In this section, an extensive search of the solution space for a specific case of sound radiated from a DPS with specific design constraints is conducted, and these results are used to investigate the advantages and disadvantages of the three design strategies outlined above. The cost function used to evaluate performance is the sound power radiation from the receiver panel (trim) from 0-500Hz, for a double panel system excited by a broadband point force at a specific location. Both the modal design and the optimal design were tested experimentally in order to validate the model and to verify

the predicted performance. The measured vibration levels on source panel (fuselage) and the trim panel were used to explain the large variation in performance between the two designs. The HG blanket used in this paper has two mass inclusions with weights specified as 6g and 17g. Although the forcing in this case is not the same as the forcing that would be expected in the real application, the objective here is to investigate the design approach itself. Realistic forcing such as turbulent boundary layer noise and shock cell noise is the subject of other current and future work.

4.1.1 Numerical studies on HG blanket

This section presents a comparison of different design strategies used to position the masses inside the poro-elastic media. The three design strategies—random placement, modal design and optimized design—are discussed and the sound radiated from the trim panel of all three cases is compared.

4.1.1.1. Physical system studied

The physical system studied is a double panel system (DPS) with sandwiched air cavity and HG blanket, which consists of a poro-elastic material with embedded masses identical to the validated model in chapter 2. Figure 4-1 presents a schematic of the DPS used in the design tool. The HG blanket is glued to the top of the fuselage panel and an air gap is located between the HG blanket and the trim panel. The schematic shows that the input force is placed at an off center position on the fuselage panel in order to avoid nodal lines and to excite a wide range of modes. The velocity at 25 locations on both the fuselage and trim panels was used to estimate the spatially averaged squared velocity response of the panels (both with clamped BC's). Figure 3 shows the grid distribution used for the computational model of the DPS, which is constant through all components of the DPS numerical model. Twenty-five nodes are shown including the off-center node at x/L_x=0.3 and y/L_y=0.7 where the force was applied to the fuselage panel as shown in Figure 2-2(b). Note that the numerical model uses a finer grid but the number of positions for the mass insertions is limited to 25 nodes in two layers of the porous model (i.e. 50 potential mass locations) in order to obtain a manageable solution space.

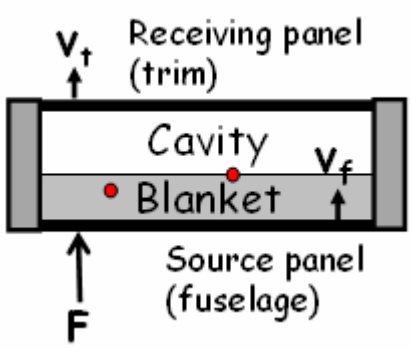

Figure 4-1: Schematic of measured source and trim panel. Mass inclusions inside blanket are represented by red dots. Force applied at an off center position, response measured with accelerometer.

4.1.1.2. Modal design

This section discusses the design process for the HG blanket using modal design. The results are later compared to the other design strategies.

The HG blanket in the DPS is attached directly to the fuselage panel and hence the control of the trim panel is due mainly to vibration control on the fuselage panel. In order to properly tune the masses inside the HG blanket to target the resonant peaks of the fuselage panel, information about the panel's resonant frequencies and mode shapes is required. This is because the mass inclusions are theoretically most efficient when positioned near to the anti-node of a targeted mode (where they vibrate "against" the structural deformation of the fuselage panel) and tuned to the resonant frequency of this mode.

Figure 4-2 shows the response of a double panel system which consists of four components: the fuselage and trim panel, the rectangular cavity and the acoustic far field. Plotted are the predicted fuselage and trim panel velocity with an applied unit point force acting at x/L_x=0.3 and y/L_y=0.7 on the fuselage panel as shown in Figure 2-2(b). Two circles are drawn showing the first and second mode of the fuselage panel. For the modal design strategy it was decided that these first two modes would be targeted using the two mass inclusions.

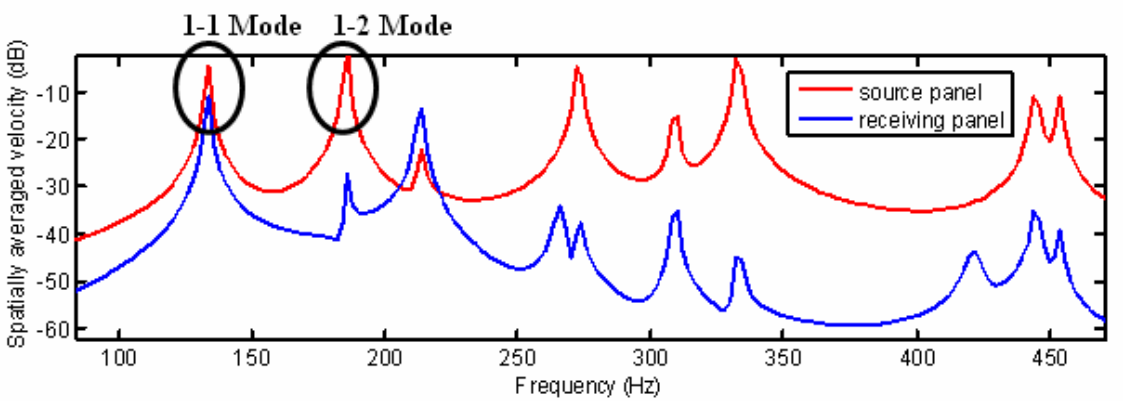

Figure 4-2: Predicted response of a DPS. Plotted is the spatially averaged velocity of the source and receiving panel from 50-500Hz

To target the first two modes, the mode shapes are needed and a review of the plate mode shapes can be found in Refs. [58] and [73]. Figure 4-3 shows the operating deflection shape of the fuselage panel at the first two resonant frequencies. The 1-1 mode is resonating at the fundamental frequency 133Hz. At 181Hz the plate moves at the 2-1 mode.

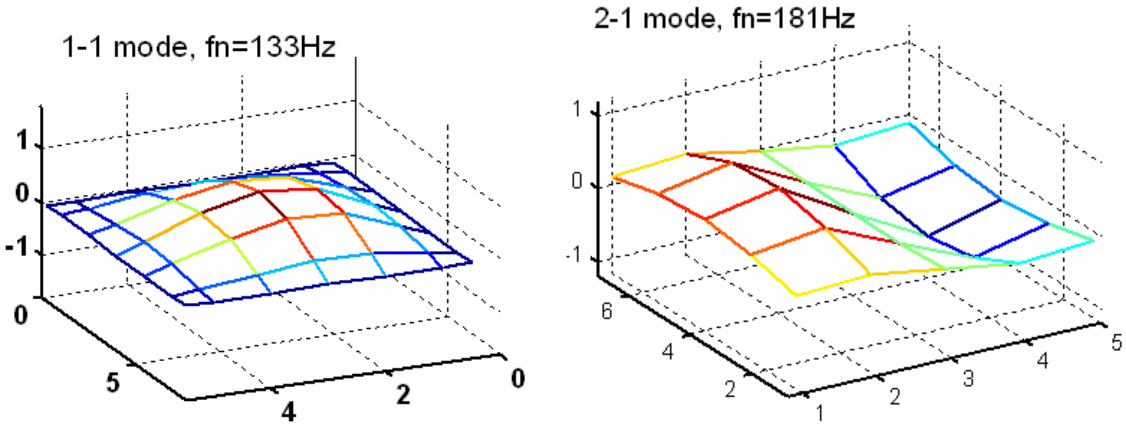

Figure 4-3: Operating deflection shape of the source panel at its first two resonant frequencies.

Figure 4-4(a) Figure 6(a) shows the position of the two mass inclusions inside the HG blanket using the above analysis. The HG-blanket has one mass (17g) inserted inside the poro-elastic media, placed in the center of the plate, near the surface of the poro-elastic media to target the 1-1 mode. The mass weight is approximately 74% of the total added mass (23g), which is because the fundamental frequency is very low and the resonant frequency decreases with increasing the weight of the mass inclusion.

The resonant frequency of the mass inclusion increases with decreasing the depth as shown in Ref. [32], and the anti-node of the 1-1 mode is in the center of the plate. To target the 2-1 mode, a 6g mass was positioned at an off center position at *x/Lx*=0.3 and *y/Ly*=0.7 following a similar physical principle as discussed above. The second resonant frequency of the fuselage panel is higher than the fundamental frequency. Hence, the resonant frequency of the mass inclusion is tuned to a higher frequency by decreasing its weight and depth inside the porous layer. Consideration was also given to the interaction of the second mass inclusion with the 1-2 and 2-2 modes. Therefore, the inclusion was not placed exactly on the anti-node of the 2-1, but slightly off so that the mass also interacted with the 1-2 and 2-2 modes. For comparison, the best solution found in the extensive search described below is shown in Figure 4-4(b).

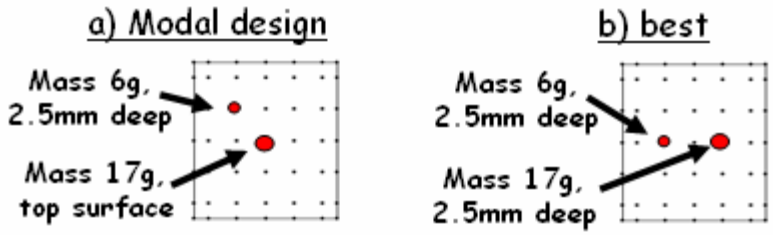

Figure 4-4: Mass positions of the HG blanket using a) the modal design strategy and b) the best result in terms of attenuation of radiated sound power using the exhaustive design search

The modal design used here is intended to be simple and does not use any optimization routines. It is based simply on targeting the modes as if the addition of the first mass, targeting the first mode, does not change the behavior of the second mode. It also assumes that all the modes are likely to transmit sound through the system where this is usually not the case. The modal design approach is in practice very difficult to do for any but the simplest structures.

4.1.1.3. Random and extensive design search

This section discusses the results of an extensive search of the mass positions inside the porous media. The design tool used for this search uses a 5x5x3 grid of locations for the mass inclusions. Figure 2-2(b) shows the grid distribution of the DPS looking through the system. The first layer is at the top surface of the HG blanket, the

second layer is at the center, and the third layer is at the bottom near the interface between the fuselage panel and the HG blanket. For the extensive search presented in this chapter, masses were positioned at all 25 nodes of the first two layers. Hence, a total of 50x50 possible mass positions are run with the two mass inclusions (6g and 17g). The material properties, as well as the number of mass inclusions and mass weights, are kept constant. It should be noted that the results presented below are only valid for a DPS with a point force acting at the fuselage panel (position shown in Figure 2-2 (b)).

The above described scope for the extensive search gives 2500 mass locations in the HG blankets. The DPS design tool including the HG blanket was run 2500 times and the spatially averaged velocities, as well as sound power radiation from the trim panel, were predicted and compared to the response of the DPS with sandwiched porous media, i.e. an HG blanket without mass inclusions. Figure 4-5 shows a histogram of the 2500 mass positions vs. attenuation of the sound power radiated from the trim panel (0-500Hz) where the attenuation is relative to the baseline of a blanket treatment without masses. This histogram is effectively a description of the performance due to random placement, and represents the statistics of a random design. The histogram shows that most HG blanket configurations result in an attenuation (0-500Hz) of 1-3.75dB. Only 3% of the configurations give an attenuation of more than 8dB.

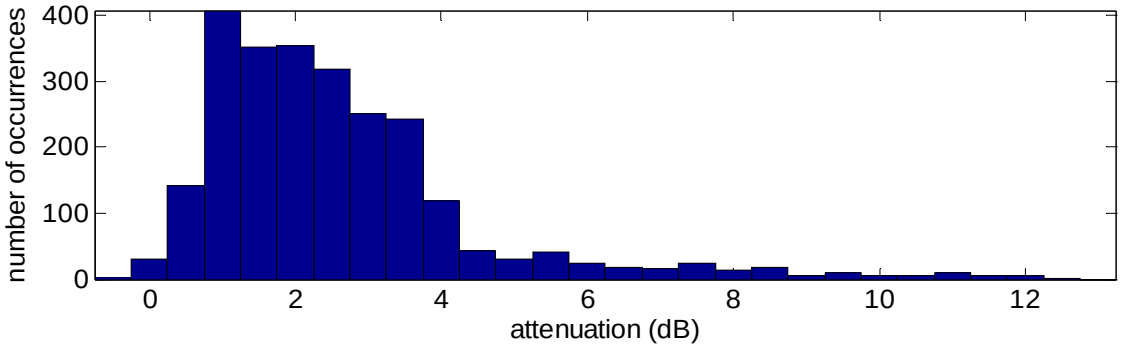

Figure 4-5: Histogram of the 2500 mass positions vs. attenuation of the sound power radiated from the receiving panel using HG blanket vs. using just porous media

Figure 4-6 shows a schematic of the subset of the top ten best performing HG blankets. The schematic is broken down into two parts: the first layer at the top surface of the HG blanket, and the second layer at 2.5mm depth (half of the porous layer thickness). The 17g mass is shown only once due the fact that the subset of the best ten performers had the 17g mass inclusion at the same position: at the top surface, off center as shown in Figure 4-6. The second mass is shown at ten different locations which leads to the conclusion that for the special chosen input point force the set of best performers includes the heavy mass at the position x/L_x=0.7 and y/L_y=0.5 and the lighter mass on the other half (x-axis) of the plate at various positions shown in Figure 4-6. The best location was shown in Figure 4-4(b).

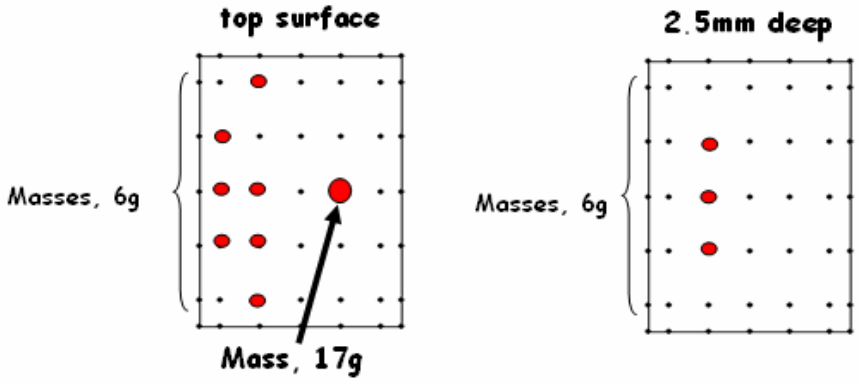

Figure 4-6: Schematic of the (top ten) subset of best performers in two layers: top surface and 2.5mmm deep

4.1.2 Comparison of results

The performance of three HG blankets are compared in this section: the random placement of the mass inclusions represented by the average attenuation of the results shown in Figure 4-5, the modal design shown in Figure 4-4(a) and the best performer (scheme shown in Figure 4-4(b)) using the exhaustive search shown in the previous section. Table 4-1 presents the attenuation from 0-500Hz of sound radiated from the receiving panel inside a DPS using a porous layer vs. HG-blanket designed with the three different strategies. The modal design performance is slightly better than the random placement. However, the best performer gives an attenuation of 12.5dB which is almost 10dB more than the other two cases. The reason why the modal design is not

as effective is due to the fact that the heavier mass is positioned at the center position of the plate (see: Figure 4-4(a)) which is not the most efficient location.

Table 4-1: Average attenuation from 0-500Hz of sound radiated from the trim panel inside a DPS using a porous layer vs. HG-blanket designed with three different strategies

Design strategy	Attenuation (dB)
Mean performer in extensive design search	2.6
Modal design	2.74
Best performer in extensive design search	12.5

In order to compare the responses of the DPS built with the modal design strategy, the best performer result in the extensive search and DPS with porous media (HG blanket without mass inclusions), the sound power radiated from the trim panel was plotted over the frequency of interest (50-500Hz) as shown in Figure 4-7.

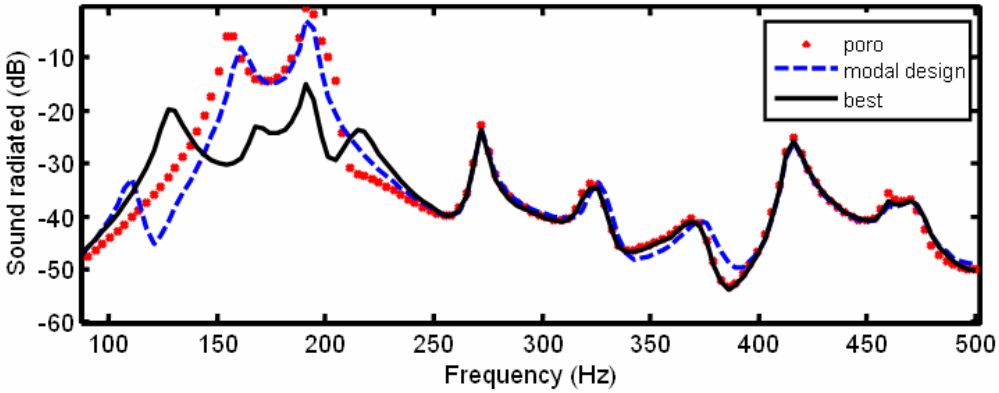

Figure 4-7: Predicted response of a DPS. Plotted is the sound radiated from the trim panel with acoustic blanket glued on top and an HG blanket glued on top (modal design vs. best performer in extensive search).

The response of the DPS with porous media is a reference showing the effectiveness of the designed HG blanket. The modal case targeted the first mode of the trim panel with the large mass. The second mass inside the modal designed HG blanket had little effect. This will be further discussed in the experimental section below.

However, the best performing HG blanket from the extensive search achieves broad control over the 140-220Hz range where the first two modes dominate. All HG blankets have similar performances above 250Hz.

There are two main consequences of adding the masses to the blanket. First, the masses interact with individual fuselage modes in order to add damping to these modes (also tends to split the mode). Second, the masses couple the modes of the fuselage panel together such that the resulting system has coupled modes with different mode shapes. Therefore the masses can achieve attenuation by either directly controlling resonances or altering the mode shapes of the fuselage panel (modal reconstruction) in order to reduce coupling **between the panels** [76]. Locating the heavier mass off center, away from nodal lines, allows the mass to couple into higher order modes and thus increases the opportunity for both control mechanisms to be exploited. In light of this, it is not surprising that the optimal mass location is not in the center of the panel. It should be noted that strictly speaking all of the modes as described here represent the **coupled** modes of the DPS and therefore fuselage panel modes do not really exist. However, with relatively weakly coupled systems, such as this one, many of the coupled modes are still dominated by individual components such that the above analysis is still valid.

4.1.3 Experimental studies on designed HG blankets

This section presents experimental control results used to discuss the results presented for the modal design method. Furthermore, experimental results of the modal design method and the best performer for the exhaustive search are used to validate the above presented results.

4.1.3.1. Experimental investigation on the modal design case

Figure 4-8 presents the experimental vibration response of the fuselage panel in the DSP without passive noise control and with sandwiched passive noise control device (poro-elastic media vs. HG-blanket build with the modal design method). The porous material utilized was melamine foam, fairly stiff acoustic foam with a typically high porosity (properties given in Table 2-3). Plotted is the spatially averaged velocity

of the fuselage panel driven by a point force at x/L_x=0.3 and y/L_y=0.7 on the fuselage panel as shown Figure 2-2(b). It can be seen that by adding the poro-elastic media to the plate, stiffness is added to the plate which causes an upward shift of the natural frequencies. Note that at frequencies over 450Hz, the poro-elastic media dampens the vibration response of the plate significantly. When adding the heavy mass inside the poro-elastic media on top of the plate at the top center position of the poro-elastic media, as shown in Figure 4-4(a), the HG-blanket causes a mode split of the 1-1 Mode of the plate and reduces the vibration response of the first mode. Adding the second, lighter mass causes a mode split of the 2-1 mode which further reduces the response of the fuselage panel.

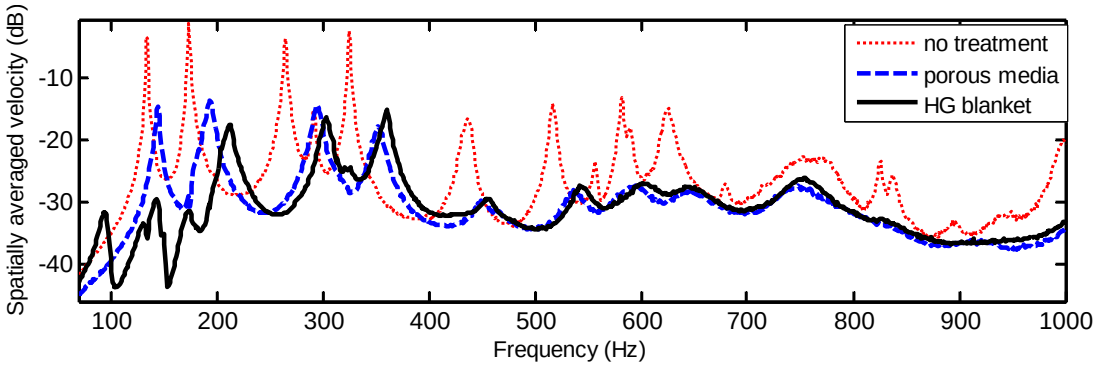

Figure 4-8: Experimental vibration response of a clamped DPS. Plotted is the spatially averaged velocity of the fuselage panel with no treatment, an acoustic blanket glued on top and an HG blanket (build with the modal design method) glued on top

Figure 4-9 shows the experimental vibration response of the trim panel in the DSP without passive noise control and with sandwiched passive noise control device (poro-elastic media vs. HG blanket). Plotted is the spatially averaged velocity of the trim panel. Due to the mode split of the 1-1 mode discussed in the prior plot, the HG blanket significantly lowers the vibration response up to 160Hz. At the frequencies above 550Hz, the poro-elastic media in both passive vibration control devices (poro-elastic media and HG-blanket) damp out the response of the trim. The above numerical analysis has shown that the second mass targeting the 2-1 mode on the fuselage panel has no effect on the trim side and indeed, Figure 4-9 verifies this result.

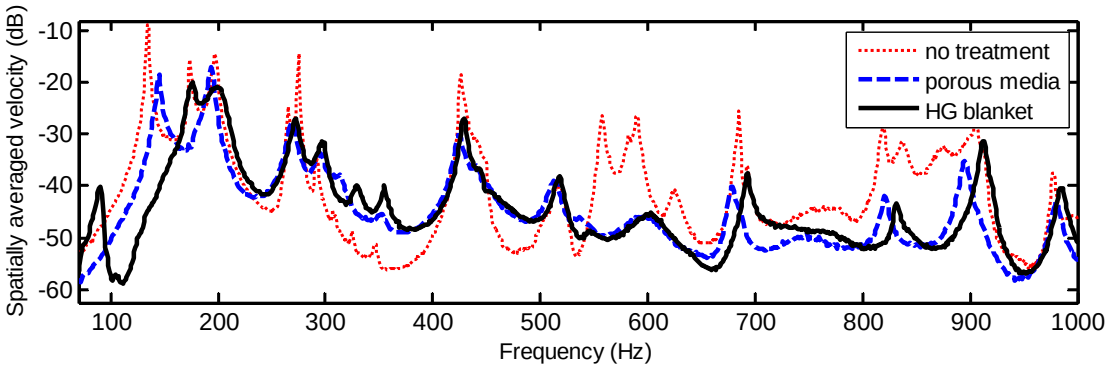

Figure 4-9: Measured response of a clamped DPS. Plotted is the spatially averaged velocity of the trim panel with no treatment, an acoustic blanket glued on top and an HG blanket (build with the modal design method) glued on top

In conclusion, the above DPS-HG blanket experiments show that while the poro-elastic media by itself mainly reduces the vibration level at higher frequencies, the HG blanket can be used to attack certain modes at low frequencies. Furthermore, the coupling between the modes of the two panels varies from mode to mode. Thus, only certain modes of the fuselage panel couple strongly to the trim panel, so a modal design strategy requires a significant amount of information about the structure of the DPS and knowledge on the part of the designer.

4.1.3.2. Experimental validation for the design strategies

In order to validate the above presented numerical results of the clamped DPS with HG blanket built with the modal design strategy, the best performer result in the extensive search and DPS with porous media (HG blanket without mass inclusions), the predicted spatially averaged velocity of the trim panel was plotted over the frequency of interest (50-500Hz) as shown in Figure 4-10. The validation of the clamped DPS without the HG blankets can be found in Ref. [44].

Figure 4-11 shows the corresponding measurements to Figure 4-10. Although the mode splits occur in the experiments at lower frequencies than in the predictions, the relative characteristics of both results are similar. The experimental result for the "best" HG blanket shows that the first mode split produced larger attenuation than the second mode split whereas the theoretical model shows similar attenuation at both mode splits.

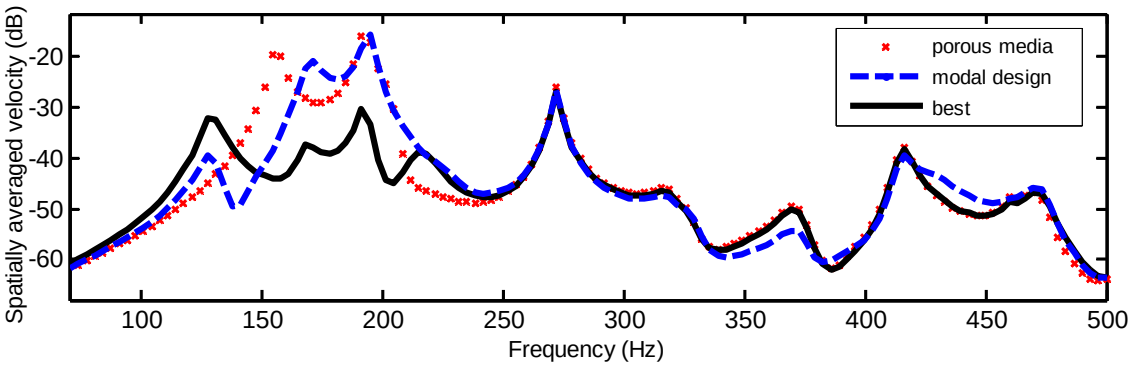

Figure 4-10: Predicted response of a DPS. Plotted is the spatially averaged velocity of the trim panel with acoustic blanket glued on top and an HG blanket glued on top (modal design vs. best performer in extensive search)

In summary, theory and experiment show similar trends for the mode splits at low frequencies and the design tool for the DPS with sandwiched HG blanket captures the important dynamics of the coupled system. However, the results indicate that the optimal design strategy may be somewhat sensitive since the resulting attenuation is not as good as that predicted.

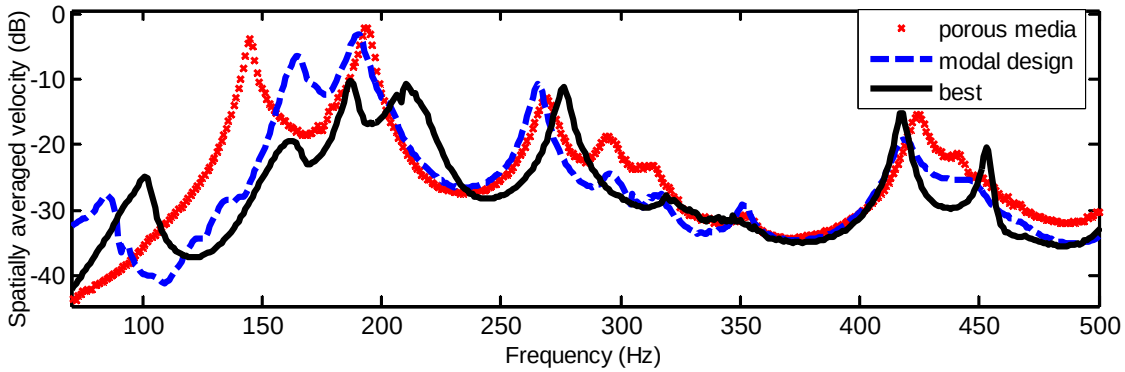

Figure 4-11: Measured response of a DPS. Plotted is the spatially averaged velocity of the trim panel with acoustic blanket glued on top and an HG blanket glued on top (modal design vs. best performer in extensive search)

The main conclusion from this work is that there is a strong need for optimization routines such as genetic algorithms or interactive routines since optimal performance is substantially better than the performance achieved using the other simple design strategies. A comparison of different design strategies is presented in the next section.

4.2. Comparison of optimization routines for the design of HG blankets

In this section two optimization routines, used to design the HG blankets in order to minimize the trim vibration of a DPS, are compared. The first optimization strategy couples the design tool developed previously with the "Genetic Algorithm and Direct Search Toolbox" from MATLAB and the second routine uses a novel iterative optimization strategy developed at the Vibrations and Acoustics Laboratories at Virginia Tech. Throughout the development and comparison of optimization routines for the HG blanket, gradient based algorithms were not considered. This is because the solution space is not characterized by a single minimum but my multiple minima. This is borne out by the fact that the optimized HG blankets obtained with the above described algorithms are similar in results but vary significantly in their design especially when there are a large number of optimization parameters (e.g. mass positions and number of skin pockets). Specifically this can be seen by comparing the optimized HG blankets for the full scale fuselage tests in chapter 6. Although the HG blankets perform similarly, in terms of attenuation of the trim panel vibration, the mass inclusion positions for each optimized HG blanket varies significantly.

4.2.1 System studied

The DPS design tool used in this section is identical to the design tool used for the previous section. HG blanket is modeled to be on top of the fuselage panel and an air gap is located between the HG blanket and the trim panel. The velocity at 25 locations on both the fuselage and trim panels can then be used to estimate the spatially averaged squared velocity response of the panels (both with clamped BC's). Figure 2-2(b) shows the grid distribution used for the computational model of the DPS, which is constant through all components of the DPS numerical model. The fuselage panel is excited using plane wave pressure excitation [13,14] $\theta = 30^{\circ}$ (angle from the vector normal to the surface) and $\varphi = 60^{\circ}$ (angle from the positive x direction on the plate). Note that the numerical model uses a finer grid but the number of positions for the mass insertions is limited to 25 nodes in two layers of the porous model (i.e. 50

potential mass locations) in order to obtain a manageable solution space as shown in Figure 4-12. Furthermore the optimization process is constrained to four mass inclusions (3.5g, 4.5g, 6g and 9g) with the total mass of 23g which is approximately 10% of the fuselage weight.

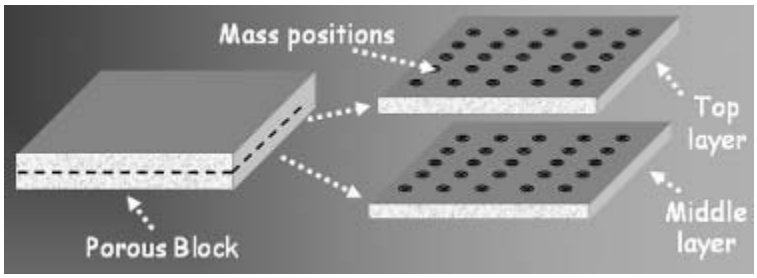

Figure 4-12: Schematic of mass positions inside design tool

4.2.2 Comparison of optimization routines for DPS

This section presents a comparison of the performance obtained using MATLAB's "Genetic Algorithm and Direct Search Toolbox" and an iterative optimization routine based on the sequential addition of massed in the blanket. Figure 4-13 presents a flow chart with the concept of the iterative routine.

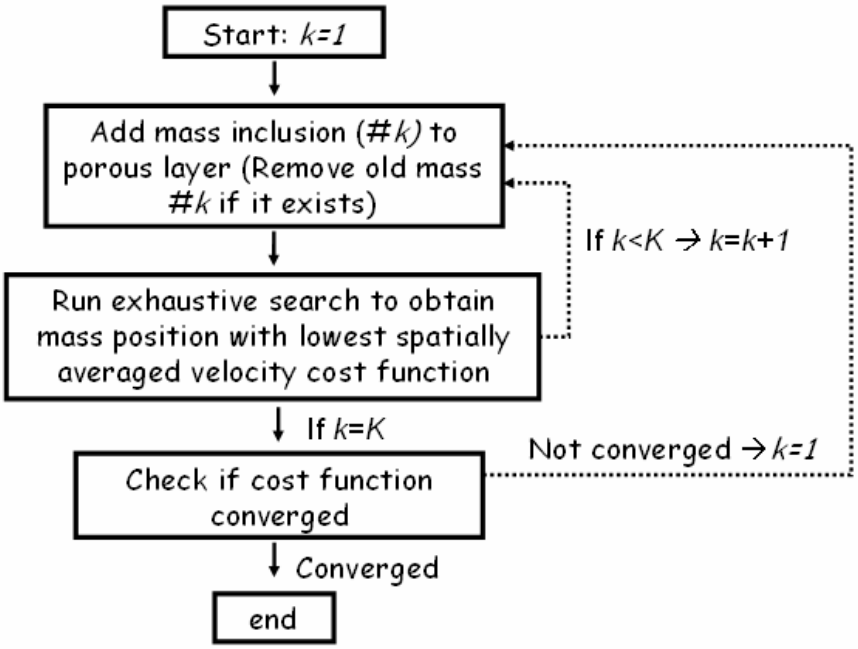

Figure 4-13: Flow chart of iterative optimization routine

The routine is based on the sequentially addition of mass inclusions, one by one until the maximum number of mass inclusions is reached. After each mass is added the optimal location/design for the next mass is found doing an exhaustive search for each mass (i.e. 50 locations) individually choosing the mass location with the highest trim attenuation in terms of velocity. When all of the masses are added the algorithm then reassesses the design of the first mass and continues with each mass inclusion one by one until the design is converged. The genetic algorithm from MATLAB will be compared to two different runs of the iterative process. The genetic algorithm runs for 120 generations with a population of 10 per generation. The first iterative routine will add the mass inclusions one by one with the heaviest mass (9g) first and the lightest mass (3.5g) last. The second iterative routine will have a different mass order (4.5g, 9g, 6g and 3.5g). Note that running an exhaustive search with all four masses inside the design tool would mean 50^4 runs. This novel iterative approach runs exhaustive search of the solution space of each mass individually which, in the case of successful result would mean that the number of results would decrease to 4x50 times the number of outer loop iterations (where the optimal location positions are reassessed). All iterative routines converged after three outer loop iterations which is a promising result in terms of computational efficiency for this method.

In order to compare the responses, DPS with the HG blankets designed with the genetic algorithm from MATLAB with the two iterative routines the spatially averaged velocity of the trim panel is plotted over the frequency of interest (50-500Hz) as shown in Figure 4-14 including a reference plot of the layer of melamine foam without any mass inclusions (blue line).

At first glance, one can see that both the genetic and the iterative algorithm routines work very well by reducing the first two modes of the DPS (blue line) by a significant amount. The iterative process with the mass order going from heaviest to lightest seems to have targeted the first resonance of the reference plot with one mass more that the other two cases which had a noticeable impact around 140Hz.

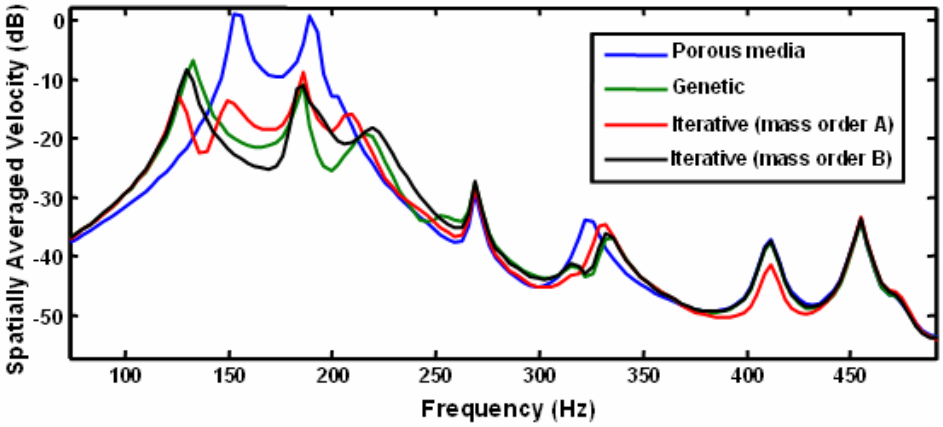

Figure 4-14: Predicted response of a DPS. Plotted is the spatially averaged velocity of the trim panel with porous media glued on top and an HG blanket glued on top. Compared are three optimization routines.

Table 4-2 presents the attenuation of all three optimized HG blankets. The average attenuation over from 0-500Hz was computed in respect of the velocity of the plate with a porous layer on top.

Table 4-2: Average attenuation from 0-500Hz of velocity of the trim panel using three optimization routines

Optimization Routine	Attenuation (dB)
Genetic Algorithm	8.8
Iterative Method (mass order A)	9.2
Iterative Method (mass order B)	9.1

The iterative method was a little more effective than the genetic algorithm in terms of attenuation of trim vibration. However, the iterative processes run for half as long as the genetic algorithm before the routine converged. Therefore one would benefit from using the iterative method especially in cases of HG blanket designs with more than four mass inclusions or larger numbers of potential mass locations.

There has been a similar technique in the past targeting one mode using one mass, recalculate the behavior of the plate before adding the second mass and so on, up to the desired number of inclusions. This specific optimization routine has been successfully used to tune and locate a vibration absorber treatment to control the shock

transmission through an aerospace structure by Johnson et al. [77]. Note that the difference in the two methods is the fact that the method in this paper uses an exhaustive search for each mass individually minimizing the plate velocity whereas in Johnson's algorithm specific modes are targeted individually, meaning the algorithm assigns each mass inclusion a mode to target which consequently results in additional constrains to the process.

4.2.3 Iterative method for MPS

The main conclusion in the last section was that both, the MATLAB genetic algorithm as well as the iterative method, have the potential to equally optimize HG blankets. However, the iterative method was computationally more efficient for the single bay double panel system (DPS). Going from the DPS to the multi bay double panel system (MPS), one would expect the iterative method to be even more efficient as the number of mass inclusions increases. This section shows an optimized HG blanket using the MPS design tool validated in section 3.2. The iterative method for the DPS is more straight forward than for the MPS because four individual skin pockets have to be optimized and the interaction between those skin pockets needs to be taken into account. The iterative method, in this case, adds two mass inclusions to each skin pocket (thus, eight inclusions total) to four poro-elastic layers distributed over the MPS with a total mass of 5% of the fuselage mass. The fastest converging results were obtained by adding the first mass inclusion on each skin pocket starting with the largest skin pocket. Once an exhaustive search is run for each of these skin pockets, a second mass is added, again starting with the largest skin pocket.

The genetic algorithm uses a population of 16 per generation using the same mass insertion configuration as in the iterative process. It was stopped once the iterative algorithm converged, creating approx. 23 generations. The iterative method converged to a satisfactory level after the second run. Figure 4-15 presents the predicted spatially averaged velocity of the MPS trim with four porous-media blankets, as well as the two HG blanket configurations, obtained with the iterative method and the genetic algorithm. As expected, the iterative method gives a better result than the genetic algorithm. However, the difference is not as significant as expected.

Table 4-3 presents the average attenuation of the trim panel inside the MPS from 0-450Hz. The two optimization methods are compared. After adding 5% of the fuselage mass, the genetic algorithm resulted in an average attenuation of 3.16dB. The iterative method achieved an average attenuation of 4.01dB, beating the genetic algorithm in the direct comparison.

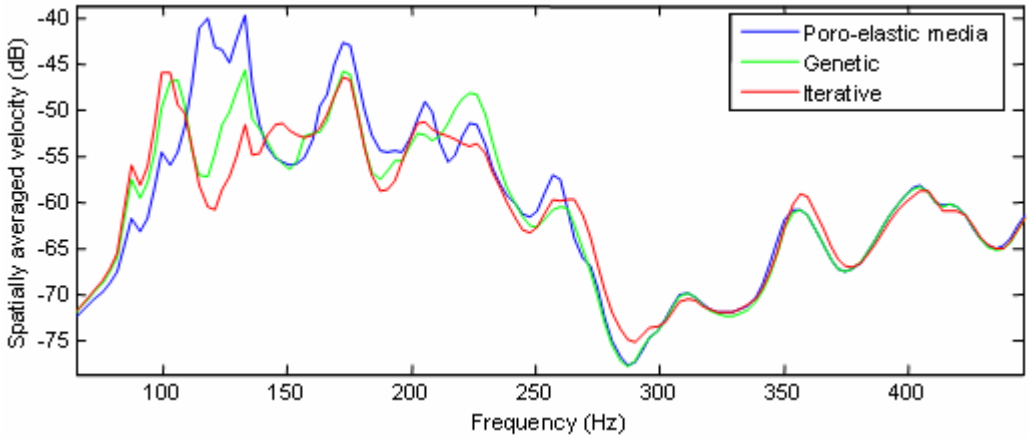

Figure 4-15: Predicted response of a MPS trim. The spatially averaged velocity of the trim panel is plotted. The poro-leatic layer case to the two optimization routines is compared.

However, the previous section shows that the genetic algorithm has the potential to optimize the HG blanket equally well as the iterative method when time is not a constraint. Therefore, for the full-scale fuselage measurements in chapter 5, both optimization techniques can be used.

Table 4-3: Average attenuation from 0-450Hz of velocity of the trim panel using two optimization routines

Optimization Routine	Attenuation (dB)
Genetic Algorithm	3.16
Iterative Method	4.01

4.3. Sensitivity of HG blanket design to parameter variation

Although the concept of an HG blanket is fully defined in the present literature [31], deficiencies on knowledge of the sensitivity of the HG blanket design to variations in mass location exist. Therefore, a prime objective of this research is to provide insight into how to obtain practical manufacturing tolerances for HG blankets. In order to achieve that the effectiveness of the HG blanket, obtained through a design process (e.g. through the use of genetic algorithms as discussed in the previous section), must be evaluated for small variation in mass location. For this purpose a simplified model of the HG blanket was developed by modeling a dynamic vibration absorber (DVA) acting on a plate (see Figure 4-16).

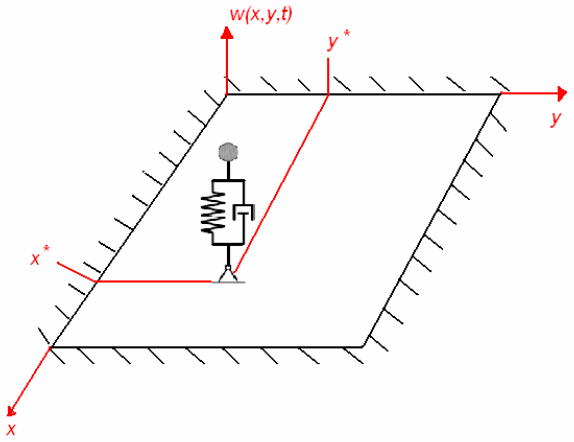

Figure 4-16: System to be modelled: mass-spring-damper-system on a plate

In general DVA's are devices attached to vibrating systems in order to attenuate vibration. As early as 1909 Frahm [78] investigated a DVA as a mass-spring system attached to a main device. When the sinusoidal excitation frequency corresponds to the natural frequency of the attached DVA, the steady state magnitude of the main structure would vanish completely (assuming no damping in the DVA and that the main structure acted as a solid body). At this frequency the force applied through the DVA to the main structure creates a balance. Den Hartog [37] considered a damped vibration absorber modelled as a mass-spring-damper system attached to a single degree of freedom system. Damping prevents the magnitude of the main structure at the

excitation frequency from becoming zero but decreases the sensitivity of the DVA due to variations in the excitation frequency. Further research has been done to investigate multi degree of freedom systems. Analytical and semi analytical methods have been developed to design a DVA optimally. Since most structures are damped, Thompson [36] showed an analytical way to tune the DVA parameters using the frequency locus method. A relationship has been found describing the optimal constellation of these values. Dayou and Brennan [79] focused on the positioning of DVAs on continuous structures and developed a positioning method for multiple passive DVAs resulting in attenuation close to active DVAs. In 2001 Jaquot [80] investigated a simply supported plate with attached DVA and Jaquot's model is similar to the model used in this study. It is stated that attaching the DVA at a location which is driven by all modes dissipates the energy of every mode in the entire frequency range of interest.

This section specifically presents the mathematical model of a clamped plate with DVA on top. The sensitivity of HG blankets with respect to their effectiveness with change in mass position is analyzed using one and two DVA's. Finally the model is validated experimentally using modal hammer tests.

4.3.1 Mathematical model

This section presents the governing equations of DVAs acting on top of a clamped plate used as a simplified model of HG blankets controlling a plate. The mass inclusions inside the porous layer interact in reality at a certain distance away from each other [35]. For simplification purposes, the masses are assumed to be uncoupled masses acting as dynamic vibration absorbers with a certain effective stiffness and damping value obtained experimentally [31]. The plate is modelled using Kirchhoff plate theory. A Dirac-function [81] is used to distribute the force on an infinitesimal small area. This means physically that a point force is applied. The equation of motion for a plate and a DVA, including all assumptions, is given by

$$D\Delta\Delta w + \rho h \frac{\partial^2 w}{\partial t^2} = p(x,y)\cdot e^{i\omega t} - F\cdot\delta(x-x^*)\delta(y-y^*), \qquad (4\text{-}1)$$

where x^* and y^* are the positions of the DVA with the DVA force F and $p(x,y,t)$ representing the excitation, (generally due to turbulent boundary layer

noise in this application). The displacement *w* and velocity *v* of the plate can be written respectively as

$$w(x,y,t)=\sum_{n,m} C_{nm}\phi_{nm}(x,y)\cdot e^{i\omega t}\ , \tag{4-2}$$

and

$$v(x,y,t)=\frac{\partial\ w(x,y,t)}{\partial t}=i\omega\sum_{n,m} C_{nm}\phi_{nm}e^{i\omega t}=i\omega\cdot w(x,y,t)\ . \tag{4-3}$$

The previous set of equations can then be rewritten to solve for the coefficients C_{nm} due to N DVAs:

$$\underbrace{\begin{bmatrix} \omega_{11}^2-\omega^2 & 0 & 0 & \cdots & 0 \\ 0 & \omega_{12}^2-\omega^2 & 0 & \ddots & \vdots \\ 0 & 0 & \ddots & \ddots & \vdots \\ \vdots & \ddots & \ddots & \ddots & 0 \\ 0 & \cdots & \cdots & 0 & \omega_{mn}^2-\omega^2 \end{bmatrix}}_{resonance-matrix}\begin{pmatrix} C_{11} \\ C_{12} \\ \vdots \\ C_{mn} \end{pmatrix}= \tag{4-4}$$

$$\underbrace{\underset{\sim}{f}}_{\substack{external \\ excitation}} \quad -\sum_{i=1}^{N}(k_i+i\omega b_i)(1-\underline{V}_i)\underbrace{\begin{bmatrix} \phi_{11}\phi_{11} & \phi_{11}\phi_{12} & \cdots & \cdots & \phi_{11}\phi_{mn} \\ \phi_{12}\phi_{11} & \phi_{22}\phi_{22} & \ddots & \ddots & \vdots \\ \vdots & \ddots & \ddots & \ddots & \vdots \\ \vdots & \ddots & \ddots & \ddots & \vdots \\ \phi_{rs}\phi_{11} & \cdots & \cdots & \cdots & \phi_{rs}\phi_{mn} \end{bmatrix}_i}_{DVA-matrix}\begin{pmatrix} C_{11} \\ C_{12} \\ \vdots \\ C_{mn} \end{pmatrix}$$

The DVA-matrix has to be evaluated at the positions of the DVA. The effective stiffness k_i and damping b_i are in reality given by the properties of the porous material as well as by the interaction between the mass inclusion and the porous layer [35]. The vector *f* contains a set of random complex numbers and the velocity of the plate is computed 20 times, to simulate a random excitation which is similar in effect to a turbulent boundary layer excitation [82].

4.3.2 Sensitivity study

This section uses the previous model to discuss the sensitivity of the DVA in terms of attenuation of the plate due to a change in mass position. In this chapter the

general definition of the sensitivity S is the change of the value *c(u)* with respect to a parameter *u* and can be written as $S = \frac{\partial c}{\partial u}$. In this study, *u* is the postion of the DVA and c is the velocity. In the study with two DVA's, *u* represents the position of these DVA's that are moved within the plate. The parameters for the clamped plate used throughout the whole thesis are given in Table 2-1.

4.3.2.1. Sensitivity study on one DVA

To analyze the sensitivity of one dynamic vibration absorber acting on a plate, the velocity spectrum in the frequency range of interest is computed. Thus, the best position in terms of broad-band attenuation can be found by considering the attenuation in a defined frequency range. The mass ratio of the DVA to the plate depends on the frequency the DVA is tuned to. Therefore, the mass varies since the stiffness of the foam is assumed to be constant. For example the mass ratio using one DVA is 0.1364 for the mass targeting the 1-1 mode and 0.02 for the mass targeting the 3-1 mode. The criterion applied to target the 1-1 mode leads to the range from 70*Hz* to 200*Hz* is calculated and plotted over the DVA positions marked with a "+". The best position is in the middle of the plate where the dominating mode has its highest magnitude, in this case the 1-1 mode. The sensitivity, as expected, is strongly dependent on the dominant mode shape. Figure 4-17 b) shows the magnitude of the gradient $\left|\vec{S}\right|$ of the spatially averaged velocity between each DVA position. The magnitude of the gradient is less in the *x*-direction than in the *y*-direction since the plate is longer in the *x*-direction and therefore the shorter the distance to the edge, the more sensitive is the DVA position. The shape with lowest sensitivity can therefore be defined by an ellipse around the best position and is dependent on the dimensions of the plate. Around the middle of the plate the magnitude of the gradient is low and therefore the sensitivity is low as well.

In the following, the sensitivity with respect to the DVA position while targeting the 2-1, 1-2 and 3-1 mode is presented. The average velocity and the gradient of the average velocity for the DVA targeting the 2-1 mode are plotted in Figure 4-18 a) and b), respectively. The best position is where the 2-1 mode shape is at a maximum (anti-node). Additionally, the positioning of the DVA targeting the 2-1 mode is more

sensitive than the positioning targeting the 1-1 mode. This is caused by the smaller area that is provided by the 2-1 mode shape since the plate is divided into two halves by the nodal line at $x/L_x=0.5$. As a result, the mass has to be positioned more accurately in order to ensure that efficiency is not lost. It should be noted that Figure 4-18 a) is not symmetric and this is caused by coupling with multiple modes (even though the 2-1 mode is clearly dominant) and the finite number of averages used to approximate the turbulent boundary layer excitation.

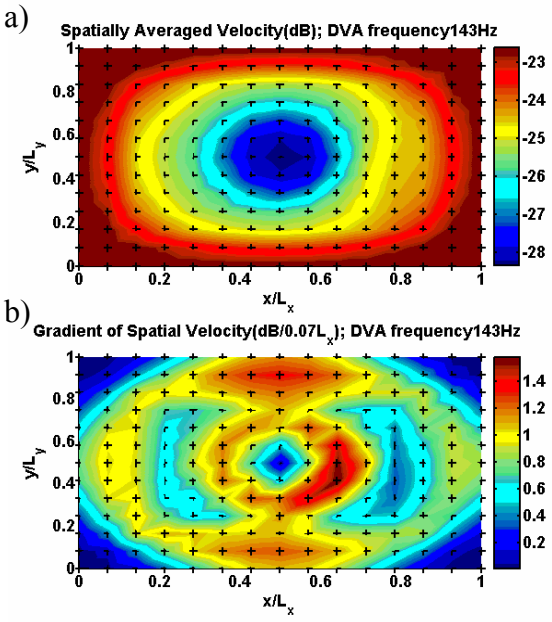

Figure 4-17: Average velocity in the frequency range from 70*Hz*-200*Hz*; DVA targeting the 1-1 mode at 143*Hz*; crosses symbolize DVA positions on the plate. b) Magnitude of gradient of average velocity describing the change in magnitude (*dB*) among different DVA positions.

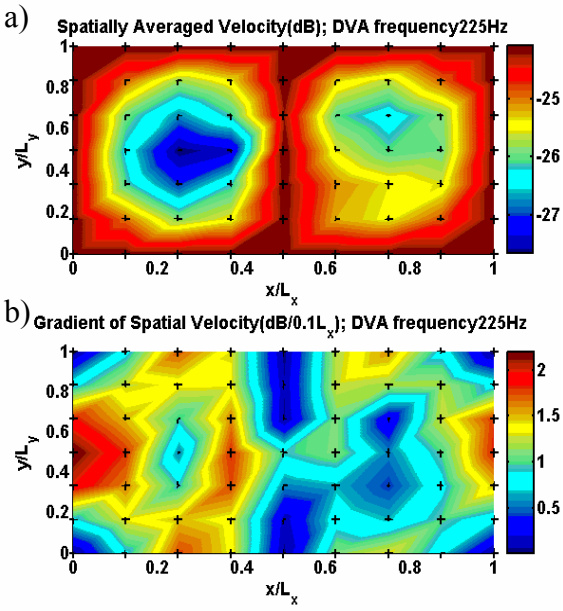

Figure 4-18: a) Average velocity in the frequency range from 180*Hz*-270*Hz*; DVA targeting the 2-1 mode at 225*Hz*; crosses symbolize DVA positions on the plate. b) Gradient of average velocity describing the change in magnitude (*dB*) among different DVA positions.

In Figure 4-19 a) the averaged velocity targeting the 1-2 mode is shown. As would be expected, the plots for the 2-1 and 1-2 mode are similar.

Considering the DVA positions to target the 3-1 mode, Figure 4-20 a) presents the average velocity. Again, the areas with the highest attenuation can be found on the

anti-node lines of the mode shape and the most effective locations for the DVA are separated by a further nodal line. There is an increase in the sensitivity as seen in Figure 4-20 b) due to the shorter wavelengths.

In conclusion, the design concept following the highest magnitude of the targeting mode shape is sufficient and leads in all considered cases to the most efficient position. Additionally, the sensitivity increases with the amount of nodal lines of the dominating mode shape (i.e. in proportion to wavenumber).

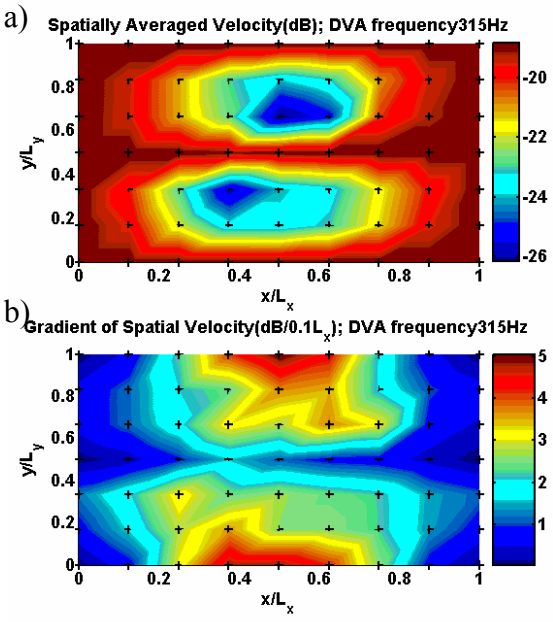

Figure 4-19: a) Average velocity in the frequency range from 270*Hz*-340*Hz*; DVA targeting the 1-2 mode at 315*Hz*; crosses symbolize DVA positions on one quarter of the plate. b) Gradient of average velocity describing the change in magnitude (*dB*) among different DVA positions.

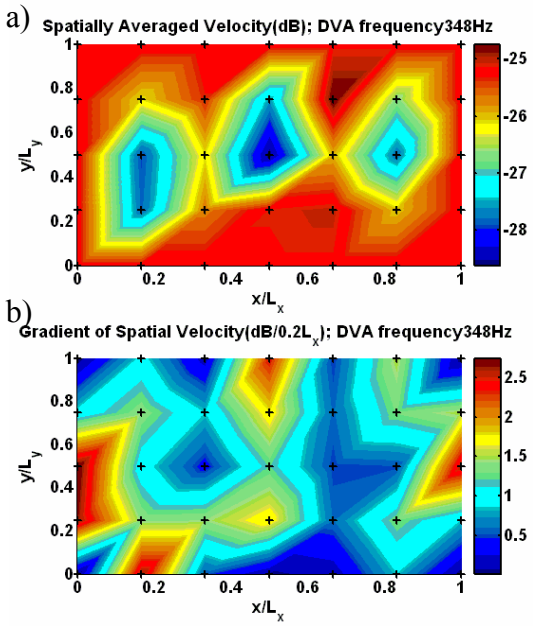

Figure 4-20: a) Average velocity in the frequency range from 320*Hz*-390*Hz*; DVA targeting the 3-1 mode at 348*Hz*; crosses symbolize DVA positions on one quarter of the plate. b) Gradient of average velocity describing the change in magnitude (*dB*) among different DVA positions.

4.3.2.2. Sensitivity study on two DVAs

In this study the sensitivity a combination of 48 DVA positions for each of two DVAs was performed. Therefore 48*48 possibilities are evaluated. To describe the sensitivity of a system with two DVAs, a way has to be found to compare and plot the

results. The positioning of two DVAs is based on the grid shown in Figure 4-21. Due to the symmetry of the plate and the modes, one quarter of the plate is sufficient for the placement of the DVAs. The plot principle can be described as "a picture in the picture". The first DVA has to be placed on the quarter of the plate (red dots on the big plate in Figure 4-21). The green grid to the right of the 1st DVA represents the 48 possible positions on one quarter of the plate for the 2nd DVA. For example, the 1st DVA is placed on the blue cross indicated in the figure by "Position of 1st DVA" and the 2nd DVA is placed by the red cross. The red cross on the green grid describes the DVA combination. Above this position the magnitude of the averaged velocity created due to the action of both DVAs is plotted. This way a convenient plot can be created including all details necessary for the DVA study.

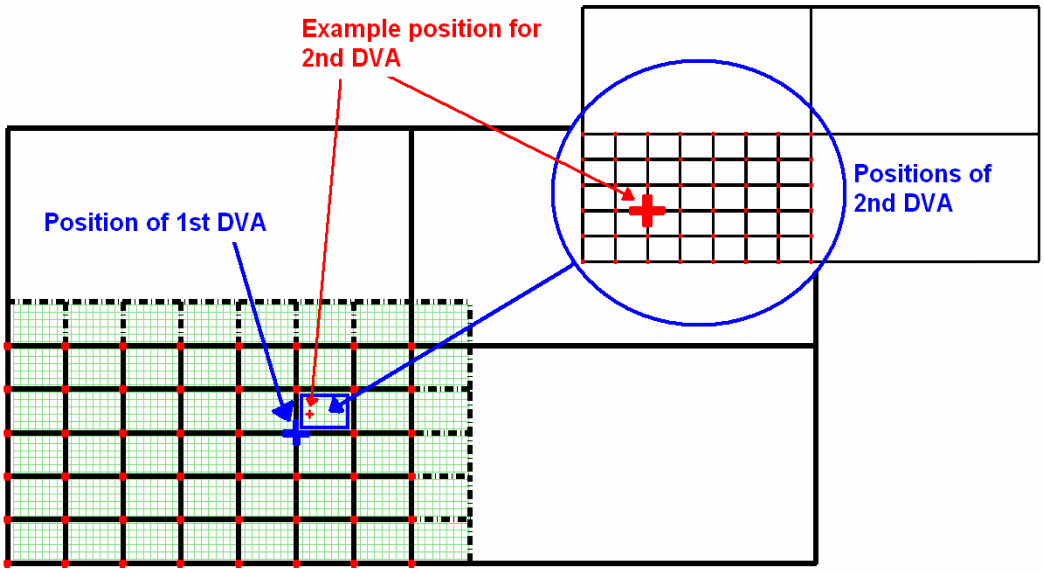

Figure 4-21: Principle of DVA plot concerning different positions

In the following the combination with one DVA targeting the 1-1 mode at 143*Hz* and another one targeting the 3-1 mode at 348*Hz* will be considered. The 1-1 and 3-1 mode are the modes radiating most in the frequency range up to 500*Hz* and therefore these modes should be attenuated.

Figure 4-22 shows the average velocity of two DVAs acting on a plate. The regions with the lowest average velocity can be found in the middle of the whole plate, where the first DVA acts most efficiently. The highest attenuation can be achieved if each DVA is placed where the corresponding mode shape has its maxima.

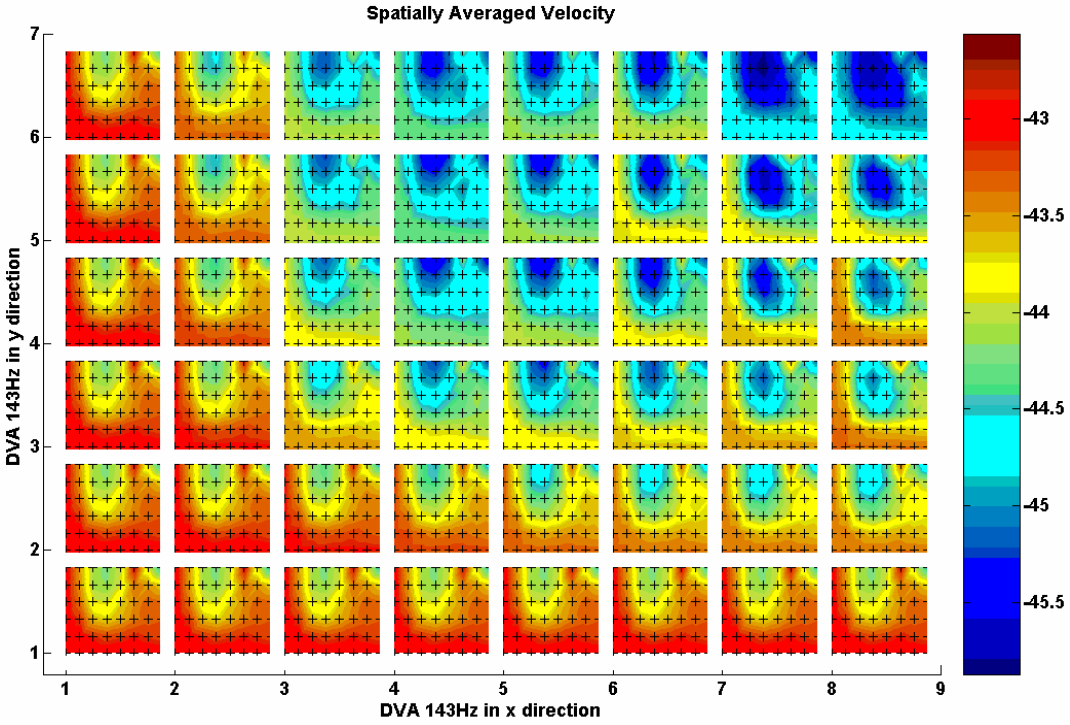

Figure 4-22: Spatially averaged velocity (dB) with first DVA targeting the 1-1 mode and second one targeting the 3-1 mode. Principle of plot is presented in Figure 4-21

Figure 4-23 shows the gradient of spatially averaged velocity (dB/DVA position distance) with the first DVA targeting the 1-1 mode and the second one targeting the 3-1 mode.

Generally, the sensitivity of the system is decreased compared to the sensitivity with one DVA. If one DVA is placed at the best position, the sensitivity for the second DVA is decreased. The results with two DVAs are therefore a combination of the results given by the sensitivity analysis of the two DVAs performed separately.

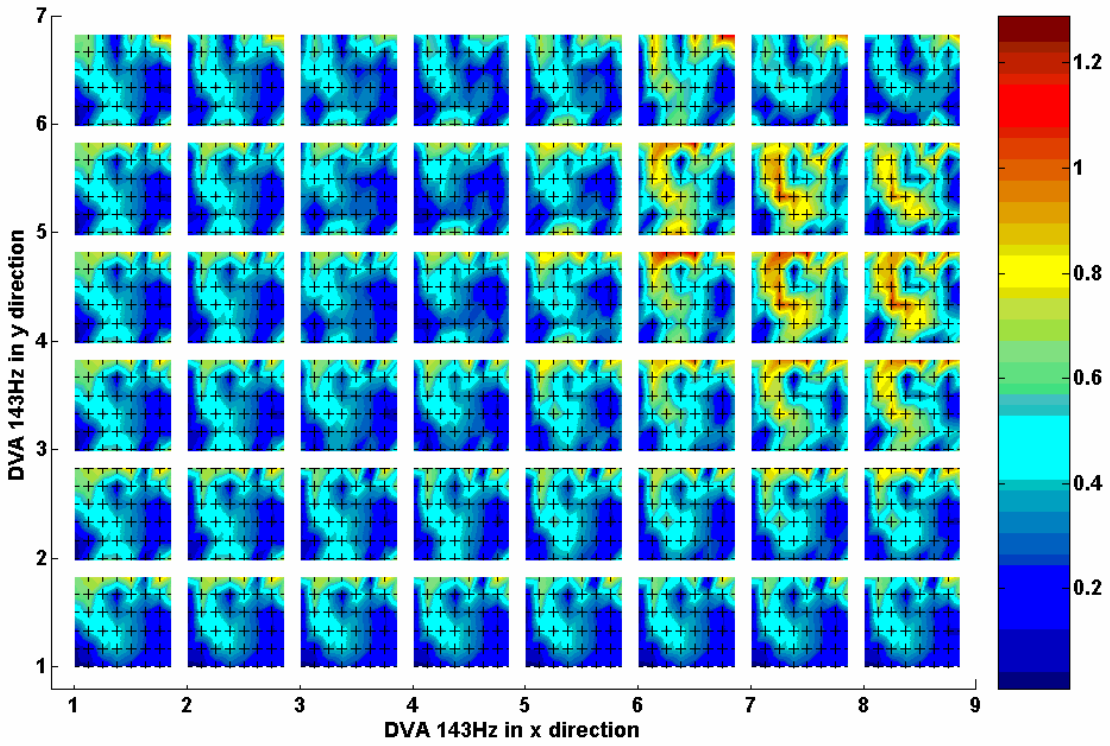

Figure 4-23: Gradient of spatially averaged velocity (dB/DVA position distance) with first DVA targeting the 1-1 mode and second one targeting the 3-1 mode. Principle of plot is presented in Figure 4-21

4.3.3 Experimental validation

In the previous sections the analytical model is used to determine the sensitivity of a DVA acting on a rectangular clamped plate. This section provides experimental data to validate the predictions made with respect to the positioning of the DVA. At first the physical system studied will be presented followed by the comparison of the measurements and the data computed with the numerical model.

The physical system studied in order to validate the model used in the previous section consists of a heavy aluminum frame with one clamped panel and acoustic foam (melamine foam) glued on top of the panel. The dimensions for the physical system coincide with the dimensions used throughout the entire thesis and are presented in Table 2-1. The whole setup is suspended on bungee cords as seen in Figure 4-24, to shift the frame motion to low frequencies (see Appendix A).

Figure 4-24: Experimental setup and grid for modal hammer excitement (ellipse)

Figure 4-25: DVA grid for experiments

To obtain an HG blanket acting as a DVA targeting the 1-1 mode of the clamped, a rectangular mass (10mm x 10mm; 5.5g) was glued on top of the acoustic foam (schematic is shown in Figure 4-26). In the measurements the mass is moved on a grid presented in Figure 4-25. The DVA is only moved on one quarter of the plate since the results for the remaining quarters are similar due to symmetry.

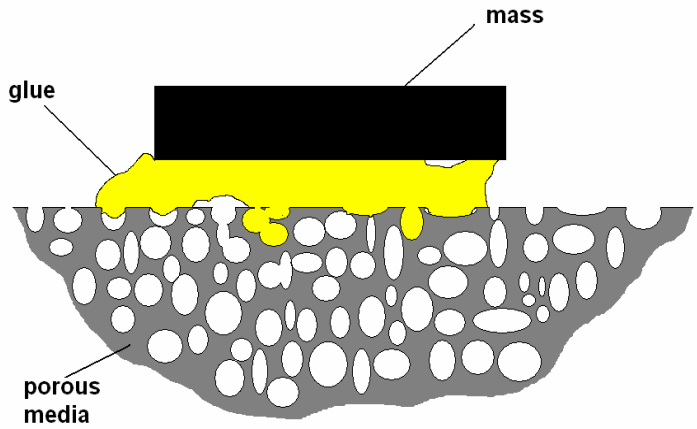

Figure 4-26: Schematic of HG blanket with mass glued on top of a porous layer

The excitation in the experiment is done with a point force at a constant position. To match this excitation a point force is calculated for the model and the transfer function is determined. The point force replaces the external excitation $p(x,y)$ in Eq. (1) with $F \cdot \delta(x-x^F)\delta(y-y^F)$, where $x^F = 0.6L_x$ and $y^F = 0.6L_y$ represent the

position on the plate. The position of the force is adapted to the position of the accelerometer in the experiment. A random "boundary layer type" excitation was too impractical to test, as it requires an enormous number of measurements, and therefore this point force excitation was used to validate the model.

The maximum velocity of the measurement in a frequency range from 70*Hz* up to 170*Hz* is plotted over the corresponding DVA position in Figure 4-27. The corresponding prediction is shown in Figure 4-28. The tendency and observations made in the prior section can also be applied to the results of the measurement. The best position is found in the experiment close to the middle of the plate. An attenuation of 6*dB* is possible even if the DVA is adjusted slightly to a non-optimal position.

It should be noted that the results from the analytical model and the experiments have not been scaled but the attenuation by the DVA is similar in theory and experiment. In both cases an attenuation of about 6*dB* is achieved. In addition, the tendency of the DVA position is equal and can be described by the dominating 1-1 mode shape.

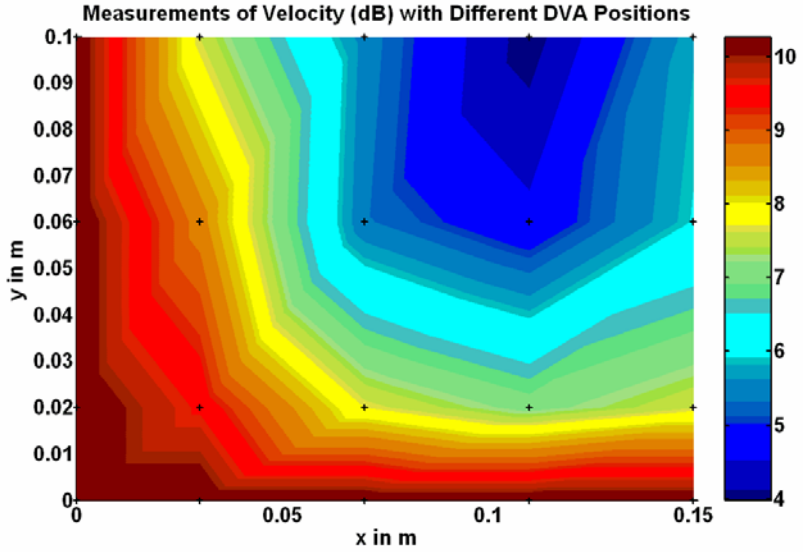

Figure 4-27: Maximum velocity in the frequency range from 70Hz to 170Hz determined by experiment

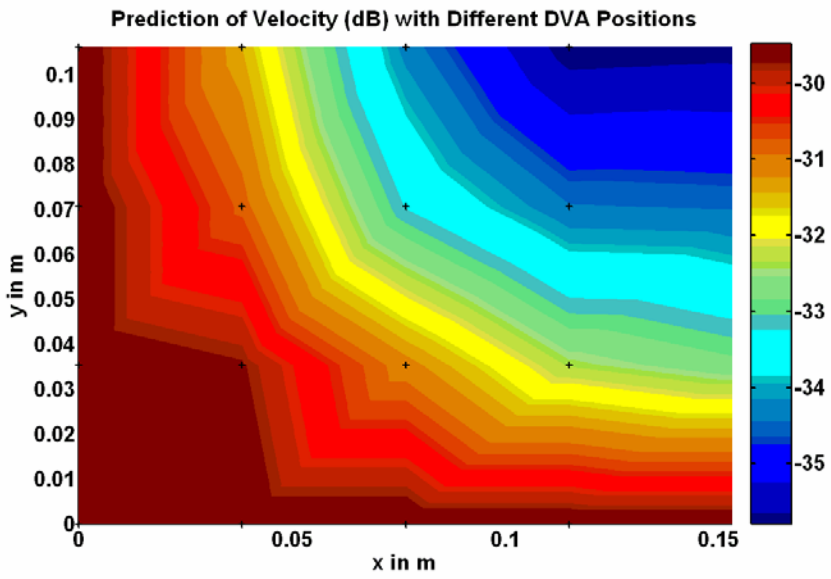

Figure 4-28: Maximum velocity in the frequency range from 70Hz to 170Hz determined by the analytical model. DVA frequency adapted to 139Hz

In conclusion, a simple mathematical model is proposed to analyse the sensitivety of a nominal optimized HG blanket. The model was verified and theory and the experiment match well and the magnitude decay depending on the DVA position is captured with a desired level of detail.

5. STUDY ON THE BEHAVIOR OF MASS INCLUSIONS ADDED TO A PORO-ELASTIC LAYER

This chapter presents a study of the behavior of the embedded masses inside the poro-elastic media. A parametric analysis of mass inclusion behavior is presented, probing both mass and stiffness variations inside the HG blanket. The parametric analysis is conducted to tune the mass inclusions to the required HG blanket natural frequencies. This can be done by either changing the mass or changing the stiffness. The mass inclusion, acting like a distributed mass-spring-damper system, interacts with a "finite volume" of the poro-elastic layer. This behaviour leads to HG blanket characteristics such as the "footprint", the "effective area" and the "mass interaction distance". An empherical approach is found and used to predict the natural frequencies of different mass shapes embedded in porous media. An analytical approach is then developed to describe the interaction of the mass inclusions with a poro-elastic layer by simplifying a model for poro-elastic materials originally proposed by Biot [52] and Allard [53] for low frequencies and by implementing basic elastomechanical concepts. Both, the empherical as well as the analytical approach are compared to measurements and shown to be accurate within 8% and 6%, respectively, over a range of porous materials and mass shapes.

5.1. A study on the characteristic behavior of HG blankets

The objective of this section is to outline the characteristic behavior of mass inclusions added to a layer of poro-elastic material. Furthermore, novel techniques for predicting and tuning the resonance frequencies of the mass inclusions will be presented.

5.1.1 FE model and experimental investigation

This section presents the finite element (FE) model and experimental setup used to analyze the HG blanket characteristics and the behavior of the mass inclusions. FE results are used in cases where experimental results are difficult to obtain. The FE model of the HG blanket is based on fundamental fluid, structural, and coupled fluid-

structural equations and was used in the previous chapters to develop the single-bay as well as the multi-bay double panel system design tool.

5.1.1.1. FE model

The details of the finite element code used for this work are well presented in Chapter 2 and therefore this section will only explain how the model was used for this work.

The FE model of the HG blanket was used to analyze the interaction between the mass and a block of foam (Melamine #1a in Table 5-1). Mass inclusions were placed at single nodes in the FE mesh and the stress and displacement fields generated by the masses could then be calculated. The foam block was excited with a uniform velocity over its base, thus each node at the base was driven with a constant unit velocity. Transfer functions between the input base velocity and the nodes corresponding to mass inclusions could then be used to investigate the characteristics of the masses (such as natural frequency and damping). In addition, the stress fields created by the masses when excited could also be investigated.

Table 5-1: Model parameters of the FE model of an HG blanket.

Poro type	Modulus of elasticity (N/m^2)	Density (kg/m^3)	Flow resistively (Ns/m^4)
Melamine #1a (white)	4.76 * 10^5	8.44	$1.14 * 10^4$
Melamine #2 (grey)	3.83 * 10^5	9.07	$0.99 * 10^4$
Polyurethane	1.05 * 10^5	28.98	$1.3 * 10^4$
Polyamide	3.0 * 10^5	7.86	$35.3 * 10^4$

5.1.1.2. Experimental Investigation

To study the fundamental behavior of a mass inclusion, block of porous material with a single mass inclusion was used to determine the natural frequencies and damping of the HG blanket. The test could then be repeated for various masses (various shapes and weights). The mass inclusion was either glued on top of the porous block,

or inserted into the middle of the block after cutting the block in two pieces (half of the depth). The two pieces were subsequently glued back together. Experimental studies have shown minimal variations of the porous material properties using this technique.

An acoustic foam block (melamine#1 if not stated otherwise) was placed on top of a shaker with the block glued to a stiff honeycomb platform (see Figure 5-1). An accelerometer on top of the honeycomb platform and one on the mass inclusion allowed the transfer function between the drive acceleration at the base and the acceleration of the mass inclusion to be measured and natural frequency determined. Figure 5-1 shows the data acquisition system with the HG blanket and the shaker.

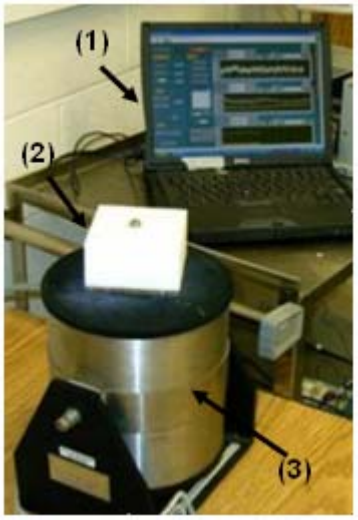

Figure 5-1: Experimental setup to measure the natural frequencies of the mass inclusions inside the HG blanket. Shown is the data acquisition system (1), the HG blanket (2) and the shaker (3)

For the corroboration of the "effective area" approach (described below), three additional porous media were used: a different type of melamine foam (Melamine #2), polyurethane, and polyamide. The parameters for the four types of porous material were measured and are presented in Table 5-2. The flow resistivity was measured using the Ingard and Dear method [83] and the elasticity taken from a dynamic shaker test [84]. The two melamine foams were acquired from two different companies and exhibit similar, although not identical, properties. The polyurethane and the polyamide parameters vary significantly from those of the melamine foam; the polyurethane has high density while the polyamide has high flow resistivity. Only "typical" values are

defined since the properties of the foam can vary from sample to sample. The aim here is to outline a universal approach to predicting and controlling mass inclusion behavior in HG samples.

The material properties of a nominally identical acoustic foam produced in two different batches can vary significantly and can also vary within a single batch even within the same sheet. The five porous layers with melamine #1a utilized for results in Table 5-2 (discussed in section 5.1.2.2) were all from the same large sheet of foam. Melamine #1b comes from a different batch entirely. Provided experiments indicate that the poro-elastic blocks cut from different batches can result in a five-fold increase in the standard deviation of the natural frequencies as shown in Appendix C.

5.1.2 Parametric studies

This chapter outlines vital HG blanket characteristics including the "footprint", the "mass interaction distance" and the "effective area" to allow prediction of mass inclusion behavior.

The parametric studies of the HG blanket are performed to tune the mass inclusions to the required natural frequency. There are two ways to tune a mass-spring system: changing the mass or changing the stiffness. Since the poro-elastic layer acts as a distributed spring, there are many parameters that can be varied to change the effective stiffness, and these are investigated in detail and presented in the following sections.

5.1.2.1. Tuning with varied mass

One way to tune the inclusion behavior is to change the mass of the inclusion. A foam block (Melamine #1a) with dimensions 140x140x50 mm (length, width, and thickness respectively), three inclusions, and an attached accelerometer were used. The inclusions were individually glued on top of the porous block and tested sequentially. Three different mass inclusions with the same surface shape and area were used. Mass was varied from 11.7 g to 27.0 g. Figure 5-2 shows the measured transfer function between the input acceleration of the base and output velocity of the three inclusions.

The resonance frequency follows accepted mass law since the natural frequencies were proportional to the inverse square root of the mass.

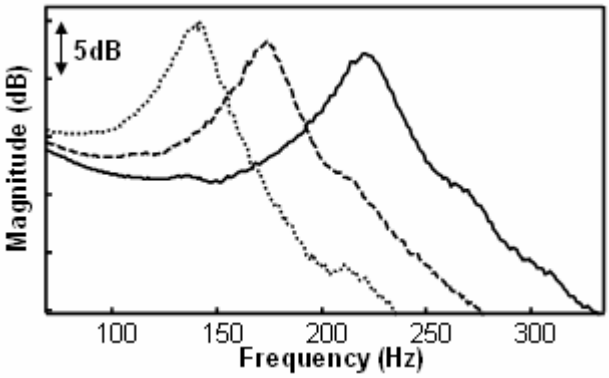

Figure 5-2: Measured transfer function between the input acceleration of the base and output velocity of three different mass inclusions: 11.7g (———), 18.7g (- - - - -), 27g (·····)

5.1.2.2. Tuning with varied stiffness

The stiffness of the HG blanket mass-spring-damper system is created when a region of the porous media interacts with the mass inclusion. Tuning the mass inclusions by varying the stiffness is a complicated process. To accurately predict behavior, tuning with varied stiffness requires the definition of mass depth, a "footprint," "mass interaction distance," and "effective area."

Mass depth

Varying mass depth is the simplest way to change the stiffness and thus the natural frequency of a mass embedded in a layer of poro-elastic media like melamine #1a. Figure 5-3 depicts the variation in resonant frequency of an 8g mass in a melamine foam block (140×140×110mm) versus layer thickness. The resonant frequency of the mass inclusion increases with decreasing depth x. To indicate the trend of the natural frequency measurements, the solid line represents a curve fit through the data points given as

$$f_n = 83.42 + \frac{6.044}{\sqrt{x}}, \qquad (5\text{-}1)$$

Where the resonant frequency f_n is inversely proportional to the square root of the mass depth x converging at 83.42Hz. 83.42Hz is therefore the natural frequency that would be expected for masses placed in very thick blocks of melamine.

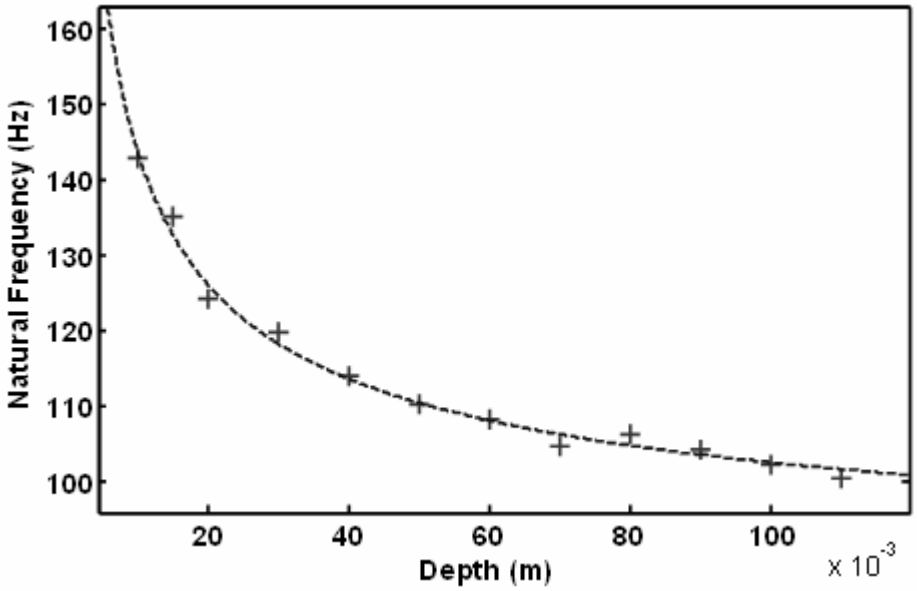

Figure 5-3: Variation of resonant frequency of an 8 g mass in a melamine foam block as a function of the thickness of foam beneath the mass. Plotted are experimental measurements (+) and a curve fitted through measured data (-----)

Kidner et. al [32] validated this measurement in a previous experiment with a 35×35×100mm melamine foam block. The analysis in the next section signifies that Kidner et. al. used a porous block too small to take into account all stiffness effects.

Footprint

When varying material stiffness, the concept of the "footprint" is vital. Since the poro-elastic media acts as a distributed spring, a mass moving inside this media will have a region of influence. The poro-elastic material directly adjacent to an inclusion will move with the same displacement as the inclusion, but the displacement decreases with increasing distance from the inclusion. Beyond a certain distance from the inclusion the motion of the media becomes negligible. Therefore the inclusion can be considered to have a finite region of influence, or footprint. Similarly the forces generated by the inclusion only affect a finite region on the base of the poro-elastic

media. The forces are the largest directly underneath the inclusion, and increased distance from the inclusion results in decreased forces. The footprint embodies the volume of poro-elastic media that a mass inclusion influences and therefore also delineates the stiffness. The definition of the footprint is dependent on what is considered to be a "negligible" influence and in this chapter a working definition of "footprint distance" is suggested. However, other definitions could also be used.

This section presents the basic concept of a footprint, defines the footprint distance and investigates this concept in detail for a specific type of acoustic foam. However, the footprint is likely to vary for different porous materials with varied physical properties. Defining the footprint for a range of materials and for various poro block thicknesses is a future endeavor and is beyond the scope of this document. The aim is simply to provide a novel, systematic method to evaluate and define mass inclusion interactions and performance.

To investigate the basic behavior of a HG blanket (Melamine #1a), the FE model was run with a 20x8x8 uniform grid and simulated on a base plate that was driven with a uniform velocity v in the z-direction (Figure 5-4(a)). Figure 5-4(b) shows the operating deflection shape of the HG blanket when driven at resonance. This operating deflection shape is a cut-out of the x-z plane of the blanket at the y-coordinate corresponding to the mass position. In this example, the length and width of the block of foam are 0.1 m and the thickness is approximately 0.05 m. The weight of the mass inclusion is 5.6 g. The nodes of the FE model in its static position are noted with +'s, and the displacements after moving the base plate are noted with x's connected with lines. A uniform velocity (and displacement) was applied to the base of the HG blanket. The lowest row of static nodes has a constant distance to the displaced node lines since they are directly attached to the base. As expected, the porous media provides less motion with greater distance from the mass. One can see that the region of influence is a non-uniform area around the mass inclusion, therefore the footprint is a non-uniform volume considering that the operating deflection shape only shows the x-z plane of the blanket. The key is to define and compute a horizontal distance to be able to account for the interaction between the mass inclusions. This distance will be defined in the next paragraph and denoted as "footprint distance".

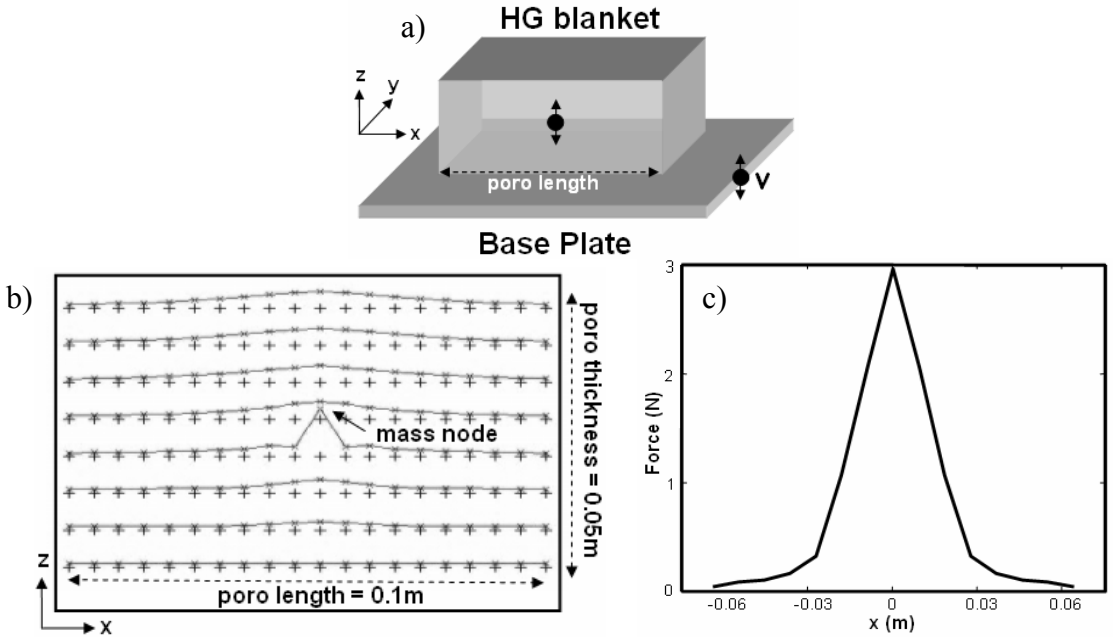

Figure 5-4: (a) Schematic of the HG blanket glued on a base plate moving with the velocity v. (b) An operating deflection shape of a layer of porous media with one mass inclusion (2-D). (c) Force at the base versus the distance x from the middle of the mass inclusion placed at the center of the 150x100x50 mm poro-elastic layer, or the numerical "footprint distance" computation

Similarly, Figure 5-4(c) shows a plot of the force at the base versus the horizontal distance x from the mass inclusion that is placed at the center of a 140x140x90 mm (length, width and thickness respectively) poro-elastic layer. The plot shows that the maximum force is directly below the mass and drops down to 5% of the maximum force at a distance of approximately x=0.04 m. Therefore this distance can be used as a working definition of the footprint distance.

In order to determine the footprint distance experimentally and to verify mathematical results presented, a shaker experiment was chosen with the allocations shown in Figure 5-1. A mass inclusion inside a very small porous block with length and width much smaller than the footprint should experience lower stiffness than an inclusion embedded inside a porous layer with infinite x and y dimensions. Increasing the x and y dimensions of a small block of porous material with an inclusion should lead to an increase in the natural frequency (i.e. more stiffness). This increase will continue until the dimensions of the poro-block reach the volume in which the

inclusions interact, i.e. the footprint. Above this dimension, the natural frequency of the mass inclusion should not change significantly. Figure 5-5(a) shows a schematic of this concept. A block of melamine foam with a 5.6 g mass embedded in the center position was used in the experimental design shown in Figure 5-1. Figure 5-5(b) shows the top view of the porous block. As with the mathematical example, the dimensions are 140x140x91 mm (length, width, and thickness respectively). The measurement was repeated while holding the thickness constant and cutting 10 mm off of each of the sides. For the last measurement, only 5 mm was removed. Consequently, the maximum distance *X* from the center of the mass inclusion to the side of the poro-block is 7 cm. The distance *X* for the second measurement was 6 cm, and the remainder followed the same trend. Figure 5-5(c) shows the experimentally determined natural frequency versus the distance *X*. At *X*=0.07 m, the natural frequency is higher than the one at *X*=0.015 m due to previously described stiffness effects. At *X*=0.04 m the natural frequency of the embedded mass converges to 175 Hz, indicating that the natural frequency does not increase significantly with enlargement of foam block dimensions beyond this point. Thus, the footprint distance can be considered to be approximately 0.04 m for this case and is in agreement with the numerically computed footprint distance described above.

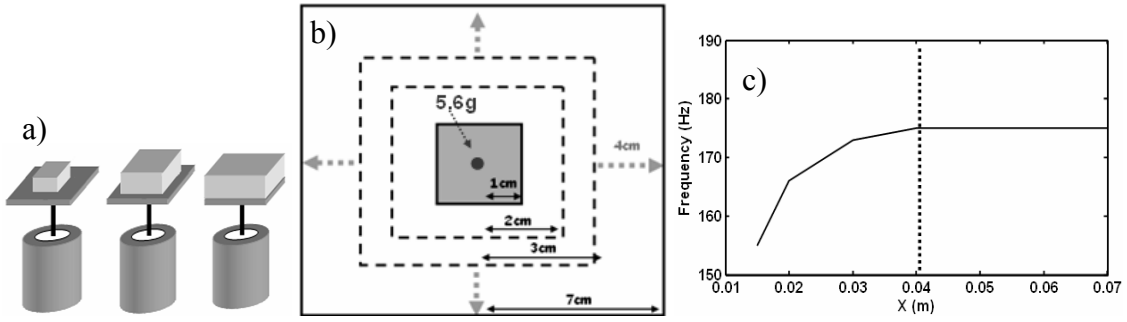

Figure 5-5: (a) Schematic of the experimental "footprint distance" measurement, (b) Dimensions of the poro-layer, (c) Natural frequency versus the distance X of the experimental "footprint distance" measurement

Mass interaction distance

When designing the HG blanket, inclusions interactions within a block of poro-elastic material (like melamine #1a) are important. Two inclusions positioned a large distance from each other within a porous layer will not interact, but two inclusions

directly next to each other will interact a great deal or even act as one large mass thus have a large impact on the natural frequency of the HG blanket. The FE model of the porous material presented in section 5.1.1.1 is used to investigate the distance when the two mass inclusions are independent of each other, the "mass interaction distance." A foam block of dimensions 200x100x100 mm (length, width and thickness respectively) with a 21x7x7 FE grid was used with two 5.6 g mass inclusions. The previous section showed that the footprint distance for a 5.6 g inclusion in melamine foam is approximately 0.04 m. Therefore one mass inclusion was positioned 0.04 m from the side of the foam in a center-depth position and the second mass inclusion was positioned 0.12 m away. In this configuration there are two identical natural frequencies, one for each of the masses. However as the second mass is moved closer to the first, the masses become coupled and the system must now be considered to have *two modes* of vibration each with a different natural frequency (see Figure 5-6(a)). The natural frequencies for the two modes were computed for various separation distances and are presented in Figure 5-6(b).

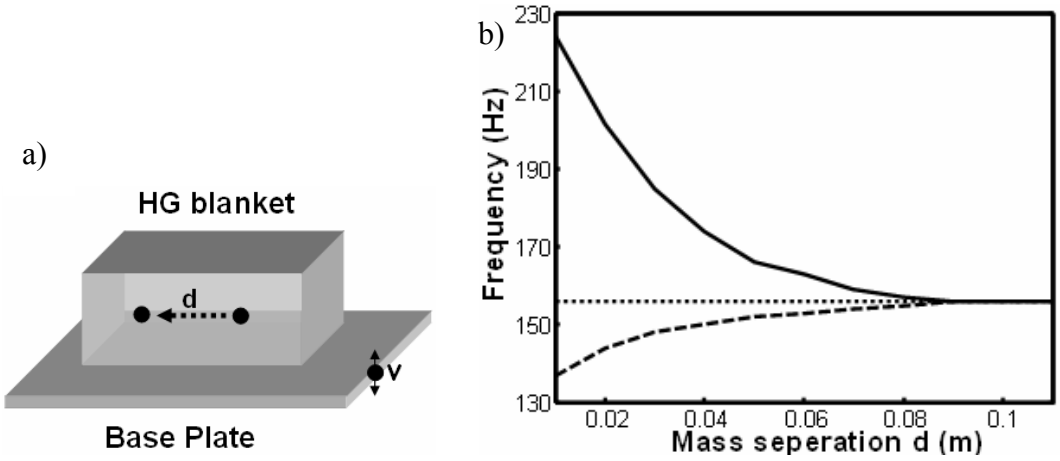

Figure 5-6: (a) Schematic of numerical estimation of "mass interaction distance" and (b) FE results of natural frequencies of mass inclusions versus mass separation. Plotted is the mode of the first mass (———), the mode of the second mass (- - - - -), and the natural frequency of a single mass by itself (·····)

One would expect that the inclusions stop interacting when the two footprints no longer overlap and the two modal natural frequencies should converge to the

uncoupled natural frequencies. When the inclusions are very close together, the natural frequency of one mode (masses moving out of phase) will tend to infinity, but the second mode (masses moving in phase) will tend towards the natural frequency of a single inclusion with twice the mass. This is bourne out in Figure 5-6(b) and it can be seen that the masses stop interacting when they are 0.085 m away from each other i.e. the mass interaction distance is roughly twice the footprint distance.

Effective area

Masses embedded inside a porous layer interact with a certain volume of the porous media. However, the footprint may change if the mass shape is changed. By increasing the surface area of an inclusion (i.e. its projected area), it can be expected to interact with a larger volume of the porous media. Therefore, the stiffness of the mass-spring-damper system inside the HG blanket is expected to increase. A shaker experiment, similar to the one shown in Figure 5-1, was used to measure the natural frequencies of four inclusions with different shapes yet with similar mass. Figure 5-7(a) shows a scheme of the HG blanket used in the shaker experiment with a mass glued on the top of the porous block.

Table 5-2 displays the result of this experiment. The first two columns show the mass and the projected area of the mass shapes. The ball, the beam, and the square have significantly different projected areas. The projected area of the beam and the coin, however, are roughly the same.

Table 5-2: Parameters and results from masses embedded in "melamine #1a".

Mass shape	Weight (g)	Projected area (m^2)	Effective area (m^2)	Average mean of nat. frequency (Hz)	One-sided 90% confidence interval (Hz)	Theoretical nat. frequency (Hz)
Ball	5.6	$1.0*10^{-4}$	$0.8*10^{-3}$	120.2	3.2	110.7
Coin	5.8	$4.6*10^{-4}$	$1.6*10^{-3}$	154.8	7.9	156.7
Beam	5.9	$6.5*10^{-4}$	$2.3*10^{-3}$	190.8	6.4	188.9
Square	5.9	$18.0*10^{-4}$	$4.0*10^{-3}$	240.2	8.7	246.1

Figure 5-7(b) presents the transfer functions between the input acceleration of the base and output velocity of the four mass inclusions. Each measurement was repeated five times using five different blocks of melamine foam #1a. The mean and the one-sided confidence interval with a 90% probability are shown in Table 5-2. The maximum standard deviation of the natural frequency is below 9 Hz for all of the mass shapes (with a probability of 90%). As expected, the natural frequency increases when the area of the masses is increased. Interestingly, although the areas of the beam and the coin are very similar, the natural frequency of the coin is significantly lower than the natural frequency of the beam. The results presented in Figure 5-7(b) and Table 5-2 indicates that the natural frequency does not simply change linearly with projected area, but is also dependent on the *shape* of the inclusion.

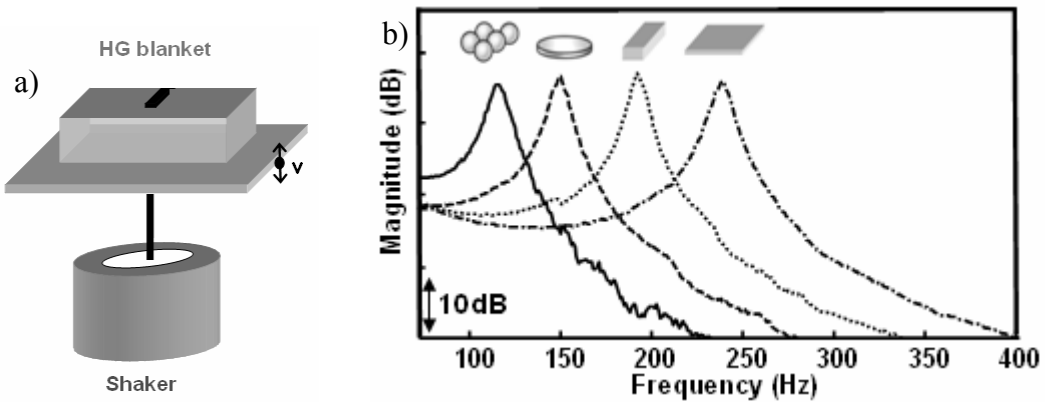

Figure 5-7: (a) Schematic of the HG blanket experiments used for the "effective area" experiments, and (b) Natural frequencies of different mass shapes measured in shaker experiment. 5.6g ball (——), 5.8g coin (- - - - -), 5.8g beam (·····), 5.9g square (-·-·-·)

As a first-order approximation, the stiffness of the mass inclusion can be considered to change with an "effective area" that is defined in Figure 5-8(a) as a perimeter a distance *d* away from the perimeter of the projected area. Consequently, the "effective area" of a beam with the same projected area as a coin would result in a significantly larger "effective area" and thus consequently in a larger footprint and stiffness. This approximation assumes that the equivalent stiffness constant k_{eq} in the

mass-spring-damper system inside the HG blanket is a function of the effective area *a(d)* and a porous material constant c_{poro} (assumes a constant depth):

$$k_{eq} = a(d)\, c_{poro}\,, \tag{5-2}$$

Given the porous material constant c_{poro}, the distance *d* and the mass weight *m*, one can compute the natural frequency in Hz:

$$f_n = \frac{1}{2\pi}\sqrt{\frac{a(d)\, c_{poro}}{m}}\,, \tag{5-3}$$

Figure 5-8(b) shows the projected areas as a function of measured natural frequencies (+'s connected with the solid line). The dashed line is the approximation of the natural frequencies plotted as a function of effective area and using Eq.(5-3). A family of curves with different *d*'s and c_{poro}'s was plotted, and the dashed curve in Figure 5-8(b) is the curve with the best fit through all measurements. The distance *d* that best fits the data is used to calculate the effective areas listed in Table 5-2: and is 0.0105 m with c_{poro}=3.9*10^6 N/m^3.

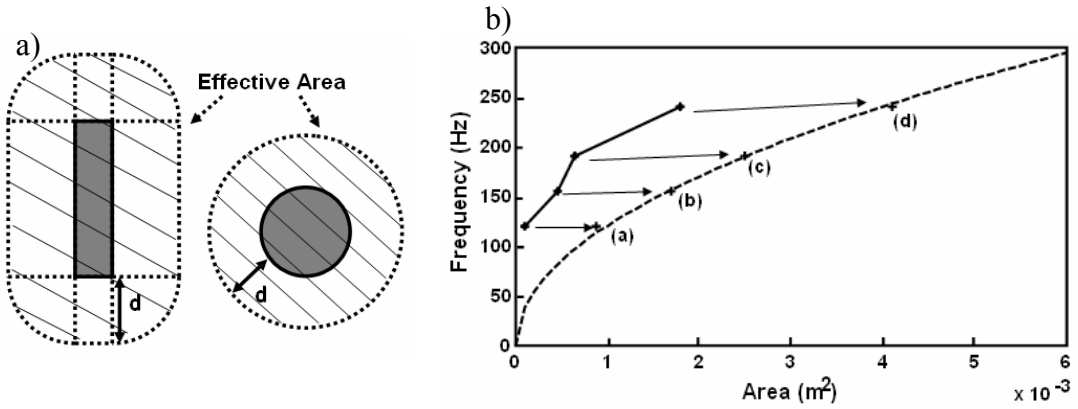

Figure 5-8: (a) Schematic of the "effective area" concept and (b) comparison of the "projected" (—x—) and the predicted "effective area" (- - - - -) along with the measurements (+) of the ball (a), coin (b), beam (c) and square (d) versus frequency

To define this method as a universal predictive tool, a second type of melamine foam block, melamine #1b, with different material properties was studied. The porous block used in the previous experiments is denoted melamine #1a..

In order to predict the natural frequency as described in Eq. (5-3), one must define the distance *d* and the material property c_{poro}. The c_{poro} depends on the material

properties of the porous material used, but the distance *d* depends on geometry and is not strongly affected by small changes in the material properties. Therefore, *d* is assumed to be equal for melamine #1a and melamine #1b. Measurement of only c_{poro} is needed to predict the natural frequency for a given mass shape (i.e. effective area). In order to determine c_{poro} for melamine #1b, the natural frequencies of the beam and the coin were measured using the same experimental design used in the previous test on poro #1. Eq. (5-3) was then used to calculate c_{poro} as $8.2*10^6 N/m^3$. Note that only one measurement, either the coin or the beam's, is needed to compute c_{poro}. However, a best fit between the two points was used.

Figure 5-9 shows a plot with the two theoretical curves of the natural frequencies as a function of effective areas of the mass inclusions of melamine #1a (dashed) and melamine #1b (dotted). The already presented natural frequencies of melamine #1a are noted as +'s, identically to Figure 5-8(b).

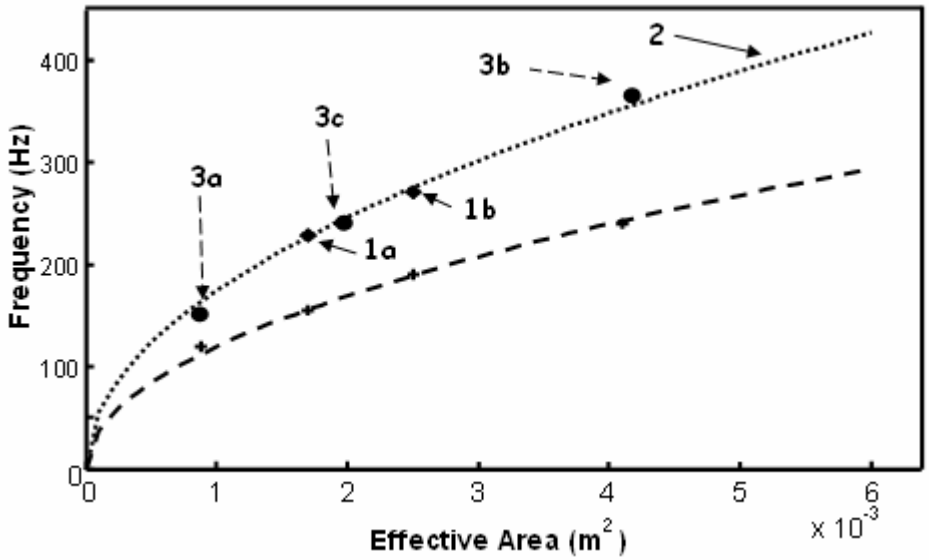

Figure 5-9: Experimental validation of "effective area" approach. Shown is the predicted natural frequency for melamine #1a (-----) along with the measurements (+). The coin (1a) and beam (1b) measurement for melamine #1b were used to plot prediction (2, ·····) for the ball (3a) , square (3b) and an additional shape, a triangle (3c)

The measured natural frequencies of the beam and the coin glued to melamine #1b are noted with squares. As the second step, the natural frequencies of the ball and

the plate glued to melamine #1b were measured. Both lie on top of the predicted dotted curve in Figure 5-9, noted as circles. The proposed formula works for porous media with the four mass shapes: ball, coin, beam and plate. In addition a "new" mass shape: a triangle with roughly the same weight as the other masses is introduced and the "effective area" of the triangle lies between the "effective area" of the coin and the beam. The natural frequency was measured and plotted in Figure 5-9 and is shown to lie within 2% of the predicted value further validating this approach. The results are summarized in Table 5-3.

Table 5-3: Parameters and results from masses embedded in "melamine #1b".

Mass shape	Weight (g)	Projected area (m^2)	Effective area (m^2)	Nat. frequency (Hz)	Theoretical nat. frequency (Hz)
Ball	5.6	$1.0*10^{-4}$	$0.8*10^{-3}$	150	161.1
Coin	5.8	$4.6*10^{-4}$	$1.6*10^{-3}$	230	227.5
Beam	5.9	$6.5*10^{-4}$	$2.3*10^{-3}$	270	274.9
Square	5.9	$18.0*10^{-4}$	$4.0*10^{-3}$	370	358.1
Triangle	6.1	$4.9*10^{-4}$	$2.0*10^{-3}$	249	252.5

To prove that the "effective area" approach is not only valid for one type of porous medium, three additional types of acoustic foam were used: melamine foam #2, polyamide, and the polyurethane. These three types of porous media are some of the most common materials used for interior noise control applications. Figure 5-10(1) shows the comparison of the predicted and the experimental natural frequency of five mass inclusions (a: ball, b: coin, c: triangle, d: beam, e: square plate) versus the effective area for the melamine foam #2. All five mass shapes have the same weight of approximately 6 g. The natural frequencies of the mass inclusions inside the melamine foam remain close to the predicted curve with a maximum error of 5 Hz. Furthermore, Figure 5-10 presents the validation for polyamide (2) and polyurethane (3). Both plots show excellent correlation between theory and experiment. The experiments for

polyamide were executed carefully due to the compressibility of this porous media. However, polyurethane use was in accordance with the use of melamine foam.

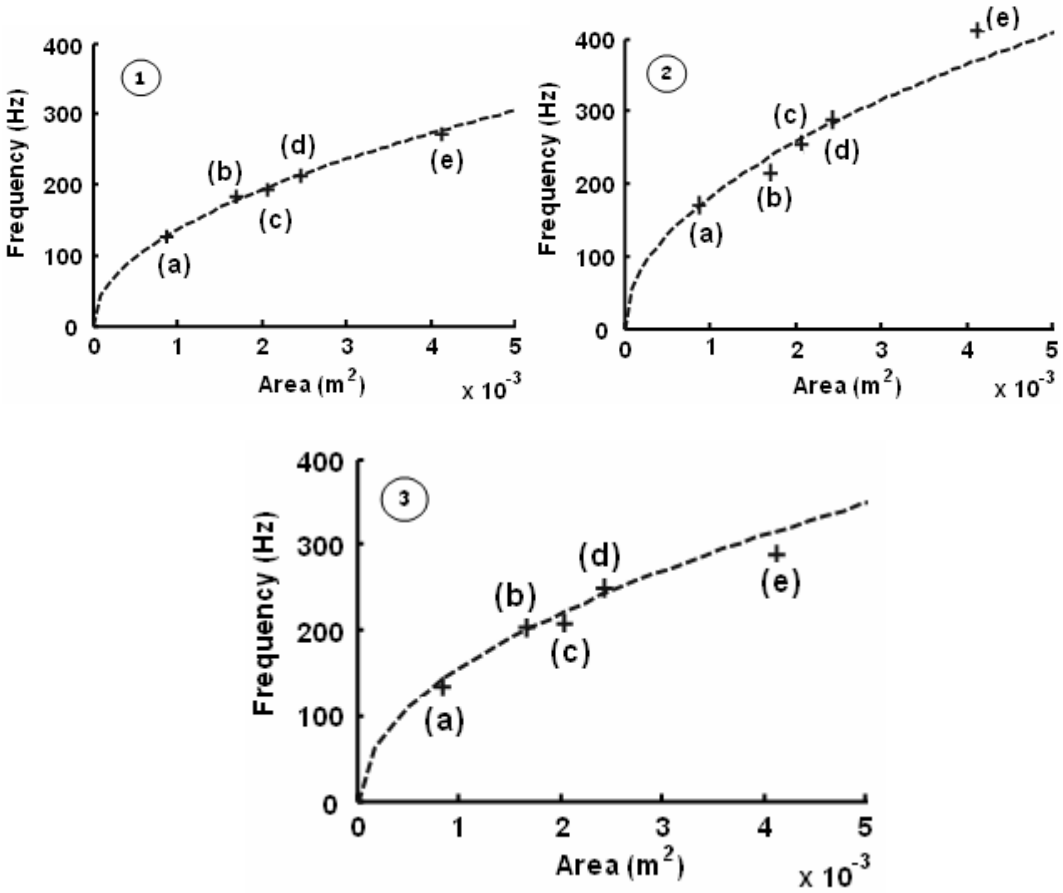

Figure 5-10: Comparison of theory (-----) and experiment (+) of "effective area" approach with (1) melamine foam, (2) polyamide, and (3) polyurethane. Measured are the natural frequencies of ball (a), coin (b), triangle (c), beam (d) and square (e).

In conclusion, the "effective area" approach was validated for three of the most commonly used porous media: polyamide, polyurethane and melamine foam. The results presented indicate a major step towards making the HG blankets a serviceable treatment for interior-noise control applications. Using this approach, the natural frequencies of the mass inclusions inside the HG blanket can be controlled entirely by changing the shape of the inclusion. This allows all of the inclusions to be placed on one layer, instead of varying the depth, and will make the blankets much easier to manufacture. In addition, the use of the "effective area" theory is not limited to a

certain type of melamine but is applicable to a variety of foams. Most importantly the proposed effective area approach, used to explain the natural frequency of different mass shapes with constant embedded mass in porous media, has a maximum error of 8% for all the predictions made in this paper.

5.2. An analytical model for the interaction of mass inclusions with the poro-elastic layer in heterogeneous (HG) blankets

The previous section introduced the "effective area approach" to determine the resonant frequencies of a mass inclusion glued on top of a poro-elastic layer acting as single dynamic vibration absorbers. The approach replaces the absorbers' stiffness k and determines the resonant frequencies of the dynamic vibration absorbers with $\omega = \sqrt{k/m}$. This can be achieved by obtaining an effective stiffness provided by the foam, which depends on the mass shape and poro-elastic material. Nevertheless, the approach does not include all effects contributing to the resonant frequency of the dynamic vibration absorber because the approach is too empirical. A novel approach has thus been developed, which is analytically derived from the basic model for poro-elastic materials proposed by Biot [52] and Allard [53] to backup and extend the existing effective area approach. The proposed analytical model offers far more options than the effective area approach. For example, the stress and displacement fields inside the porous material can be calculated. Furthermore, the solution includes not only the elastic properties of the material and influence of the mass shape but also the thickness of the poro-elastic layer.

After presenting the derivation of the model and its two different modelling strategies in the next section, the results and predictions of the model are shown with special regard to the effective stiffness and the stress and displacement fields inside the layer material of the HG blanket. An experimental validation of the effective stiffness prediction is also included.

5.2.1 Mathematical model

5.2.1.1. Simplification of the Biot-Allard model for poro-elastic materials

Since the beginning of the 20th century, the mechanics of poro-elastic media have been studied. Initial development came from the fields of geophysics and civil engineering, leading to models for fluid-saturated soils. Later models were extended to dynamics and the wave propagation inside the poro-elastic media, which not only included soil-like materials but also air-saturated foams. Papers concerning the development of models for fluid-saturated poro-elastic material have been published in large quantities. An overview can be found in Ref. [85] and [86]. In this work, the authors concentrate on a model which has originally been proposed by Biot in 1956 [52] and further developed by Allard [53] in 1993. This study assumes the material to be an elastic frame with a fluid saturating inside. The constitutive equations for the solid are written as follows when the summation convention is used:

$$\sigma_{ij} = 2G\varepsilon_{ij} + \left(K - \frac{2G}{3} \right) \delta_{ij}\varepsilon_{kk} - \alpha\delta_{ij} p \,, \tag{5-4}$$

where i,j = 1, 2, 3 (representing *x, y, z*), δ_{ij} is the Kronecker symbol (1 for $i = j$, 0 otherwise), σ_{ij} represents the components of the stress tensor and ε_{ij} represents the strain tensor (given by the derivative of the displacement vector **u**). G is the shear modulus of the material, K the bulk modulus and α accounts for the fact that the fluid inside the poro-elastic material contributes to the normal stresses with its pressure p. Shear stresses are not affected.

The first part of Eq. (5-4) (without $-\alpha\delta_{ij} p$) is the constitutive equation for a linear elastic, isotropic material, while the additional term couples the fluid and the frame phase. This coupling is the reason that it is difficult to model the poro-elastic material properly and that the equations of motion (which can be found in Ref. [53]) get rather complicated.

In the previous chapters, the HG blanket was modelled using a FE scheme proposed by Panneton and Atalla [57]. However, for HG blankets, the FE method offers limited grid resolution and requires very high computation times. These

disadvantages, and the understanding that for a fast and efficient optimization of HG blankets an easily manageable prediction of the effective stiffness is necessary, have led to the conclusion that the Biot-Allard model has to be reasonably simplified until an analytical and efficient solution can be obtained.

The assumption is made that the dynamic vibration absorber created by the interaction of mass inclusions and foam layer does not couple to the acoustic field, and its modelling, can be treated as a separate problem. This assumption has also been made by Kidner et al. [32]. Furthermore, it is assumed that the air and the elastic frame of the HG blanket are moving in phase at lower frequencies, and the air does not present a large amount of stiffness to the poro-elastic material. The interaction between fluid and frame is the main reason for energy dissipation and results in high frequency noise reduction [53,87]. However, because the noise reduction nearly disappears at low frequencies (only very thick foams still reduce low-frequency noise); the interaction is hardly present in this state. It is therefore assumed that no energy dissipation is provided by the interaction of fluid and frame.

Under these assumptions, the coupling between the fluid and the elastic solid phase of the poro-elastic material might be present but is likely negligible for low frequencies. Thus, the term $-\alpha\delta_{ij}p$ can then be neglected.

Under this condition, the constitutive equation of the poro-elastic material can be reduced to:

$$\sigma_{ij} = 2G\varepsilon_{ij} + \left(K - \frac{2G}{3} \right)\delta_{ij}\varepsilon_{kk} . \tag{5-5}$$

This simplified form of the stress-strain relationship represents a linear-elastic, isotropic material. It is not an accurate description of the HG blankets' foam layer for the whole frequency range since the bulk modulus of air is highly frequency dependent and the interaction between the elastic solid frame and its saturating fluid is a central characteristic of the poro-elastic medium. Yet, it is a valid assumption for the considered low frequency range up to about 500 Hz.

The obtained linear elastic and isotropic constitutive equation (5-5) will be used to develop a model to calculate the effective stiffness of the poro-elastic material and will also explain certain other aspects of HG blankets. However, since the layer

material is now described as linear elastic, the following modelling steps can be performed for all elastic (layer) materials. In order to highlight this generalization, the layer of the HG blanket will be referred to in this section as an elastic layer.

5.2.1.2. Modelling of the elastic layer with added mass

In order to complete the modelling of the elastic layer, kinematical relationships and equations of motion are necessary. However, for many applications it is assumed that the stiffness for a static state is the same as for a dynamic state when the material is considered linear-elastic and isotropic. The same assumption is made for the poro-elastic layer of the HG blanket. The further modelling process will focus on a static state. If a linear-elastic and isotropic material is assumed and volume forces (such as weight, which is a small influence in foam and many other elastic materials due to the low density) can be neglected, then the equilibrium conditions, the constitutive equations and the kinematical relationships can be combined to the Lamé-Navier equations [88],

$$\left(\lambda + G\right)\nabla\left(\nabla \cdot \mathbf{u}\right) + G\nabla^2\mathbf{u} = 0\,. \tag{5-6}$$

u represents the displacement vector, G is the shear modulus and λ is known as the first Lamé constant, which can also be represented by other elastic constants as shown in Table 5-4.

Although the material is now fully described, mass inclusions still have to be modelled. The following modelling steps describe the HG blankets as mass inclusions glued on top of the base layer instead of distributing them inside it, since this is very convenient for the manufacturing process. In order to model a mass inhomogeneity on top of a layer, a force acting in the z-direction (also denoted in this paper as "3-direction") is distributed over the mass shape's cross-sectional area. Two modelling strategies will be introduced in the next section. One with a constant force applied and one with a constant displacement applied in 3-direction.

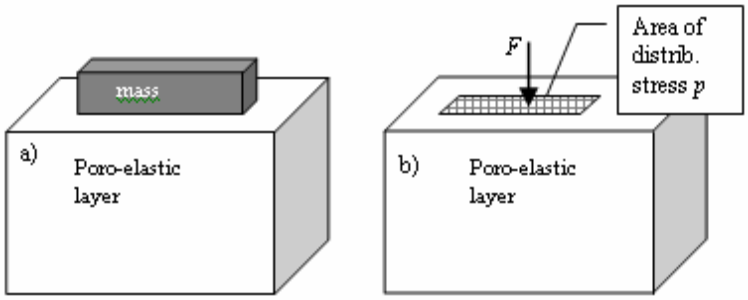

Figure 5-11: Schematic of the "real" HG blanket with a mass glued on top of a poro-elastic layer (a). Approximation with a force F distributed over the area of the mass leading to the pressure distribution *p* (b)

A direct analytical solution for the mentioned case is not known in literature, but a solution in analytical form can be obtained by modifying a principal solution to Eq. (5-6). This solution was discovered in the late 19th century by Boussinesq and describes a single force oriented in the 3-direction acting on the top plane of a three dimensional space, often called 3D "half-space" or "semi-infinite" space [88]. The coordinate system used is presented in Figure 5-12. The position of the force F applied at a point on top of the layer is described by the vector $\mathbf{x_f} = \{x_{1f}, x_{2f}, x_{3f}\}$ while the position of interest inside the material is described by the vector $\mathbf{x} = \{x_1, x_2, x_3\}$.

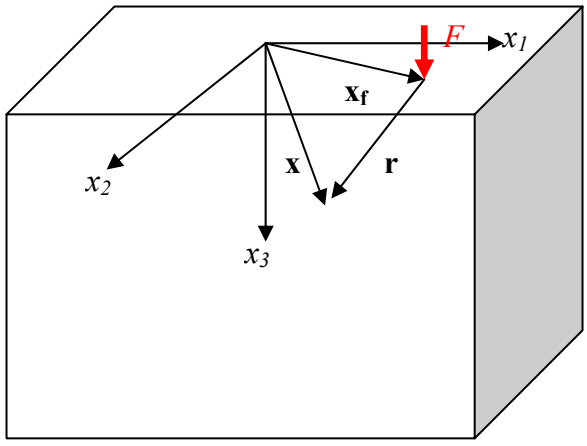

Figure 5-12: The coordinate system for the "3D Halfspace" of the Boussinesq solution. The force *F* is applied at a point whose coordinates are described with the vector $\mathbf{x_f}$, while the actual position in the material is marked by x. The vector $\mathbf{r} = \mathbf{x} - \mathbf{x_f}$ represents the difference of both vectors and has the magnitude *R*

Table 5-4: Linear elastic, isotropic material constants and their expressions in terms of modulus of elasticity E and Poisson´s ratio ν

Material constant	Abbreviation	Expression
Lamé´s constant	λ	$\lambda = \frac{\nu E}{(1+\nu)(1-2\nu)}$
Lamé´s constant	μ	$\mu = G = \frac{E}{2(1+\nu)}$
Shear modulus	G	$G = \mu = \frac{E}{2(1+\nu)}$
Bulk modulus	K	$K = \frac{E}{3(1-2\nu)}$

The Boussinesq solution directly presents the displacement and stress field for the whole body and includes the boundary conditions (e.g. the top plane of the 3D "half-space" has to be stress-free in the 3-direction). The displacement in the 3-direction created by the applied force in the 3-direction is

$$\hat{u}_3 = \frac{F}{4\pi GR}\left[2(1-\nu) + \frac{\left(x_3 - x_{3f}\right)^2}{R^2}\right]. \tag{5-7}$$

F is the single force applied, G represents the shear modulus of the material and ν is Poisson´s ratio, x_3 is the actual position in the 3-direction inside the material (the "z"-coordinate), and x_{f3} is the position of force application in the 3-direction while $R = |\mathbf{x} - \mathbf{x_f}|$ (see Figure 5-12) is the distance from the applied force. Also, the normal stress in the 3-direction is given by:

$$\hat{\sigma}_3 = -\frac{3F\left(x_3 - x_{3f}\right)^3}{2\pi R^5}. \tag{5-8}$$

The negative-sign is a result of the fact that compressive stresses are defined negative, and that a force in the positive 3-direction creates a compressive normal stress

in the 3-direction (see coordinate system in Figure 5-12). The displacement in the 3-direction is essential because it will be used to define the effective stiffness. The stresses in the 3-direction are important at the plane where the foam material is glued onto the fuselage, while all other less important displacement and stress components can be found in Ref. [88].

The elastic layer with its force on top is now described as a "semi-infinite" space with an applied force. In real HG blankets the size in the 1- and 2-direction is clearly not infinite but the assumption of "semi-infinite" is reasonable since the stresses decline very fast ($\sigma \propto 1/R^2$) and therefore can be neglected after a certain distance between force application and point of interest. Boundaries have little effect if they are in the range of very low stresses, which is the case for most HG blanket applications where the masses normally are applied away from boundaries. The reason is that for the targeting of low order modes the masses are typically placed near the middle of the plate. Nevertheless, the model has to include the boundary in the 3-direction between the blanket layer and the fuselage plate. This boundary will be represented as rigid since the static model does not cover dynamic boundaries. The rigid boundary represents the limited thickness *d* of the elastic layer of the HG blanket. The correct modelling of HG blankets requires the introduction of boundaries in the Boussinesq solution. The "free" surfaces of the blanket have to be stress free while the base of the blanket can be modelled as rigid in the static case. In order to create a rigid boundary in the Boussinesq solution, an image of the original force is applied at $x_{3f} = 2d$ in the opposite direction. This method is referred to as the "image method." Figure 5-13 shows how the image is applied in the material and where the rigid boundary can be seen. This "image" force leads to the disappearance of the displacement in 3-direction at $x_{3f} = d$ and therefore induces the rigid boundary correctly.

The geometry of Figure 5-13 will assume: $x_{f3} = 0$ for F_1 and $x_{f3} = 2d$ for F_2 and $F_2 = F_1$. Then the displacement in 3-direction in general is given by

$$u_3 = \frac{F_1}{4\pi G R_1}\left[2(1-\nu) + \frac{x_3^2}{R_1^2}\right] - \frac{F_2}{4\pi G R_2}\left[2(1-\nu) + \frac{(x_3 - 2d)^2}{R_2^2}\right]. \qquad (5\text{-}9)$$

Where $R_1=|\mathbf{r_1}|$ and $R_2=|\mathbf{r_2}|$. Therefore, the resulting 3-direction displacement at the rigid boundary $x_3 = d$ is zero, regardless of the values of x_1 and x_2, and this satisfies the boundary condition, As a consequence of the method, the solution gained by the superposition of two opposing forces can only be used for $0 \le x_3 \le d$. In direct analogy to the approach made above, it is possible to show that all stress components disappear at the rigid boundary when the image method is used, except the stresses in 3-direction, which double their value and are solely responsible for maintaining the force balance. This behaviour must be expected for a correct representation of a rigid boundary and is successfully implemented by using the image method.

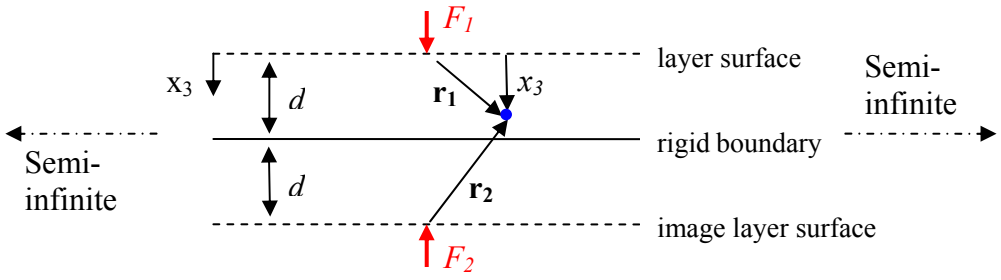

Figure 5-13: The Image method leads to the introduction of a limited layer thickness d when $|F_1| = |F_2|$

The stress expression in general can be written analougus to the above shown equation, such as:

$$\sigma_3 = -\frac{3F_1(x_3)^3}{2\pi R_1^5} + \frac{3F_2(x_3 - 2d)^3}{2\pi R_2^5}. \qquad (5\text{-}10)$$

Therefore, one disadvantage of the method is that the "image" force creates stresses at the boundary at $x_3 = 0$ disagreeing with the stress free condition as the stress in that case is not zero. Nevertheless, this stress is negligible when the foam layer thickness d is large enough, which is normally the case for HG blankets, where the layer is thicker than 0.02 or 0.03m.

In order to describe the interaction between a mass inclusion and the blanket material it is necessary to distribute the applied force over the cross-sectional (projected) area of the mass. This is best described by a pressure p, which can be

constant or a function of a coordinates x_1 and x_2. This pressure acts on the masses cross-sectional area A in the 3-direction (see Figure 5-12). If the pressure p replaces the single force F in Eq. (5-7) and Eq. (5-8) then the solution must be integrated over the cross-sectional area of the mass to obtain the resulting displacement. Therefore, the compliance V is defined as

$$V(\mathbf{x},\mathbf{x_f}) = \frac{u_3}{F} = \frac{1}{4\pi Gd}\left[2(1-\nu) + \frac{x_3^2}{R_1^2}\right] - \frac{1}{4\pi Gd}\left[2(1-\nu) + \frac{(x_3-2d)^2}{R_2^2}\right] \qquad (5\text{-}11)$$

,

this essentially allows the displacement in 3-direction to be expressed anywhere in space as an integral over the surface area:

$$u_3(\mathbf{x}) = \int_A V(\mathbf{x},\mathbf{x_f})\, p(\mathbf{x_f})\, dA\,. \qquad (5\text{-}12)$$

A "stress to force ratio" term is defined analogous to the compliance V, where

$$Q(\mathbf{x},\mathbf{x_f}) = \frac{\sigma_3}{F} = -\frac{3(x_3)^3}{2\pi R_1^5} + \frac{3(x_3-2d)^3}{2\pi R_2^5}\,. \qquad (5\text{-}13)$$

Thus, the stress in 3-direction can now be computed anywhere in space as

$$\sigma_3(\mathbf{x}) = \int_A Q(\mathbf{x},\mathbf{x_f})\, p(\mathbf{x_f})\, dA\,. \qquad (5\text{-}14)$$

Numerical evaluation of displacement and stress in 3-direction

The above derived equations (5-12) and (5-14) are the analytical solutions for the diaplacement and stress in 3-direction for any point inside the layer due to a distributed pressure applied at the surface. In order to be able to solve these equations it is most convenient to evaluate the integral numerically and the surface will therefore be divided in $i=1...I$ elements such that the numerical solution for the displacement can be approximated as

$$u_3(\mathbf{x}) = \sum_i V(\mathbf{x},\mathbf{x_{if}})\, p(\mathbf{x_{if}}) S_i\,, \qquad (5\text{-}15)$$

And the numerical solution for the stress is then:

$$\sigma_3(\mathbf{x}) = \sum_i Q(\mathbf{x}, \mathbf{x_{if}})\, p(\mathbf{x_{if}}) S_i \,. \tag{5-16}$$

where S_i is the surface area of each element i and p_i is the pressure applied on the surface of each element S_i.

Numerical evaluation of effective stiffness

The effect of one mass placed on top of the poro-elastic layer can be approximated by a single degree of freedom dynamic vibration absorber with a spring whose effective stiffness is provided by the elastic layer material. The spring stiffness of a dynamic vibration absorber is assumed constant for the static and dynamic case and can be written statically as a force over deviation of the spring: $k = F/u_3$. In direct analogy the effective stiffness calculated by the proposed model for the elastic layer will be defined as an applied force over a displacement of the area of the distributed force:

$$k_{eff} = \frac{F}{u_{avg}} \,. \tag{5-17}$$

The elastic layer is assumed to be massless, thus, there is no need to define an "effective mass" analougus to the "effective stiffness". The force can then be approximated by:

$$F = \sum_i p_i S_i \,. \tag{5-18}$$

The resulting displacement is introduced by u_{avg} using Eq. (5-7) such that:

$$u_{avg} = \frac{\sum_i u_{3i} S_i}{A} \,, \tag{5-19}$$

where A represents the cross-sectional area of the mass.

The displacement and force at the surface are dependent and related to each other by Eq. (5-11). Therefore, the displacement at all the elements can be decribed as a vector **u** which is related to the pressures **p** through the I by I compliance matrix **V** such that:

$$\mathbf{u} = \mathbf{V}\mathbf{p}\,, \tag{5-20}$$

where surface of the elastic layer under the mass is split up into *i= 1...I* small identical rectangular elements with coordinates $x_{1,i}$ and $x_{2,i}$ and side lengths of Δx_1 and Δx_2. The displacement and pressure vectors, respectively, are then:

$$\mathbf{u} = \{u_1, u_2 ... u_I\}\,,\ \mathbf{p} = \{p_1, p_2 ... p_I\}\,, \tag{5-21}$$

where the compliance matrix includes the surface area of the rectangular elements such that:

$$V_{ij} = V(x_i, x_{jf})\Delta x_1 \Delta x_2\,. \tag{5-22}$$

for each matrix element *ij*. Since all evaluations of the model use Eq. (5-7) as a basis to calculate the effective stiffness, a singularity of the equation, and therefore of the diagonal matrix elements of the matrix **V,** occurs when the displacement has to be evaluated at $R = 0$.

Essentially, the approach is to replace $R = 0$ (see Eq. (5-7)) of the singular elements V_{ii} in Eq. (5-22) with an effective radius to generate an equivalent displacement at the center of the evaluation element due to the pressure over that element. The required displacement due to a constant pressure over the element´s surface can be found analytically by replacing the rectangular element with an equivalent circular element. When the constant pressure *p* is applied on the element, u_3 Eq. (5-7) for a general element of area S can be written as

$$u_3 = \frac{1-\nu}{2\pi G}\int_S \frac{p}{R} ds\,. \tag{5-23}$$

For the general case, *R* may be a complicated function of the location of the element *ds*. However, if the area in question is a circle and the displacement in the center is evaluated, one gets $ds = Rd\varphi dr$ and the integral becomes

$$u_3 = \frac{1-\nu}{2\pi G}\int_S \frac{p}{R} ds = \frac{1-\nu}{2\pi G}\int_0^a \int_0^{2\pi} \frac{p}{R} Rd\varphi dr = \frac{1-\nu}{G} ap\,, \tag{5-24}$$

with the radius of the circular element *a*. The total force of the circular element F_{el} is given by

$$F_{el} = \int_S p ds = \pi a^2 p \,. \tag{5-25}$$

u_3 is then

$$u_3 = \frac{1-\nu}{G}\frac{a}{\pi a^2} F_{el} = \frac{1-\nu}{\pi a G} F_{el} \,. \tag{5-26}$$

If the circular area is chosen to be the same as the rectangular elemental area $\pi a^2 = \Delta x_1 \Delta x_2$, then $a = \sqrt{\Delta x_1 \Delta x_2 / \pi}$. Substituting this into the equation for u_3 and considering that $F_{el} = p\pi a^2 = p\Delta x_1 \Delta x_2$, leads to

$$u_3 = \frac{1-\nu}{\pi a G} F_{el} = \frac{1-\nu}{2\pi G}\frac{F_{el}}{\frac{a}{2}} = \frac{1-\nu}{2\pi G}\frac{p\Delta x_1 \Delta x_2}{\sqrt{\frac{\Delta x_1 \Delta x_2}{4\pi}}} \,. \tag{5-27}$$

By comparing this equation to Eq. (5-23), it can be seen that the displacement in the center of the rectangular singular element can be approximated by assuming an effective radius of

$$R_{eff} = \sqrt{\frac{\Delta x_1 \Delta x_2}{4\pi}} \,. \tag{5-28}$$

This effective radius is applied to all singular elements in the Eq. (5-11), where the **V** matrix shown in (5-20), can be evaluated at $R = 0$. However, the assumption of an effective radius is only valid for very small and square element sizes Δx_1 and Δx_2, which has been considered for the computation of the results in this section.

In order to evaluate Eq. (5-17) to obtain an effective stiffness, two approaches are proposed. One applies a constant pressure on the blanket surface across the projected area of the mass using Eqs. (5-18) and (5-19) (strategy #1) and the other specifies a constant displacement of the mass (stategy #2).

If a desired pressure distribution $\mathbf{p_{des}}$ is specified, in our case a constant pressure, then Eq. (5-20) can be directly used to calculate the resultant displacements **u** (this implies that the mass bends and is essentially limp). Once the pressure and displacements under the mass are calculated an effective stiffness can be calculated using Eqns. (5-17), (5-18) and (5-19).

If the force on top the elastic layer is applied evenly (strategy #1), the resulting displacement of the mass's cross-sectional area is not constant but shows approximately a quadratic form, which can be seen in Figure 5-14.

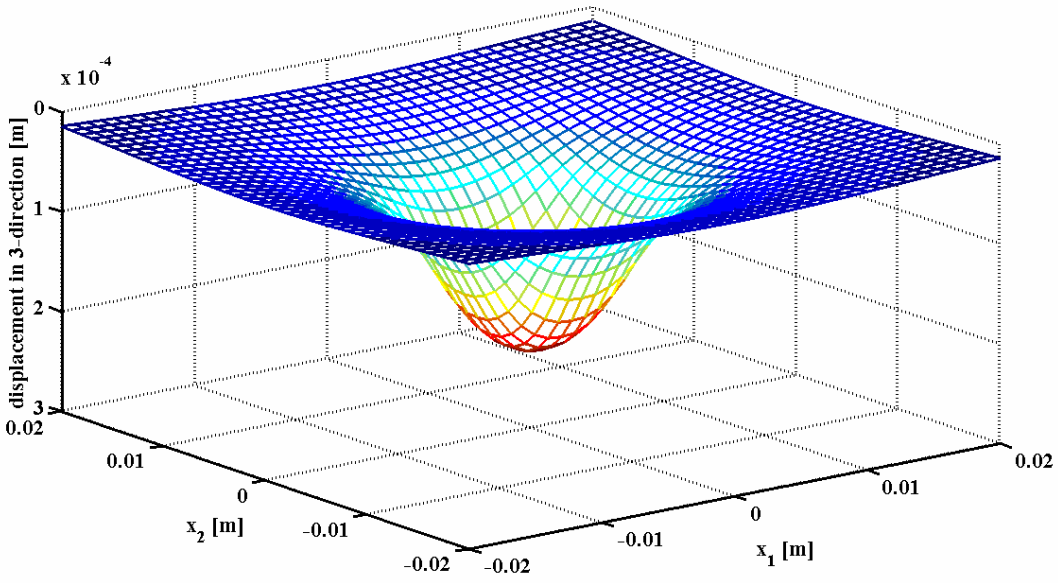

Figure 5-14: Simulation of the displacement in 3-direction when a force of 1N is distributed over an area of 0.01m x 0.01m

For the second strategy, a displacement distribution $\mathbf{u}_{\mathbf{des}}$ is specified, which for the case of constant displacement is simply an I length vector of velocities u_{des}. In this case the resulting pressures can be calculated as

$$\mathbf{p} = \mathbf{V}^{-1}\mathbf{u}_{\mathbf{des}} . \tag{5-29}$$

Since $\mathbf{V}$ is not singular, $\mathbf{p}$ can easily be computed. Again, once the pressure and displacement distributions are known then the effective stiffness can be calculated using Eqns. (5-17), (5-18) and (5-19).

It will be shown in the next section that both modelling strategies lead to nearly the same results, when the prediction of the effective stiffness is considered.

5.2.2 Results

With the help of the displacement field and stress field of the model, it is possible to describe many properties of the HG blanket as well its behavior. These results and a comparison of the two modelling strategies described in the last section will be presented in the following sections, starting with the prediction of the effective stiffness and leading to a description of the interaction between two masses on top of an elastic layer.

5.2.2.1. Effective stiffness

In this section, the most important parameters influencing the effective stiffness will be analyzed: The geometry of the mass and the thickness of the blanket layer. The material parameters used in both strategies can be found in Table 5-5.

Table 5-5: Material values for evaluation of influence parameters on the effective stiffness

Parameter	Value
Thickness of foam layer	0.051 m except when noted otherwise
Modulus of Elasticity E	380000 N m^{-2} except when noted otherwise
Poisson´s ratio v	0.3

A higher cross-sectional area of the mass leads to the deformation of more layer material. Therefore, the effective stiffness will increase since it is provided by the interaction between the mass inhomogeneity and the blanket. This effect can be seen in Figure 5-15.

The cross-sectional areas, natural frequencies, and effective stiffnesses for the experimental validation of the model are presented in Table 5-6. Experiments have been conducted using a shaker (similar to section 5.1.1.2) with a mass glued on top of a poro-elastic layer to measure the transfer functions and natural frequencies of masses with different shapes and areas. The experimental stiffness has been calculated from the measured natural frequencies (deviation of ± 6 Hz) by evaluating the analogy of the

described setting with a single dynamic vibration absorber. The experiments were conducted using melamine foam with the modulus of elasticity E = 320000 N m^{-2}.

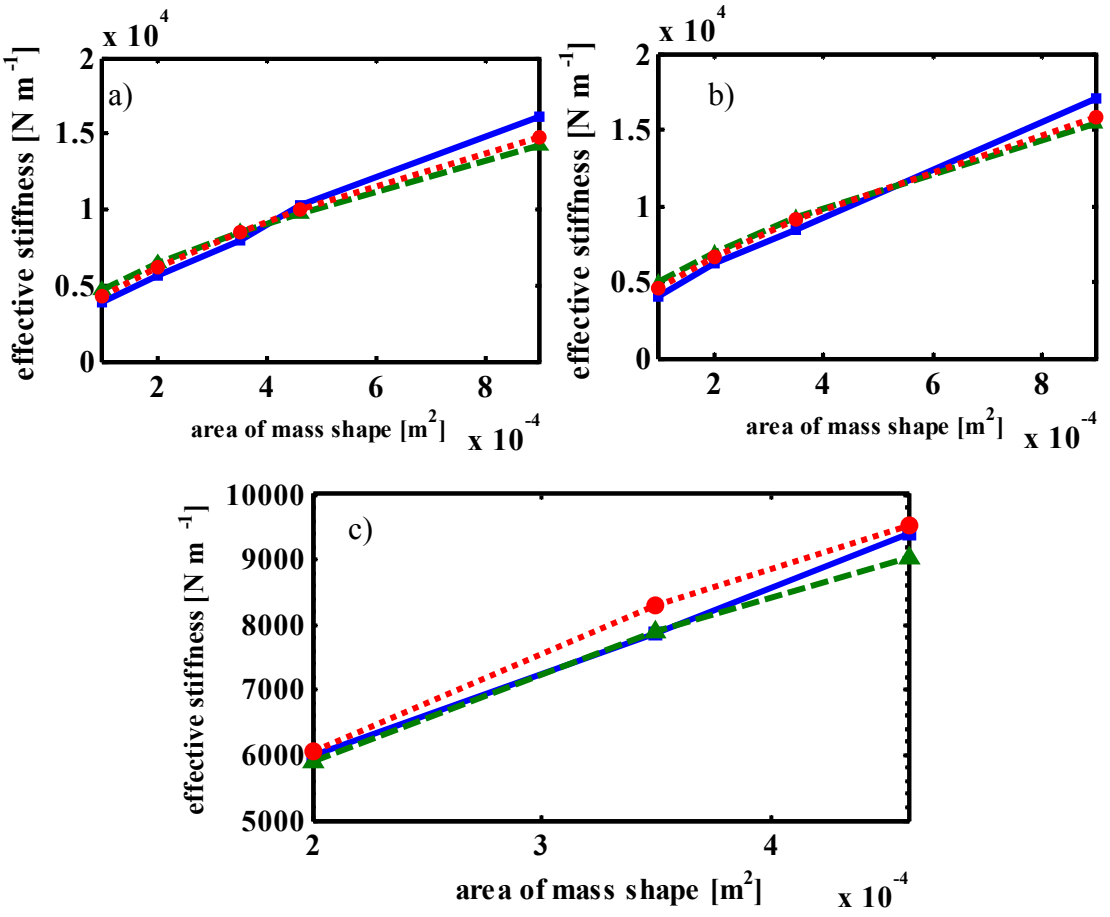

Figure 5-15: Change of the effective stiffness with the area of the mass shape. A comparison between measurements (—), predictions of the constant pressure (- - -), and constant displacement (···) model is included for all mass shapes. Part (a) shows the square mass shape, part (b) the rectangular shape with a side length ratio of 1:3, and part (c) the circular shape.

Both modelling strategies hardly diverge from each other and match experiments well. Two significant conclusions can be drawn. The first conclusion is that the stiffness does not linearly increase with the cross-sectional area *A*, as might be suspected at first glance. Instead, the effective stiffness can be approximately described as directly proportional to the square-root of the area for the presented area range

$k_{eff} \propto \sqrt{A}$. The second conclusion is that the mass shape also has an influence on the stiffness, even if the cross-sectional areas are identical. A circular shape leads to less stiffness than a square shape, which has less stiffness than a rectangular shape with side length ratios $L = a/b > 1$. This is because the rectangular shape deforms more layer material than the circular and square shapes. A more detailed study with the analytical model leads to Figure 5-16(a), where the effective stiffness is calculated for a fixed cross-sectional area while the side length ratio changes from 1 to 5.

Table 5-6: Comparison between experimental effective stiffness and the predictions of both modelling strategies for the effective stiffness of square, rectangular, and circular mass shapes with different cross-sectional areas

Cross-sectional area [m^2]	Measured stiffness [N m^{-1}]	Constant pressure strategy [N m^{-1}]	Constant displacement strategy [N m^{-1}]
	Square shape		
0.0001	3943	4652	4298
0.0002	5590	6409	6248
0.00035	7973	8501	8535
0.00046	10333	9789	9941
0.0009	16064	14196	14726
	Rectangular shape (side length ratio 1 : 3)		
0.0001	4067	5007	4580
0.0002	6222	6916	6669
0.00035	8447	9244	9123
0.0009	17023	15437	15783
	Circular shape		
0.0002	6000	5903	6064
0.00035	7869	7892	8299
0.00046	9416	9046	9521

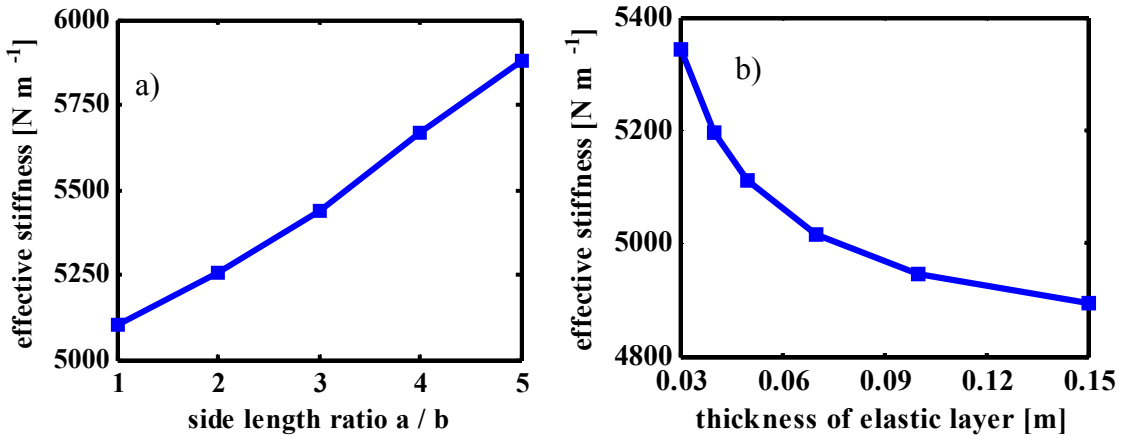

Figure 5-16: Part a) Dependence of the effective stiffness on the side length ratio *a*:*b* of an rectangular mass shape. Part b) Dependence of the effective stiffness on the thickness of the poro-elastic layer of the HG blanket. The cross-sectional area of the mass is 0.0001 m^2. The evaluation is done with the constant displacement strategy.

The effective stiffness varies with the side length ratio *a*/*b*: The most elongated mass piece leads to a nearly 20 percent higher stiffness than that of a square shaped piece. This effect is very useful for tuning the mass inhomogeneity to a certain natural frequency of the fuselage by simply varying the side length ratio while keeping its area and mass constant. An additional benefit is the fact that the relationship between length ratio and effective stiffness is approximately linear.

An important influence on the effective stiffness is the thickness of the poro-elastic layer, which was based on experimental results in the previous section. The proposed analytical model in this section takes the thickness of the poro-elastic layer into account. Figure 5-16(b), shows that the effective stiffness increases with decreasing layer thickness. This behavior is not unique to HG blankets, for example, the stiffness of a rod with cross-sectional area *A*, length *l* and modulus of elasticity *E* is defined as $c = EA/l$. If the length *l* is reduced the stiffness increases. The more material is available, the more deformation is possible. The poro-elastic layer act in same way: When *l* is representative of its thickness while its other geometry and elastic behavior is similar to *EA*, its effective stiffness will increase with decreasing thickness. Figure 5-16(b) also shows that when the thickness passes a certain limit the stiffness hardly changes anymore. This is because the mass only influences and deforms a finite

volume of embedding material. If this volume is not limited by the boundaries, the further increase of the thickness does not lead to the deformation of more material, thus the effective stiffness remains the same. The effects of changing the thickness of the elastic layer and the area of a square-shaped mass have been evaluated using the model with the constant displacement strategy and plotted on different axes in Figure 5-17.

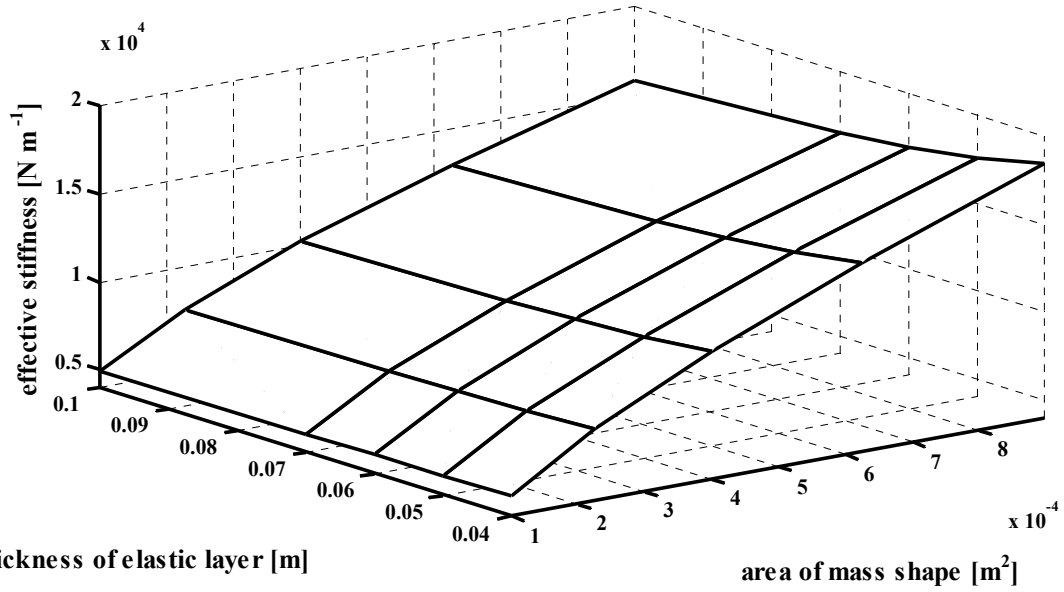

Figure 5-17: Prediction of the effective stiffness based on the thickness of the poro-elastic layer and the area of a square-shaped mass

For a constant thickness, the dependence of the effective stiffness on the area takes the same square root shape as in Figure 5-15, while for a constant area the dependence on the thickness shows a relationship similar to Figure 5-16(b). Figure 5-17 shows that this is valid for all combinations and leads to the assumption that both relationships can be superposed by multiplying the single influences. Furthermore, it can be taken into account that the relationship between the side length ratio and the effective stiffness is approximately linear, and that the effective stiffness is directly proportional to the shear modulus G, and therefore also directly proportional to the modulus of elasticity E. The combination of all these relationships has led to the following formula for a rectangular mass inclusion:

$$k_{eff} = E \cdot d^{-0.122} \cdot \sqrt{A} \cdot \left(1 + 0.03\left(L - 1\right)\right), \tag{5-30}$$

in which k_{eff} is the effective stiffness, d the thickness of the elastic layer, A the cross-sectional area of the mass and L the side length ratio $L = a/b$.

The formula has been developed iteratively, evaluating predictions of the model with the constant displacement strategy for melamine foam with the material parameters presented in Table 5-5. This simplified equation is not a perfectly precise prediction, but nevertheless the relative deviation between effective stiffness predictions of the model and the simplified equation does not exceed 11%. Since the maximum error of 11% for the effective stiffness only leads to an error of about 5% in the natural frequency of the mass inclusion, the error is acceptable for first steps in the tuning process of HG blankets, as long as only a low frequency range of up to about 400 Hz is considered.

The usage of one single simplified equation for the prediction of the effective stiffness can be beneficial, especially when an approach is chosen which follows in its basic form Eq.(5-30), but allows the application to different materials by "free values":

$$k_{eff} = E \cdot \delta \cdot d^{-\alpha} \cdot A^{\beta} \cdot \left(1 + \gamma\left(L - 1\right)\right), \tag{5-31}$$

while the notation is the same as in Eq. (5-30), the constants α, β, γ and δ represent the new degrees of freedom which allow the application of the formula to be considered for different materials. They can be evaluated by conducting experiments or from the model. Eq. (5-31) is a direct consequence of the novel analytical model and could be seen as its equivalent to the formerly developed effective area approach introduced in section 5.1.2.2. While the effective area approach has been experimentally validated using two degrees of freedom, the new approach has four, as the model includes more influence parameters, e.g. the thickness of the blanket.

5.2.2.2. Mass interaction

Another huge advantage of the analytical model is that the complete displacement and stress fields inside the layer can be predicted when distributed forces are applied to simulate the mass inhomogeneities. While the displacement field can be used to define and calculate the effective stiffness, the stress field gives insight to the

interaction between two (or more) masses which are applied onto the same layer. Since it must be assumed that for an efficient tuning of HG blankets more than one mass may be necessary it is important that this mass interaction be studied. Finite element calculations were performed in section 5.1.2.2, which led to the conclusion that masses interact with each other when placed close together and their interaction increases with decreasing distance. This critical distance is denoted as "mass-interaction distance" and will be the main subject of this section.

Since the analytical model represents a static solution to the description of the poro-elastic layer, the dynamic behavior cannot be included. The dynamics of the poro-elastic layer will certainly determine its stress field, but a qualitative approximation can be done with the static model discussed in this work. The most important stress is the normal stress in the 3-direction, for it determines the pressure on the fuselage (the "rigid" boundary) and thus the effect of the mass-created dynamic vibration absorber on the fuselage-plate. Therefore, only the stress in 3-direction will be shown here. Also, the mass interaction effects directly follow from the interaction of the stress fields of both masses.

The stress distribution for the two masses is shown in Figure 5-18. The masses hardly interact with each other in the whole poro-elastic material, which can be seen from the very small stress values (200 Pa or even just 100 Pa compared to the applied stress of 10^4 Pa) in the middle plane between the masses. There is a small interaction on the base plate, however, the stresses in between the masses are far smaller than the stresses directly below the masses (less than 200 Pa to over 550 Pa). The exact values should always be seen in comparison to the applied pressure, but a tendency is clearly visible. If the distance between the two masses exceeds a certain value (in Figure 5-18, 0.08 m) the interaction will be negligible. This distance between the two masses is the critical "mass-interaction distance" which has been conceptualized in section 5.1.2.2. If the mass distance falls below the critical distance, the displacement and stress of one mass affects the second mass leading e.g. to a change in the stiffness provided by the second mass and vice versa. Figure 5-19 presents similar plots to Figure 5-18, but the distance between the masses is only 0.03 m instead of 0.08 m.

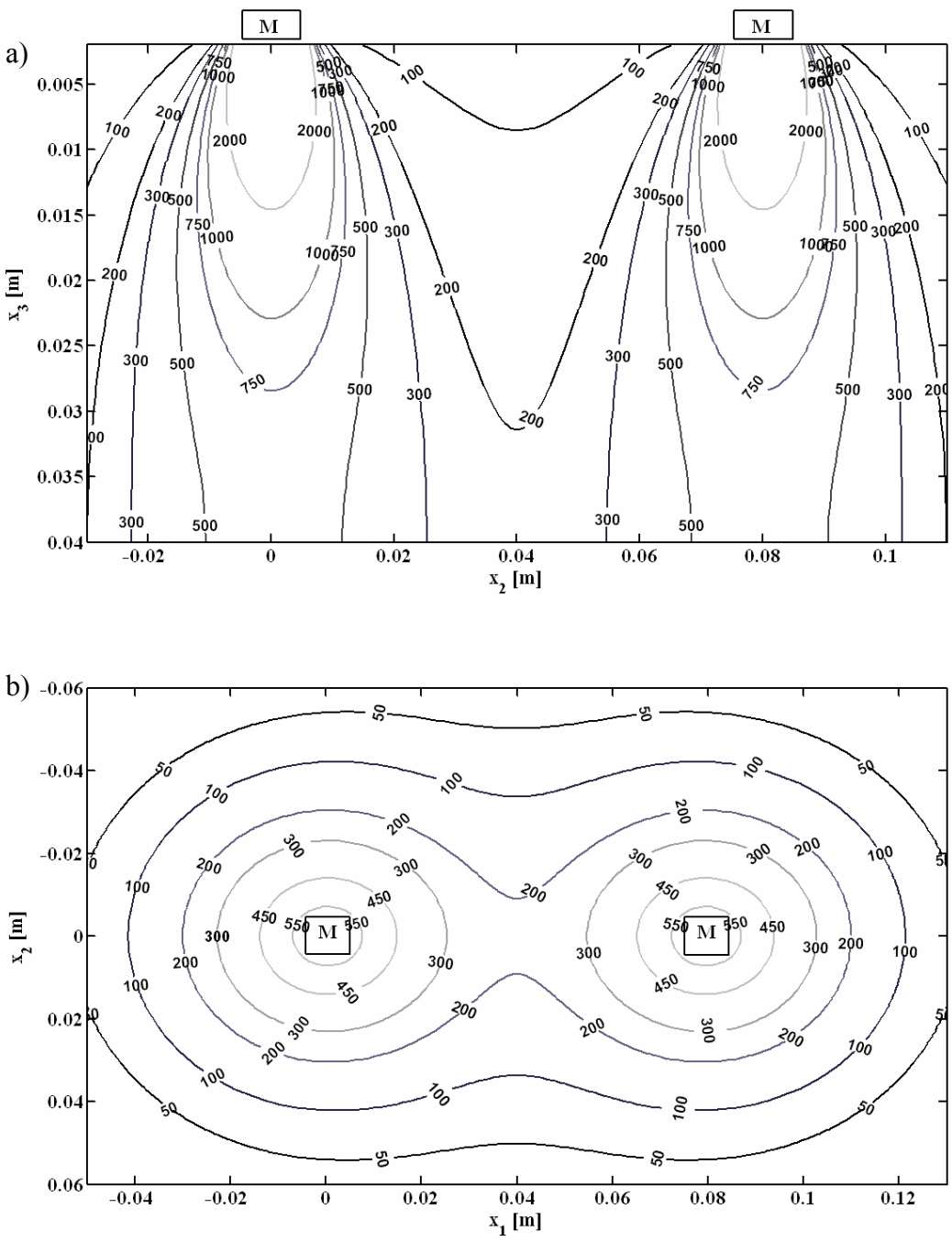

Figure 5-18: Contour plots of the compressive stress in 3-direction (in Pa) for two applied masses on top of a poro-elastic layer of 0.04 m thickness. Both masses are represented by a pressure $p = 10^4$ Pa applied on an area of 0.01 m * 0.01 m and their middle points are 0.08 m away from each other and symbolized in the plots as black quadrangles. Part (a) shows the x_2-x_3 plane at $x_1 = 0$ ("side view" of the layer) while part (b) shows the stress distribution in the x_1-x_2-plane at $x_3 = 0.04$ m ("top view" onto the base-plate or fuselage)

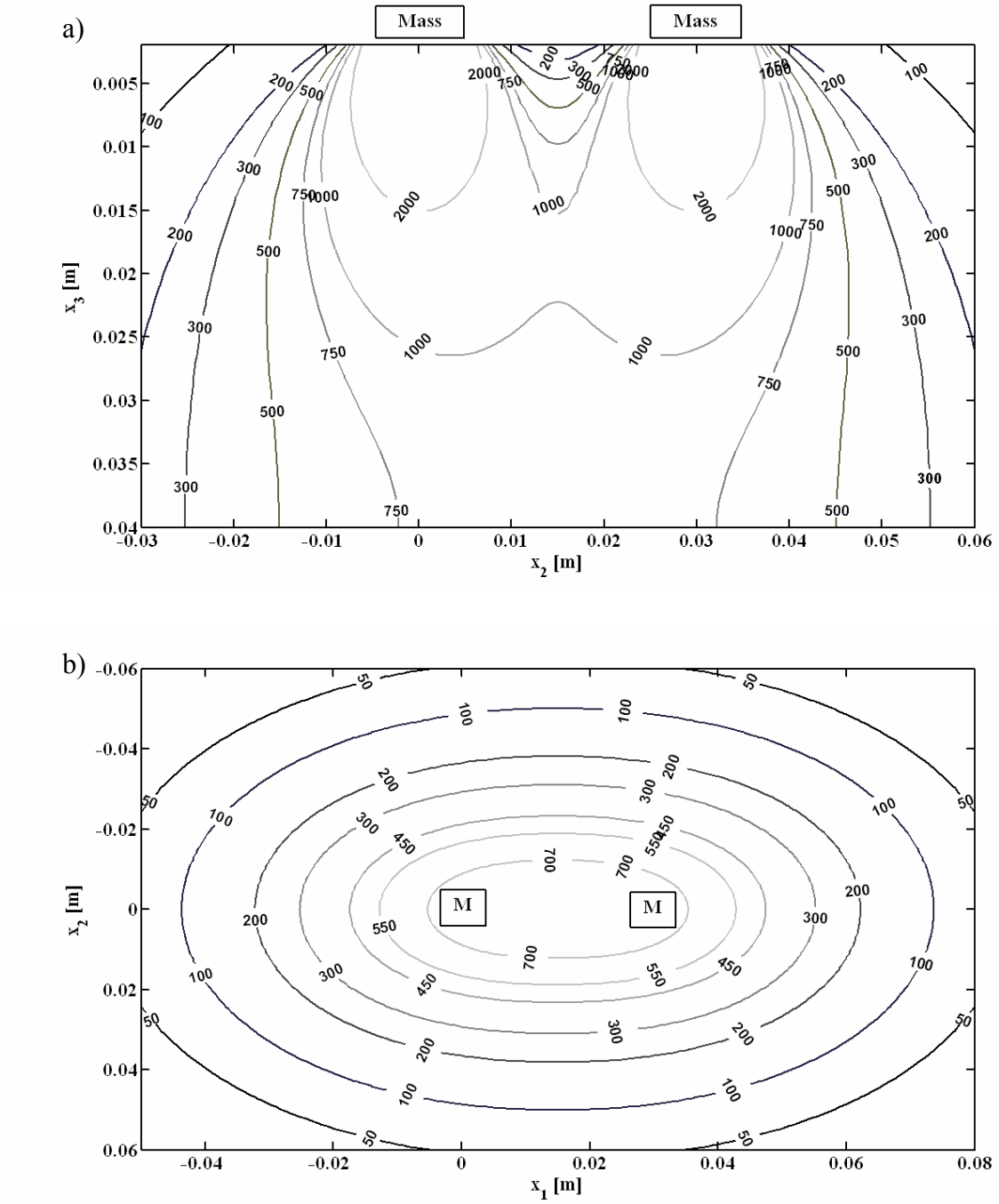

Figure 5-19: Contour plots of the compressive stress in 3-direction (in Pa) for two applied masses on top of a poro-elastic layer of 0.04 m thickness. Both masses are represented by a pressure $p = 10^4$ Pa applied on an area of 0.01 m * 0.01 m and their middle points are 0.03 m away from each other and symbolized in the plots as black quadrangles. Part (a) shows the x_2-x_3 plane at $x_1 = 0$ ("side view" of the layer) while part (b) shows the stress distribution in the x_1-x_2-plane at $x_3 = 0.04$ m ("top view" onto the base-plate or fuselage)

The stress fields created by the masses overlap, which leads to huge interactions. On the base plate (at $x_3 = 0.04$ m), the stresses are completely converged to a single distribution so that the masses act as one. Qualitatively the stress distribution for a long single mass looks alike.

In conclusion, both masses can be treated independent from each other when the critical "mass-interaction distance" is exceeded. Furthermore, the stresses are independent from the shear modulus (see Eq. (5-8)), indicating that the critical distance is not affected by the material itself as long as the assumption, to model the HG blanket as linear isotropic material, is valid. However, as soon as the masses are applied too close to each other they will strongly interact leading, for example, to changes in the effective stiffness.

6. EXPERIMENTS ON A GULFSTREAM FUSELAGE SECTION

This section gives an overview of the experiments conducted to demonstrate the effectiveness of optimized HG blankets used to reduce the interior noise levels of civil aircraft. These experiments are the final work of this thesis.

6.1. Preparation of fuselage measurements

The objective of these tests is to compare the sound transmitted through the fuselage using two different passive noise control treatments (poro-elastic material vs. HG blankets). A section of a Gulfstream fuselage formerly used in experiments with Helmholtz resonators will be used for these experiments. Figure 6-1 shows the outside of the Gulfstream section which is 10.7' long with a diameter if 8.2'. Shown is also the end cap on the front as well as on the back (not visible in the picture).

Figure 6-1: Section of a Gulfstream fuselage

Since the Gulfstream fuselage was used approximately 10 years ago for Helmholtz resonator experiments, it had to be modified for the final HG blanket measurements. Figure 6-2 shows the fuselage before (a) and after (b) the modifications. The Helmholtz resonator experiments required an internal frame attached only to the base to isolate the trim from the fuselage vibration. These internal frames were removed. Additional screws on the fuselage were removed and holes due to corrosion were filled out with paste. All windows were reinsulated with rubber mass. The

fuselage interior surface was grinded and cleaned. To decrease the floor vibration, the mass of the floor was increased with an additional MDF board. In addition, the space between the floor and the 1st layer of MDF was filled with fiberglass.

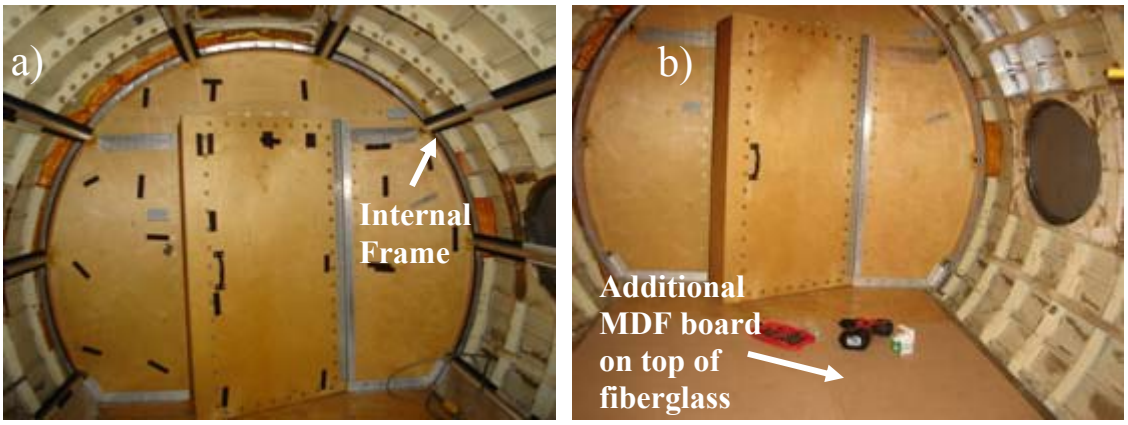

Figure 6-2: Gulfstream fuselage section before (a) and after (b) preparation for final measurements

Figure 6-3 presents the 2'' thick melamine foam cut-outs that were be used to build the HG blankets. All blocks were numbered using an indexing system of the fuselage interior created with a CAD model.


Figure 6-3: Poro-elastic cut-outs

To measure the interior sound pressure level with the different experimental configurations, a microphone array had to be designed. The array was designed to accurately record frequencies up to 550Hz. Several possibilities were discussed and

eventually the arrangement shown in Figure 6-4 a) was chosen. The main constraint was to avoid aliasing, which means that the maximum distance between the microphones and the trim panel had to be a half of the smallest wavelength. Because the smallest wavelength is inversely proportional to the frequency, this constraint would specify the upper wavelength limit. The array was mounted to the floor and was moved to six different locations along the center line of the fuselage to capture the whole cylindrical space. The array was turned 180 degrees after each measurement to measure both sides of the fuselage interior. Figure 6-4 shows a picture of the microphone array inside the Gulfstream fuselage.

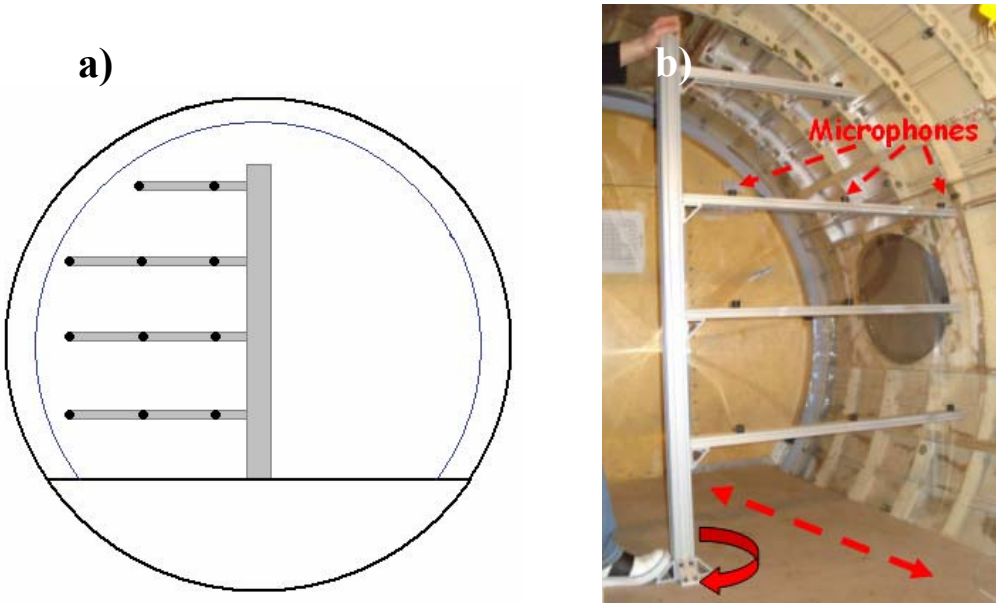

Figure 6-4: Drawing of the microphone array, microphones marked with black dots (a) and real microphone array (b) for full scale fuselage measurement

Figure 6-5 presents the side view of the aircraft interior. The mounts (i) used to connect the fuselage with the trim panel are neoprene bubble mounts, which are similar to those used in the multi-bay double panel system (MPS) experiments in chapter 2.3 except they have a tripled maximum loading value. The trim panel used for this experiment consists of four transparent, 5mm-thick, curved lexan sheets.

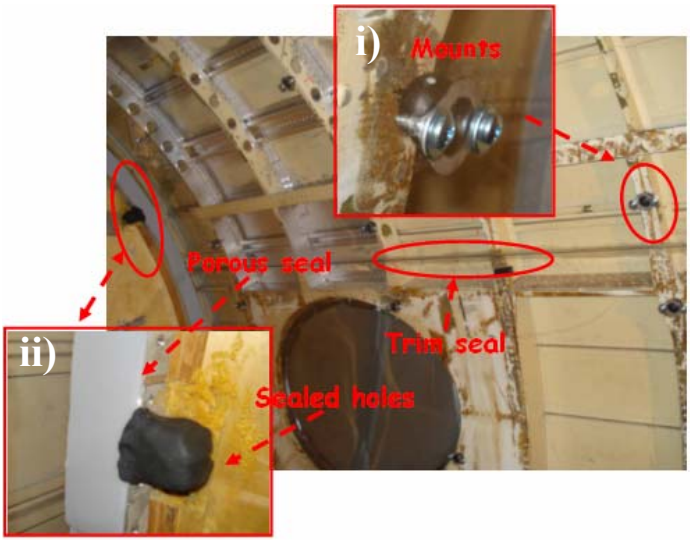

Figure 6-5: Side view of fuselage interior.

These lexan sheets are connected with silicon on the sides as shown in Figure 6-5, with an additional narrow lexan sheet that connects the two sheets on the upper center line of the fuselage as shown in Figure 6-6 (a). To reduce flanking, all holes in the fuselage were sealed and a layer of melamine foam was positioned on the sides (Figure 6-5, ii) of the trim panel and sealed with tape. In addition, the trim edges were sealed as shown in Figure 6-6 (b).

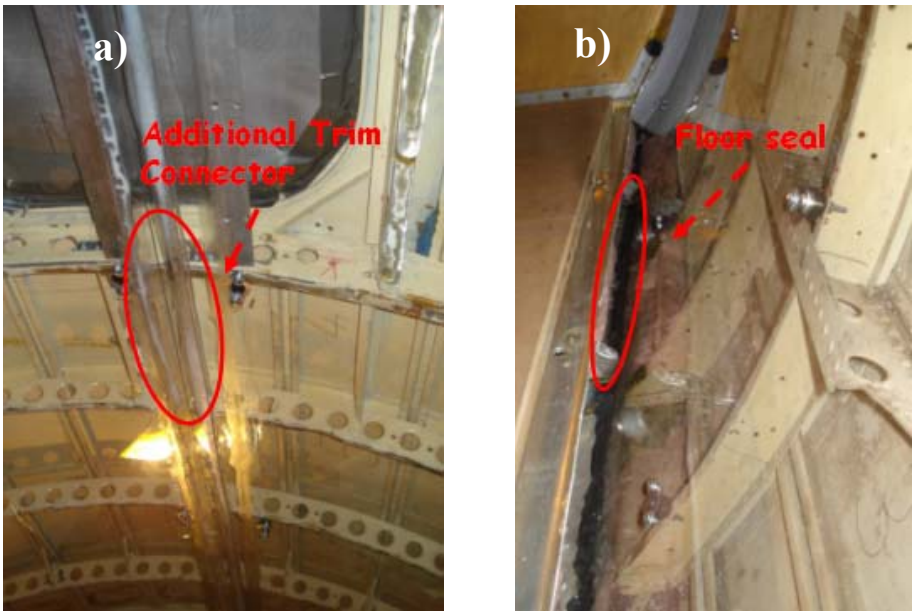

Figure 6-6: Floor sealing (a) and trim connector sheet (b).

Figure 6-7 presents a drawing of the experimental setup of the microphone array (a, microphones marked with black dots, additional accelerometers marked with red dots) and the real fuselage exterior (b) with a speaker to excite the fuselage and one of three reference microphones positioned in front of the speaker.

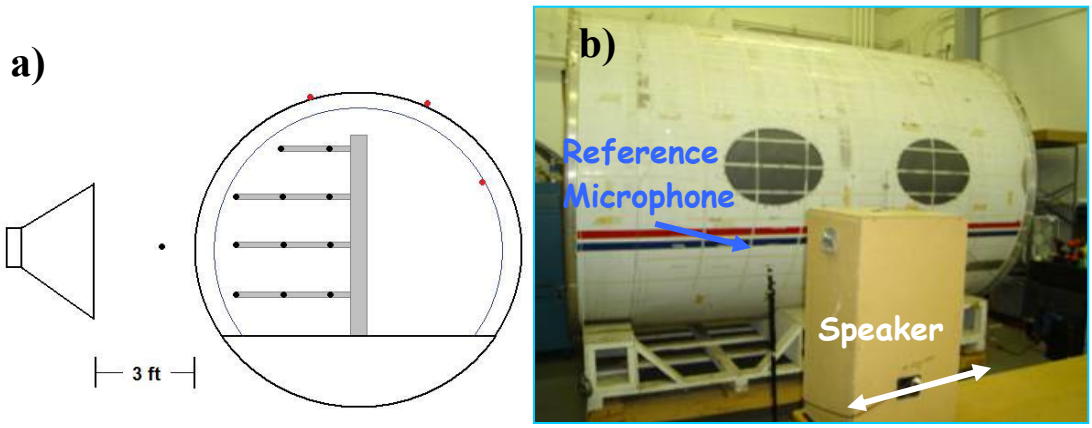

Figure 6-7: Drawing of the experimental setup and the microphone array, microphones marked with black dots (a) accelerometers marked with red dots and picture of fuselage exterior with reference microphone and speaker (b)

Figure 6-8 presents the top view of the entire experimental setup including all speaker and microphone array positions as well as the reference microphones. In summary, the setup included three positions for a speaker (A to C Figure 6-8). The speaker was emitting white noise with a frequency bandwidth from 0-1000Hz. It was placed at a distance of 3ft away from the fuselage. To assure the repeatability of the measurements, a reference microphone was set up at three positions synchronized with the speaker (labeled Ref A to C in Figure 6-8). The reference microphone was placed at a distance of 2ft from the speaker and 1ft from the fuselage.

The microphone array was moved along the center line and fixed at six different positions (labeled I to VI in Figure 6-8). Furthermore, the microphone array was alternately turned to the left and the right side of the fuselage (labeled L and R in Figure 6-8). This setup enabled the sound pressure level throughout the fuselage interior to be determined.

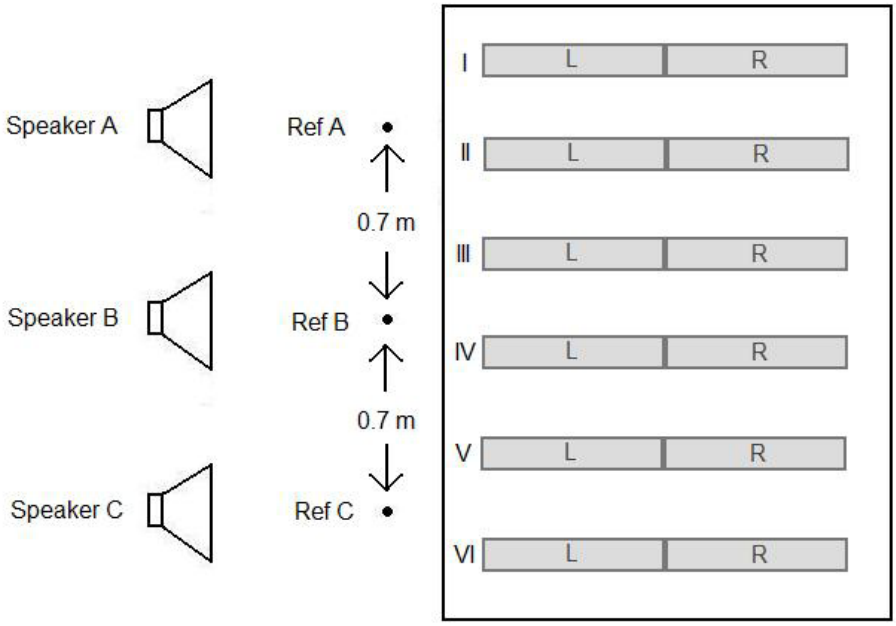

Figure 6-8: Top view of the experimental setup, showing the various positions of the speaker, the reference microphone and the array (I-VI R/L)

6.2. First fuselage measurements

This section presents the first measurements of the skin pocket vibration of the Gulfstream fuselage and trim panel. The objective of these first measurements is to get an idea of the skin pocket behavior. Five skin pocket groups were tested with different configurations as shown in Figure 6-9. Three single skin pockets are tested as well as two larger skin pocket groups with various hammer and accelerometer positions. Looking at the light blue box in Figure 6-9, three frames divide the skin pocket group. Note that this group is not touching the frames. Hence, although some skin pockets look like they are subdivided by the frames, they actually act like one large skin pocket. The same applies for the large skin pocket group highlighted in red in Figure 6-9. Hammer positions are shown as "o's" and accelerometer positions are represented by "x's."

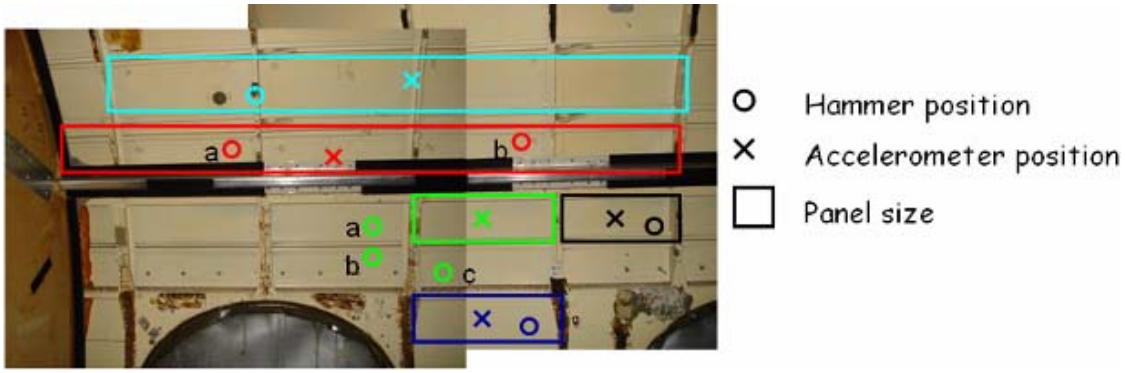

Figure 6-9: Picture of the interior of the Gulfstream section with the five skin pockets/ skin pocket groups used for the first measurements

Figure 6-10 shows the magnitude of the transfer mobility spectrum of the first skin pocket observed i.e. it was excited with a modal hammer on a non-center position with a measured response at the center of the panel. The first resonant frequency of the skin pocket occurs around 330Hz.

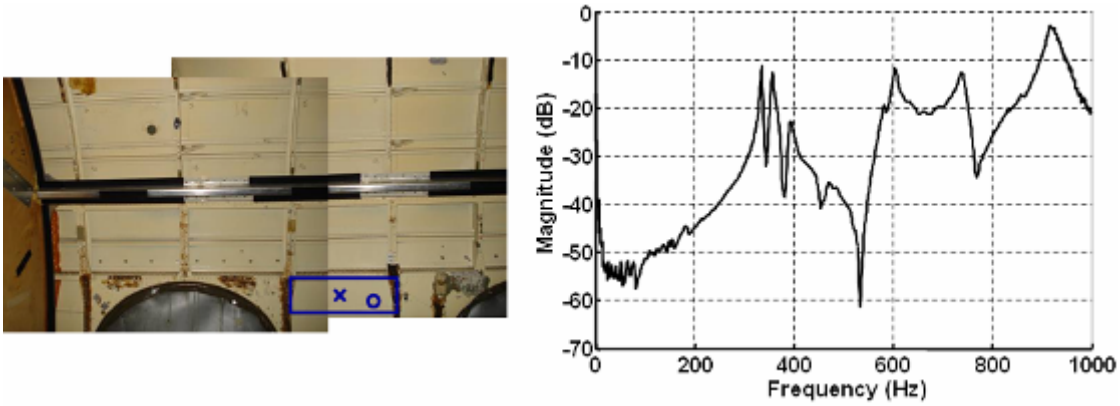

Figure 6-10: Averaged mobility squared of 1st skin pocket measured at center position excited with modal hammer as shown in left picture

Figure 6-11, much like Figure 6-10, presents a plot of the magnitude of the transfer mobility spectrum of the 2nd skin pocket excited with a modal hammer on a non-center position with measured response at the center of the panel. The first modes of this skin pocket are higher than those shown in the prior plot because the skin pocket used for the measurement in Figure 6-11 has smaller dimensions.

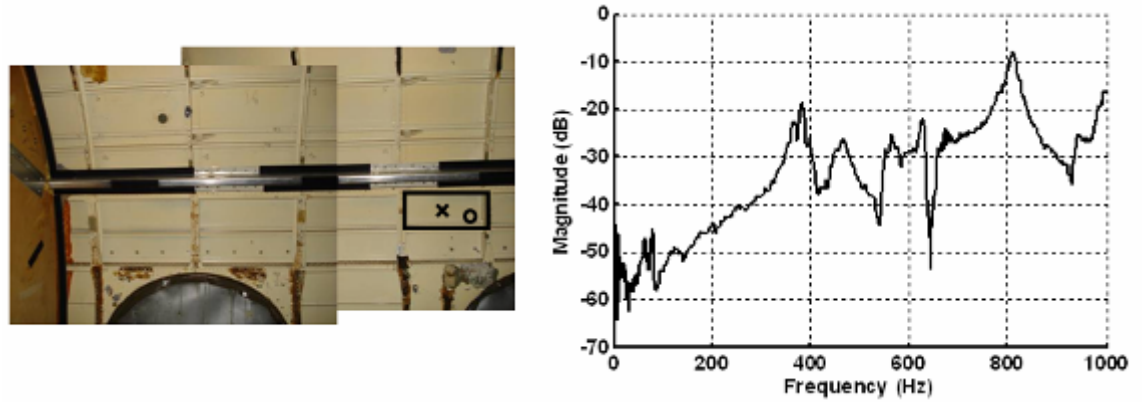

Figure 6-11: Averaged mobility squared of 2nd skin pocket measured at center position excited with modal hammer as shown in left picture

Figure 6-12 shows the magnitude of the measured transfer mobility spectrum of a large group of skin pockets excited with a modal hammer on a non-center position with the accelerometer in the center of the panel. The first mode is below 200Hz, as this skin pocket group has larger dimensions than the previous two skin pockets.

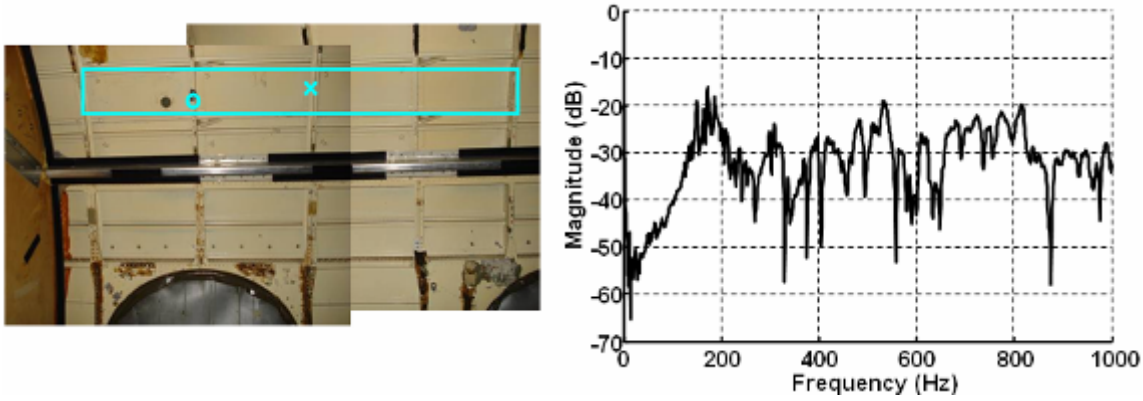

Figure 6-12: Averaged mobility squared of 1st group of skin pockets measured at center position excited with modal hammer as shown in left picture

Figure 6-13 presents two plots of measured transfer mobilities of the second large group of skin pockets excited with a modal hammer on two non-center position (a and b) with the accelerometer in the center of the panel. The responses of the two curves are very similar at frequencies below 700Hz. This is expected because the response to the same subset of skin pockets is measured at two different positions and both attenuate most of the panel modes.

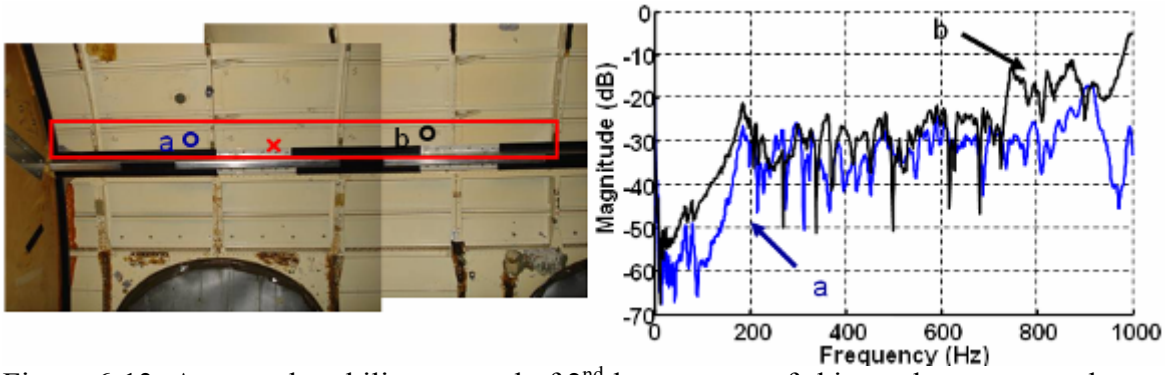

Figure 6-13: Averaged mobility squared of 2nd large group of skin pockets measured at center position excited with modal hammer on two positions as shown in left picture

The last measurement shown in Figure 6-14 presents a plot with three measured transfer mobilities between panels with the accelerometer at the center of the third small skin pocket. The skin pocket's velocity is measured while exciting three surrounding skin pockets; all three measurements look similar over the broadband. Interpreting these results is quite complex because the three excited skin pockets (e.g. the skin pockets with the hammer positions) are surrounded by different frames and stringers. These three skin pockets also have different dimensions.

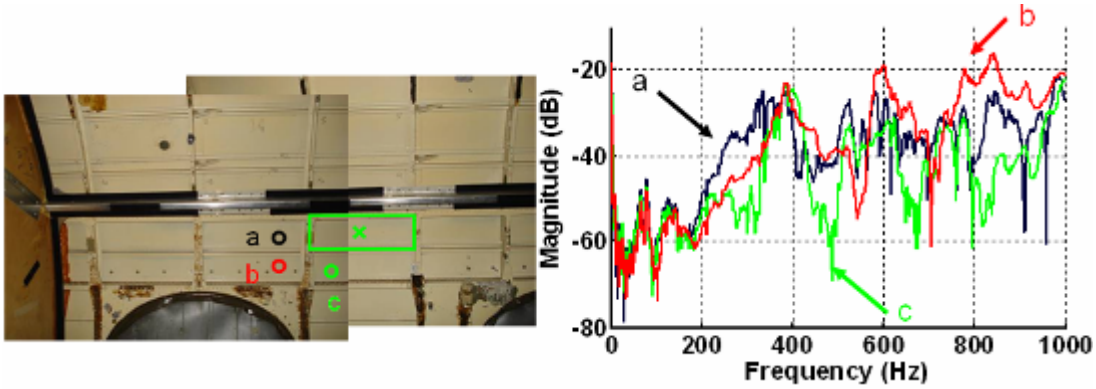

Figure 6-14: Averaged mobility squared of 3rd small panel measured at non-center position excited with modal hammer on three positions outside the panel, as shown in left picture

The above presented measurements show a wide range of "cut-on" frequencies (i.e. 1st resonance frequency) of each skin pocket. They vary from 110Hz to frequencies as high as 470Hz. Therefore, skin pockets with high cut-on frequencies should be treated with different HG blankets than skin pockets with low cut-on frequencies. The poro-elastic media damps out all skin pocket resonances above a certain frequency (usually above 500Hz). Skin pockets with high cut-on frequencies only have a limited

number of low frequency modes that need to be controlled before the porous media damps out those modes at higher frequencies. Thus, it was decided to measure each skin pocket cut-on frequency individually in order to treat each skin pocket with its own HG blanket design Figure 6-15 shows a histogram with the cut-on frequencies, obtained with modal hammer tests, of each individual skin pocket. One can see that the cut-on frequencies are distributed over a frequency range of 100-500Hz. However, it appears that these cut-on frequencies occur in groups of certain small frequency intervals, which show that the fuselage really consists of similar behaving skin pocket groups. To simplify the HG blanket design process, the skin pockets were divided into six groups with the natural frequencies of 127 Hz, 164 Hz, 263 Hz, 296 Hz, 347 Hz, and 374 Hz.

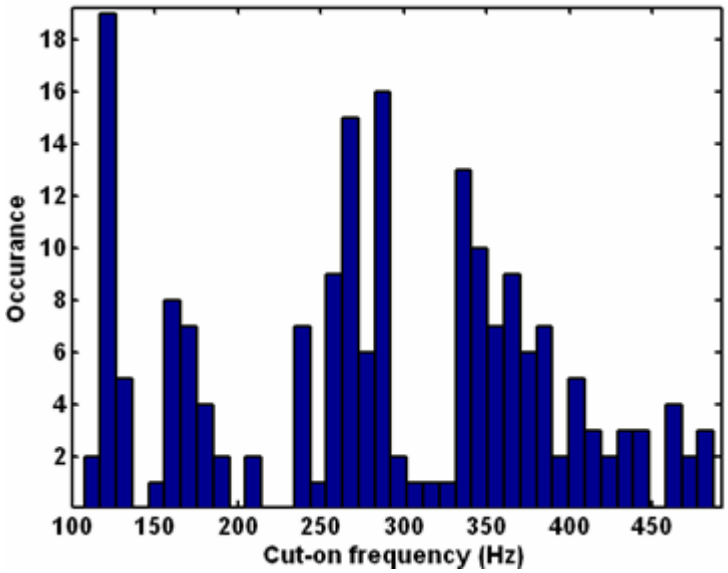

Figure 6-15: Histogram of skin pocket cut-on frequencies

Figure 6-16 presents a plot with the measured spatially averaged squared velocity of a trim panel over ten random points while the trim panel was excited at an off-center position. This measurement was needed for the genetic algorithm design tool (details in the next section), which is used to optimize the HG blanket. One can see a significant amount of low frequency modes that need to be controlled with the HG blankets.

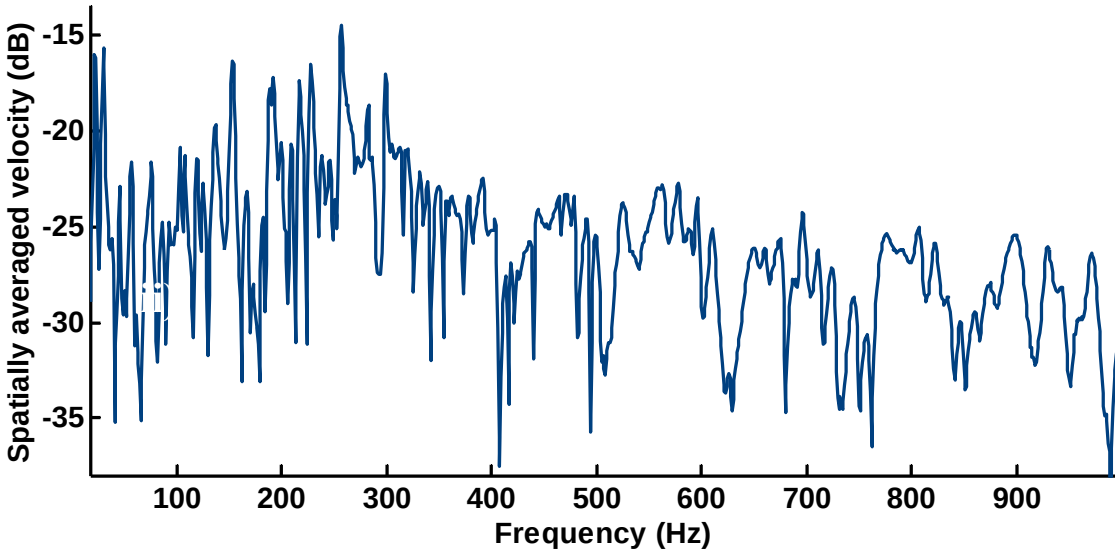

Figure 6-16: Measured spatially averaged squared velocity of a trim panel over ten random points and excited at an off-center position

The measurements shown in this section include three skin pockets and two large skin pocket groups. All the skin pockets are very lightly damped. Skin pockets with roughly the same dimensions act similarly even if surrounded by different BC's. For the full scale fuselage experiments, the design tool will take the different skin pocket dimensions and BC's into account when optimizing the HG blankets. Furthermore, a modal hammer test with the trim panel revealed a significant amount of modes to be controlled at low frequencies.

6.3. Procedure

This section briefly describes the procedure for the final HG blanket optimization. The goal is to obtain the final optimized HG blanket design by modeling the fuselage interior as realistically as possible and applying a genetic algorithm using the design tool. The first step was to apply plane wave pressure excitation to the fuselage as a more rigorous forcing function, as described in section 2.1.6. A genetic algorithm was then applied to the MPS design tool. The genetic algorithm used is the "Genetic Algorithm and Direct Search Toolbox" from MATLAB, as described in section 4.2. The iterative optimization routine, also described in section 4.2, ran for a certain configuration of the MPS and it was found that the MATLAB genetic

algorithm, when run for several weeks, converges to the results obtained with the iterative method. The MPS experimental rig was designed similar to the fuselage structure. Assumptions were made about the panel curvature as flat panels were used for both fuselage and trim. The skin pockets inside the fuselage have various dimensions which makes it difficult to capture all the dynamics of the fuselage using the design tool. The MPS dimensions were changed to the most frequent dimensions of skin pockets, frames and stringers inside the Gulfstream fuselage. Measurements of fuselage and trim response have shown that the theoretical modes in the design tool have to be adjusted to match the experiments due to the curvature of both panels as well as the lexan material of the trim panel. The number of mass insertions has been limited to four due to mass interaction distance limitations. The first test runs indicated that the attenuation converged with four mass insertions while keeping the total mass insertion weight constant. The mass has been unevenly distributed over the four mass insertions and set as a constraint in the MATLAB toolbox. The fuselage and trim modes vary throughout the fuselage section, thus, it was decided to run six different cases (with different modes for fuselage and trim panel) on six machines. Figure 6-17 shows one of six possible HG blanket configurations.

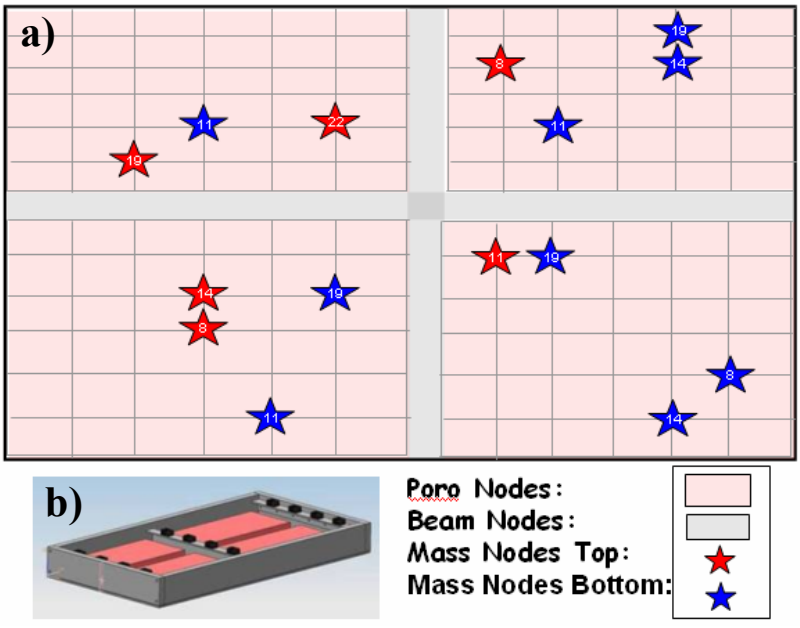

Figure 6-17: One of six HG blanket designs (a) obtained with optimization routine and schematic of MPS (b).

Presented is the top view of the MPS with stars showing the mass positions (red for top- and blue for bottom-nodes). The numbers inside the stars represent the mass of the inclusions in grams. The genetic algorithm results give a good idea of the positions and natural frequencies of the mass insertions inside the poro-elastic media.

The mass insertions of the final HG design are then tuned to the desired natural frequencies using the "effective area" approach described in the previous chapter.

6.4. Comparison

This section discusses the final full scale fuselage measurements. The first part of this section presents the comparison of the magnitude of the pressure ratios between the 132 microphones inside the fuselage cabin with trim panel and the reference microphone shown in Figure 6-8. Compared is the fuselage bare and treated with melamine foam versus HG blankets. The resulted effect of the mass inclusions added to the melamine foam was disappointing due to flanking transmission problems through the windows, the floor or the doors. However, the second part of this section presents measured spatially velocities of skin pockets, demonstrating that the HG blankets are able to control the vibration of each skin pocket individually. Therefore, it is shown that the fuselage structure can be controlled at low frequencies using HG blankets.

Figure 6-18 presents the magnitude of the pressure ratios between the 132 microphones inside the fuselage cabin (without trim panel) and the reference microphone between the sound source and the fuselage from 30-530Hz. Compared is the bare fuselage versus the porous media attached versus the HG blankets attached. The melamine foam starts damping out the fuselage structure around 380Hz. Therefore, all HG blankets target modes below 380Hz. Consequently, skin pockets with a cut-on frequency above 380Hz were not treated with additional mass inclusions. The higher the cut-on frequency of a skin pocket is, the fewer mass inclusions were added to the melamine blocks. Effectively, a total mass of 3% of the fuselage weight was added to the melamine foam in the form of mass inclusions (a maximum number of four mass inclusions per block with mass varying from 3.5g to 19g). Unfortunately, no large effect can be seen with the added mass inclusions.

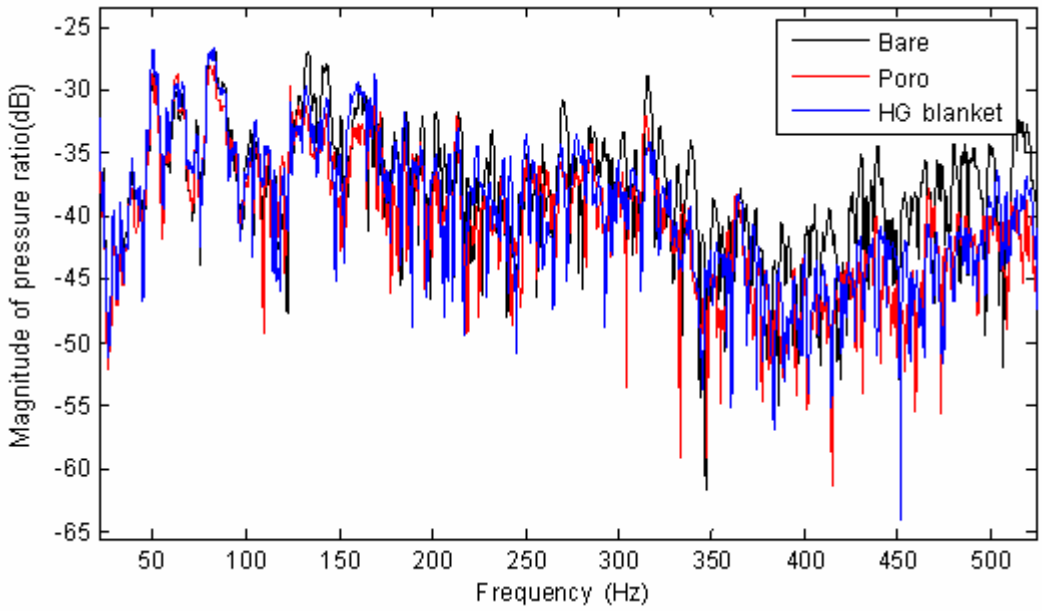

Figure 6-18: Magnitude of the pressure ratio between the 132 microphones (inside the fuselage cabin without trim panel) and the reference microphone from 30-530Hz. Compared is the bare fuselage vs. porous media attached vs. HG blanket attached.

Figure 6-19 presents the magnitude of the pressure ratio between the 132 microphones inside the fuselage cabin (without trim panel) and the reference microphone between the sound source and the fuselage from 30-1000Hz. Compared is the bare fuselage versus the porous media attached versus the HG blanket attached. The porous media controls the transmitted sound pressure through the fuselage by a significant amount. Note the large number of modes over the bandwidth.

Figure 6-20 presents an a-weighted 1/12 octave band plot of the magnitude of the pressure ratio between the 132 microphones inside the fuselage cabin (without trim panel) and the reference microphone. Compared is the bare fuselage versus the porous media attached versus the HG blanket attached. The porous media adds a significant amount of damping to the skin pockets. No additional effect due to the mass inclusions can be seen at low frequencies. The measured pressure ratios inside the cabin of the porous media and the HG blanket are very similar.

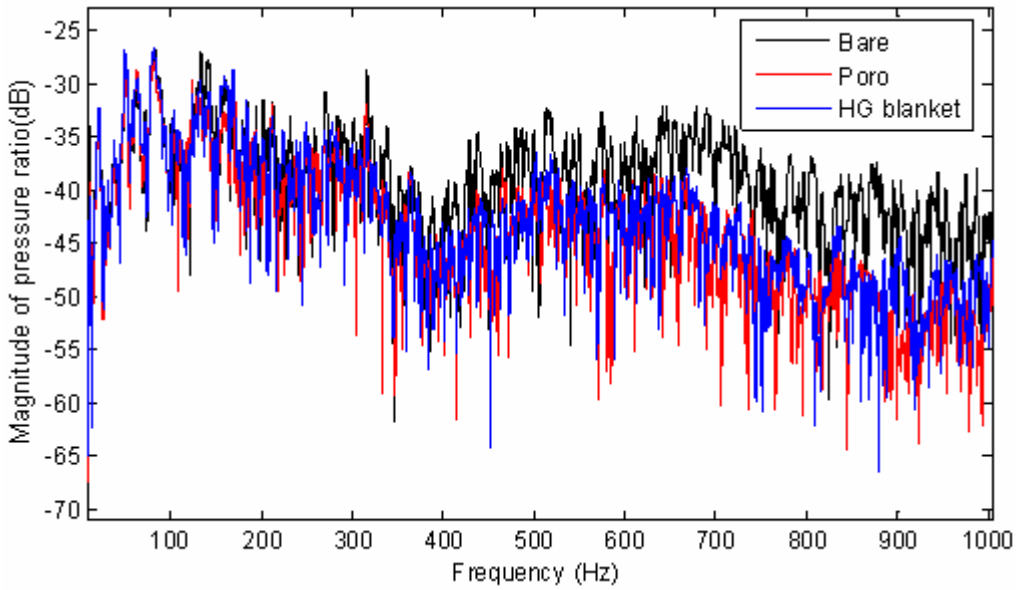

Figure 6-19: Magnitude of the pressure ratio between the 132 microphones (inside the fuselage cabin without trim panel) and the reference microphone from -1000Hz. Compared is the bare fuselage vs. porous media attached vs. HG blanket attached.

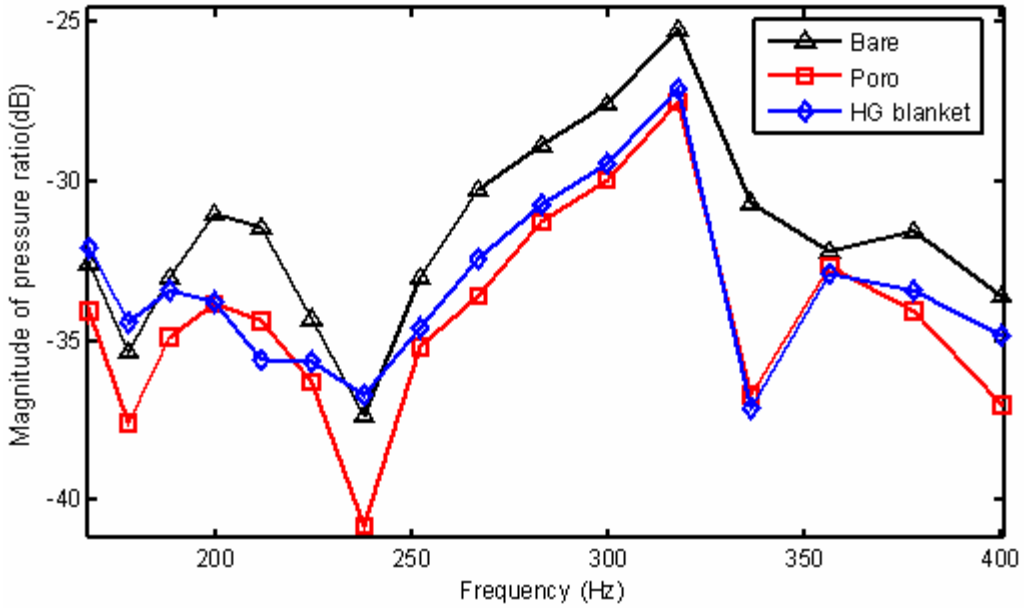

Figure 6-20: Magnitude of the pressure ratio between the 132 microphones (inside the fuselage cabin without trim panel) and the reference microphone. Compared is the bare fuselage vs. porous media attached vs. HG blanket attached in 1/12 octave band (A-weighted).

Figure 6-21 presents the magnitude of the pressure ratio between the 132 microphones inside the fuselage cabin (with trim panel built in) and the reference microphone between the sound source and the fuselage from 40-550Hz. Compared is the bare fuselage versus the porous media versus the HG blanket attached. The pressure ratio inside the cabin drops by a significant amount above 400Hz going from "Bare" to "Poro" due to the porous media controlling the base structure at frequencies above 380Hz. No additional effect can be seen from adding mass inclusions to the melamine foam blocks, which makes sense as there was no effect due to the mass inclusions without the trim panel attached to the fuselage structure.

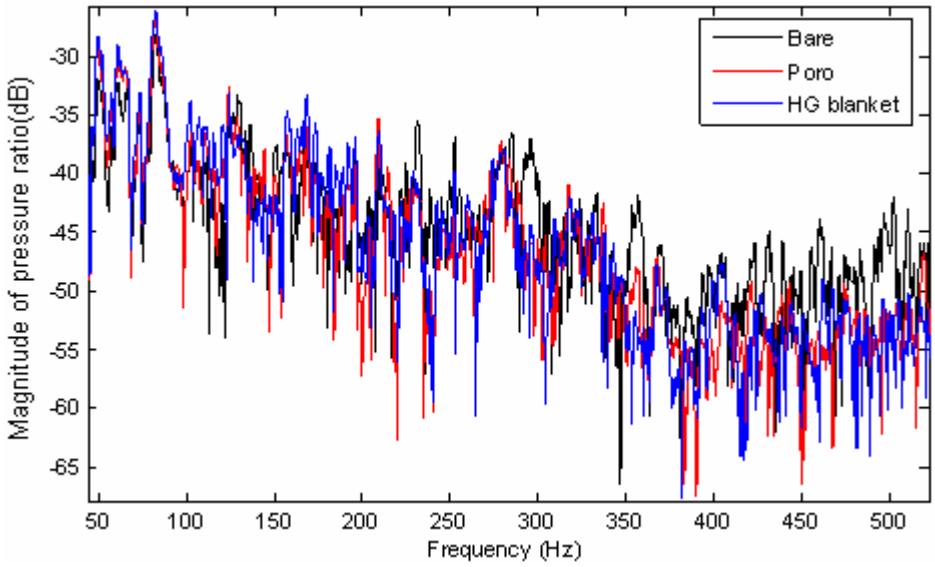

Figure 6-21: Magnitude of the pressure ratio between the 132 microphones (inside the fuselage cabin with trim panel) and the reference microphone from 40-550Hz. Compared is the bare fuselage vs. porous media attached vs. HG blanket attached.

Figure 6-22 presents the magnitude of the pressure ratio between the 132 microphones inside the fuselage cabin (with trim panel built in) and the reference microphone from 30-1000Hz. Compared is the bare fuselage versus the porous media attached versus the HG blanket attached. The mounts above 400Hz are damped out due to the porous media attached to the skin pockets. Comparing the porous media case to the HG blanket case, the noise level inside the cabin is once more very similar.

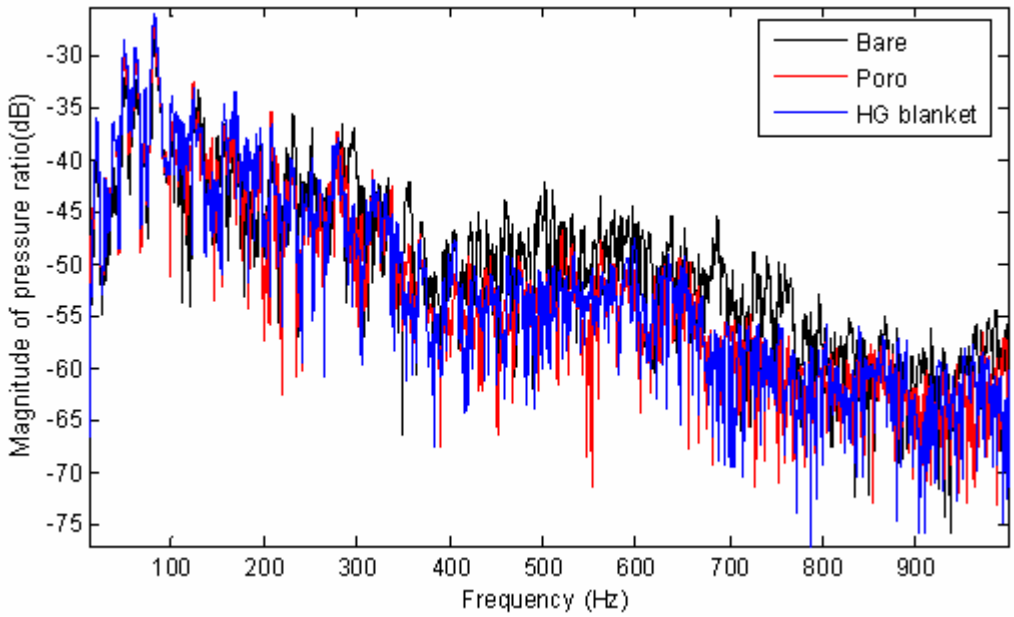

Figure 6-22: Magnitude of the pressure ratio between the 132 microphones (inside the fuselage cabin with trim panel) and the reference microphone from 30-1000Hz. Compared is the bare fuselage vs. porous media attached vs. HG blanket attached.

Figure 6-23 shows an a-weighted 1/12 octave band plot of the magnitude of the pressure ratio between the 132 microphones inside the fuselage cabin (with trim panel built in) and the reference microphone. Compared is the bare fuselage versus the porous media attached versus the HG blanket attached. One can see a small drop of the magnitude of the pressure ratio around 320Hz going from the porous media to the HG blanket. However, there is no proof that this is really due to the mass inclusions as the rest of the pressure distribution is similar in both cases, with and without added mass inclusions.

Figure 6-24 shows the measured spatially averaged velocity of a skin pocket with a cut-on frequency of 125Hz in 1/12 octave band. Compared is the vibration of the skin pocket with the porous block and with the HG blanket. The HG blanket has four mass inclusions tuned to 125Hz, 170Hz, 240Hz and 340Hz. The mass inclusions cause a significant drop in the skin pocket vibration at all targeted frequencies. Note that at 280Hz the HG blanket has a reverse effect by increasing the skin pocket vibration. However, the HG blanket proved to be a very effective passive vibration control treatment over the frequency band of 100Hz – 350Hz.

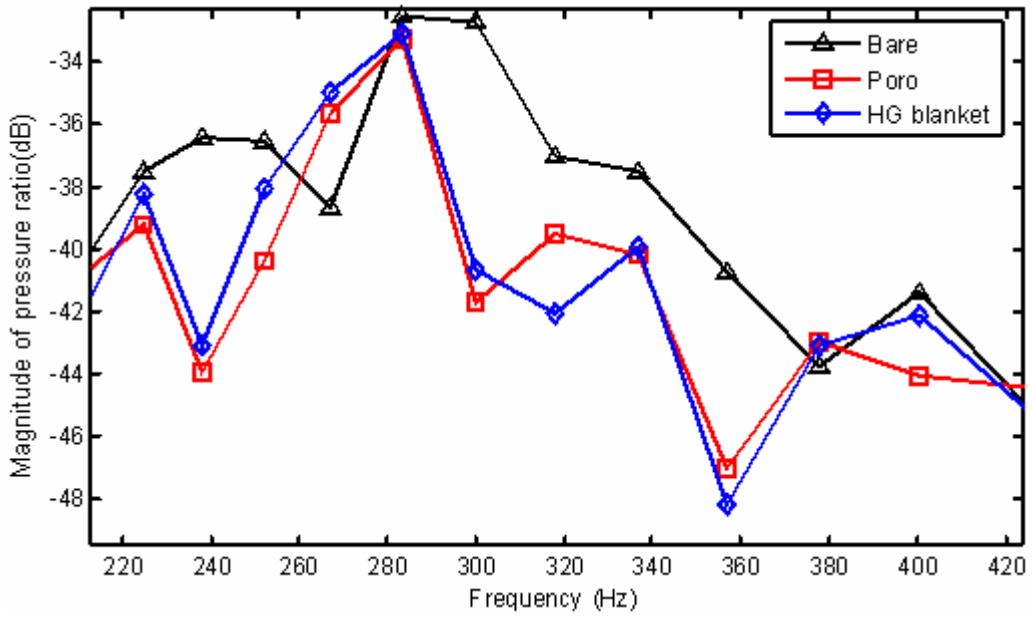

Figure 6-23: Magnitude of the pressure ratio between the 132 microphones (inside the fuselage cabin with trim panel) and the reference microphone. Compared is the bare fuselage vs. porous media attached vs. HG blanket attached in 1/12 octave band (A-weighted).

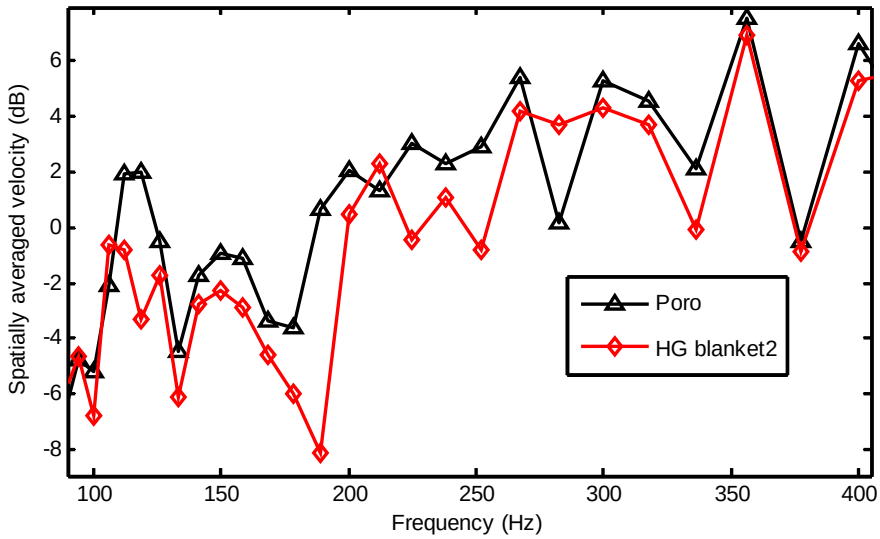

Figure 6-24: Spatially averaged velocity of skin pocket with cut-on frequency of 125 in 1/12 octave band. Compared is the skin pocket with porous block and with HG blanket. HG blanket has four masses inclusions tuned to 125Hz, 170Hz, 240Hz and 340Hz.

To show that the HG blanket also works well for skin pockets with high cut-on frequencies Figure 6-25 presents the spatially averaged velocity of a skin pocket with a cut-on frequency of 330Hz in 1/12 octave band. Compared is the skin pocket with porous block and with HG blanket. The HG blanket has one mass inclusion tuned to

340Hz. One can see that the vibration of the skin pocket is almost identical going from the porous media to the HG blanket which proves the repeatability of the modal hammer tests. However, the HG blanket causes a drop in velocity at the targeted frequency. The reason for the attenuation being rather small compared to the previous case is due to the mass of the inclusion. The mass of the inclusion used in this HG blanket is only 4.5g because only light mass inclusions can be tuned to such high frequencies with still having a reasonable area for the inclusion.

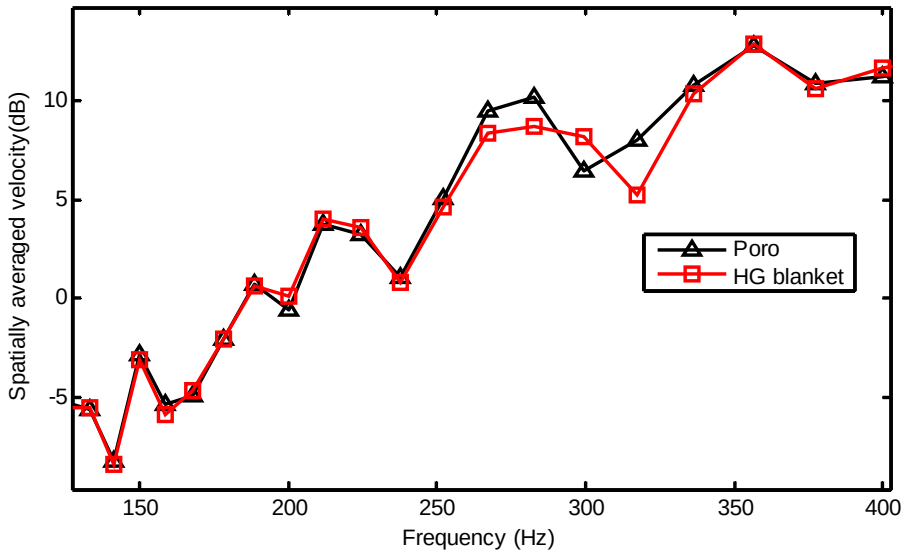

Figure 6-25: Spatially averaged velocity of skin pocket with cut-on frequency of 330Hz in 1/12 octave band. Compared is the skin pocket with porous block and with HG blanket. HG blanket has one mass inclusion tuned to 340Hz.

This section presented a full scale fuselage measurement of the sound pressure of the cabin interior. The bare fuselage was measured and compared to the cases with added melamine foam blocks and HG blankets attached to the skin pockets. Unfortunately, no effect could be seen adding the mass inclusions to the porous layer possibly due to flanking transmission problems. Flanking can be either caused through the windows, the floor or the doors. However, the second part of this section presented measured spatially averaged velocities of skin pockets with and without mass inclusions added to the porous layer. It is shown that HG blankets are able to control the vibration of each skin pocket individually by adding a total mass of 3% of the fuselage mass distributed over all skin pockets.

7. CONCLUSIONS AND FUTURE WORK

7.1. Conclusions

In this thesis a numerical model has been developed that predicts the response of a single-bay double panel system with sandwiched HG blanket and air cavity inside. An impedance and mobility method approach (IMM) was used to couple the analytical solutions of the fuselage and trim panel and air cavity with the FE model of the HG blanket. This model was then validated experimentally and shown to accurately capture the behavior of the double panel – HG blanket system.

The experimental and numerical results presented indicate that the analytical model correctly predicts the experimental response of the double panel system with HG blankets, and can be used as a design tool. It was also shown that it is possible to target certain modes of the fuselage panel in a double panel system by tuning the masses inside the HG blanket to the resonant frequencies of the fuselage panel. This results in the reduction of the vibration levels of both the fuselage and trim panels, and a reduction in the radiated sound field at low frequencies. It is also shown that the HG blanket achieves this low frequency control while maintaining the high frequency performance of the passive blankets (i.e. at frequencies above 500Hz).

An experimental investigation using the single bay DPS was presented, attaching an HG blanket on both, the fuselage and the trim panel. These double HG blanket measurements have shown promising results as the additional HG blanket on the trim panel can be used to target modes that are tough to control from the fuselage panel.

As a more rigorous model for an aircraft fuselage, the single-bay double panel system was extended to include frames, stringer, mounts and four HG blanket. This multi-bay double panel system was once again modeled using the IMM approach and presented in chapter 3 of this thesis. A comparison between theory and experiment showed a good match of the fuselage panel behavior and the predicted response of the trim panel captured the main physical characteristics. However, the measured trim panel results indicated problems in the repeatability of the experiments as the trim panel has to be removed in order to change the HG blanket configuration.

Chapter 4 of this thesis presented a comparison of three different approaches to the design of an HG blanket used to control the sound radiation from a double panel system (random placement, modal design and best result in extensive search). An extensive search of the solution space for a specific case of sound radiated from a DPS with two mass HG blanket, was conducted and used to compare the different strategies. The results showed that the best performing designs were substantially better than the average "random" design with the best performer achieving 12.5dB attenuation (0-500Hz), whereas the median performer achieved only 2.6dB attenuation in sound radiation. The performance of the "modal designed" HG blanket was not much better because the heavier of the two masses, used to attack the 1-1 mode, was positioned in the middle of the fuselage panel, which turned out not to be the ideal position. In addition the second mass in the model design case was used to target the 2-1 mode of the fuselage panel. However, some of the modes of the fuselage panel, such as the 2-1 mode, are not all equally coupled to the trim panel and hence optimal control of the fuselage panel does not lead to optimal control of the sound radiation.

Experimental results, based on the modal design method, show that the HG-blanket has potential to significantly lower the vibration level of the fuselage panel at lower frequencies while keeping the good performance of typical blanket treatments at frequencies above 500Hz. The results also support the conclusions of the numerical study: control of the fuselage panel by modal response does not lead to optimal results. In addition, the comparison of theory and experiment for the presented "HG blanket designs" has validated the design strategy.

The main conclusion from this work is that there is a strong need for optimization routines such as genetic algorithms or iterative routines since optimal performance is substantially better than the performance achieved using the other simple design strategies. Therefore, a novel iterative routine for the HG blanket design was introduced based on the sequential addition of massed in the blanket. After each mass is added the optimal location/design for the next mass is found. When all of the masses are added the algorithm then reassesses the design of the first mass and continues until the design is converged. The iterative process was compared to the results of an optimized HG blanket design obtained with the "Genetic Algorithm and

Direct Search Toolbox" from MATLAB. The optimized HG blankets obtained with the above described algorithms are similar in results but vary significantly in their design when increasing the solution space (e.g. mass positions and number of skin pockets) due to the nonlinear relationship between design parameters and the cost function. Thus, the solution space is not characterized by a single minimum but my multiple minima and therefore gradient based algorithms were not considered in this work.

The design tool used to compare the optimization routines consisted of the previously discussed DPS and MPS with sandwiched HG blanket and air cavity. For this work the system was excited with an acoustic plane wave incident on the fuselage panel. For the DPS the HG blanket was constrained to have four mass inclusions with a given mass distribution to be placed on 50 positions. For the MPS the four HG blankets were constrained to have two mass inclusions each with a given mass distribution to be placed on 50 positions. The attenuation obtained with the HG blanket built with the genetic algorithm as well as the iterative routine were similar. However, the iterative routine managed to obtain its solution twice as fast as the genetic algorithm by converging quickly after three runs in each of the two observed cases. Thus, the iterative process has the potential to be even more computationally efficient when the number of mass inclusions inside the HG blanket increases.

Furthermore, the sensitivity of HG blankets modeled of DVAs acting on a rectangular clamped plate is investigated with respect to altering positioning of the DVAs in order to analyze the performance of nominally optimal HG blankets. An analytical model is derived using a Kirchhoff-plate and a DVA modeled as a mass-spring-damper-system. The steady state response of the plate with DVA is calculated and evaluated. To capture the effect of different excitations, the response due to different excitation forces is calculated and averaged, thus simulating a random "boundary layer type" excitation. The sensitivity of the placement of a DVA can be predicted by a combination of the modes determining the velocity. Each mode shape contributes at certain frequencies differently to the velocity of the plate. The analysis done using the average velocity in the frequency range around the targeted frequency reveals that the dominating mode shapes are indicators for sensitivity and the best position. The highest magnitude of the mode shapes shows the best position. The slope

of the dominating mode shapes can be used to obtain the sensitivity of the positioning. The sensitivity also depends on the amount of nodal lines. Every nodal line reduces the area to place a DVA effectively and therefore increases the losses if the DVA is moved from the best position. The model was also extended to include two DVAs and reveals that the sensitivity of each DVA is fairly independent and therefore the results of a single DVA can be used to describe the sensitivity of the positions for two DVAs. Furthermore, the sensitivity of a system with more than one DVA decreases if one DVA is placed at an optimal spot. In addition, the DVAs must be placed a certain distance away from each other to avoid interaction caused by the foam. The model is validated by experiments with different DVA positions. The results match well with the theory and confirm the sensitivity analysis presented.

Chapter 5 presented a mathematical and experimental study of the behavior of mass inclusions placed inside a poro-elastic media. The inclusions were shown to interact with a finite volume of the poro-elastic media termed the "footprint" and it was shown that this footprint impacted the tuning frequency of the mass inclusion and the interaction distance between multiple masses. Inclusion mass and depth were shown to alter the natural frequency of the inclusion and in addition it was also shown that both the area and shape of the inclusion controlled the natural frequency by changing the footprint.

A novel, empirical "effective area" approach to predict the natural frequency of different mass shapes embedded in porous media was found and experimentally verified for many different types of porous media, including melamine foam, polyurethane, and polyamide. A maximum error of 8% existed for all the predictions made.

By defining effective mass inclusion parameters, novel property control methodologies for HG blanket materials were discovered that allow better control of natural frequencies by controlling the mass, depth, area and shape of the inclusions. In principle, inclusions of various shapes, placed on a single layer in the foam, can be used to control a wide range of frequencies and this will make the blankets much easier to manufacture.

Also in chapter 5 a new model for the interaction of mass inclusions with the poro-elastic layer in heterogeneous (HG) blankets is presented. Since the previous mentioned empirical effective area approach does not cover all parameters influencing the interaction between masses and poro-elastic layer, the development of a more sophisticated model to include more influence parameters was undertaken. This new model was directly derived from the general constitutive equations for elastic media. Basic elastomechanical solutions are implemented in the model making it computationally far more effective than the finite element models. The model assumes the system is essentially static and its limitations include a linear elastic and isotropic constitutive relationship, which is critical for higher frequencies. However, the analytical model covers all elastic materials and thus can be used in a far more generalised way. The model is used to calculate the effective "dynamic vibration absorber" stiffness created by the interaction between embedding material and the added masses for low frequencies. The predictions are validated by experiments and summarized in a simplified direct equation to calculate the effective stiffness, which can be useful when dealing with experimental data in the HG blanket design process. All known major influences on the effective stiffness of the elastic layer, namely the material parameters, the mass shape and area, and the layer thickness are included in the model. Furthermore, the model can also be used to predict the stress and displacement fields in the elastic layer. Thus, the critical "mass-interaction distance", which is a necessary parameter in the HG blanket tuning and optimization process can be computed. However, since the analytical model is static, it cannot be used to investigate highly dynamic effects occurring when two masses are placed close to each other leading to e.g. stiffness variations.

A full scale fuselage measurement of the cabin noise inside a Gulfsream fuselage was presented in chapter 6 with and without an attached lexan-trim panel. The bare fuselage was measured and compared to the cases with added melamine foam blocks and HG blankets attached to the skin pockets. No significant effect could be seen by adding the mass inclusions to the porous layer and this is probably due to flanking transmission problems. It is assumed that the three possible flanking paths are through the windows, the floor or the fuselage doors. However, modal hammer tests

measuring the vibration of individual skin pockets have shown the potential of the HG blanket to control the vibration response of the fuselage structure at low frequencies by a significant amount with only 3% (of the total fuselage mass) added to the 2'' thick melamine foam blocks. Overall, the HG blanket has shown potential for providing good noise reduction over a wide frequency bandwidth.

7.2. Future work

As mentioned throughout this work, some issues are still unresolved or could be further developed. The mathematical model for the single bay DPS was proved to be accurate. However, the MPS measurements showed repeatability problems on the trim side, thus the experimental rig could be further improved to have a good basis for a comparison of theory and measurements. The double HG blanket measurements have shown potential to further reduce the total HG blanket mass by controlling the trim modes which are difficult to control with HG blankets attached to the fuselage side, which is achieved by attaching an additional HG blanket directly on the trim. However, this work needs some further investigation. The double HG blankets have not been used in a full scale fuselage experiment with an additional HG blanket directly attached to the trim panel.

Design and optimization strategies for HG blankets have been discussed in chapter 4 where the mass inclusion position as well as the mass of the inclusions (where a total mass was distributed over a limited number of inclusions) itself was optimized. In order to further improve the HG blanket optimization, more parameters, such as the poro-elastic material properties, the numbers of mass inclusions, as well as the number of different mass distributions for the inclusions have to be taken into account. In terms of the sensitivity analysis, future work should focus on variations in the material parameters of the foam and plate boundary conditions which were not considered in this work. Only by knowing these uncertainties can a reasonable quantitative prediction of HG performance be made.

Mathematical and experimental approaches to describe the behavior of the mass inclusions added to a porous layer have been presented. Yet, there is still a need to

analyze more types of poro-elastic material as well as fiberglass and other types of damping material to fully define the HG blanket characteristics.

As for the analytical model of the mass-blanket interaction, future work is needed concerning the study of the effects between masses in more detail, especially to assess the influence of the mass shapes in this context. However, if this is the case, a dynamic analytical or finite element model will have to be applied.

The full scale fuselage measurements have shown possible flanking issues. Therefore, it is suggested to retake the measurements after treating the fuselage section to reduce flanking path problems. Furthermore, in-flight measurements would provide an opportunity to demonstrate the HG blankets potential to improve the interior noise reduction at low frequencies in a more realistic environment.

Additional research is needed in order to investigate optimal manufacturing processes for the HG blanket. The "effective area" approach allows the inclusions to be placed in one level of the poro-elastic layer which makes the process easier. However, there is still a need to investigate how applicable the HG blanket would be for aircrafts with skin pockets of different dimensions throughout the fuselage. This could make the HG blankets impractical.

Even though the HG blanket has shown its potential to reduce the vibration and the noise transmitted from single and double panel partitions, it was only tested for aircraft applications. More research needs to be done to test the HG blankets for acoustic fields such as community noise, room acoustics and the interior noise control of cars and trucks to fully explore the usage of the HG blankets in the market.

APPENDIX

A. Experimental measurement techniques - Improved validation of the DPS

This section presents some experimental techniques that improved the experimental validation for the double panel system (DPS) in chapter 2. In the first attempt to match the theory with the experiments of the DPS without HG blankets, the major physics of the trim panel (at frequencies between 250Hz and 500Hz) were not matched to a desired level of accuracy.

The inaccuracy on the experimental validation of the DPS without HG blankets was most likely caused by three reasons. First, the design tool assumes absolutely no frame motion. Different experimental approaches have been carried out in order to reduce the frame motion and are presented in the next section. Second, the "trim panel" has been removed from the excitation side and mounted on the receiver side. There is always a change in the clamped BC due to imprecise torque on the bolts. This is further analyzed by testing the repeatability of measuring the response of a clamped plate. Third, the analytical solution for the cavity could be inaccurate. Improving the accuracy of the single bay DPS experimental validation is vital because a more complicated system will be used to optimize the HG blanket for the full scale fuselage measurements, the multi-bay double panel system (MPS) discussed in chapter 2.3. Finding mistakes in a DPS is a lot easier than finding them in a MPS, where the level of complexity has increased significantly.

This section presents the process of solving problems due to frame motion and repeatability of the experiments. After improving the experimental test rig, an experimental validation is presented and shows that the desired level of accuracy is met so that the analytical solution for the cavity is assumed to be correct.

A.1. Frame motion

In the introduction to this appendix, it was mentioned that one possible reason for an inaccurate measurement could be the frame of the experimental rig moving in phase with one of the plates. As an alternative experimental setup, three different cases

have been considered. First, the frame was mounted to a heavy worktable. Second, the frame was placed on top of a piece of acoustic foam. Third, the frame was hung on a crane.

In all three cases, the spatially averaged velocity of the clamped plate of a DPS at 25 measurement points has been compared to the spatially averaged velocity of the frame at four measurement points. In order to measure the plate velocity, an accelerometer was placed at an off-center position and a modal hammer was used to excite the plate at all 25 points. To measure the frame velocity, an accelerometer was placed at four positions on the frame. The clamped plate was excited by a modal hammer at the same position the accelerometer was placed for the experimental validation in chapter 2. All the frame motion measurements in this section are presented by using the 1.2mm plate, which was used for the trim panel in the experimental validation throughout chapter 2.

Rigidly attached frame

In the design process of stopping the frame from moving, one alternative was to bolt the frame to a heavier structure. In the first variation of the improved DPS experiments, the frame was attached to a heavy worktable. Figure A-1 shows the comparison of theory (red) vs. experiment (blue) of the spatially averaged velocity of a clamped plate with the frame mounted to a heavy worktable (a). Furthermore, a picture and the 3-D model (b) of the test case is presented in Figure A-1. The comparison of the measurement and the design tool shows an additional peak and an additional zero around 100Hz. In order to analyze if this was caused by the frame motion, the frame motion itself was measured.

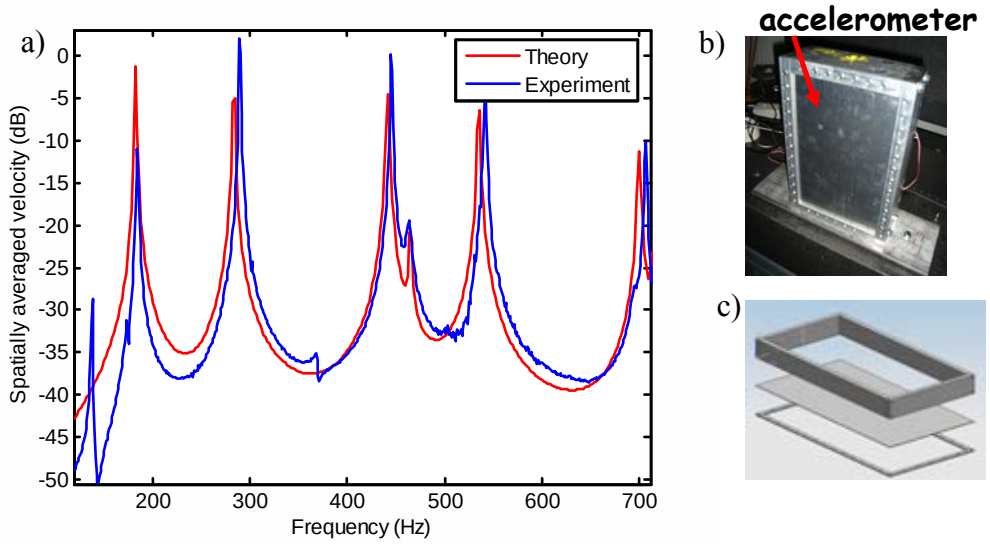

Figure A-1: (a) Comparison of theory vs. experiment of the spatially averaged velocity of a clamped plate with frame mounted to a heavy worktable, (b) picture of the experimental setup, (c) 3-D model of the experimental configuration

Figure A-2 shows the spatially averaged velocity of the clamped plate at 25 points compared to the spatially averaged velocity of the frame at four points (a), a picture of the four accelerometer positions, and the position at which a point force was applied (b).

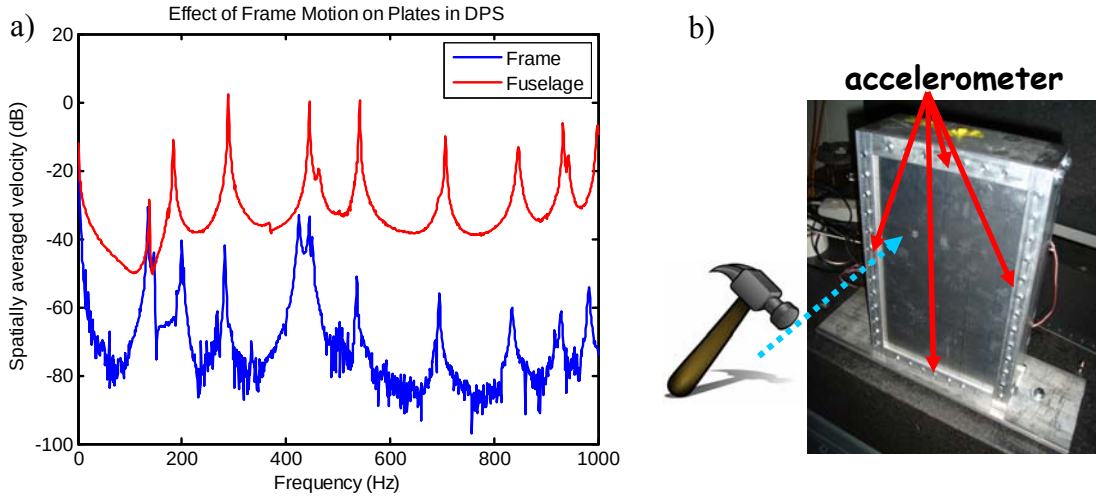

Figure A-2: (a) Measured plate and frame spatially averaged velocity a clamped plate with frame mounted on a heavy worktable, (b) Picture of experimental setup measuring frame motion on four points while hammering on an off center position

The result in Figure A-2 shows that the additional peak shown in Figure A-1 is caused by the frame moving in phase with the clamped plate around 100Hz, which shows two additional facts. First, the frame motion can be measured and compared to the plate motion with the proposed setup of four measurement points on the frame. Therefore, for the next experimental setups, the same experimental method will be used in order to analyze the frame motion. Second, the frame motion at frequencies above the lowest resonant frequency is much less than the motion of the plate and can be neglected.

Frame on top of foam

Another method to reduce the frame motion is to damp it out by setting the frame on top of acoustic foam. In this experiment, 2'' thick melamine foam was used. Figure A-3 shows the spatially averaged velocity of the clamped plate at 25 points compared to that of the frame at four points (a), a picture of the four accelerometer positions, and the position at which a point force was applied (b).

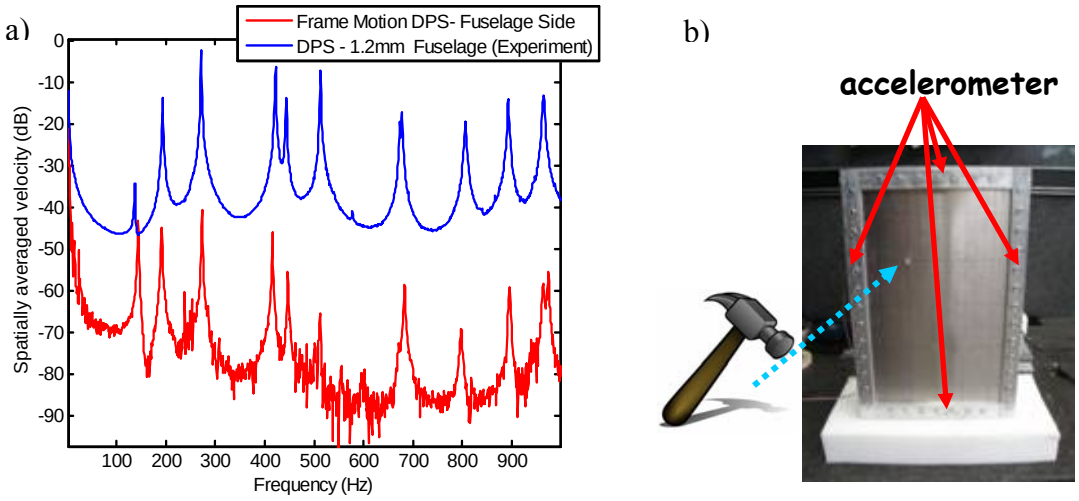

Figure A-3: (a) Measured plate and frame spatially averaged velocity a clamped plate with frame placed on top of a 2'' thick piece of melamine foam, (b) picture of experimental setup measuring frame motion on four points while hammering on an off-center position

The results in Figure A-3 are an improvement compared to those found with the frame mounted to the worktable, as presented in the previous section. At 150Hz, the

frame still moves with a sufficient velocity to influence the plate motion. However, the influence is rather insignificant, yet at higher frequencies, the frame motion is reduced significantly. A disadvantage of this configuration is the decrease of coherence over the frequency of interest.

Hung frame

The two previous experiments have shown that it is, in fact, a tough task to reduce the frame motion to a level that it does not influence the motion of the plate at low frequencies. Instead of reducing the frame motion, one can try to shift it to lower frequencies. By hanging the frame on a crane, the frame has a rigid body mode and the rocking modes; hence, the natural frequency of the major frame motion is shifted to near 0Hz. Figure A-4 shows the crane with the hung frame (a) and a picture of the modal hammer pointing at the accelerometer position for the hung single bay DPS experiments (b).

a) b)

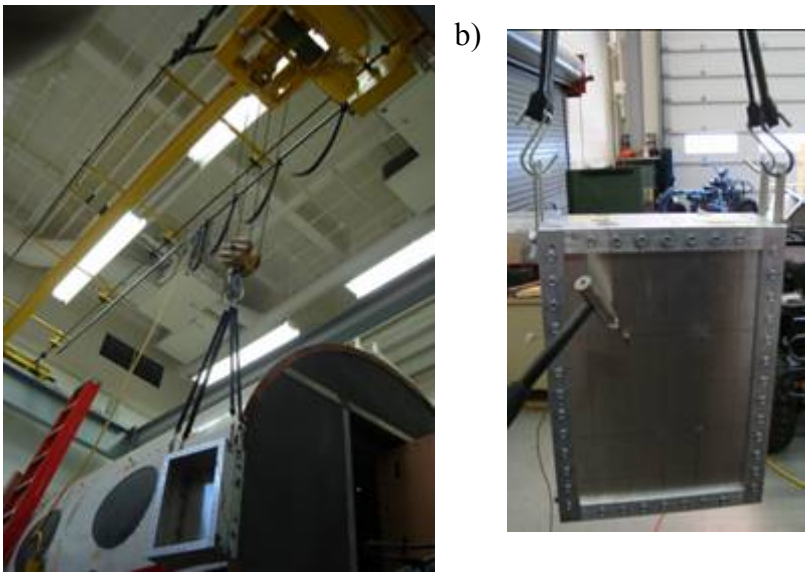

Figure A-4: (a) Picture of the frame for the single bay experiments hung on a crane, (b) Picture of the modal hammer pointing at the accelerometer position for the hung single bay experiments

Figure A-5 shows the spatially averaged velocity of the clamped plate at 25 points compared to that of the frame at four points (a) and a picture of the four

accelerometer positions (red) and the position at which a point force was applied (light blue).

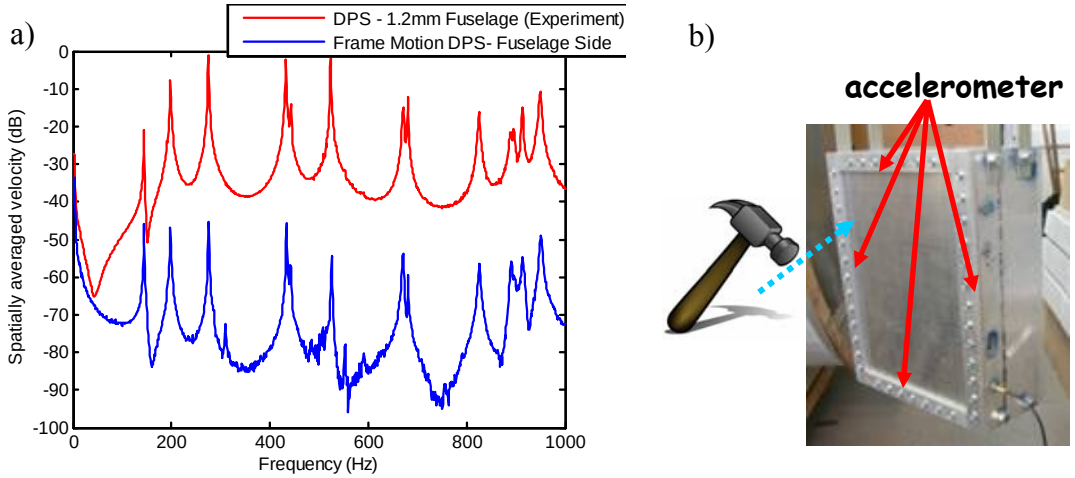

Figure A-5: (a) Measured plate and frame spatially averaged velocity a clamped plate with hung on a crane, (b) picture of experimental setup measuring frame motion on four points while hammering on an off center position

The results in Figure A-5 show an additional improvement on reducing the frame motion of the clamped plate measurements for the single bay DPS measurements. The velocity at lower frequencies is small enough to not cause any major problems in experimentally validating the design tool for the DPS.

In conclusion, three different experimental setups for the DPS were tested and the frame motion was compared to the plate motion in each case. From all three cases, it could be seen that the frame motion was only significant at frequencies lower than the fundamental frequency of the plate. Mounting the frame to a worktable has shown a significant frame motion below the first resonance of the plate, due to tension between frame and plate. Placing the frame on top of poro- elastic material has damped out the frame motion enough to not be significant. Hanging the frame of the DPS has shifted the modes of the frame to lower frequencies. The reduction of the frame motion in the last two cases is satisfactory. Therefore, the single and multi bay double panel system measurements will all be taken by either placing the frame on top of poro-elastic material or by hanging the frame.

A.2. Improved preciseness of torque on frame bolts

After analyzing the frame motion, the second point to check was the repeatability of the DPS measurements. The DPS consists of two clamped plates. The responses of both panels are measured and verified just by themselves before they are validated in the DPS. The response of a single plate was almost identical in theory and experiment as shown in section 2.2.1. In order to build the DPS, one of the two plates has to be removed from the source side and bolted to the receiving side. In an ideal scenario, where the cavity in between the two panels is modeled correctly as well as the coupling between the two panels, the DPS system consequently would match in theory and experiment. This would only be the case if removing the plate from the source to the receiving side would not have any effect, seeing how the frame motion was reduced significantly in the previous section. One way to check the repeatability is to match the DPS measurements with the design tool predictions and then change the source panel to the receiving panel and the receiving panel to the source panel (in other words: swap the DPS around) and see if theory and experimental results still match without changing the aspect ratio of in the design tool. This has been done, and it turned out that this was not the case; hence, the repeatability of this experiment had to be improved. In order to analyze the repeatability of the experiment, the simplest experimental configuration was chosen: a clamped plate by itself. A clamped plate was measured, removed and bolted back to the frame, and it could be seen that the natural frequency of these two measurements were significantly different. The assumed reason for this was a lack in preciseness of the torque on the bolts. In order to solve this problem, a torque wrench was used.

Figure A-6 shows the spatially averaged velocity of the clamped plate (a) using a manual torque wrench (blue), an electric torque wrench (red), and no torque wrench at all (black). An electric drill with torque setting is shown in Figure A-6 (b) and was found to be accurate enough to replace the manual torque wrench. The blue and red lines are almost identical. The black line, in comparison, has some significant variation.

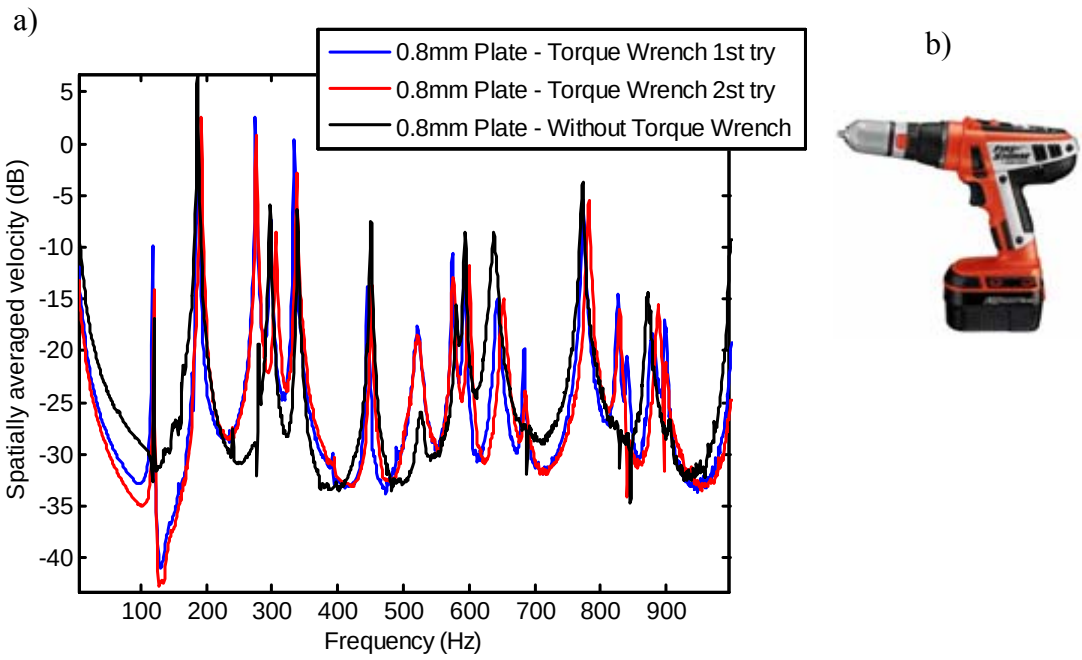

Figure A-6: (a) Comparison between a clamped plated measurement of the spatially averaged velocity using with (red and blue line) and without (black line) using a torque wrench to mount the plate to the frame, (b) picture of used electronic torque wrench

Figure A-6 points out two important facts. First, the preciseness of the torque on the frame bolts could be increased by using a torque wrench. Second, there is no difference in the performance of the DPS between using a manual or electric drill for bolting the plate to the frame. The only difference is, when using a manual torque wrench, one can read the torque off the display; with an electric drill, one can only set the torque to an unspecified level. Seeing how in our case there is no need of knowing the exact torque, the drill was used, because it is easier and faster.

A.3. Improved validation for DPS

After solving the frame motion and repeatability problems in the previous two sections, the experimental validation of the DPS has been redone. The experimental validation before and after improving the DPS are compared (trim panel) in this section.

Figure A-7 shows the experimental validation of the receiving side of the old DPS (a). This validation is compared to the experimental validation with the improved experimental techniques (b). The experimental validation in (a) shows that the dynamics of the trim panel were captured correctly at frequencies below the first four

modes. After that frequency, one can see the correct trends, but it is hard to tell which modes in the experiment belong to the predicted modes. The new experimental validation (b) captures all the modes at the frequency of interest. Note that the discrepancies at low frequencies are most likely caused by the frame motion as the frame is not completely stopped from moving.

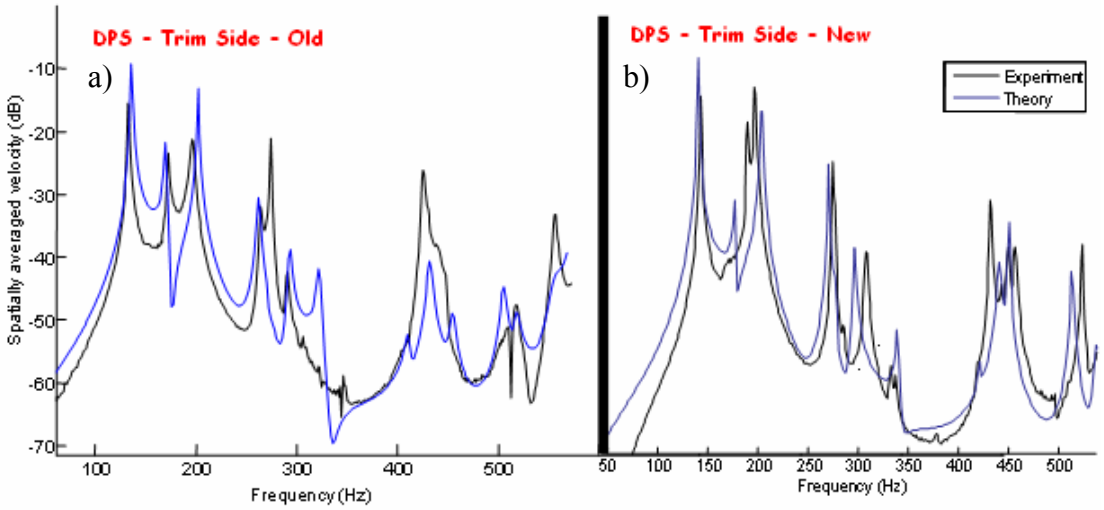

Figure A-7: Comparison of the experimental validation of a single bay DPS on the receiver side (trim), excited at a non center position (a) with and (b) without new improvements

In conclusion, three problems have been considered in order to improve the experimental validation of the DPS. First, the frame motion of the experimental test rig was suspected to influence the plate motion of the DPS plates. Second, the repeatability of the measurements was doubted. Third, the equations for the cavity, coupling the two plates, were assumed to be another source of error. The frame motion was reduced by placing the frame on top of poro-elastic media as well as by hanging the DPS. The repeatability of the DPS measurement was increased by using a torque wrench, which improved the preciseness of the bolts. An experimental validation with the new improvements was compared to the validation obtained before the improvements. The dynamics of the trim panel are now all captured in the frequency of interest. Therefore, there is no need in further analyzing the cavity model for the DPS.

B. HG interface

Going from the FE model to the fully coupled double panel system (DPS) presented in chapter 2, it became difficult to use the design tool by just running the code. In order to clearly lay out the code, the HG interface was developed. The software is composed by several graphical user interfaces (GUIs) that are front ends for the original FE code for the poro-elastic media and other utility functions for the performance evaluation of dynamic systems composed by plates, poro-elastic media and cavity.

The main function loads the default parameters, defines some global variables and runs the main interface. All routines are working with a global structure which contains all the variables that the user can change operating on GUIs.

Figure B-1 shows the main HG interface as it appears by running the main program. Plate and poro-elastic media configurations, parameters and grid size can be chosen dependent or independent from each other. Also, the frequency range for the transfer function plots can be chosen from this interface. Furthermore, there is the option to save and load certain parameter configurations and material properties.

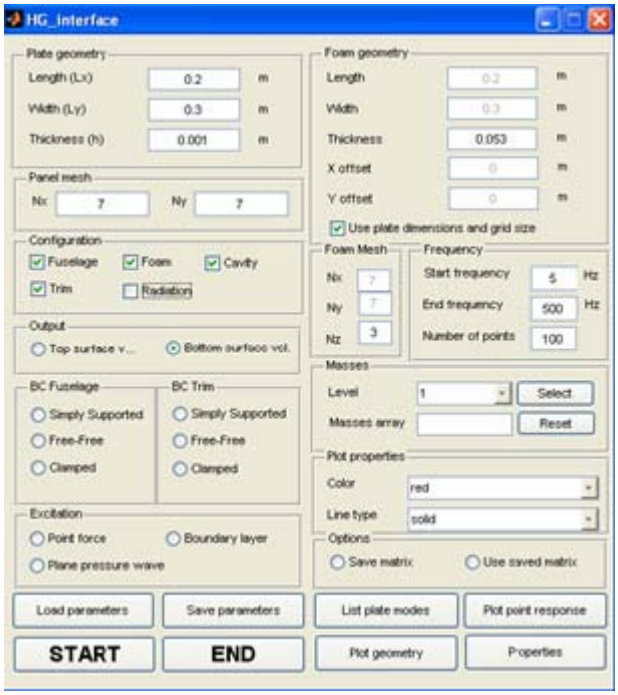

Figure B-1: HG Interface developed for a clearly laid out usage of the developed code for the coupled DPS

Different configurations for the various physics can be chosen as shown in Figure B-2. This is a useful feature when analyzing and debugging the program. Also, for the experimental validation, it is useful to be able to just compute the response of certain configurations first before validating the whole model. Furthermore, different boundary conditions for the fuselage as well as for the trim can be chosen. Another feature is the choice between the different force excitations.

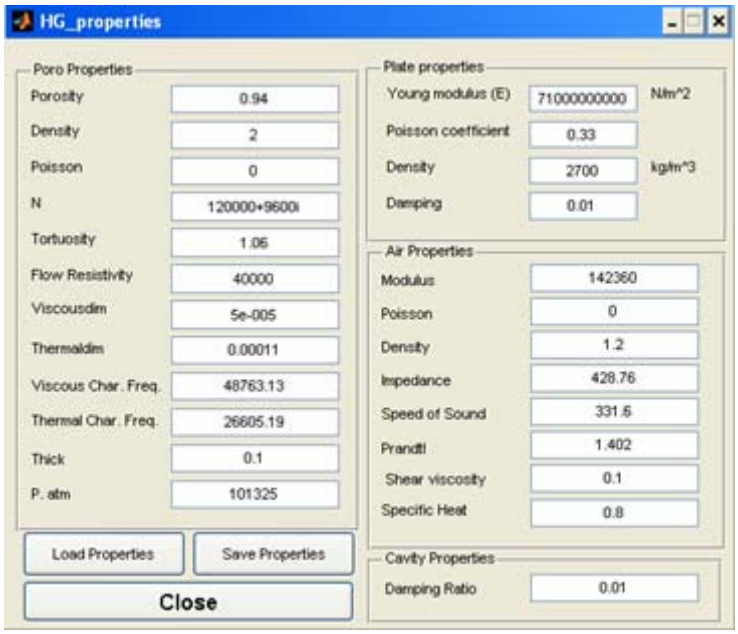

Figure B-2: Material properties in HG interface for DPS

When analyzing the poro-elastic media with the masses inside, it is useful to look at the top and the bottom velocity of the poro-elastic block. Choosing between those velocities is another feature in the HG interface. Since this project deals with masses inside the poro-elastic media, an easy way to add those masses has been developed. Figure B-3 shows the *x-y* plane of the poro-elastic block on the left and a plot of the masses added inside the poro-elastic media on the right. In case the positions for the masses are unsatisfactory, one would just have to push the "reset" button.

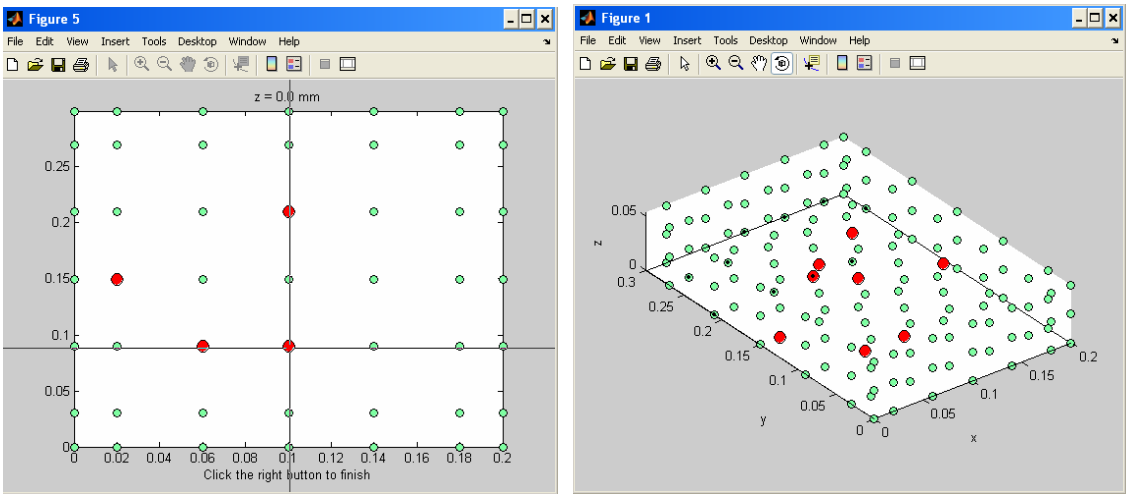

Figure B-3: Choosing the positions of the masses after choosing the level (height) inside the porous media (left). Plot of the masses (red) inside the porous media (right)

Furthermore, magnitude and phase plots for a point response can be created with the HG interface. This is a strong tool when analytically validating the model. Finally, error warnings occur when mistakes are made in the usage of the HG interface. Some error messages are shown in Figure B-4.

Figure B-4: Some Error Warnings in HG interface

C. Verifying repeatability of poro-elastic media test

One major issue when dealing with poro-elastic media is the repeatability of the experiments. Since the poro-elastic media is a synthetic material, the material properties depend on the manufacturing process. A small change in this process can result in a variation of the foam properties. After preliminary tests were performed, it turned out that the poro-elastic material properties vary from sample to sample. If one compares the different measurements (obtained with a shaker experiment described in section 5.1.1.2) in Figure C-1, one can see the high variance of the material properties

of the poro-elastic media. Figure C-1 shows the measured transfer function between the input acceleration of the shaker base and output velocity of a 5.6g ball inside a poro-elastic media block. This measurement was repeated several times with foam from different samples.

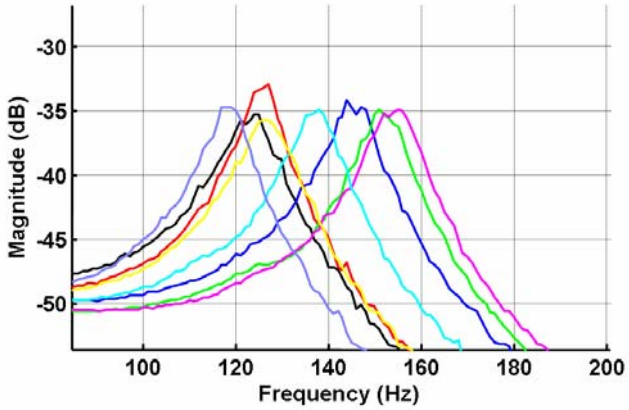

Figure C-1: Measured transfer function between the input acceleration of the base and output velocity of a single mass inclusion of 5.6g in different porous media blocks (140x140x50mm) from different samples

Since the variance of the distribution is unknown, the standard distribution cannot be used for a statistical analysis. However, the relative one-sided confidence interval, s_r, of those measurements can be calculated using the Student's t-distribution that takes the unknown variance with a correction factor *t(p,n)* into account:

$$s_r = \frac{t(p,n)}{\bar{X}} \sqrt{\frac{1}{n(n-1)} \sum_{i=1}^{n} (X_i - \bar{X})^2} \qquad \text{(C-1)}$$

The parameter *t(p,n)* in eq. (C-1) depends on the sample size and the confidence level. X is the stochastic variable of the sample and $\bar{X}$ is the average mean of the variable. Using a *p*=90% confidence level and the above sample size, *n*, the relative one-sided confidence interval can be calculated to 6.8%. This is a comparatively high value, which makes it difficult to derive meaningful conclusions from an experimental investigation.

Figure C-2, in contrast, pictures the same configuration just with porous media from one batch. The variance of this configuration is considerably smaller and the relative one-sided confidence interval can be calculated to 0.6% using eq. (C-1) with a 90% confidence level again. While the physical behavior of the different samples is the

same, the material properties differ. These measurements show that it is important to use only one sample of poro-elastic media for one series of measurements in order to get reasonable results.

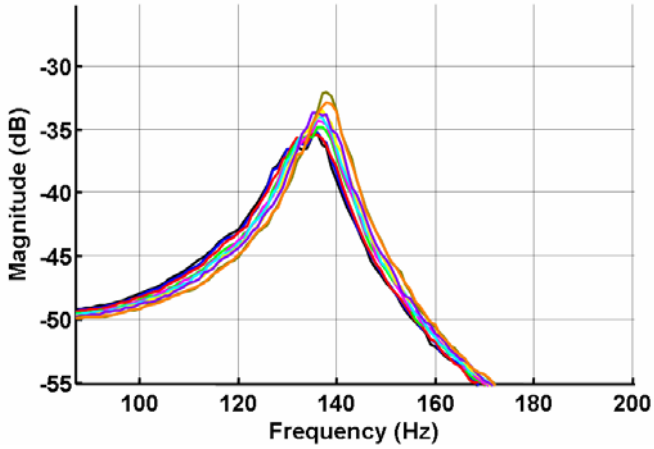

Figure C-2: Resonance frequency for a single mass 5.6g in different porous media blocks (140x140x50mm) from one sample

Another important point is the influence of the adhesive material used for many experiments, whenever a mass was not included in the foam but bonded on top of it. A test showed that the influence of the dried adhesive, in terms of changing the resonance frequency, could be neglected. This validation was performed by measuring the resonance frequency of a disk-shaped mass on top of a poro-elastic block. After the measurement, the block was cut in half and then glued back together. The measurement was repeated and the two resonant frequencies were compared. The whole sequence was repeated ten times to exclude measurement mistakes. The relative deviation between glued and original foam was found to be smaller than 0.1% and can therefore be neglected. However, caution is required with the wet adhesive. For some poro-elastic media, a change in stiffness occurs until the poro-elastic block has completely dried. This process takes up to one hour and therefore makes the experiments very time intensive.

BIBLIOGRAPHY

[1] V. Mellert, I. Baumann, N. Freese, R. Weber, Impact of sound and vibration on health, travel comfort and performance of flight attendants and pilots, *Aerospace Science and Technology (2007), doi:10.1016/j.ast.2007.10.009.*

[2] M.A. Bellmann, H. Remmers, A. Röder, Environmental conditions for cockpit and cabin crew members during long-haul flights. From experimental results to a representative vibro-acoustic input vector for ANN and statistical approaches*, In 33rd German Annual Conference on Acoustics in Stuttgart, DAGA, 2007.*

[3] J.F. Wilby, Aircraft interior noise, *Journal of Sound and Vibration* 190 (1996) 545-564.

[4] M. Carley, Propeller noise fields, *Journal of Sound and Vibration*, 233(2):255-277, 2000.

[5] D.E. Bishop, Cruise flight noise levels in a turbojet transport airplane*, Noise Control* 7, 37-42 (1961).

[6] N.J. Fleming, The silencing of aircraft, *Journal of the Royal Aeronautical Society*, 50, pp. 639-676, 1946.

[7] R.E. Hayden, B.S. Murray, and M.A. Theobald, Boundary-layer-induced noise in the interior of aircraft, *NASA CR-172152*, 1983.

[8] J.F. Wilby and E.G. Wilby, Measurements of propeller noise in a light turboprop airplane, *Journal of Aircraft* 26, 40-47 (1989).

[9] W.V. Bhat, Use of correlation technique for estimating in-flight noise radiated by wing-mounted jet engines on a fuselage, *Journal of Sound and* Vibration 17, 349-355 (1971).

[10] J.F. Wilby and F.L. Gloyna, Vibration measurements of an airplane fuselage structure, II: jet noise excitation, *Journal of Sound and Vibration* 23, 467-486 (1972).

[11] E.J. Richards, Foreword, *Journal of Sound and Vibration* 17, 290-294.

[12] J.P. Carneal, Active structural acoustic control of double panel systems including hierarchical control approaches, PhD Thesis, Virginia Polytechnic Institute and State University, 1996.

[13] P.A. Nelson and S.J. Elliott, *Active control of sound.* Academic Press London, 1993.

[14] C.R. Fuller, Active control of sound transmission/radiation from elastic plates by vibration inputs. I-Analysis, *Journal of Sound and Vibration*, 136 (1990) 1-15.

[15] H.H. Bruderlin, Developments in aircraft sound control, *Journal of the Acoustical Society of America*, 8, pp. 181-184, 1937.

[16] J.P. Carneal, Active structural acoustic control of double panel systems including hierarchical control approaches, PhD Thesis, Virginia Polytechnic Institute and State University, 1996.

[17] P. Gardonio, S.J. Elliott, Active control of structure-borne and airborne sound transmission through double panel. *Journal of Aircraft* 36 (1999) 1023-1032.

[18] R.P.Goss, Acoustic program for the Grumman Gulfstream, *AIAA Paper* (1971) 71-783.

[19] G. SenGupta, Reduction of low frequency cabin noise during cruise condition by stringer and frame damping, *American Institute of Aeronautics and Astronautics Journal* 17 (1979) 229-236.

[20] C.I. Holmer, Approach to interior noise control, part I: damped trim panels, *Journal of Aircraft* 22 (1985) 618-623.

[21] K.E. Heitman, J.S. Mixson, Laboratory study of cabin acoustic treatments installed in an aircraft fuselage, *Journal of Aircraft* 23 (1986) 32–38.

[22] J.S. Mixson, L.A. Roussos, C.K. Barton, R. Vaicaitis, M. Slazak, Laboratory tudy of add-on treatments for interior noise control in light aircraft, *Journal of Aircraft* 20 (1983) 516-522.

[23] H. Baumgartl, Lightweight, Versatile All-rounder, *Kunststoffe international* 5/2006

[24] S.J. Estève and M.E. Johnson, Reduction of sound transmission into a circular cylindrical shell using distribute vibration absorbers and helmholtz resonators, *Journal of the Acoustical Society of America* 112 (2002) 2840–2848.

[25] C.I. Holmer, Approach to interior noise control, part II: self-supporting damped interior shell, *Journal of Aircraft* 22 (1985) 729-733.

[26] H. Osman, M.E. Johnson, C.R. Fuller, P. Marcotte, Interior noise reduction of composite cylinders using distributed vibration absorbers, *7th AIAA/CEAS Aeroacoustics Conference (2001).*

[27] M. Brennan, Vibration control using a tunable vibration neutraliser, *in Proc Instn Mech Engrs, vol. 211 part C, pp. 91–108, 1997.*

[28] S. M. Lee, Normal vibration frequencies of a rectangular two-dimensional array of identical point masses, *Journal of Sound and Vibration*, vol. 45(4), pp. 595–600, 1975.

[29] D.M. Photiadis, Acoustics of a fluid loaded plate with attached oscillators. part 1. feynman rules, *Journal of the Acoustical Society of America*, vol. 102(1), pp. 348–357, 1997.

[30] C.R. Fuller, M.R.F. Kidner, X. Li, and C.H. Hansen, Active-Passive Heterogeneous Blankets for Control of Vibration and Sound Radiation, *In. Proc. Active 04,Williamsburg, VA, USA,, Sep. 20–24 2004.*

[31] M.R.F. Kidner, C.R. Fuller, B. Gardner, Increase in transmission loss of single panels by addition of mass inclusions to a poro-ealstic layer: Experimental investigation, *Journal of Sound and Vibration*, 294 (2006) 466–472.

[32] M.R.F. Kidner, K. Idrisi, J.P. Carneal and M.E. Johnson, Comparison of Experiment, Finite Element and Wave Based Models for Mass Inclusions in Poro-Elastic Layers, *14th International Congress on Sound and Vibration (ICSV14), Cairns, Queensland, Australia, July 9-12, Paper 577 (2007).*

[33] F. Sgard, N. Atalla., C.K. Amedin. “Vibro-acoustic behavior of a cavity backed by a plate coated with a meso-heterogeneous porous material" Acta Acustica United with Acustica, 93 (2007) 106-114.

[34] N. Atalla, C.K. Amedin, F. Sgard “Numerical and experimental investigation of the vibro-acoustics of a plate backed cavity coated with a heterogeneous porous material”, SAE meeting, Traverse City, USA, 2003, 2003-01-1453.

[35] K. Idrisi, M.E .Johnson, J.P. Carneal and M.R.F. Kidner, Passive control of sound transmission through a double panel system using heterogeneous (HG) blankets, Part II: HG parametric studies, *Noise Con ’07 (2007).*

[36] W.T. Thomson, *Vibration Theory and Applications*, Prentice-Hall, IncEnglewood Cliffs, N.J., 1965.

[37] J.P. Den Hartog, *Mechanical Vibrations*, Dover Publications, McGraw Hill, NY, 1934.

[38] F.A. Firestone, A new analogy between mechanical and electrical systems. *Journal of the Acoustical Society of America,* 4 (1933) 249-267.

[39] F.A. Firestone, Twixt earth and sky with road and tube; mobility and classical impedance analogies, *Journal of the Acoustical Society of America,* 4, 28(6), 1117-1153 (1956).

[40] G.J. O'Hara, Mechanical, *Impedance and Mobility Concepts*, U.S. Naval Research Laboratory, Washington, D.C (1966).

[41] P. Gardonio, M.J. Brennan, On the origin and development of mobility and impedance methods in structural dynamics, *Journal of Sound and Vibration*, 249 (2002) 557-573.

[42] R. Panneton, N. Atalla, An efficient finite element scheme for solving the three-dimensional poroelastic problem in acoustics, *Journal of the Acoustical Society of America*, 101 (1997) 3287 – 3298.

[43] Idrisi K., Johnson M. E., Carneal J. P., Toso A., *Addition of mass inclusions to a poro-elastic layer for improved passive control of aircraft interior noise: A comparison between theory and experiment*, Accepted for publication in Journal of Sound and Vibration

[44] Idrisi K., Johnson M. E., Carneal J. P., *Control of aircraft interior noise using heterogeneous (HG) blankets*, Proceedings of Meetings on Acoustics, Vol.1, 065001 (2008)

[45] Idrisi K., Johnson M. E., Carneal J. P., *Passive control of sound transmission through a double panel using heterogeneous (HG) blankets, Part I: Modeling and validation*, In. Proc. Noise-Con 2007 Reno Nevada, Oct. 22–24 2007

[46] Idrisi K., Johnson M. E., *Multi-Bay double panel system with heterogeneous blanket treatment: a comparison between theory and experiment,* In 155th Meeting Of The Acoustical Society Of America, 5th Forum Acusticum, And 9th Congrès Français d'Acoustique, Paris, France, 29 June-4 July 2008

[47] Idrisi K., Johnson M. E., Carneal J. P., *Passive control of sound transmission through a double panel using heterogeneous (HG) blankets, Part III: HG design strategies*, In. Proc. Noise-Con 2007 Reno Nevada, Oct. 22–24 2007

[48] Idrisi K., Johnson M. E., Carneal J. P., *Heterogeneous (HG) blanket design strategies for passive control of aircraft interior noise*, Accepted for publication in Noise Control Engineering Journal

[49] Idrisi K., Johnson M. E, Toso A., *Comparison of optimization routines for the design of heterogeneous blankets,* In. Proc. Noise-Con 2008, Dearborn, MI, 29-30 July 2008

[50] Idrisi K., Bartylla D., Johnson M. E., Wagner A., *Sensitivity of heterogeneous blanket design to parameter variation*, In. Proc. Noise-Con 2008, Dearborn, MI, 29-30 July 2008

[51] Idrisi K., Johnson M. E., Carneal J. P., Theurich D., *A study on the behavior of mass inclusions added to a poro-elastic layer*, manuscript submitted in October 2008 to Journal of Sound and Vibration

[52] M.A. Biot, Theory of propagation of elastic waves in a fluid-saturated porous solid. I. Low-frequency range. *The Journal of the Acoustical Society of America*, 28 (1956) 168 – 178.

[53] J.F. Allard, *Propagation of sound in porous media, modeling sound absorbing materials*, Elsevier Science Publishers LTD., London, 1993.

[54] Idrisi K., Wagner A., Johnson M. E., Bartylla D., *On heterogeneous blankets: Analytical solution for the interaction between masses and poro-elastic layers,* In 155th Meeting Of The Acoustical Society Of America, 5th Forum Acusticum, And 9th Congrès Français d'Acoustique, Paris, France, 29 June-4 July 2008

[55] P. Gardonio, M.J. Brennan, Active isolation of structural vibration on a multiple- degree-of-freedom system, Part I: The dynamics of the system. *Journal of Sound and Vibration* 207 (1997) 61-93.

[56] G. Warburton, The vibration of rectangular plates. *Proceedings of the Institution of Mechanical Engineers,* 168 (1954) 371-384.

[57] R. Panneton, N. Atalla, An efficient finite element scheme for solving the three-dimensional poroelastic problem in acoustics. *Journal of the Acoustical Society of America*, 101 (1997) 3287 – 3298.

[58] L. Kinsler, A. Frey, A. Coppens, J. Sanders, *Fundamentals of acoustics*, Wiley, New York, 1999.

[59] P.A. Nelson and S.J. Elliott: *Active control of sound.* Academic Press, London, 1993

[60] S.J. Elliott and M.E. Johnson, Radiation modes and the active control of sound power. *Journal of the Acoustical Society of America,* 94 (1993) 2194–2204.

[61] M.R. Bai, M. Tsao, Estimation of sound power of baffled planar sources using radiation matrices. *Journal of the Acoustical Society of America*, 112 (2002) 876-883.

[62] A.P. Berkhoff, Sensor scheme design for active structural acoustic control. *Journal of the Acoustical Society of America*, 108 (2000) 1037-1045.

[63] P. Gardonio, M.J. Brennan, On the origin and development of mobility and impedance methods in structural dynamics. *Journal of Sound and Vibration*, 249 (2002) 557-573.

[64] P. Gardonio, M.J. Brennan, *Mobility and impedance methods in structural dynamics*, Spon Press, New York, 2004.

[65] P. Gardonio, and M.J. Brennan, *Mobility and impedance methods in structural dynamics: an historical review,* ISVR Technical Report 289, Southampton, University of Southampton, 2000.

[66] K.A. Mulholland, H.D. Parbrook, A. Cummings, The transmission loss of a double panel. *Journal of Sound and Vibration,* 6 (1967) 324-334.

[67] A. Gautam, C.R. Fuller, J.P. Carneal, Application of the Heterogeneous blankets (HG blankemts) for controlling the base structure vibration levels, *Noise Con '05 (2005).*

[68] C.R. Fuller, S.J. Elliott and P.A. Nelson. *Active Control of Vibration* (1st Edition ed.), Academic Press, London (1996).

[69] B.T. Wang, C.R. Fuller and E.K. Dimitriadis, "Active control of noise transmission through rectangular plates using multiple piezoelectric or point

force actuators. *Journal of the Acoustical Society of America*, 90 (1991) 2820 – 2830.

[70] M.E. Johnson, Active Control of Sound Transmission, PhD Thesis, University of Southampton, 1996.

[71] K.R. Matthews, Elementary linear Algebra, Dept. of Mathematics, University of Queensland (1991), http://www.numbertheory.org/book/ (Accessed 21 February 6, 2008).

[72] Idrisi K., Johnson M. E., Carneal J. P., Kidner M. R. F., Passive control of sound transmission through a double panel using heterogeneous (HG) blankets, *In. 153rd Meeting of Acoustical Society of America (2007) in Salt Lake City, Journal of the Acoustical Society of America,* Vol. 121, No. 5, Pt. 2, *May 2007.*

[73] A.W. Leissa, *Vibration of Plates*, NASA SP-160, 1969.

[74] F.A. Firestone, "The mobility method of computing the vibration of linear mechanical and acoustical systems: mechanical-electrical analogies, *Journal of Applied Physics*, 9, 373-387 (1938).

[75] C.R. Fuller, M.R.F. Kidner, X. Li, and C.H. Hansen, Active-Passive Heterogeneous Blankets for Control of Vibration and Sound Radiation, *In. Proc. Active 04,Williamsburg, VA, USA,, Sep. 20–24 2004.*

[76] N. Alujević, K.D. Frampton, P. Gardonio, Stability and performance of a smart double panel with decentralized active dampers, *The American Institute of Aeronautics and Astronautics Journal. 46(7), 2008, 1747-1756.*

[77] M.E. Johnson, J.P. Carneal, C. R. Fuller and H. Osman, Control of shock transmission through an aerospace structure using optimally damped distributed vibration absorbers, *12th International Congress on Sound and Vibration Jul. 11-14th 2005.*

[78] H. Frahm, Device for damping vibrations of bodies, U.S. Patent No. 989958, 1909.

[79] J. Dayou, M.J. Brennan, Global control of structural vibration using multiple-tuned tunable vibration neutralizers, *Journal of Sound and Vibration (2002) 258(2), 345–357.*

[80] R.G. Jaquot, Suppression of random vibration in plates using vibration absorbers, *Journal of Sound and Vibration (2001) 248(4), 585-596*.

[81] P. Hagedorn, Lineare Schwingungen kontinuierlicher mechanischer Systeme, Springer-Verlag, Berlin, Heidelberg, New York, 1989.

[82] N.H. Schiller, Decentralized control of sound radiation from periodically stiffened panels, PhD Thesis, Virginia Polytechnic Institute and State University, 2007.

[83] K.U. Ingard and T.A. Dear, Measurements of acoustic flow resistance. *Journal of Sound and Vibration* 103 (1985) 567–572.

[84] J. Park, Measurements of the frame acoustic properties of porous and granular materials. *Journal of the Acoustical Society of America*, 118 (2005) 3483 – 3490.

[85] A. P. S. Selvadurai: *Mechanics of poroelastic media ,* Kluwer Academic Publishers, Dordrecht, 1996

[86] R. de Boer: Theory of porous media: Highlights in historical development and current state, Springer, Berlin, Heidelberg and New York, 2000

[87] K. Attenborough: Acoustical characteristics of porous materials, *Physics Reports* 82(3), 1982, 179 – 227

[88] W. Becker and D. Gross: *Mechanik elastischer Körper und Strukturen*. Springer, Berlin and Heidelberg, 2002